HYDRAZONE EXCHANGE IN NANOPARTICLE MONOLAYERS: A DYNAMIC COVALENT APPROACH FOR CONTROLLING NANOMATERIAL PROPERTIES
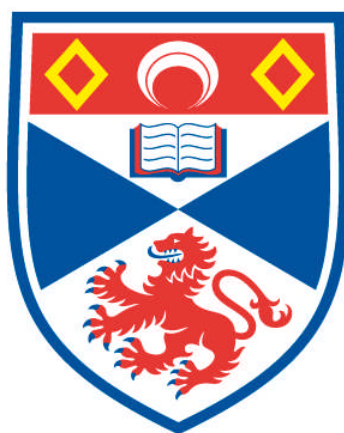
Flavio della Sala

**A Thesis Submitted for the Degree of PhD
at the
University of St Andrews**

2015

**Full metadata for this item is available in
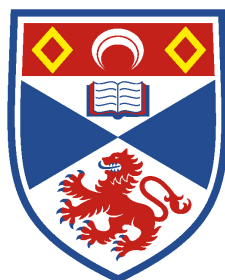Research@StAndrews:FullText
at:
http://research-repository.st-andrews.ac.uk/**

**Please use this identifier to cite or link to this item:
http://hdl.handle.net/10023/6766**

Hydrazone Exchange in Nanoparticle Monolayers: a Dynamic Covalent Approach for Controlling Nanomaterial Properties

by
Flavio della Sala

University of
St Andrews

This Thesis is submitted in partial fulfilment
for the degree of
Doctor of Philosophy
at the
School of Chemistry
University of St Andrews

April 2015

1. Candidate's declarations:

I, Flavio della Sala, hereby certify that this thesis, which is approximately 52,000 words in length, has been written by me, and that it is the record of work carried out by me and that it has not been submitted in any previous application for a higher degree.

I was admitted as a research student in January 2011 and as a candidate for the degree of PhD in January 2015; the higher study for which this is a record was carried out in the University of St Andrews between 2011 and 2015.

Date 02/04/2015 signature of candidate ………

2. Supervisor's declaration:

I hereby certify that the candidate has fulfilled the conditions of the Resolution and Regulations appropriate for the degree of PhD in the University of St Andrews and that the candidate is qualified to submit this thesis in application for that degree.

Date 02/04/2015 signature of supervisor ………

3. Permission for publication:

In submitting this thesis to the University of St Andrews I understand that I am giving permission for it to be made available for use in accordance with the regulations of the University Library for the time being in force, subject to any copyright vested in the work not being affected thereby. I also understand that the title and the abstract will be published, and that a copy of the work may be made and supplied to any bona fide library or research worker, that my thesis will be electronically accessible for personal or research use unless exempt by award of an embargo as requested below, and that the library has the right to migrate my thesis into new electronic forms as required to ensure continued access to the thesis. I have obtained any third-party copyright permissions that may be required in order to allow such access and migration, or have requested the appropriate embargo below.

The following is an agreed request by candidate and supervisor regarding the publication of this thesis:

PRINTED COPY
a) No embargo on print copy

ELECTRONIC COPY
a) No embargo on electronic copy

Date 02/04/2015 signature of candidate ……   signature of supervisor ………

Table of contents

Synopsis

This Thesis reports the synthesis, purification and characterisation of gold nanoparticles (NPs) functionalised with a monolayer of hydrazone ligands in order to perform post-synthetic manipulations of the NP-bound monolayer exploiting dynamic covalent chemistry. NP post-synthetic manipulation based on reversible non-covalent interactions between oligonucleotides represents a promising approach to achieve functionalisation and self-assembly for potential applications in biology and medicine. However, the stability of these nanosystems is ensured only in a narrow window of environmental conditions. On the other hand, irreversible covalent strategies potentially allow the full range of synthetic chemistry to be exploited but they provide poor control over the manipulation of the NP-bound monolayer and can only produce kinetically controlled amorphous NP aggregates. Dynamic covalent chemistry represents an interesting and an attractive alternative approach because it would combine the reversibility of non-covalent interactions with the stability of covalent bonds. By this way, ligand-functionalised NPs could be manipulated in order to introduce a large variety of molecular functionalities on the NP surface not only to subtly tune the NP physicochemical properties but also to access an entire range of novel nanomaterials.

Chapter **1** introduces the concept and background to ligand-stabilised inorganic NPs, with a particular focus on AuNPs. The leading synthetic routes to AuNPs are presented and strategies for introducing functionality to the stabilising surface molecular monolayer are discussed. The mechanisms involved in NP growth and stabilisation are also explained.

A variety of analytical techniques is required in order to assess different features of ligand-functionalised AuNPs including successful NP synthesis and functionalisation, NP size reproducibility, structural integrity of the NP-bound organic ligand and sample purity. Among the many available characterisation approaches, the analytical techniques employed in this study are reviewed.

Post-synthetic strategies for NP functionalisation are then introduced, including reversible non-covalent and irreversible covalent approaches. The advantages, disadvantages and applications of each approach are discussed. In order to combine the advantages of both strategies, dynamic covalent chemistry, and in particular dynamic hydrazone exchange, is presented as an alternative for the functionalisation and post-synthetic manipulation of ligand-functionalised AuNPs.

Chapter **2** reports the design, synthesis and characterisation of two classes of hydrazone ligand for AuNPs: *N*-acyl and *N*-aroyl hydrazones. Synthesis of AuNPs functionalised with these ligands is explored *via* two alternative approaches (ligand exchange and direct synthesis) and optimised routes to achieve functionalised AuNPs with reproducible size and low dispersity are described. A rigorous characterisation protocol is then established in order to achieve both the 'nanoparticulate' characteristics and the structure of the NP-bound hydrazone monolayer.

Chapter **3** reports the first examples of dynamic hydrazone exchange in a NP-bound monolayer. Investigations of the reactivity of the NP-bound hydrazone monolayer under hydrolysis and dynamic exchange conditions with an acid catalyst are illustrated. The reversibility of hydrazone exchange on NP-bound monolayer is assessed by a combination of several analytical techniques. Subsequently, the reactivity of the hydrazone monolayer under hydrolysis and hydrazone exchange conditions is quantitatively investigated and compared to the reactivity, under identical conditions, of analogous molecular hydrazone species.

Chapter **4** reports the reversible switching of hydrazone-functionalised AuNPs between polar organic, apolar organic and aqueous solvents based on dynamic hydrazone exchange. A combination of optical, spectroscopic and spectrometric techniques provides evidence that changes in NP solvent compatibility result from dynamic hydrazone exchange within the NP-bound monolayer.
Non-covalent self-assembly of hydrazone-functionalised AuNPs dependent on solvent polarity, and preliminary observations of covalent NP self-assembly with a bifunctional linker *via* dynamic hydrazone exchange under acidic conditions are also reported.

Chapter **5** includes the experimental and synthetic procedures for the synthesis of all non-commercial chemical entities; methods for AuNP synthesis and functionalisation; and NP post-synthetic manipulation of the hydrazone monolayer.
Additional data and analysis are also included to support: the kinetic studies on the reactivity of NP-bound and unbound hydrazone species, NP solubility switching and the non-covalent and dynamic covalent NP self-assembly.

A preliminary communication reporting the preparation of hydrazone-functionalised gold nanoparticles, the characterisation of the nanoparticle-bound dynamic covalent hydrazone exchange process and its exploitation to control nanoparticle solubility properties has been published in *Angewandte Chemie* (a reprint can be found in the Appendix).

Acknowledgements

Abbreviations

A	Absorbance	s.d.	Standard deviation
Ac	Acetyl	SEC	Size exclusion chromatography
Ald	Aldehyde		
Ar	Aryl	SPR	Surface plasmon resonance
(Au)NP(s)	(Gold) nanoparticle(s)		
Bu	Butyl	t	Time *or* triplet
calc.	Calculated	T_1	Spin-lattice relaxation time
c-Hex	Cyclohexane	T_2	Spin-spin relaxation time
d	Diameter *or* doublet	TBAB	*tert*-Butylamine borane complex
dd	Doublet of doublets		
D1	Delay time	TEG	Tetraethylene glycol
δ	Chemical shift	TEM	Transmission electron microscopy
DCC	Dynamic covalent chemistry		
		TFA	Trifluoroacetic acid
DLS	Dynamic light scattering	THF	Tetrahydrofuran
DMF	*N,N*-Dimethylformamide	TLC	Thin layer chromatography
DMSO	Dimethyl sulfoxide	TOAB	Tetraoctylammonium bromide
DNA	Deoxyribonucleic acid		
ε	Molar extinction coefficient	Trt	Trityl
Eq	Equivalent	*p*-TSA	*p*-Toluenesufonic acid
ESI	Electrospray ionisation	UV-Vis	Ultraviolet-visible
Et	Ethyl	W	Watt
φ	Volume fraction		
h	Hour		
HexH	Hexane		
(HR)MS	High resolution mass spectrometry		
Hy	Hydrazone		
J	Coupling constant		
LDI	Laser desorption ionisation		
lit.	Literature		
Me	Methyl		
(M)Hz	(Mega)hertz		
m	Multiplet		
min	Minute		
(m)M	(Milli)molar		
μM	Micromolar		
M.p.	Melting point		
Ms	Mesyl		
MS	Mass spectrometry		
MW	Microwave		
NMR	Nuclear magnetic resonance		
Ph	Phenyl		
ppm	Parts per million		
Q	Reaction quotient		
R*f*	Retention factor		
RNA	Ribonucleic acid		
rt	Room temperature		
s	Second *or* singlet		

Chapter 1: Introduction

This Chapter introduces the preparation, characterisation and manipulation of ligand-functionalised gold nanoparticles (AuNPs). The most used liquid-phase methods for NP synthesis are presented, introducing the mechanistic understanding of the processes of NP growth and stabilisation.

The characterisation of both 'nanoparticulate' properties (i.e. core size, optical and colloidal properties) and the NP-bound organic monolayer is then introduced and discussed.

The NP functionalisation and post-synthetic manipulation is then introduced, including methods based on non-covalent interactions (e.g. oligonucleotide functionalisation) and methods based on irreversible covalent functionalisation, including a series of irreversible covalent reactions, which can be performed in the NP-bound monolayer.

Finally, dynamic covalent chemistry (DCC), and in particular dynamic hydrazone exchange, is presented as a valid approach for the functionalisation and post-synthetic manipulation of hydrazone functionalised AuNPs.

1.1 Nanoparticulate functional materials

In the last two decades, metal NPs have attracted considerable interest because they have unique optical,[1–5] magnetic[6,7] and electronic[8–10] properties, which make them different from atoms and bulk materials. These properties are a result of NP size, size-quantum effects and surface-dependant effects.[11] The investigation of these effects has dramatically increased as synthetic methods for the preparation of metal NPs became accessible.[12–14]

In order to prevent irreversible aggregation and precipitation, metal NPs must be functionalised with a ligand shell. Such functionalisation, which can be achieved by using a large variety of ligands in terms of structure and properties, can in theory confer a wide range of potential physical and chemical properties to NPs and, thus, potential applications in many fields: electronics,[15,16] analytical chemistry,[17] heterogeneous catalysis,[18–21] biology,[22] drug delivery and medicine.[23,24] Unfortunately, the number of ligand that can be used for NP functionalisation is limited

by the ligand compatibility with the NP synthetic conditions. In addition, few strategies for the post-synthetic manipulation of NP-bound ligands are available[14,25–27] if compared to the numberless methods available for the transformation of molecular functionalities.

By using ligand-functionalised metal NPs, an ideal further step would be the preparation of ordered materials by connecting NPs covalently to each other, where the organic ligands play a crucial role in a similar manner in which chemical bonds connect atoms to form molecules. However, the preparation of this type of nanomaterial is still extremely challenging because a full comprehension of the reactivity of the NP-bound organic monolayer is poorly understood.[28] Yet, the reactivity of the monolayer cannot be deeply investigated without first achieving high control over the functionalisation and purification processes.

1.2 Noble metal nanoparticle synthesis

NPs can be prepared from many materials including noble metals such as gold, silver and platinum; polymers, semi-conducting materials to give quantum dots, carbon and silica.[12,14,29]

Colloidal solutions of various metal NPs are commercially available. However, there are a number of routinely employed methods, developed in recent years, which allow the preparation of NPs starting from their corresponding metal precursors. Synthetic methods can be divided into three main groups: grinding methods, gas-phase methods and liquid-phase methods.[1]

Grinding methods are usually quite cheap but, on the other hand, provide highly polydisperse NPs and aggregates. In addition, it is common to obtain NPs contaminated with unreacted starting materials and only a small portion of them has a mean diameter less than 50 nm. However, considering the relatively low production costs, grinding methods are particularly used for industrial processes, for instance in the preparation of drugs.[30]

Gas-phase methods usually consist of continuous processes providing high quality but non-functionalised NPs. Since the working temperatures are usually higher than 500 °C, gas-phase methods are not suitable for routine preparations. As for grinding methods, gas-phase methods are particularly popular in industry, for example in the preparation of pigments for inks, coatings and plastics.[31]

Liquid-phase methods are most widely used because they allow a good control of size distribution and shape. In addition, a careful control of the nucleation and growth

processes[32] to avoid aggregate formation can be achieved by functionalising NPs with organic ligands, which work as stabilisers and form a shell that prevents NPs from irreversibly aggregating and can be a handle for further manipulations.

Noble metal NPs, and in particular gold NPs, have long been one of the most intensively investigated nanomaterials. The distinguish size-quantum and surface-dependent effect shown by AuNPs inspired the development of many synthetic routes.[29] By this way, AuNPs can be obtained with relative ease for potential applications in analytical chemistry, heterogeneous catalysis and optics. In addition, gold is inert and stable under the conditions optimised for NP synthesis. It is also cheaper than other noble metals and, moreover, it is relatively non-toxic, making it a very good candidate for potential biological and medical applications.[29]

1.2.1   Liquid-phase nanoparticle synthesis

According to the model developed by LaMer and Dinegar,[32] two main processes are involved in NP formation: nucleation and growth. This model was developed in 1950 and is still generally accepted. Nucleation is an endothermic process, since energy is required to break bonds of the initial metal precursor, to remove the solvate shells and to overcome the surface tension of the solvent. On the other hand, particle growth, independent from the nucleation process, is an exothermic process because the enthalpy of formation of the solid is released. Particle aggregation is also exothermic because it reduces the overall surface area. As a result of this balance of energetic contributions, any method chosen for the NP synthesis will afford an uncontrolled NP aggregation, hard to re-disperse in any solvent, if the growing NPs are not stabilised (Figure **1.1**).[1]
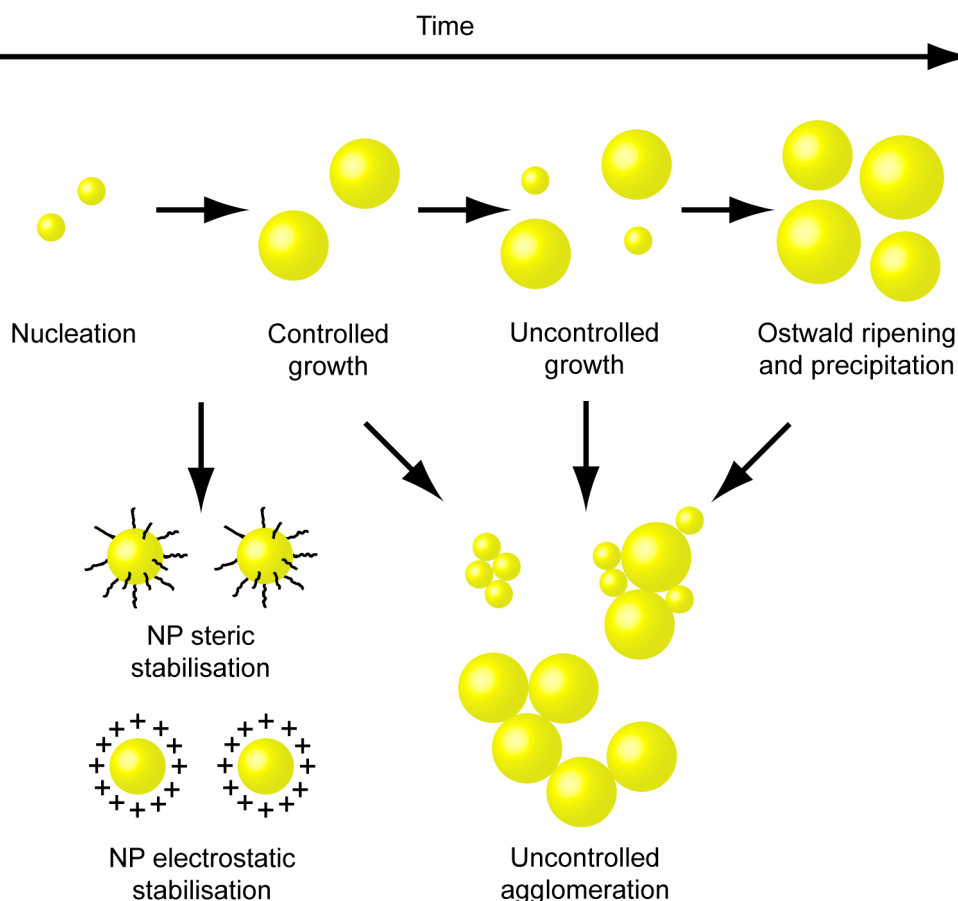
Figure 1.1   General scheme for the growth and stabilisation of NPs. After nucleation, NPs tend to grow without control because the agglomeration is energetically favoured. The result is insoluble NP aggregates, which precipitate from the reaction solvent. NP growth can be controlled by a steric or an electrostatic stabilisation.[1]

The growing particle surfaces must be saturated immediately to avoid irreversible NP aggregation. The stabilisation can be electrostatic, steric or a combination of the two. The NP size is determined by the amount of stabiliser used and by the rate of addition of the stabiliser to the reaction mixture. Electrostatic stabilisation can be achieved by adsorption of charged inorganic or organic species (e.g. H^+, OH^-, SO_4^{2-}, NO_3^-, $RCOO^-$, RSO_3^-, R_4N^+ etc.). Steric stabilisation is obtained by using long-chain organic molecules containing at one end phosphorus, nitrogen or sulfur atoms, which form strong interactions with the metal atoms.[14,29]

1.2.1.1 *Electrostatic stabilisation: the Turkevich–Frens method*

One of the first methods for the preparation of water-soluble AuNPs was developed by Turkevich and co-workers in 1951.[33] This procedure, generally known as the 'citrate method', was further optimised by Frens in 1973.[34] This method allows a broad size range of citrate-stabilised AuNPs, with reproducible mean diameters (15–150 nm)

although NPs > 20 nm are always polydisperse.[14,34] The original Turkevich method involves heating tetrachloroaurate solutions to boiling and subsequent addition of sodium citrate under vigorous mechanical stirring. After a few minutes, the solution turns a blue-purple colour, which is an indication of NP formation (see Section **1.3.2**).[33] Temperature and citrate concentration affect the size and the dispersity of the forming AuNPs. The dispersity is generally quantified as one unit of standard deviation in relation with the average diameter.

Turkevich provided a mechanism for the nucleation process, postulating that the citrate ions act as nucleating agent and gradually form a complex with the gold ions. When a sufficient number of gold ions is incorporated into this large 'macromolecule', a 'molecular rearrangement' occurs to produce metallic AuNPs reduced by the citrate with concurrent production of oxidation products of the reducing agent.[33] The mechanism of NP formation and the role of the citrate as stabiliser is still under debate.[35] A generally accepted mechanism is shown in Scheme **1.1**. The citrate is oxidised to dicarboxyacetone as the auric salt is reduced to aurous salt (a). Then, a disproportionation of the aurous species occurs forming gold(0) atoms (b).[36,37]
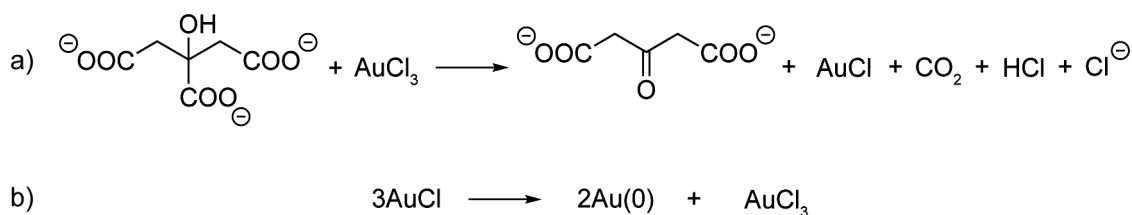
Scheme 1.1   Proposed mechanism for the reduction of Au(III) species for the preparation of AuNPs using citrate as reducing agent. a): oxidation of the citrate to dicarboxyacetone. b): disproportionation of Au(I) to Au(0) and Au(III).[36,37]

The disproportionation step requires three aurous chloride molecules (Scheme **1.1B**) that are coordinated by the dicarboxyacetone molecules (Scheme **1.2**). In this way, the citrate plays a double role as both reducing agent and stabiliser.[14]

Although the 'citrate method' is used in the vast majority for both commercial and research water-soluble AuNP production, few improvements have been made in order to achieve better control over size and dispersity because the basis procedure remains the same. By this method, obtaining AuNPs < 5 nm in size remains challenging. On the other hand, for AuNPs > 50 nm the size dispersity increases and NPs tend to aggregate.[34]
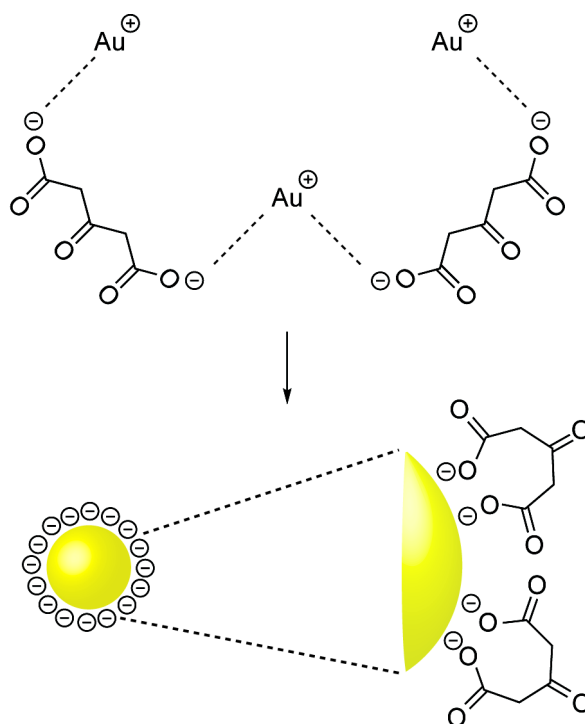
Scheme 1.2   Proposed formation of the complex of Au(I) with dicarboxyacetone during the synthesis of AuNPs *via* the citrate reduction. Au(I) is coordinated by a minimum of two dicarboxyacetone molecules. Au(I) undergoes disproportionation followed by AuNP growth.[14,36]

In order to improve control over size and dispersity, citrate-stabilised AuNPs can be prepared employing a 'seeded-growth' approach. This method involves two steps. In the first step, small pre-synthesised AuNP 'seeds' are prepared. In the second step, the seeds are added to a solution containing tetrachloroauric acid and a reducing agent. By this way, bigger AuNPs are formed by gradual enlargement of the small NP seeds. Control over the NP final size is achieved by tuning the composition of the 'growth' solution. In addition, better control over size dispersity is also obtained because Au(III) ions in solution are gradually reduced and adsorbed on the seeds avoiding secondary nucleation processes which are the main cause of size dispersity.[14] This method was pioneered by Natan and co-workers using citrate and 12 nm AuNP seeds.[38] Murphy and co-workers reported instead the synthesis of 3.5 nm citrate-functionalised AuNP seeds by dropping an ice-cold aqueous solution of sodium borohydride into a solution containing tetrachloroauric acid and citrate.[39] Sodium borohydride is a stronger reducing agent than citrate and allows the preparation of smaller AuNPs (size range 1–5 nm) as a result of the faster nucleation process induced by this reducing agent.[40]

1.2.1.2   Steric stabilisation: the Brust–Schiffrin method

While the citrate method is widely used to prepare water-soluble AuNPs, an alternative method developed by Brust and Schiffrin in 1994 has had a tremendous impact for the synthesis of smaller AuNPs in organic solvents.[40] By this method, AuNPs could be functionalised with more complicated functionalities and at a higher concentration than could be achieved with the 'citrate method'.

The Brust–Schiffrin method was the first phase transfer approach for preparing thiol-stabilised AuNPs using tetrachloroauric acid and 1-dodecanethiol in an equimolar ratio. The procedure consists of two steps. In the first step, gold(III) ions in aqueous solution are extracted into toluene using tetraoctylammonium bromide (TOAB), which acts as both transferring and stabilising agent. In the second step, 1-dodecanethiol is added to the organic phase, before reduction of the metal is achieved by addition of sodium borohydride. The overall reaction is summarised by Equations **1.1** and **1.2**.

$$AuCl_4^-{}_{(aq)} + N(C_8H_{17})_4^+{}_{(toluene)} \rightarrow N(C_8H_{17})_4^+AuCl_4^-{}_{(toluene)}$$

Equation 1.1

$$mAuCl_4^-{}_{(aq)} + nC_{12}H_{25}SH_{(toluene)} + 3me^- \rightarrow 4mCl^-{}_{(aq)} + (Au_m)(C_{12}H_{25}SH)_{n(toluene)}$$
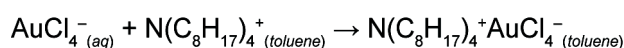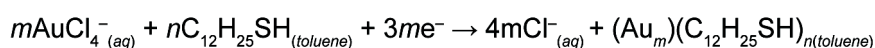
Equation 1.2

By this method, the NP growth and the formation of the stabilising monolayer are simultaneous. The amount of thiol ligand plays a crucial role in determining the final NP size. In fact, the thiol ligands are progressively adsorbed on the metal surface providing a steric stabilisation of the growing NP. The result is a more efficient control over the NP size with better dispersity when compared to those exhibited in the citrate method (Section **1.2.1.1**). By using the original Brust–Schiffrin procedure, AuNPs with diameters in the range 1–3 nm were obtained.

The Brust–Schiffrin method became extremely popular because it provided numerous advantages in comparison to all previous NP synthetic methods: facile synthesis in ambient conditions, thermal and air stability, small AuNP size with narrow dispersity, relative ease of post-functionalisation and modification by ligand exchange (Section **1.4**). However, there remains little knowledge about the mechanism involved in the NP formation and the nature of the intermediate species involved was unknown. A generally accepted hypothesis was developed by Murray,[41] who postulated the formation of a Au(I)-thiol polymer complex in the organic phase before the addition of the reducing agent (Scheme **1.3**).
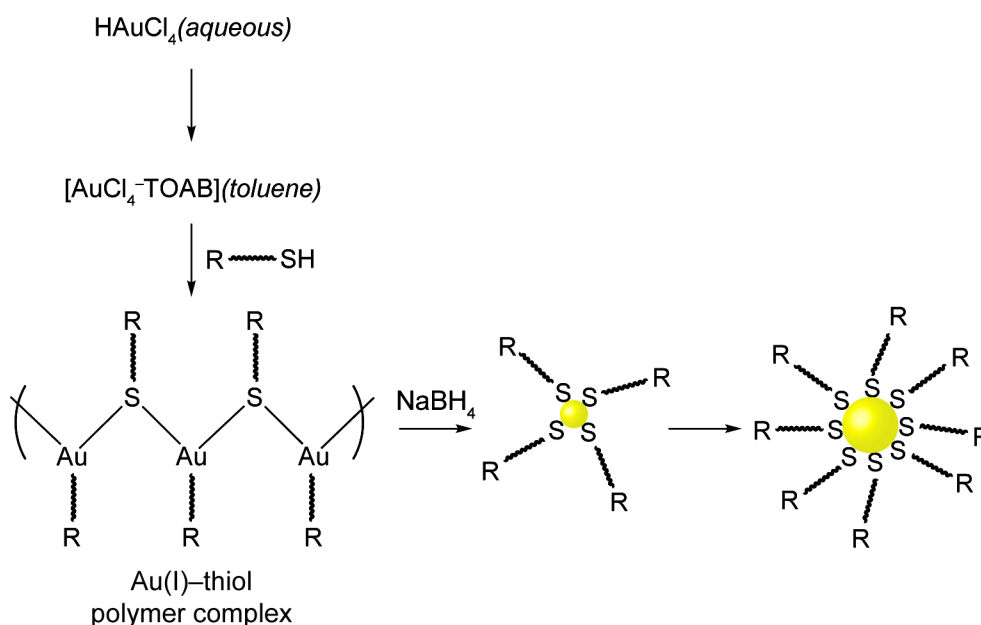
Scheme 1.3   General mechanism for the synthesis of AuNPs functionalised with 1-dodecanethiol *via* the Brust–Schiffrin method, as postulated by Murray.[41] The key precursor in Murray's hypothesis is the presence of a polymer complex in the organic phase between Au(I) and the thiol before NaBH$_4$ addition.

A deeper investigation carried out independently by Lennox[42] and Tong[43] has put the Murray postulate in doubt since the presence of the Au(I)-thiol polymer complex was not experimentally observed. By Raman spectroscopy, Tong and co-workers observed the presence of a stretching vibration corresponding to a [Au(I)–Br$_2$]$^-$ species (Scheme **1.4**).[43] The presence of the reduced Au(I) ions, instead of Au(III), was rationalised by the concurrent oxidation of the thiol to its corresponding disulfide, as also reported elsewhere in the literature.[44] The absence of any stretching vibration corresponding to the Au–S bond, further confirmed their hypothesis. In addition, Tong and co-workers observed, by ^{1}H NMR spectroscopy, a large downfield shift of the water peak. For all these reasons they proposed the formation of a [TOA]$^+$[Au(I)Br$_2$]$^-$ complex in the form of inverse micelles, where TOAB molecules in the organic phase encapsulate both Au(I) species and water. The subsequent addition of sodium borohydride reduces Au(I) species to Au(0) and the formation of small 'naked' AuNPs follows. Then, the ligands (both disulfides and unreacted thiols) diffuse through the TOAB shell and the Au–S bond is formed at the water/toluene interface, with the final formation of dodecanethiol-functionalised AuNPs.
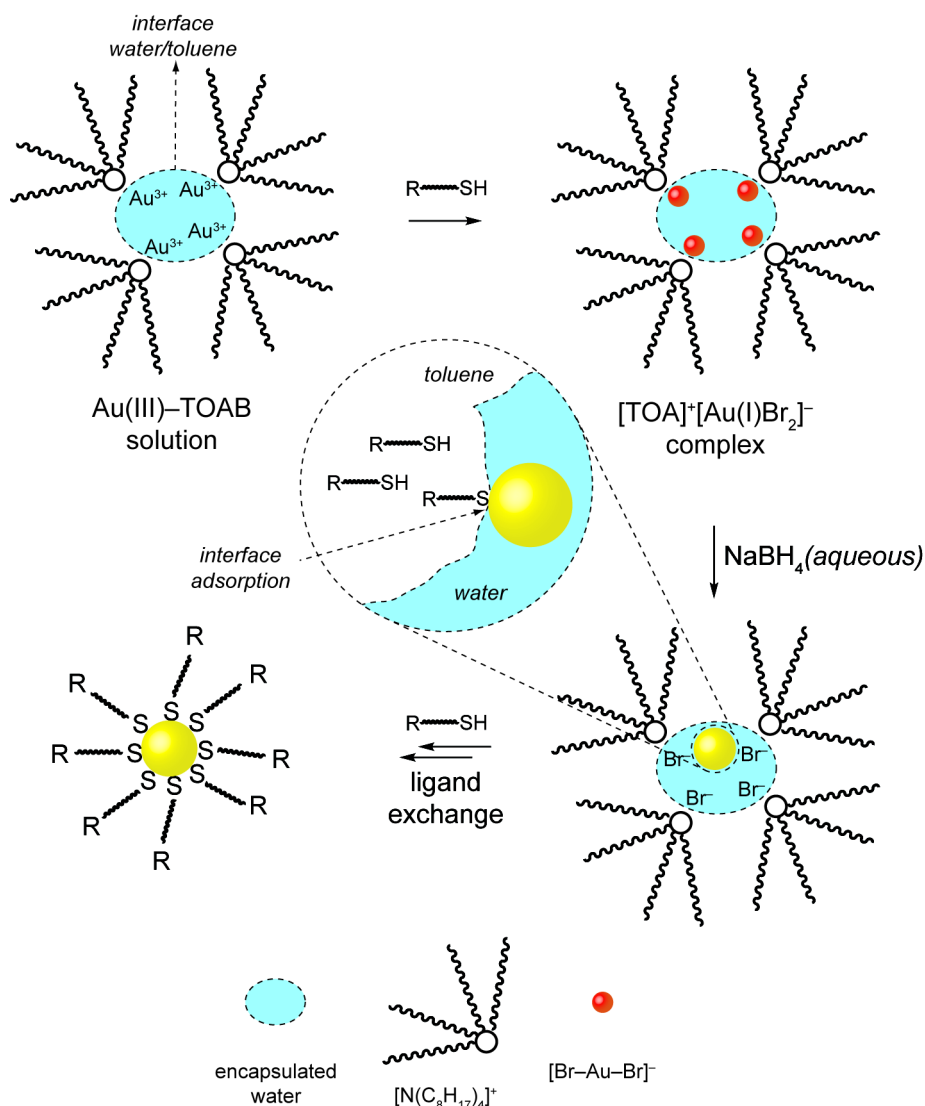
Scheme 1.4 General mechanism for the synthesis of AuNPs functionalised with 1-dodecanethiol *via* the Brust–Schiffrin method, as postulated by Tong. The presence of the [TOA]$^+$[Au(I)Br$_2$]$^-$ complex (inverse micelle) is suggested by Raman and ^{1}H NMR spectroscopy.[43]

1.2.1.3 Steric stabilisation: the Stucky method

Many of the methods available for AuNP synthesis employ a biphasic solvent mixture with Au(III) as gold source, which can be reduced to Au(0) in different ways (e.g. by using lithium aluminium hydride, sodium borohydride, hydrazine etc. as reducing agents) but all of them are based on the original Brust–Schiffrin procedure.[12]

Stucky and co-workers have developed a reproducible method for the preparation of silver, palladium and gold NPs, which presents some distinctive differences from the previous procedures.[45] For the preparation of functionalised AuNPs, this single-phase method consists of the use of triphenylphosphine gold chloride as gold source. The gold and thiol ligand are mixed together in an organic solvent (e.g. benzene, toluene or

chloroform) and heated to 55 °C. The reduction of gold is achieved with *tert*-butylamine borane complex (TBAB), a milder reducing agent compared to sodium borohydride, which allows a slower NP growth with a better control over the NP size dispersity. The Stucky method was further optimised by Lee and co-workers, who investigated the effect of solvent and gold/thiol/TBAB ratio.[46] A growth mechanism was also hypothesized (Scheme **1.5**). In the first stage, NP nuclei begin to grow when the gold is gradually reduced by the TBAB. At this stage, triphenylphosphine weakly stabilises such small aggregates. In a second stage, the surface-bound triphenylphosphine is gradually displaced from the gold surface and replaced by thiol ligands by formation of the more stable Au–S bond.
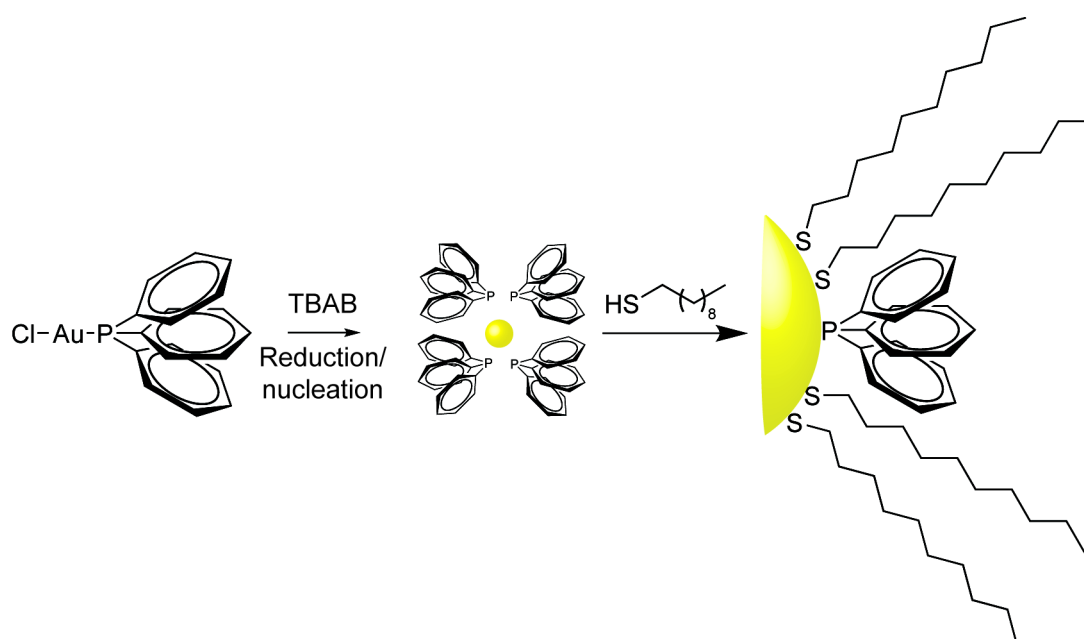
Scheme 1.5   Proposed mechanism for the synthesis of AuNPs functionalised with 1-dodecanethiol using AuPPh$_3$Cl as gold source and TBAB as reducing agent.[46]

A large variety of slightly different methods for preparing AuNPs are available in the literature.[12] The above mentioned methods are the most used because they can provide AuNPs with reproducible size and relatively small dispersity. The desired final NP size is one of the main aspects that have to be considered in order to choose the right method. If larger AuNPs are needed (> 10 nm), the Turkevich–Frens method is more appropriate than the Brust–Schiffrin or the Stucky methods, which are more suitable for obtaining smaller NPs (2–8 nm). Size dispersity is also important to choose the appropriate method. If a low NP size dispersity is desired (< 10% for instance), the Stucky procedure is probably the best available method. The solubility properties of the final ligand-functionalised AuNPs are also important for the choice of the synthetic

method. The Turkevich–Frens strategy allows the preparation of charged and water-soluble AuNPs. On the other hand, the Brust–Schiffrin and the Stucky methods provide, normally, neutral ligand-functionalised AuNPs soluble in organic solvents. Finally, the compatibility of the organic ligand with the reducing conditions has to be taken also in account. If reducible moieties are present in the ligand structure, sodium borohydride could not be indicated and, however, the ligand compatibility with citrate or TBAB has to be assessed in advance.

1.3 Nanoparticle characterisation

When a batch of functionalised metal NPs is prepared, a series of analyses must be carried out in order to characterise, where possible, both their physical (e.g. NP diameter, shape, colloidal stability etc.) and chemical properties of the ligand shell (e.g. structural characterisation).

Although different techniques were developed for the NP characterisation, a survey of the literature revealed that many studies involving NPs lack a comprehensive and consistent suite of characterisation data. In order to develop sophisticated synthetic strategies for manipulating NPs and to understand the mechanisms involved in NP functionalisation and assembly, a detailed NP characterisation is instead necessary. For instance, achieving and assessing NP sample purity is a basic requirement. In addition, achieving characterisation of NP-bound molecular structure is more challenging than characterising the 'nanoparticulate' properties, in particular for the investigation of molecular reactivity and inter-molecular interactions within the monolayer.

Although many analytical techniques are available for this purpose, the aim of this Section is to present in detail only those that have been extensively used throughout the remainder of this Thesis.

1.3.1   Transmission electron microscopy

One of the basic analyses carried out on the vast majority of NP samples is the determination of their size. Among the optical methods, TEM is still widely used for this purpose.[47]

In a common transmission electron microscope (Figure **1.2**), an electron beam is generated by a tungsten filament. The beam hits the sample, which is supported on a copper grid covered by a thin layer of carbon. When the electrons pass through the

sample, scattering occurs because different atoms interact and absorb the electrons differently. Once scattered, the electrons are focused and magnified by, respectively, objective and projective lenses. The image is formed when the scattered electrons, focussed and magnified, interact with a digital camera.
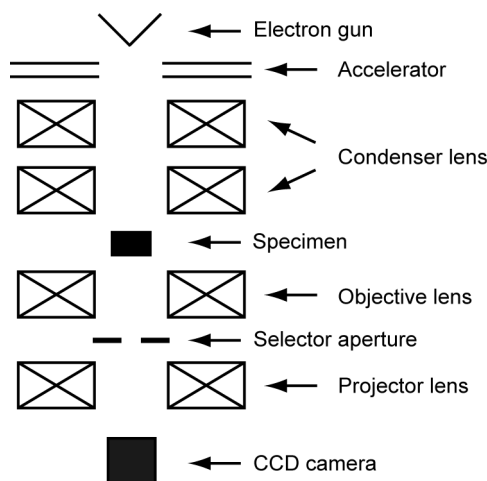
Figure 1.2   Schematic illustration of a transmission electron microscope. Simplified from ref.[47]

In a common *bright field* imaging mode, regions of the sample which contain heavy atoms (e.g. metal NPs) will appear dark in contrast with those regions, containing lighter atoms (e.g. the carbon support), where the electrons are less scattered and thus will appear bright. The result is a two-dimensional image where NPs can be observed almost at the atomic level and counted. It is well established that metal NPs are not exactly spherical but they can exhibit a variety of polyhedral shapes (e.g. octahedral, icosahedral etc.).[48,49] However to a first approximation, NPs can be considered as spheres and, by means of imaging software programs, it is possible to estimate the NP diameter and the diameter dispersity, expressed as one unit of size standard deviation. Even if TEM allows direct visualisation of NPs, some disadvantages have however to be considered. TEM analysis is relatively time-consuming and requires extensive practical experience of the microscope. TEM provides size information of the NP core only while the NP-bound ligands are usually not visible with this technique. TEM analysis can be carried out only on a small portion of the whole sample. For this reason, the calculated mean diameter and size distribution are the result of a statistical estimation from tens to hundreds counted NPs, which represents a tiny pool of the total NP sample. In addition, NPs analysed by TEM cannot be reused for further characterisation because they are irreversibly deposited on the TEM grid. Finally, the TEM picture is a result of a dried sample and, thus, it is not representative of NPs in a solution state.[50]

1.3.2 UV-Vis spectroscopy

UV-Vis spectroscopy is widely used for the characterisation of functionalised metal NPs. The NP optical properties are largely different from the bulk material counterparts. Optical properties of noble metal NPs are an explanatory example. Generally, a dispersion of AuNPs shows a characteristic deep-red colour while dispersions of silver NPs (AgNPs) are yellow. When analysed by UV-Vis spectroscopy, AuNPs and AgNPs show characteristic absorption bands around 520 and 400 nm, respectively, as a result of an optical property known as surface plasmon resonance (SPR).

The SPR band originates from collective oscillations of the electrons at the surface of NPs (essentially 6s electrons of the conduction band for AuNPs). This oscillation is induced by the electromagnetic field of the incoming light when photon frequency is resonant with this collective oscillation (Figure **1.3**).[5]
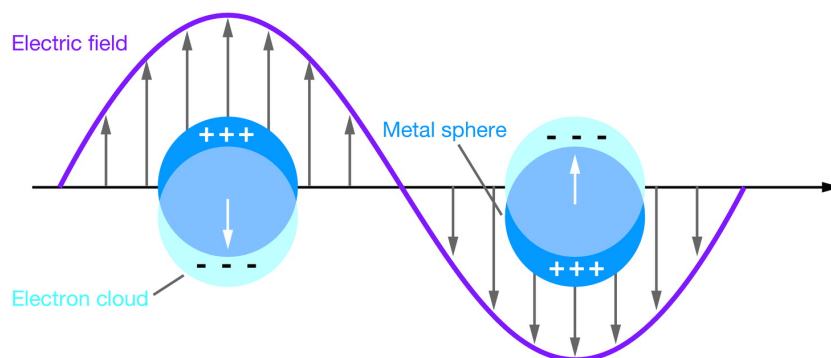
Figure 1.3   Schematic diagram illustrating a localised surface plasmon. Figure taken from ref.[51]

The SPR band was explained for the first time by Mie in 1908.[2] Mie attributed the plasmon band of spherical particles to the dipole oscillation of the free electrons in the conduction band occupying the energy states immediately above the Fermi energy level.

For AuNPs in the range 2–20 nm, the surface plasmon resonance causes an absorption of the visible light around 520 nm. The SPR band position and linewidth are size-dependent. For monodisperse NP samples, when the size of the NP core decreases, a blue-shift and a decrease of the SPR band intensity are observed together with a broadening of the SPR band width.[29] This is a consequence of the onset of quantum size effects, which become important for NP with core size < 3 nm. For this reason, NPs with a mean size of 2 nm or less do not show the SPR band in the UV-Vis spectrum. The SPR band is also influenced by NP shape, core charge, solvent dielectric constant and temperature.[52] In addition, the presence of an organic shell

around the NP core slightly modifies the refractive index of the surrounding medium leading to a further influence on the position and shape of the SPR band.

UV-Vis analysis of functionalised metal NPs is very popular because it is simple and rapid and does not require any particular knowledge of the instrument. Information about the NP colloidal properties can be obtained by monitoring the λ_{max} shift of the SPR band. In addition, approximate estimations of the NP 'concentration' can be obtained by observing the variations in the λ_{max} absorbance value.

1.3.3   Dynamic light scattering

DLS is a complementary technique to TEM for determining the mean NP size of a dispersion.[53] Compared to TEM, DLS analysis provides important advantages: the sample preparation is quick and easy and this technique does not require a deep experience for using the instrument as TEM does. DLS is a conservative analysis since samples can be recovered and used for further investigations. DLS allows NP analysis as colloidal dispersions. For this reason, information about the colloidal stability and real time changes of the colloidal dispersion (e.g. aggregation processes) can be detected by DLS.

During the DLS analysis (Figure **1.4**), the NP sample is crossed by a light beam from a laser source. The path and the intensity of the beam are modified by the suspended NPs by scattering. The angle and the intensity of the scattered beam are related to the NP size and their random motion in the dispersion.
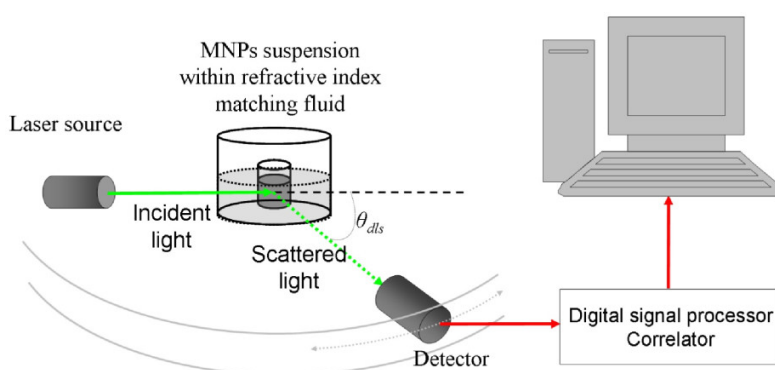
Figure 1.4   Schematic representation of a typical dynamic light scattering setup. Figure taken from ref.[53]

Information about the random motion of suspended particles can be obtained and used to calculate the diffusion coefficient of the NPs. If the NP shape is spherical, the dynamic radius of the NP (R_H) can be calculated from its diffusion coefficient from the

Stokes–Einstein relationship (Equation **1.3**), where k_B is the Boltzmann constant, T is the temperature of the suspension, and η is the viscosity of the solvent.

$$D_f = \frac{k_B T}{6\pi\eta R_H}$$

Equation 1.3

It has to be noted that the solvodynamic size of the NPs, which is larger than the NP size, is estimated by DLS. The dynamic size is the result of the NP core size, the surrounding ligands around it and the associated solvation shell (Figure **1.5**).

DLS analysis is very sensitive to NP shape and dispersity. For these reasons, if NPs are not spherical and the size distribution is large, DLS analysis is not able to provide reliable solvodynamic NP size.
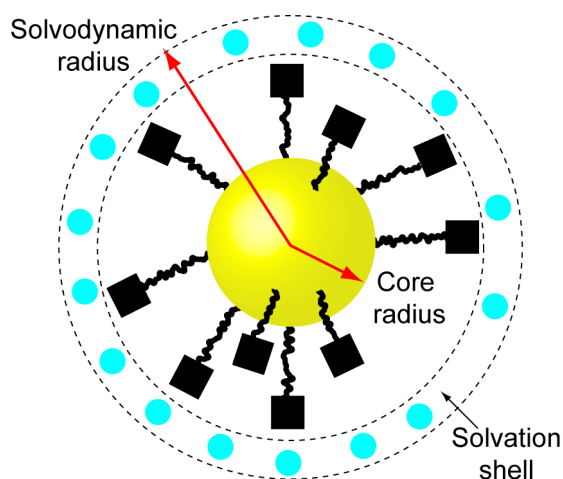
Figure 1.5   Schematic illustration of ligand-functionalised metal NPs. The ligand shell and the solvation shell contribute to the dimension of the solvodynamic radius.

1.3.4   Nuclear magnetic resonance spectroscopy

Solution-state NMR spectroscopy is a powerful tool for the characterisation of the NP-bound organic monolayers.[54] In particular, NMR spectroscopy allows the *in situ* and non-destructive analysis of NP colloidal dispersions. With appropriate experimental design, NMR spectroscopy also discriminates organic species adsorbed on the NP core from those freely dissolved in solution and can be used for monitoring exchange processes on the NP surface.

Even if the preparation of monolayer-stabilised NPs is rather common and carried out with a very large variety of organic ligands, a survey of the available literature revealed,

surprisingly, that the characterisation of the NP-bound organic shell is often incomplete, absent or even misleading.

The NMR analysis of the molecules adsorbed on the NP surface is not as straightforward as that of freely dissolved organic species. For a start, in typical NP colloidal dispersions, the concentration of NP-bound detectable ligand is very low. After the development of the Brust–Schiffrin procedure,[40] AuNPs functionalised with simple alkanethiols became accessible with sufficient concentration so that the organic ligands could be detected by NMR. Early ^{13}C NMR investigations with octanethiol (Figure **1.6**), dodecanethiol or hexadecanethiol adsorbed on the NP surface were carried out and compared with corresponding solid-state NMR analyses.[55–57] A general and consistent broadening of the methylene resonances was observed, whose extent was proportional to the methylene proximity to the gold surface. ^{13}C NMR analyses are not widely adopted because they are very time-consuming (more than 15 hours, for instance, were necessary to record the ^{13}C spectrum shown in Figure **1.6**). Significant line broadening is also a consistent feature of ^{1}H NMR spectra[55–57] where also signals corresponding, for instance, to amide protons were detectable (Figure **1.7**).[58]
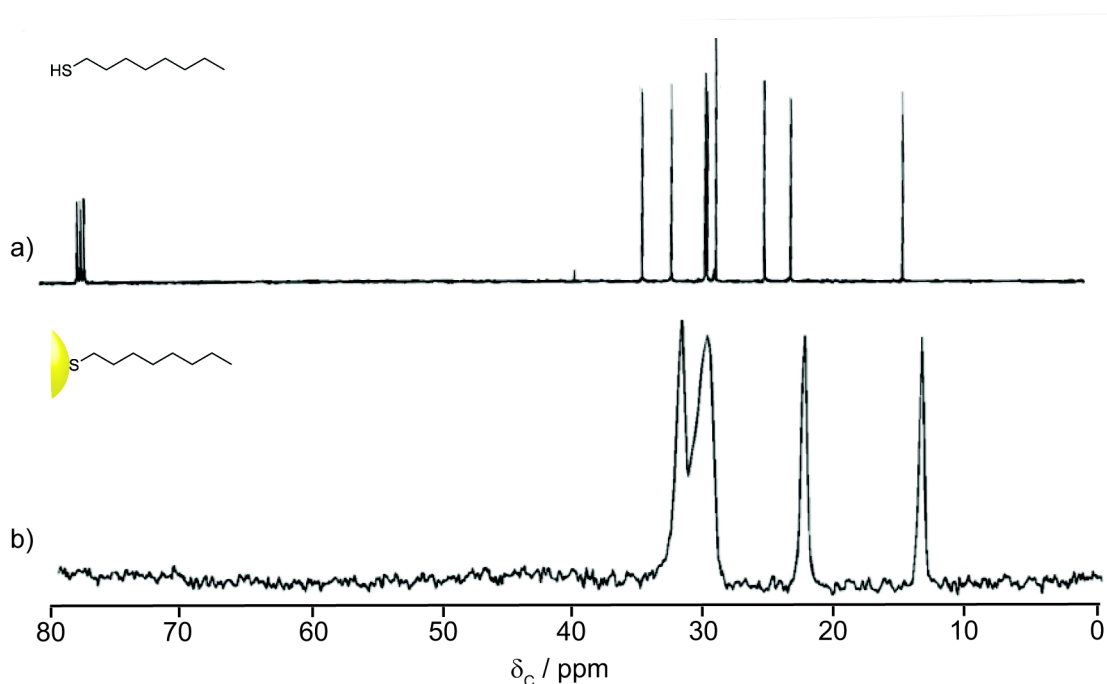
Figure 1.6 ^{13}C NMR (CDCl$_3$, 125 MHz) of 1-octanethiol (a) and octanethiol-functionalised AuNPs. Figure adapted from ref.[56]
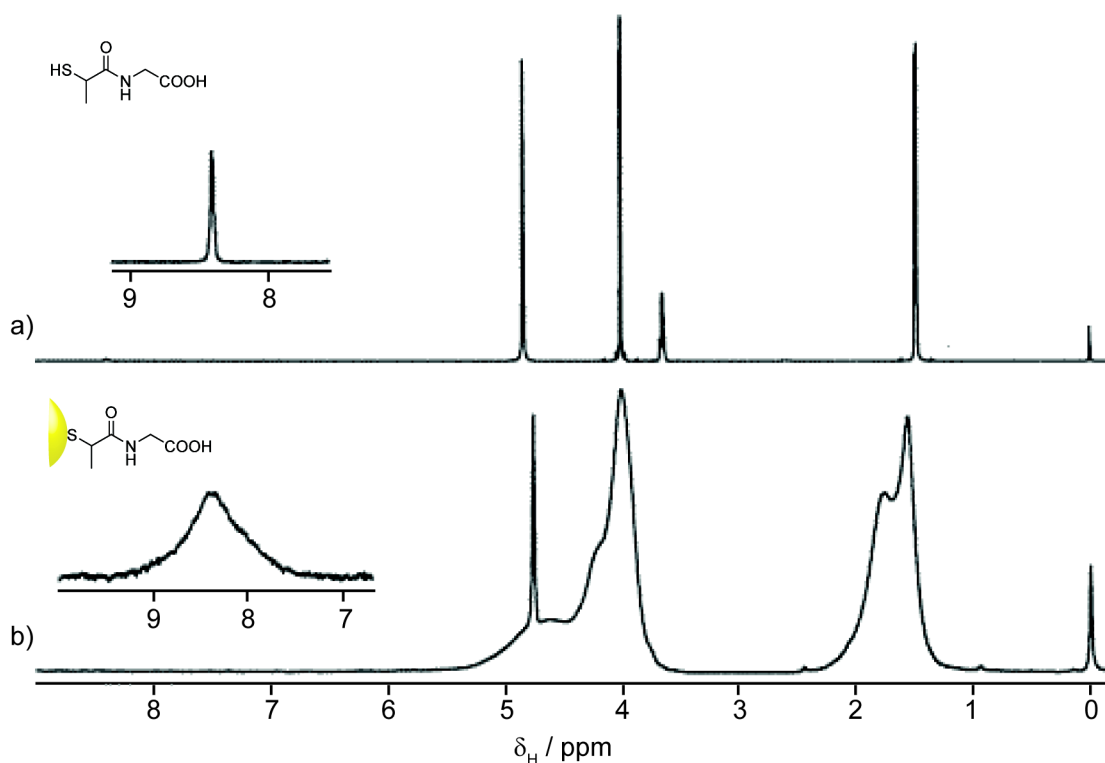
Figure 1.7 ^{1}H NMR (D$_2$O, 500 MHz) of tiopronin (a) and tiopronin-functionalised AuNPs. Figure adapted from ref.[58]

Murray and co-workers were the first to analyse the source of broadening.[58,59] Several factors, including structure of the monolayer, spin-spin relaxation times and sample dispersity, were postulated to contribute to the signal broadening. In AuNPs functionalised with alkanethiols, methylene groups closest to the gold surface are densely packed and solid-like while the degree of free motion of the farthest methylenes is higher. As a consequence of this, nuclei experience increased dipolar interactions, for increasing proximity to the NP surface, and hence increased line broadening as a result of the resulting dipolar coupling effects. Fast spin-spin relaxation (measured by the T_2 time) is an additional source of broadening. Relaxation times depend of the degree of tumbling of species in solution and they are significantly shorter for big species (proteins, polymers) when compared to smaller molecules. Functionalised NPs behave similarly to proteins and polymers, showing small rotation and low tumbling. For this reason, the T_2 times of alkanethiolates adsorbed on the NP surface are shorter than their corresponding free monomers in solution, causing the linewidth broadening.

Sample dispersion is probably the main cause for linewidth broadening in most NP samples. A distribution of chemical shifts is observed because different Au–S binding sites are present on the NP surface. In addition, different populations of NPs in the same sample can produce the same effect. Since NPs are not exactly spherical, the

Au–S binding site can be positioned on terraces, edges and vertices of the NP. This results in a range of the chemical shifts for nuclei which otherwise belong to the same molecular environment.

After the basic NMR investigations carried out by Murray and co-workers, NMR spectroscopy was employed for simple and rudimentary characterisation of the NP-bound monolayer. Only in recent years, 1D and 2D NMR experiments were used to obtain more information from ligand-functionalised NPs. Diffusion-ordered (DOSY) NMR spectroscopy can be employed for the determination of the NP size.[55,58,60] By DOSY NMR, Kubiak and co-workers calculated the diffusion constants of AuNPs functionalised with 1-dodecanethiol and 1-octanethiol in several solvents. NP size values were derived by using the Stokes–Einstein relationship (Equation **1.3**), in very good accordance with those calculated by TEM analysis.[60] This is rather surprising because, by DOSY NMR, the diameter values should be referred to the solvodynamic size of NPs (Figure **1.5**), which is larger than the core size estimated by TEM analysis. In addition, no information about the size distribution is provided by this method.

As mentioned above, ligand-functionalised AuNPs exhibit short transverse relaxation times (T_2) compared to those of small molecules freely dissolved in solution. Specific T_2-filters can be applied in order to generate NMR spectra in which only the resonances corresponding to unbound species[58,61] can be separately observed in complex NP samples. Alternatively, filtered NMR spectra can be generated to selectively show NP-bound species by applying a DOSY-type sequence, which allows differentiation of species based on their diffusion coefficient.[62,63] These NMR-filter experiments are probably the most useful to assess, in combination with traditional ^{1}H NMR experiments, the purity of ligand-functionalised NP samples from unbound species but, surprisingly, such experiments are not yet widely employed.

Only recently, NMR spectroscopy has been employed to investigate the composition and the position on the NP surface of structurally different ligands. Mancin and co-workers exploited, for instance, the paramagnetic relaxation enhancement,[64] induced by gadolinium ions, and the pseudo-contact NMR shift,[65] generated by ytterbium or terbium ions. These intermolecular effects, generated by the ion probes, provided direct information about the organisation of the ligands within a mixed monolayer (e.g. stripes, small patches or random composition). Alternatively, Stellacci and co-workers exploited the nuclear overhauser (NOE) effect.[66] By ^{1}H NMR, they observed that the dependence of the aromatic hydrogens peak position over the monolayer composition can be linear, reciprocal, or sigmoidal for, respectively, randomly mixed ligand shells, Janus particles and patchy particles. In addition for randomly mixed monolayers and patchy particles the presence of a cross-peak was observed in the 2D NOESY spectra.

1.3.5   Mass spectrometry

Mass spectrometry (MS) analysis can be used in combination with other techniques (e.g. NMR spectroscopy) for the characterisation of ligand-functionalised metal NPs and has also been successfully employed in the characterisation of self-assembled monolayers on metal surfaces.[67,68] The analysis is quick (around 5 min, including sample preparation, ionisation and fragment detection) and, although the sample cannot be recovered, MS analysis does not require a large amount of material.[69] In addition, the information obtained by MS is a statistical average of the whole analysed sample.

Electrospray and laser desorption ionisation (ESI and LDI, respectively) are particularly widespread for the analysis of functionalised NPs. Early investigations on three-dimensional structures involved the analysis of polydisperse NP samples functionalised with simple ligands. The choice of the ionisation source and the NP size are critical for obtaining specific information from MS analysis. For small NPs, information of the whole NP mass, including the adsorbed ligands, can obtained either using ESI[70,71] or LDI[44,48,69,72] as ionisation source.

For bigger NPs, MS analysis can show fragments corresponding to gold–thiolate ions as a result of the fragmentation of the metal core.[69,73–75] By employing LDI-MS analysis, strategies for the characterisation of the organic shell have recently been reported based on the selective desorption of the ligands by appropriate tune of the intensity of the laser.[76]

MS analysis can provide useful information also for characterising NP-bound mixed monolayers.[74–76] Matrix-assisted LDI-MS was employed by Cliffel and co-workers for the determination of AuNPs functionalised with a mixed monolayer of tiopronin and glutathione. A selective gas-phase separation technique was employed to separate specific gold-thiolate species and to provide structural information about the composition of the NP-bound mixed monolayer.[74,75] Rotello and co-workers developed a semi-quantitative method for the selective desorption of ligands, containing a tetraethylene glycol residue, from the NP surface. Results obtained for binary ligand mixtures by LDI-MS analysis were in very good accordance from those obtained by corresponding NMR analysis.[76] Although very promising for assessing the composition of NP-bound mixed monolayers, these strategies are still not generally applicable because the ligands must possess similar ionisation efficiency in order to obtain reliable results.

LDI-MS analysis is a powerful tool in order to investigate the structure of the desorbed ligands. However, such analysis could detect possible NP-unbound contaminants and

so generate misleading results. For these reasons, LDI-MS is a powerful tool in order to investigate the structure of the desorbed ligands but it has to be used always in combination with other analyses (e.g. NMR spectroscopy) to provide a more complete information about the ligand structure of ligand-functionalised NPs.

1.4 Nanoparticle functionalisation and monolayer post-synthetic manipulation

In the NP functionalisation, ligands are used to introduce a variety of chemical functionalities designed to bring properties in addition to the basic role of stabilising the NPs. Ligands are commonly introduced in one of two ways: concurrently during the NP formation or in a subsequent step by exchange with NPs stabilised with a temporary ligand (Figure **1.8**).[14]

In the direct synthesis approach, ligand compatibility with the NP synthetic conditions must be assessed. In the ligand exchange approach, a large excess of ligand is added to a pre-formed solution of AuNPs functionalised with a temporary ligand which can be either weakly bound (e.g. citrate,[33,34] TOAB,[40] etc.) or covalently adsorbed (e.g. thiolates) on the metal surface. The incoming ligand gradually displaces the temporary ligand from the gold surface. The exchange is complete usually within a few hours and the rate of completion depends on the excess of incoming ligand employed in combination with the relative affinities of the incoming and outgoing ligands for the NP surface.

To achieve a reasonable displacement of the temporary ligand, exchange on the NP surface requires a large excess of incoming ligands. By this way, purification issues might arise in order to remove both the excess of NP-unbound incoming ligand and of displaced ligand. In addition, ligand exchange does not ensure a full displacement of the temporary ligand with the consequence to possibly obtain NP-bound mixed monolayers whose composition can be difficult to assess. On the other hand, not all organic ligands are compatible with the reducing conditions required for a direct NP preparation. Finally, a direct synthesis strategy (e.g. Stucky[45]) provides NPs with reproducible size which is, however, dependent on solvent, temperature and nature of the ligand.[46] For this reason, a ligand exchange approach is more appropriate when NPs functionalised with structurally different ligands are required to possess the same size.

If a ligand exchange approach is necessary, starting from NPs functionalised with weakly adsorbed stabilisers (e.g. citrate or TOAB) or with strongly bound ligands (e.g.

alkanethiolates) also influences the relative ease with which ligand exchange is achieved. Weakly bound ligands provide less stable NPs but are easily exchangeable. On the other hand, strongly bound ligands improve NP stability but, at the same time, do not ensure their full displacement from the surface and so they are more difficult to exchange.

In order to overcome the limitations emerging for the NP functionalisation by direct synthesis or ligand exchange, a promising alternative is given by non-covalent (Section **1.4.1**) or covalent (Section **1.4.2**) NP post-synthetic strategies.
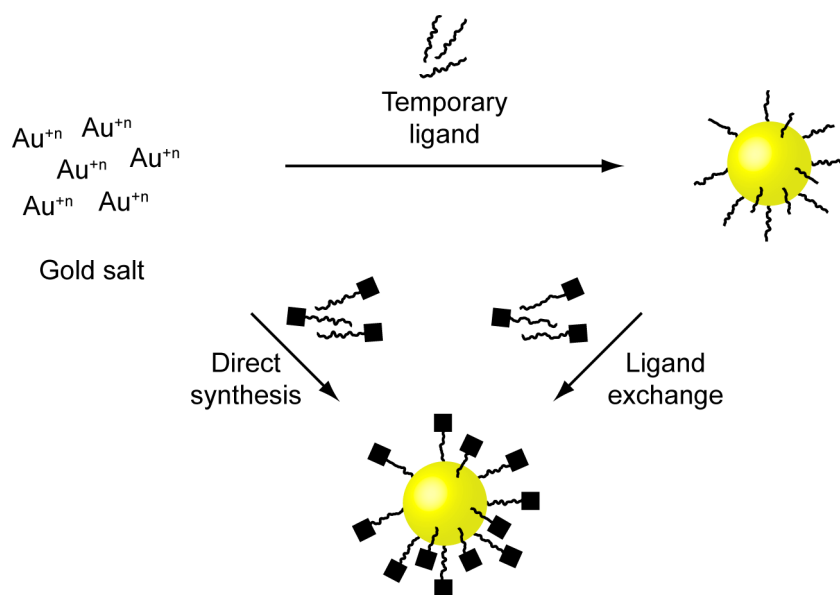
Figure 1.8   General scheme illustrating the two main approaches for the preparation of functionalised AuNPs (dimensions are arbitrary). Direct synthesis (*left*): the gold salt, the reducing agents and the ligand are mixed together in one step. Ligand exchange (*right*): the ligand is mixed together a pre-formed batch of AuNPs functionalised with a weakly-bound temporary ligand, which is gradually displaced from the gold surface by ligand exchange.

1.4.1   Functionalisation with DNA and manipulation driven by non-covalent interactions

One of the most well established NP functionalisation approaches involves the use of DNA oligonucleotides. Starting from water-soluble AuNPs stabilised with citrate or phosphine ligands, Mirkin[77] and Alivisatos[78] independently reported AuNP functionalisation with DNA oligomers. These pioneering works both reported NP passivation with oligonucleotides functionalised with a thiol group, for NP binding, at the 3' end. The formation of the stronger Au–S bond ensured displacement of the weakly NP-bound citrate or phosphine during the ligand exchange process. Mirkin and co-workers functionalised 13 nm AuNPs with non-complementary single stranded

oligonucleotides. Aggregates were subsequently obtained by adding a DNA linker bearing, at both ends, complementary oligonucleotides with those adsorbed on the NP surface (Figure **1.9A**).[77] The process was confirmed to be temperature-reversible exploiting the denaturation and regeneration of the DNA double helix, showing a sharper melting transition due to multivalent interconnections between DNA-functionalised NPs when compared to analogous oligonucleotides hybridised in solution in the absence of NPs.[4] On the other hand, Alivisatos and co-workers assembled inorganic nanocrystals into dimers and trimers by base pairing of several oligo-functionalised NPs to a single DNA template strand (Figure **1.9B**).[78]

a) Mirkin strategy   b) Alivisatos strategy

DNA template

DNA duplex linker
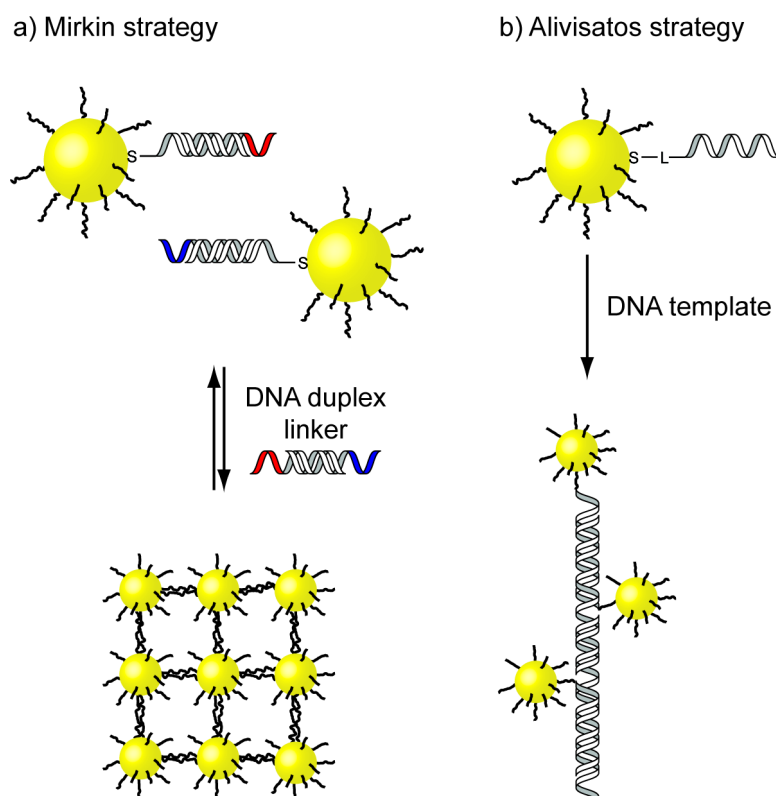
Figure 1.9   Gold nanoparticle assembly driven by DNA oligomer hybridisation. a): DNA-functionalised AuNPs which are not complementary to each other assemble by using a bifunctional complementary DNA linker (Mirkin).[77] b): DNA-functionalised AuNPs assemble in dimers or trimers by base pairing with a single-strand oligonucleotide as template (Alivisatos).[78]

The development of oligonucleotide-functionalised AuNPs had a tremendous impact in biology and medicine.[23] The combination of the AuNP optical properties and the binding properties of the NP-bound oligonucleotides has provided, for example, fluorescence-based strategies for the detection of intracellular species such as messenger RNA[79] and adenosine triphosphate,[80] gene regulation methods in the context of RNA interference[81] and colorimetric strategies for the detection of cancer

cells.[82] In addition, DNA hybridisation on NP-adsorbed oligonucleotides was studied for achieving NP programmable crystallisation. Mirkin,[83–85] and independently Gang,[86,87] exploited DNA base pairing to achieve long-range organised NP superstructures with a very high degree of control and prediction. Mirkin and co-workers, obtained the formation of different crystal structures exploiting the balance between the entropic and the enthalpic contributions involved in the assembly process at different temperatures relative to the melting temperature of DNA (Figure **1.10**).[83] Using these strategies, an impressive degree of control over the NP assembly process by appropriate specific design of the oligonucleotide ligand and choice of the NP size was achieved obtaining different crystal structures in a predictable fashion.[84,85]

Gang and co-workers observed that AuNPs functionalised with oligonucleotides can either assemble into amorphous aggregates or, on the contrary, adopt a long-range ordered crystalline superstructure depending both on the length of the oligonucleotide ligand adsorbed on the gold surface.[86] In addition, DNA-guided heterogeneous assembly was achieved also with different types of nanosystems, like AuNPs and quantum dots.[87]
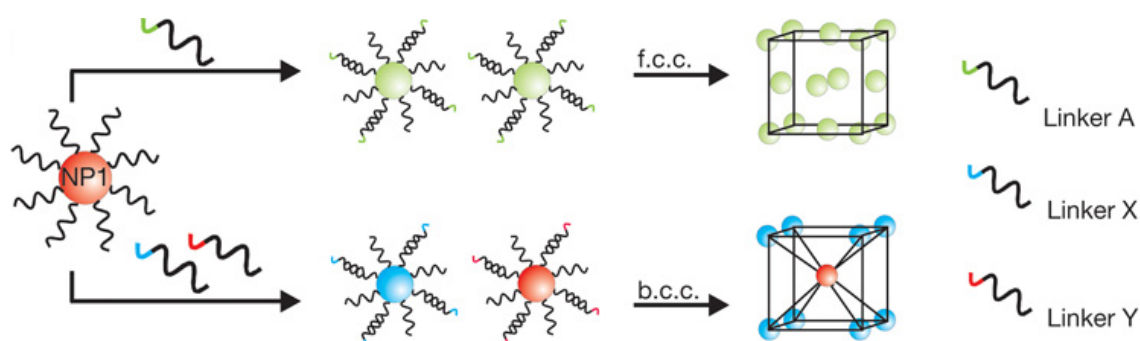
Figure 1.10   AuNPs functionalised with DNA can assemble in different ways by changing the sequence and/or the length of the DNA linker. Figure taken from ref.[83]

NP post-synthetic manipulation assembly using oligonucleotides had a tremendous impact for the achievement of functionalised nanomaterials as a result of the stability, specificity and selectivity of DNA hybridisation.[25]

Other non-covalent strategies reported in the literature include non-biomolecular NP post-synthetic manipulation and assembly exploiting hydrogen[88] and halogen[89] bonding, host-guest interactions (e.g. with cucurbiturils[90,91] or cyclodextrins[92] as host molecules), electrostatic[93–95] and dipole-dipole[96] interactions. NP post-synthetic manipulation using these interactions was, in some cases, demonstrated to be reversible[93–96] showing however poor control over the assembly process if compared to that achieved by exploiting oligonucleotide hybridisation.

1.4.2 Irreversible covalent chemistry on monolayer-functionalised nanoparticles

Post-synthetic covalent modification of the NP monolayers can be considered as an alternative to non-covalent functionalisation (Scheme **1.6**).

Many strategies have been investigated especially for NP bioconjugation,[26] but, in many cases, covalent bond formation has been inferred rather than directly confirmed by a rigorous structural characterisation on the NP-bound monolayer.
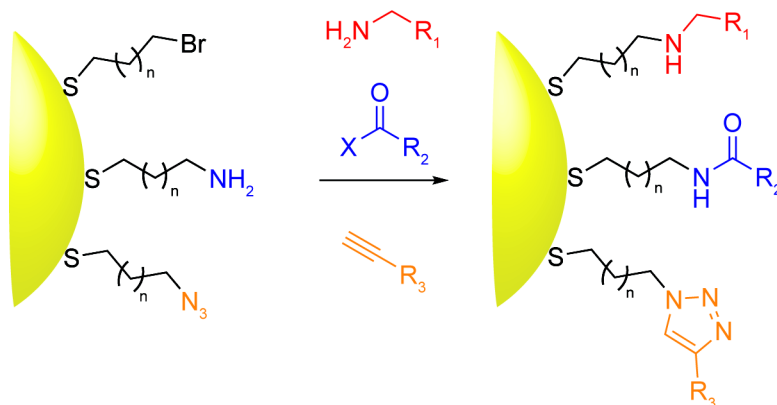
Scheme 1.6   Example of irreversible covalent bond forming reactions that have been exploited for post-synthetic modification of ligand-functionalised nanoparticles.

Early investigations were carried out by Brust and Schiffrin with AuNPs functionalised with 4-hydroxy or 4-amino phenylthiol.[97,98] Using an excess of propionic anhydride in an aqueous sodium acetate solution, they observed partial esterification in the NP-bound monolayer from infrared spectroscopic investigations. Although not deeply investigated, steric hindrance from the close packed ligands around the NP core was speculated to explain an incomplete esterification suggested by H/D exchange, which revealed the unreacted hydroxyl groups.

A more detailed investigation of nucleophilic substitution reactions on AuNP-bound ω-bromoalkanethiolates with primary amines was carried out by Murray and co-workers.[57] This study remains one of the few examples in which the reactivity of the monolayer is investigated and compared to the reaction of freely dissolved molecular species. By ^{1}H NMR spectroscopy, the extent of nucleophilic substitution was measured by using a series of primary amines. Results indicated that the substitution extent gradually decreases with bulkier amines. Furthermore, it was observed that the reactivity of ω-bromoalkanethiolate-functionalised NPs was more similar to their corresponding monomers in solution rather than their analogues adsorbed on flat surfaces, suggesting that the curved surface of NPs makes the adsorbed ligands less

packed when compared to flat surfaces. Thus, the reactive site is less hindered and so more reactive.

The use of covalent chemistry on ligand-functionalised NPs has since widened to many other types of irreversible reactions. Amide coupling is particularly widespread for biological/medical applications. This type of reaction allowed the preparation of short oligopeptides starting from carboxylate-functionalised AuNPs[99] or the conjugation of macromolecules on the NP surface for delivery or sensing.[100,101] All these examples report incomplete conversion of the NP-bound acid ligand to its corresponding amide even by employing mixed monolayer with an excess of non-reactive ligand. Copper-catalysed couplings of azide-functionalised NPs with alkynes are also often used for biocompatible NP ligations with small molecules[102,103] or biomolecules.[104,105] However, long reaction times are usually required and achieving quantitative conversion of the NP-bound azide ligands is challenging.

To conclude, post-synthetic covalent manipulation of NP-bound monolayers can be a valid alternative to non-covalent strategies (Section **1.4.1**). However, such an approach does not guarantee a good control over the NP-bound ligand functionalisation, leading to statistical mixtures of the NP monolayer and it only offers one-shot opportunities for functionalisation.

1.5 Dynamic covalent chemistry as a versatile approach for nanoparticle post-synthetic manipulation

Post-synthetic manipulation of NP-bound monolayers exploiting non-covalent interactions (Section **1.4.1**) can operate only under a limited range of experimental conditions. For example, the high stability of DNA-functionalised NPs is ensured only in a narrow window of temperature and salt concentration in order to preserve both the double-helix integrity and the colloidal stability.

Dynamic covalent chemistry (DCC) has the potential to combine the reversibility of non-covalent interactions with the intrinsic stability of covalent bonds. In addition, a wider range of synthetic chemistry is available for DCC, not limited by the stability conditions required by biomolecules.[106] As shown in Figure **1.11**, kinetically-controlled reactions are necessarily irreversible so that, when the bond is formed, it is not possible to break it again and go back to the starting reactants (under the same conditions). For this reason, compound **A** goes to **C** rather than to **B** because the transition state of the former pathway has a lower energy than the latter ($\Delta G_{AC}^{\ddagger} < \Delta G_{AB}^{\ddagger}$). To modify such reactions, features can be introduced in order to

stabilise transition states. On the other hand, for reactions occurring under thermodynamic control, when equilibration between reactants and products is sufficiently fast, the relative stabilities of the products determines if one product is favoured over the other(s). Under such conditions, compound **A** goes to **B** rather than to **C** because product **B** is thermodynamically more stable than **C** ($\Delta G_C < \Delta G_B$).
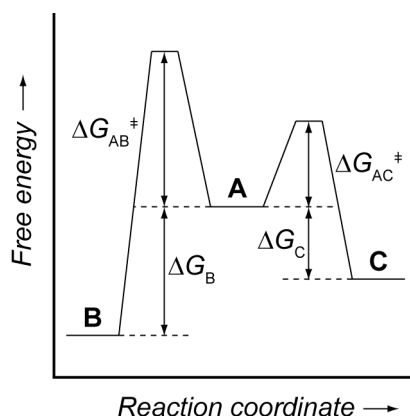
Figure 1.11   Free energy profile for reactions under thermodynamic (**A** → **B**) or kinetic control (**A** → **C**).[106]

DCC exploits thermodynamically controlled processes in order to self-assemble complex structures. The ratio between different products can be controlled and modified either by thermodynamically stabilising the desired product, by driving the reaction equilibrium towards the desired products with an excess of reactants or by removing products. Another intrinsic feature of DCC is the ability to eliminate thermodynamically less favourable products, often described as 'error-checking' and the 'proof-reading'.

The unique features of DCC have allowed key discoveries in polymer chemistry and for the preparation of mechanically interlocked molecules and molecular capsules.[106,107] In addition, the development of dynamic combinatorial chemistry has shown useful applications in drug discovery, molecular recognition, catalysis and system chemistry.[108,109]

1.5.1   The hydrazone dynamic covalent bond

Although many equilibrium reactions are known (Scheme **1.7**), not all of them are suitable for every application. For many reactions, only a proof-of-principle demonstration of reversibility has been demonstrated, while a large number of DCC

applications are based on imine-type exchange, boronic ester exchange and disulfide exchange.[106]

C=N exchange
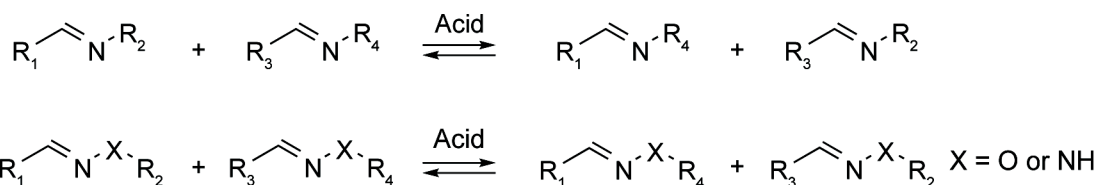
Acyl exchange
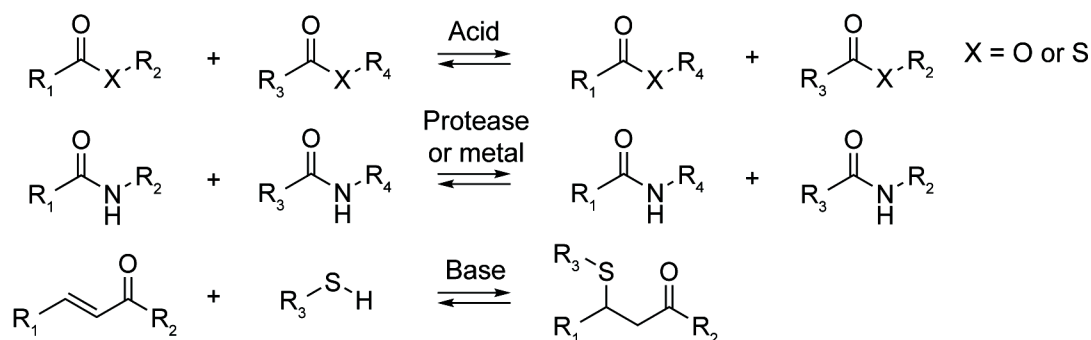
Miscellaneous
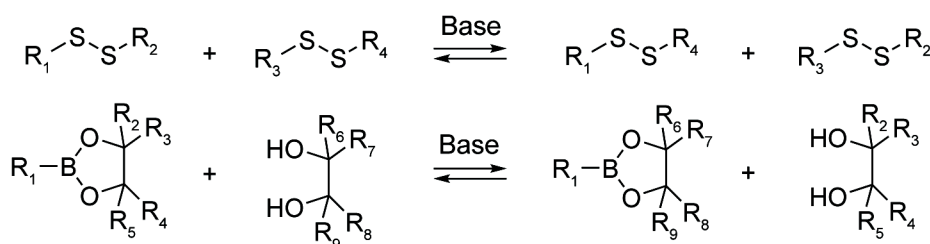
Scheme 1.7   A selection of reversible covalent reactions. Scheme adapted from ref.[106]

Imine and hydrazone compounds, known also as Schiff bases, share the same mechanism but with different reactivity for their reversible formation/hydrolysis compounds (Scheme **1.8**).[110–113]

In the formation of a Schiff base, two steps determine the rate of the reaction. The first step is a nucleophilic attack of an amine on the carbonyl group of an aldehyde or ketone and subsequent formation of a zwitterionic addition product. After a rapid proton transfer, the neutral carbinolamine intermediate undergoes dehydration with subsequent formation of the C=N double bond. Both amine attack to the carbonyl group and carbinolamine dehydration rates are pH-dependant. For imines, the rate of formation is fastest at about pH 4–6. At acidic pH (< 4), the rate-determining step is the amine attack, since the amine is in equilibrium with its corresponding conjugate acid.

On the other hand, carbinolamine dehydration is acid-catalysed and fast but becomes the rate-determining step at neutral or slightly acidic pH (> 6).
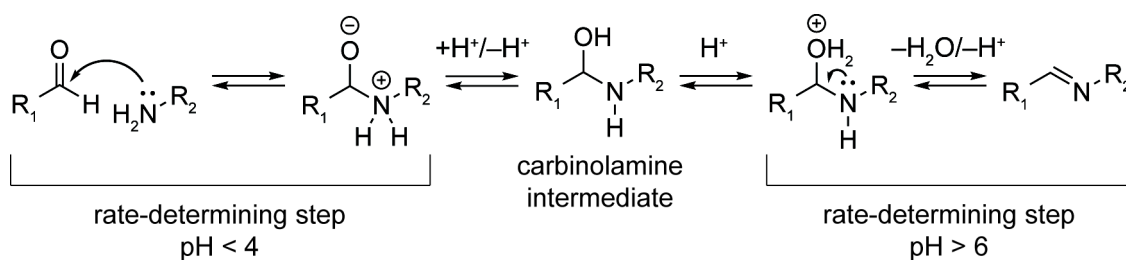
Scheme 1.8   General mechanism for the formation/hydrolysis of imines.

Hydrazone compounds, structurally similar to imines, share comparable pH-rate profiles with small variations depending on the pK_a values of the amine and the carbinolamine intermediate for, respectively, the nucleophilic attack to the carbonyl compound and the dehydration of the carbinolamine intermediate.[114,115]

Hydrazones are more stable than imines in the presence of water (Scheme **1.9**). The hydrolytic stability is the result of increased electron delocalisation involving the lone pair on the α nitrogen atom, which places an increased negative charge on the carbon atom in the C=N bond (resonance forms **II** and **IV**).[116] As a consequence of this, both hydrazone hydrolysis and exchange are usually slower than the corresponding imine reactions. In addition, the hydrazone bond is thermodynamically stable even at acidic pH, while imines are predominantly dissociated in the same pH range in aqueous environments.
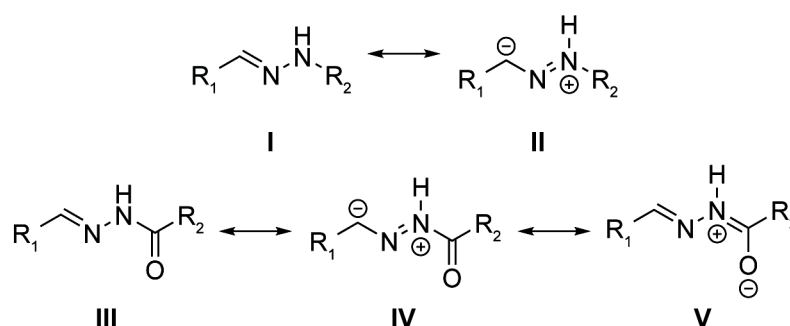
Scheme 1.9   Resonance forms of an alkyl hydrazone (**I**, **II**) and an acyl hydrazone (**III**, **IV**, and **V**). Scheme adapted from ref.[116]

The intrinsic stability of hydrazones allows their preparation under a wide range of conditions. As mentioned above, usually hydrazone synthesis is achieved with an acid catalyst while its formation at neutral pH is slow. In some cases, the acid-catalysed condensation is discouraged or inappropriate (e.g. in biological systems). Early studies

carried out by Jencks revealed that acid catalysts for hydrazone formation and exchange can be replaced by nucleophilic catalysts.[112] This observation inspired more recent investigations on aniline-type catalysts[117–121] and, more recently, variously substituted anthranilic acids as a valid alternative to acid catalysts.[122,123]

The chemoselective formation of the hydrazone bond has been used in polymer chemistry[124,125] and bioconjugation.[26,118] Applications of hydrazone-based sugar and protein ligation,[126,127] gene transferring[128] and dendrimer-based drug delivery[129] are reported.[130] In particular for NPs, several studies involved the preparation of NP conjugates for measuring enzymatic activity or for bioimaging.[131,132] NP delivery systems have been also prepared for the selective release of anticancer drugs like doxorubicin[133–136] and cisplatin.[137]

The examples provided exploit hydrazone formation (e.g. for bioconjugation) or hydrolysis (e.g. for drug release) only in an irreversible fashion and, moreover, the dynamic properties of the hydrazone bond and the reactivity of the NP-bound hydrazone monolayer are not investigated. Finally, a lacking or incomplete characterisation of the hydrazone-functionalised AuNPs emerged from these examples. The hydrazone bond formation (or hydrolysis in the case of drug delivery systems) is only inferred without appropriate characterisation of the structure of the NP-bound monolayer. Even when the characterisation is reasonable,[135,136] a careful analysis of the NMR spectra revealed the presence of NP-unbound impurities (Section **1.3.4**).

1.6 Outlook and aims

Many methods are available for the preparation of ligand-functionalised NPs starting from a large variety of materials to form the NP core (e.g. noble metals, semi-conductive materials, carbon, silica etc.). Solution-phase synthetic methods are particularly popular for metal NP synthesis because they can provide functionalised NPs with smaller size and better dispersity than those obtained by grinding or gas-phase methods. The general procedure is based on the reduction of a metal precursor by means of a reducing agent followed by electrostatic or steric stabilisation of the metal core with an organic ligand. In this way, irreversible NP aggregation and/or precipitation during the synthesis are avoided, a degree of control over the nucleation and growth processes is achieved, and functionalised NPs with reproducible mean size and low dispersity are obtained.

The current available approaches for functionality insertion on the NP surface are currently based on direct incorporation or ligand exchange. In addition, several examples have been reported for the post-synthetic manipulation of the NP-bound monolayer based either on non-covalent or covalent strategies. However, these strategies are not yet generalizable and can be successfully performed only in a narrow window of experimental conditions.

For all these reasons, the development of a generalizable approach for the design of NP building blocks is highly desirable in order to provide a robust and reliable post-synthetic optimisation of NP chemical and physical properties and to allow the construction of nanodevices and materials comprising one or more types of NP building blocks that are capable of linking with each other, of being integrated with molecular components, or being attached to surfaces. The combination of thermodynamic control with the intrinsic stability of covalent bonds is a unique feature exploited in DCC applications. Performing DCC in a NP-bound monolayer could ultimately lead to the same level of control as currently achieved for the transformation of functional groups in molecular systems and would be an attractive approach to develop flexible and scalable methods for the bottom-up construction of materials containing both metal NPs and molecular components. However, just as rational molecular synthesis depends on mechanistic understanding and structure–reactivity relationships, understanding the reactivity of NP building blocks both at the molecular level requires a full suite of characterisation data.

The aim of this Thesis is to discuss the synthesis, purification and characterisation of hydrazone-functionalised AuNPs that can undergo post-synthetic manipulations as a first example of DCC in a NP-bound environment.

The hydrazone ligands, for NP functionalisation, must contain a suitable functionality for binding the metal surface (e.g. a sulfur atom) and an appropriate design that will ensure a balance between favourable van der Waals interactions and flexibility to encourage the formation of well-ordered monolayers and sufficient access to the reactive site (i.e. the hydrazone). Functionalised NPs may be obtained by ligand exchange or by direct synthesis. The choice of one of the two approaches will depend on the compatibility of the hydrazone ligand with the NP synthetic conditions, on the desired final monolayer composition, and on the ease of purification from by-products. In addition, a method that provides hydrazone-functionalised AuNPs with reproducible size and low dispersity from batch to batch will be sought.

In order to perform DCC investigations on hydrazone-functionalised AuNPs, a rigorous protocol has to be developed for the characterisation of both the 'nanoparticulate' properties (e.g. size and colloidal stability) and the organic structure of the NP-bound

ligand. This will allow the demonstration that the structural integrity of the NP-bound hydrazones is preserved during the NP functionalisation and, moreover, that the sample is not contaminated by unbound species that can confound further investigations.

Dynamic covalent reactivity of hydrazone-functionalised AuNPs will be then investigated. Firstly, NP stability under exchange conditions will be assessed and discussed. Then, preliminary studies will demonstrate the occurrence of the hydrazone exchange within the NP-bound monolayer. Subsequently, the monolayer reactivity, towards both hydrolysis and exchange, will be quantitatively studied and compared with the reactivity of structurally similar molecular analogues.

Finally, strategies will be sought and developed in order to exploit the dynamic exchange occurring within the monolayer as a tool to tune the NP physicochemical properties (e.g. NP colloidal stability in several solvents) and to achieve NP self-assembly under dynamic conditions.

Chapter 2:
Synthesis and characterisation of hydrazone-functionalised gold nanoparticles

This chapter reports the preparation of gold nanoparticles functionalised with a monolayer of organic molecules bearing a hydrazone moiety. The design, synthesis and characterisation of two classes of ligands are reported: *N*-acyl and *N*-aroyl hydrazones. The preparation of *N*-acyl hydrazone-functionalised gold nanoparticles (AuNPs) is performed by exploiting an established ligand exchange approach. Alternatively, *N*-aroyl hydrazones are used directly with a gold source to achieve functionalised NPs by direct synthesis. Regardless of the synthetic method used, a rigorous purification protocol is developed in order to achieve pure hydrazone-functionalised AuNPs. A variety of analytical techniques is used to characterise such monolayer-stabilised AuNPs. The 'nanoparticulate' characterisation is carried out by transmission electron microscopy (TEM), UV-Vis spectroscopy and dynamic light scattering (DLS) in order to assess the reproducibility of the nanoparticle size and dispersity. Colloidal solutions of functionalised NPs are then analysed by solution nuclear magnetic resonance spectroscopy (NMR) and by laser desorption ionisation mass spectrometry (LDI-MS) in order to characterise the structure of the NP-bound hydrazone monolayer. By this way, hydrazone-functionalised AuNPs are characterised at the molecular level and, moreover, are assessed to be pure and free from any unbound species, which could make further analyses difficult or impossible.

2.1 Introduction

In order to demonstrate that dynamic covalent reactions can be exploited for the post-synthetic manipulation of NP-bound monolayers, the organic ligands must interact strongly with the metal surface. By this way, ligand desorption and unwanted reactions are avoided. At the same time, a group capable of undergoing reversible covalent chemistry must be exposed on the surface of the NP-bound ligand-shell. The ideal ligand would have a sulfur atom which strongly binds the gold surface as a thiolate.[138] The gold binding unit should be well separated from the hydrazone moiety by a spacer,

whose role is to allow the ligands to be appropriately packed around the NP core maximising van der Waals interactions between neighbouring chains.[139]

The design and the structure of the organic ligand will also affect the final NP physical properties. For example, the compatibility of the hydrazone moiety with NP synthetic strategies must be assessed in order to ensure that the reactive functionality is retained in the final functionalised NP product. In addition, the NP synthetic conditions have to be optimised to obtain reproducible NPs in terms of size and dispersity. Finally, a rigorous purification protocol is highly desirable. By this way, ligand-functionalised NPs can be characterised at the molecular level. This is an essential requirement in order to investigate dynamic covalent processes subsequently performed within the NP-bound monolayer.

2.2 Preparation of gold nanoparticles functionalised with *N*-acyl hydrazone ligands
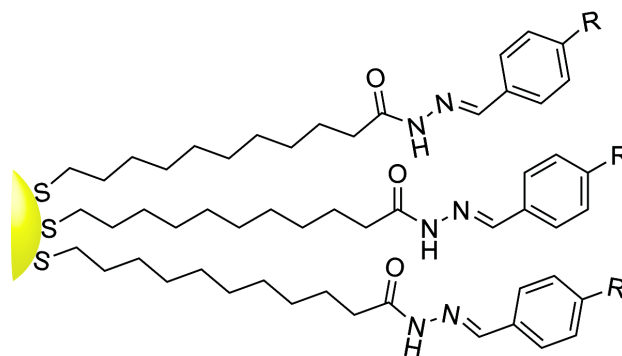
The general structure of *N*-acyl hydrazone ligands includes an alkyl chain which separates the sulfur atom from the hydrazone moiety.

2.2.1 *N*-Acyl hydrazone ligand design and synthetic strategy

Initial experiments focussed on simple ω-thioalkylhydrazide ligands and their corresponding hydrazone analogues. From commercially available 11-mercaptoundecanoic acid, the corresponding hydrazide **2** was obtained in very good yield by means of literature procedures,[140–142] in which an activated carbonyl group (ester **1**) undergoes nucleophilic substitution in the presence of hydrazine monohydrate (Scheme **2.1**).
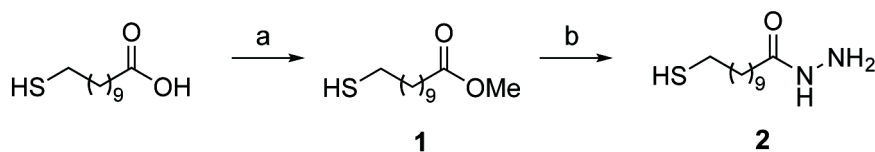
Scheme 2.1   Synthesis of hydrazide **2**. a): H_2SO_4, MeOH, 3 h, reflux, 99%. b): $N_2H_4 \cdot H_2O$, MeOH, 3 h, reflux, 80%.

Subsequently, a range of corresponding hydrazones was prepared by treating hydrazide **2** with a series of commercially available *p*-substituted benzaldehydes (Scheme **2.2**). Aldehyde **3** was instead prepared in four steps from commercially available 4-cyanobenzaldehyde (Scheme **2.3**).[143,144] All desired hydrazones (**4**H–**7**H) were obtained in very good yields within 3–17 h at room temperature.
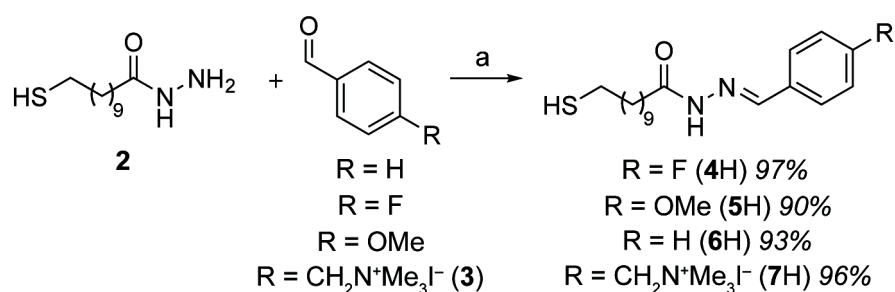
Scheme 2.2   Synthesis of hydrazones **4**H–**7**H. a): 0.1 Eq AcOH, EtOH, 3–17 h, rt, 90–97%.
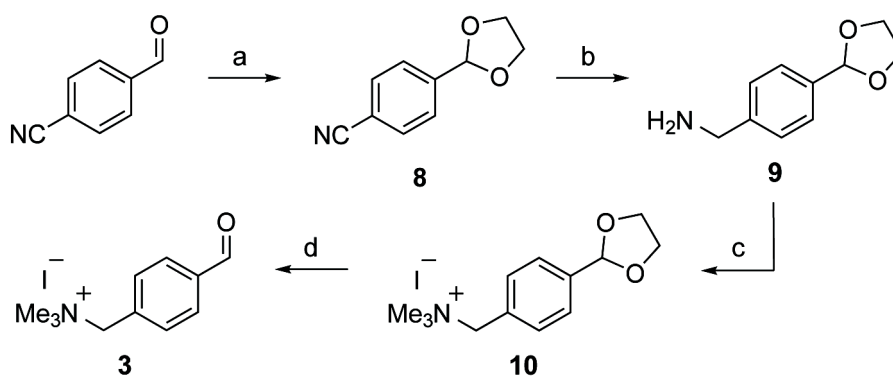
Scheme 2.3   Synthesis of aldehyde **3**. a): Ethylene glycol, *p*-TSA, toluene, 5 h, reflux, 53%. b): LiAlH$_4$, Et$_2$O, 19 h, rt, 85%. c): MeI, Bu$_3$N, DMF, 20 h, rt, 63%. d): AcOH, H$_2$O, 23 h, rt, 86%.

Ligands can be introduced on the NP surface in two ways: during the NP nucleation and growth or by ligand exchange using pre-synthetized AuNPs stabilised with a temporary ligand (Section **1.4**). A ligand exchange approach was preferred for NP functionalisation with hydrazones **4**H–**7**H in order to prevent, by this way, any possible reduction of the hydrazone moiety under the NP synthetic conditions (Section **1.2.1**). A

large variety of alkylthiolate ligands are commonly adsorbed on the NP surface by performing ligand exchange with citrate-stabilised or TOAB-stabilised AuNPs.[14,145,146]

2.2.2 Estimation of the nanoparticle concentration for ligand exchange experiments

Working with colloidal gold solutions requires certain assumptions to be made in order to work quantitatively with standardised and reproducible procedures. The first important question is how much ligand has to be used in order to achieve monolayers that completely cover the entire AuNP surface.

In order to calculate the amount of thiol ligands needed to coat the NPs, an estimation of the concentration of NPs in solution is necessary. Commonly, the concentration of colloidal nanomaterials in solution is estimated using UV-Vis absorbance (A) measurements in conjunction with the Beer–Lambert law (Equation **2.1**). This, however, requires knowledge of the NP extinction coefficient, which depends strongly on the NP size, the nature of the material and the NP shape. While relationships are well established for nanomaterials with a high degree of monodispersity, like semiconductor quantum dots,[147] the strength of the surface plasmon resonance (SPR) absorption in AuNPs is sensitive to a number of variables, including the non-negligible degree of polydispersity of commonly prepared AuNPs and the effect of ligands on the dielectric environment depending on the nature of the surface monolayer.

Nevertheless, several methods have been described in the literature to estimate the colloidal concentration by means of UV-Vis measurements exploiting the strong absorption of the SPR band.[148–150]

Khlobystov and co-workers developed an empirical relationship between size of dodecanethiol-functionalised AuNPs and molar extinction coefficient (ε) exploiting the SPR band (around 520 nm) of AuNPs.[150] They systematically measured molar extinction coefficients in relationship with the mean diameter of NPs, determining the relationship expressed in Equation **2.2**. The molar extinction coefficient is expressed in $M^{-1}cm^{-1}$, mean diameter (d) in nm and path length (l) in cm. By this way, the NP concentration was accessible from Equation **2.1**. The method, as acknowledged by Khlobystov, is limited to the size of the NPs prepared (between 2 and 4 nm).

$$A = \varepsilon \cdot l \cdot [NP]$$

Equation 2.1

$$\varepsilon_{SPR} = 26200 \cdot d^{3.83}$$

Equation 2.2

These relationships quantify the increase of molar extinction coefficient with increasing NP size, which may be determined by TEM analysis.

An alternative analysis carried out by Huo and co-workers involved more types of AuNPs (functionalised with decanethiol, citrate or oleylamine, with NP core range going from 4–40 nm) in toluene, tetrahydrofuran and water.[149] They found a linear relationship from the double logarithm plot of extinction coefficient against the NP size (Equation **2.3**). Molar extinction coefficient (ε) is expressed in $M^{-1}cm^{-1}$, *D* (expressed in nm) is the core diameter of the NPs. The dimensionless fitting parameters *k* and *a* were determined experimentally to be, 3.32 and 10.8, respectively.

$$\ln \varepsilon = k \ln D + a$$

Equation 2.3

Huo underlined the general applicability of Equation **2.3** since it appears independent of the nature of the ligand surrounding the NP core. The above mentioned relationships (Equations **2.2** and **2.3**) were developed on relatively simple models, thus it is not ensured that the same relationships can be adapted to NPs bearing monolayers with a higher degree of complexity.

Bearing in mind the above considerations, it was however decided to use the Huo method to provide an estimation of the amount of ligands required to completely cover the NP surface in a given sample. After the estimation of the nanoparticle concentration, it is then possible to estimate the number of AuNPs in solution and their total surface area, assuming that all NPs are spheres. It has been calculated that a simple thiol occupies around 0.241 nm^2 when adsorbed on flat gold surfaces.[151] Assuming that the thiol would occupy the same surface area on a sphere, it is then possible to achieve an estimation of the molar amount of ligand needed to cover the whole surface of AuNPs (see Section **5.11**). It has to be noted that this procedure involves a number of quite significant assumptions thus the results can only be treated as a rough estimate.

2.2.3 Gold nanoparticle functionalisation with *N*-acyl hydrazide 2 and simple alkanethiols

Preliminary ligand exchange experiments were performed using commercially available aqueous gold colloid solutions, stabilised with citrate anions.[152] The concentration of such solutions was estimated by exploiting the method discussed above (see Section **5.11** for explanatory calculations).

In order to optimise the conditions for ligand exchange from the weakly bound citrate ions to strongly bound thiolates, several biphasic experiments were carried out using hydrazide **2** and commercially available 1-decanethiol. The ligands were dissolved in a water-immiscible organic solvent, while citrate-capped AuNPs were dispersed in water. The exchange was investigated in the presence or absence of TOAB, employed as both stabiliser and phase transfer agent, and with AuNPs of different sizes in the aqueous phase. All the experiments, performed under a variety of conditions, are summarised in Table **5.5**. In an ideal successful experiment, a colour transfer from the aqueous to the organic phase should be observed, indicating successful attachment of the hydrophobic organic molecules to the NP surface.

Unfortunately, ligand exchange did not occur under the experimental conditions used. In fact, the organic phase remained colourless or, in some case, NP precipitation occurred at the interface.

2.2.4 Preparation of TOAB-stabilised gold colloid solutions in toluene

As discussed in Chapter **1**, the most popular method available to prepare AuNPs soluble in organic solvents was developed by Brust and Schiffrin.[40] The original two-phase procedure involves sodium borohydride as reducing agent for the gold, TOAB as phase transfer agent and stabiliser, and 1-decanethiol as passivating agent (Section **1.2.1.2**). The simultaneous presence of the reducing agent and the ligand during the NP synthesis not always is ideal because some functionalities are not chemically compatible with sodium borohydride. For this reason, the original Brust–Schiffrin procedure has been modified and optimised in order to physically separate the reducing agent from the organic ligand.[153] In this way, a large variety of different organic functional groups including ketones,[154] azo groups,[155–157] imines[158] and other reducible moieties[159] have been successfully adsorbed on the NP surface without degradation.

Grzybowski and co-workers have developed a slightly modified procedure of the Brust–Schiffrin method in which it is possible to produce TOAB-stabilised AuNPs as a stock

solution, colloidally stable over a long period of time.[160] Initially the optimised procedure developed by Grzybowski was adopted. An aqueous solution of gold tetrachloroaurate is vigorously mixed with a toluene solution of TOAB for 15 min. Then, an aqueous solution of sodium borohydride is added dropwise and the mixture is further stirred at rt for 1 h. In this way, the AuNPs are stabilised by the TOAB without addition of any other ligands and the reducing agent remains in the aqueous phase, which can be discarded before adding the sensitive ligands. By this method, AuNPs with a mean diameter of 4.58 ± 1.23 nm were obtained by Grzybowski.

In order to confirm the reproducibility of this method, the procedure was repeated several times (Figure **2.1**). The ratios of the gold salt, TOAB and sodium borohydride were kept constant. The overall concentration of the reaction mixture (with respect to the molar amount of the gold salt) was kept constant as well (30 mM). The original procedure[160] was repeated (Figure **2.1**, experiment A) and, subsequently, a scale up of the NP synthesis (Figure **2.1**, experiments B–G) was performed in order to obtain enough material (AuNP-**TOAB**) to perform further experiments from the same stock solution. Analytical data, determined by TEM and UV-Vis analyses, are summarised in Table **5.6**.
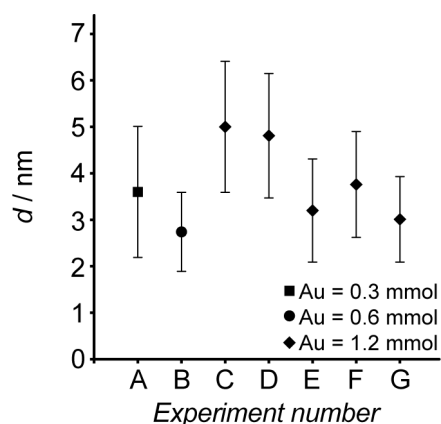
Figure 2.1   Plot illustrating the large size dispersity (around 30%) and the unpredictable diameter of TOAB-stabilised AuNPs (AuNP-**TOAB**) prepared according to the method developed by Grzybowski.[160] Experimental conditions (A–G): Au/TOAB/NaBH$_4$ = 1:5:10, [Au] = 30 mM. Error bars: ± s.d.

In every experiment the formation of some insoluble black aggregates, not described in the original procedure,[160] was always observed but their removal was relatively easy when the aqueous phase was removed from the organic phase by means of a separating funnel. AuNP mean diameter was estimated from TEM images,[161] obtaining values in a range between 2.7 and 5.0 nm (Figure **2.1**), with dispersity range

of 30–35%. UV-Vis analyses were also carried out revealing SPR λ_{max} values in a range between 517 and 538 nm (Table **5.6**).

This method therefore produces AuNPs with relatively large dispersity and somewhat unpredictable mean diameter.

2.2.5 Preparation of *N*-acyl hydrazone-functionalised gold nanoparticles by ligand exchange and purification

Ligand exchange experiments were firstly carried out by treating the TOAB-stabilised AuNPs (see Section **2.2.4**) with an excess of hydrazide **2**. Over several repetitions, irreversible and insoluble aggregates were consistently obtained. The most probable hypothesis is that hydrazide **2** is capable of multiple interactions involving both thiol and amino group adsorption on the gold surface,[162,163] resulting in a strong connection of AuNPs to each other.

In order to mask the strongly nucleophilic hydrazide functionality, subsequent ligand exchange experiments were performed using pre-formed hydrazones **4**H (Scheme **2.4**) and **5**H (Scheme **2.6**).
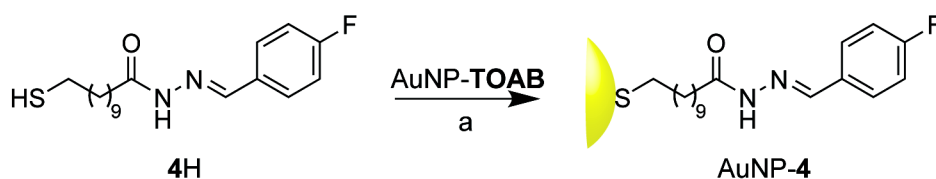
Scheme 2.4   Preparation of AuNP-**4** by ligand exchange with an excess of hydrazone **4**H. a): Toluene, 1 h, rt.

A 30-fold excess of hydrazone **4**H, with respect to the estimated number of binding sites on the gold surface, was dissolved in toluene to which gold colloid solution was added and stirred for 1 h at room temperature. Black solids (AuNP-**4**) were obtained after precipitation with ethanol. Before any analysis, the excess of ligand was removed by re-dispersion of the precipitates in toluene by sonication then precipitation by addition of ethanol, followed by centrifugation. The supernatant was discarded and the whole procedure repeated at least three times (Figure **2.2**). The sample showed identical solubility properties of hydrazone **4**H, suggesting a successful ligand adsorption on the NP surface.

The sample was re-dissolved in toluene and analysed by TEM and UV-Vis spectroscopy. For AuNP-**4**, a mean diameter of 3.90 ± 1.42 nm (36% dispersity) was determined with a SPR λ_{max} at 520 nm. The starting gold colloid solution AuNP-**TOAB**,

showed NPs with mean diameter of 2.74 ± 0.85 nm (31% dispersity) with a SPR λ_{max} at 529 nm. These values indicate that the mean NP size does not change when the ligand exchange is performed under mild conditions, as already observed in the literature.[164,165]
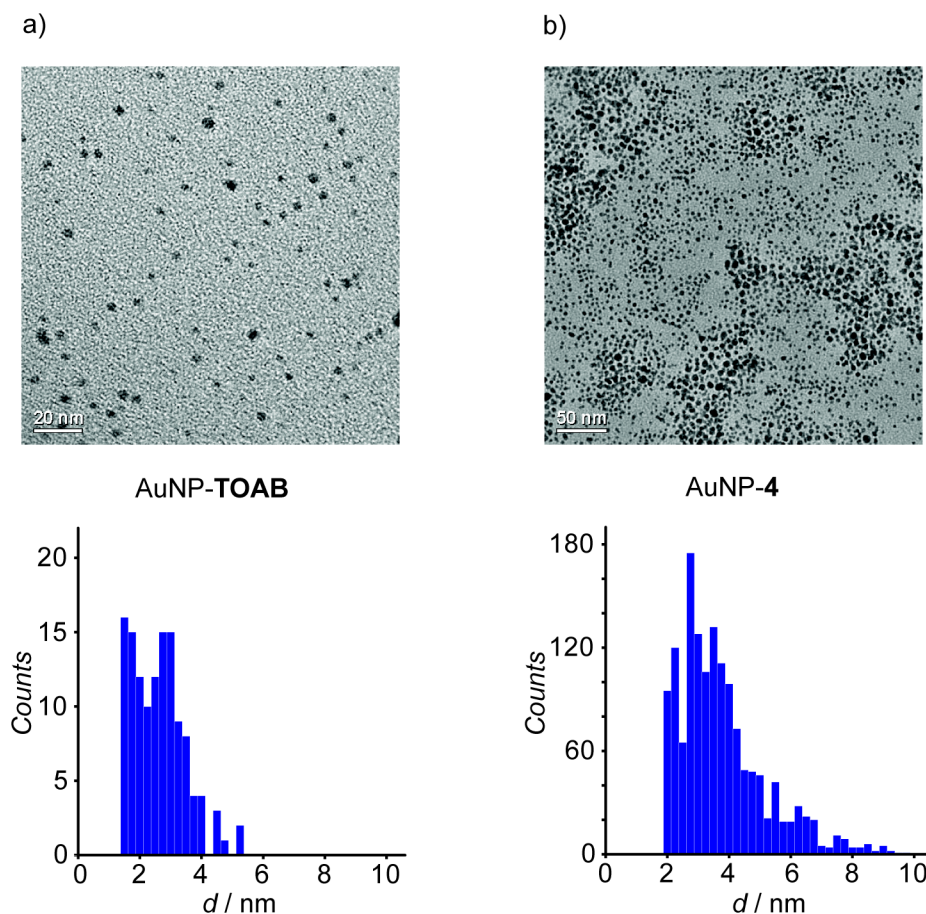
Figure 2.2   TEM micrographs of AuNP-**TOAB** before and after ligand exchange with hydrazone **4**H. a): TEM (*top*, scale bar 20 nm) and size distribution (*bottom*) of AuNP-**TOAB**: mean diameter 2.74 ± 0.85 nm (31% dispersity). b): TEM (*top*, scale bar 50 nm) and size distribution (*bottom*) of AuNP-**4**: mean diameter 3.90 ± 1.42 nm (36% dispersity).

Over several experiments the mass of the recovered material was significantly higher than the estimated upper limit, suggesting the presence of a large amount of unbound species in the sample (see Section **5.11** for an explanatory example).

The presence of residual TOAB was excluded by ^{1}H NMR spectroscopy where no signals corresponding to TOAB were detected. However, it was noted that the signals which appeared to correspond to NP-bound hydrazone **4** were as sharp as signals in the spectrum of the molecular species.

Investigation by thin layer chromatography (TLC) of a NP dispersion revealed an unbound contaminant. A black spot, corresponding to NPs which do not travel on silica,

remained on the baseline but a UV-active spot was visible although with a different R_f compared to the R_f of hydrazone **4**H.

The most probable hypothesis was that hydrazone **4**H had oxidised to the corresponding disulfide **4**$_2$ during the ligand exchange process. For this reason, an authentic example of disulfide **4**$_2$ was prepared (Scheme **2.5**). Then, ^{1}H NMR spectra of hydrazone **4**H, disulfide **4**$_2$ and impure AuNP sample were compared (Figure **2.3**).

The signal corresponding to the methylene in α position to the sulfur (H-*2*) shows a comparable chemical shift for both disulfide **4**$_2$ (spectrum b) and the AuNP sample (spectrum c). For this reason it can be concluded that the purification process did not manage to fully purify the NP samples. During the ligand exchange, thiol **4**H (spectrum a) was oxidised to its disulfide, as further confirmed by the complete disappearance of the diagnostic peak of **4**H (H-*2*, compare spectra a and c). The authentic sample of disulfide **4**$_2$ exhibited rather poor solubility in the ethanol/toluene mixture, explaining the failure of the purification strategy once oxidation had taken place.
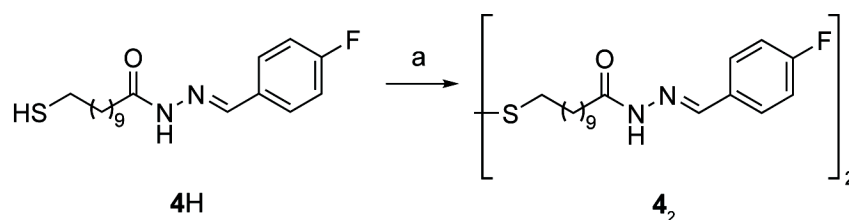
Scheme 2.5   Synthesis of disulfide **4**$_2$ from thiol **4**H. a): Iodine (2 Eq), CH$_2$Cl$_2$, rt, 30 min, 88%.
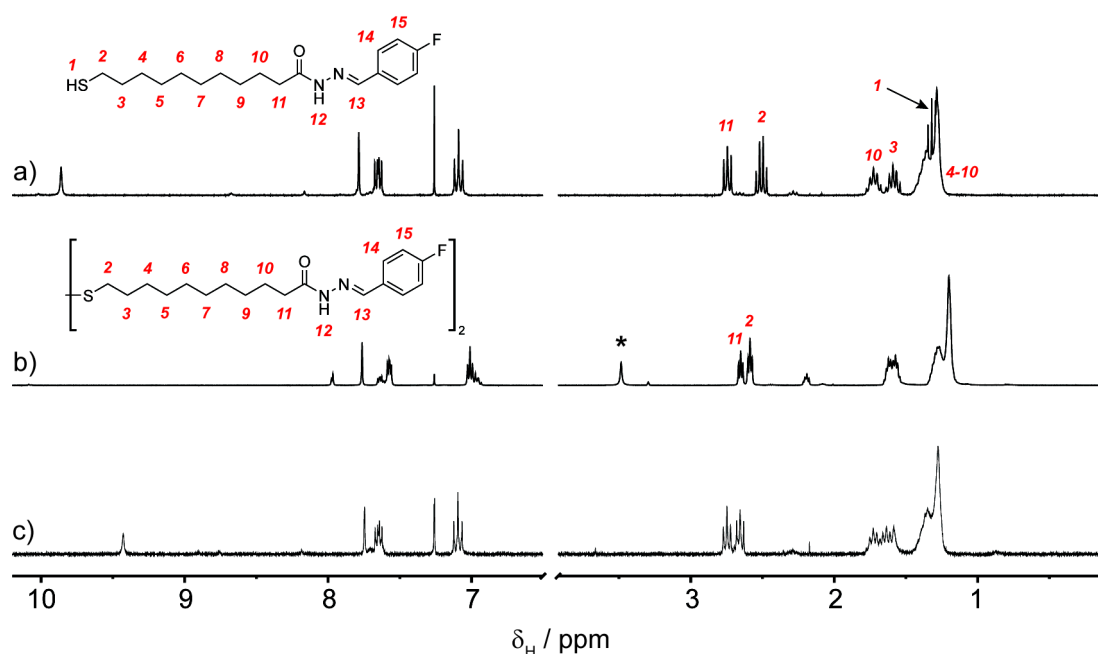
Figure 2.3   Partial ^{1}H NMR spectra (CDCl$_3$, 300.1 MHz, 295 K) of hydrazone **4**H (a), disulfide **4**$_2$ (b) and sample after ligand exchange with AuNP-**TOAB** (c). *: Solvent residual peak of CD$_3$OD (2 drops) used to completely dissolve disulfide **4**$_2$ in CDCl$_3$.

In an attempt to optimise the purification protocol, a more extensive investigation of the solubility properties of disulfide 4_2 was performed. Disulfide 4_2 was mixed with common organic solvents to give a final concentration of 1 mg mL^{-1}. The mixture was then sonicated for 10 min, heated and left to cool to room temperature. It was found that disulfide 4_2 was only partially soluble in most common solvents (toluene, ethyl acetate, tetrahydrofuran, dichloromethane, acetone, ethanol and methanol) but not enough to achieve a full removal from the NP dispersion.

Further purification attempts were carried out, either increasing the number of washing cycles or reducing the ligand excess for the ligand exchange. Unfortunately, none of the chosen conditions led to pure ligand-functionalised AuNPs.

2.2.6   Nanoparticle purification by size exclusion chromatography

Considering the extremely low solubility of the disulfide formed by oxidation during the ligand exchange process, it was decided to exploit size exclusion chromatography (SEC) as an alternative option for NP purification.

SEC is a widely used separation technique for purifying macromolecular species (e.g. proteins, synthetic polymers, dendrimers).[166–168] It is routinely applied for the purification of nanomaterials dispersed in aqueous systems,[169–171] but application to organic-dispersible NPs has only rarely been employed.[172–175]

The basic principle of chromatography is that a mobile phase containing the mixture to be separated is passed through a stationary phase, previously swollen in an appropriate solvent. SEC stationary phases contain large pores in which small molecules can enter but larger species are excluded. Such size selection results in longer retention times for smaller entities. On the contrary, large molecules cannot enter in the pores because of their size and pass through the support with shorter retention times and separation of large from small species is achieved.

An organic-compatible porous support[176] was swollen overnight in tetrahydrofuran. The ligand exchange was carried out as before, using a thiol excess of 10 equivalents. The mixture was stirred for 2 hours and then precipitated by addition of methanol. To remove the bulk of the excess of ligand, the crude black solid was washed with an excess of methanol and sonicated for 15 minutes. The supernatant was decanted and then discarded. The black precipitate was finally dried under reduced pressure. The solid was then dissolved in tetrahydrofuran. The SEC purification was carried out like a traditional chromatographic separation, dividing the eluant in fractions and monitoring for the presence of unbound disulfide by TLC. The red-coloured fractions containing

NPs and free of unbound disulfide were then collected, dried and analysed by NMR spectroscopy.

^{1}H and ^{19}F NMR analysis (Figure **2.4B** and **D**) showed weak and broad signals, typical of that expected for NP-bound organic monolayers. No sharp peaks corresponding to TOAB or unbound species were detected. Despite the degree of uncertainty in integrating such broad signals, values obtained for H-*13*, H-*14* and H-*15* were in good accordance to those expected for NP-bound hydrazone **4**H. In terms of chemical shifts, a slight upfield shift of the signals corresponding to the aromatic protons ($\Delta\delta$ = –0.20 ppm and $\Delta\delta$ = –0.27 ppm for H-*14* and H-*15* respectively, Figure **2.4A–B**), consistent with the presence of weak edge-to-face π-π interactions. On the contrary, the imine signal (H-*13*) was shifted downfield ($\Delta\delta$ = 0.59 ppm). The NH resonance is barely visible around 12 ppm. Assignment of signals in the aliphatic region was more difficult because of the overlapping of the methylene peaks from about 0.5 to 1.5 ppm. This results from the relative proximity of the methylene protons to the gold core. Ligands strongly adsorbed on the gold surface are densely packed, in a solid-like environment, resulting in faster spin-spin relaxation from dipolar interactions when compared to those of freely dissolved species. In addition and perhaps more significantly, a distribution of chemical shifts also originates from the diversity of ligand binding site to the NP (faces, edges, vertices)[59] and furthermore from the range of NP sizes and shapes in each sample. The combination of such phenomena causes the broadening of the peak linewidths (see Section **1.3.4**).

^{19}F NMR spectroscopy has the potential to be a powerful technique for the characterisation of ligand-functionalised NPs. The ^{19}F nucleus is 100% abundant in nature and has spin ½. [19]F and ^{1}H nuclei have comparable gyromagnetic ratios (40.052 and 42.576 MHz T[−1], respectively). Thus ^{19}F NMR exhibits high sensitivity, comparable to ^{1}H NMR. In addition, proton-decoupled ^{19}F NMR spectroscopy provides less complicated spectra than ^{1}H NMR with also a wide range of potential resonances (usually from 0 to –275 ppm), allowing the analysis of complex molecules, bearing a selected number of fluorine atoms at specific points. Surprisingly, ^{19}F NMR analysis of monolayer-functionalised NPs has not been widely exploited. Only a few reports about the use of solid state ^{19}F NMR spectroscopy for NP characterisation are available in the literature.[177–179] For solution-state NMR, applications of ^{19}F NMR spectroscopy are reported by Murray and Pasquato.[180–183]

The ^{19}F NMR spectrum of AuNP-**4** (Figure **2.4D**) shows the presence of only one broad peak at –110.56 ppm, just slightly upfield shifted to that of the free thiol (–111.63 ppm), confirming the presence of the fluorinated species strongly adsorbed on the gold

surface. The absence of any sharp fluorine peaks also confirmed that the sample was free from any unbound fluorinated species (hydrazone **4**H or disulfide **4**$_2$).
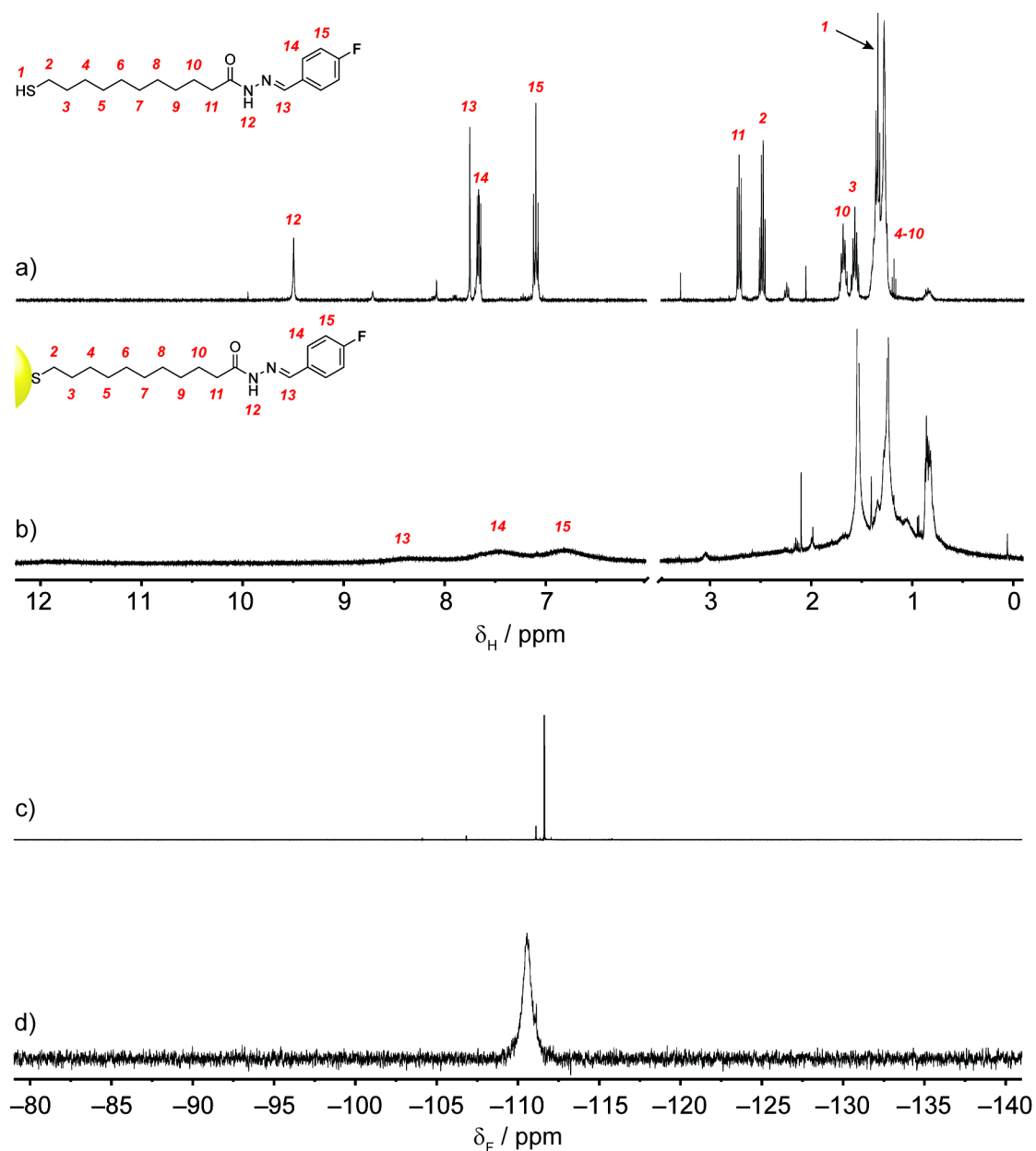
Figure 2.4   Partial ^{1}H NMR (CD$_2$Cl$_2$, 500.1 MHz, 295 K) and ^{19}F NMR spectra (CD$_2$Cl$_2$, 470.3 MHz, 295 K) of hydrazone **4**H (spectra a and c) and corresponding AuNP-**4** (spectra b and d).

TEM analysis allowed the mean diameter estimation of 3.71 ± 0.86 nm (23% dispersity), with no significant size change from the starting TOAB-stabilised colloidal gold solution (3.76 ± 1.14 nm, 30% dispersity). A monomodal size distribution was also observed (Figure **2.5**).

a) AuNP-**TOAB**

b) AuNP-**4**
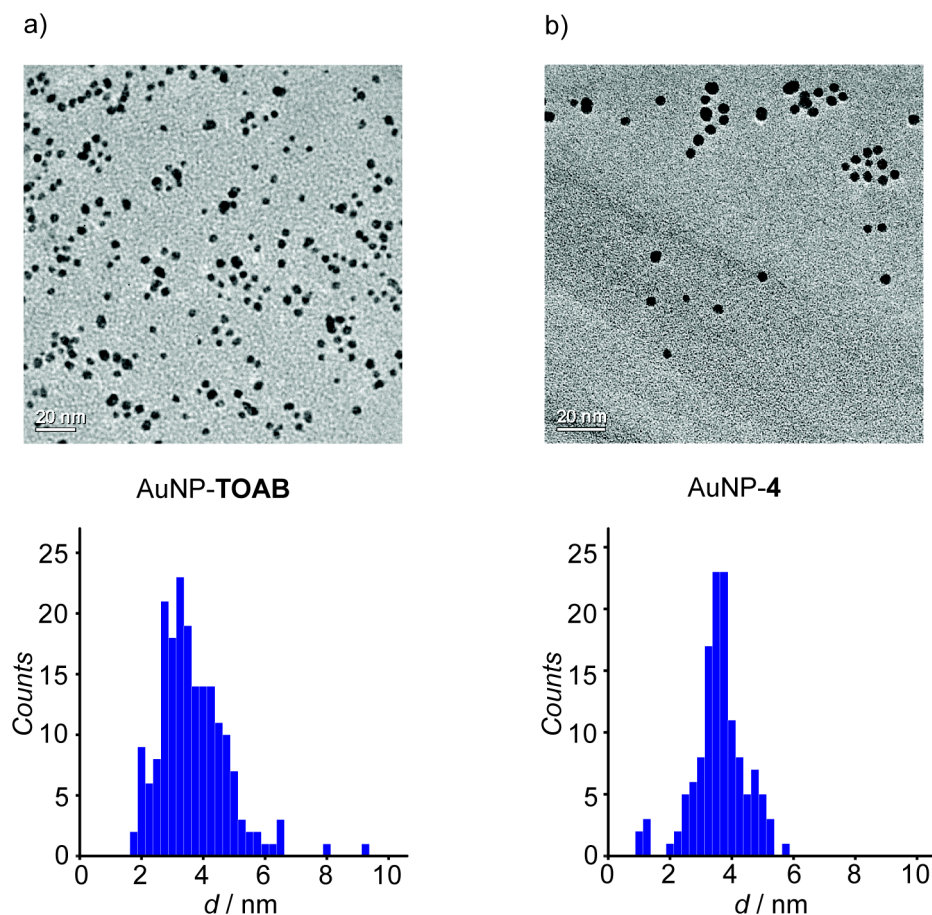
Figure 2.5   TEM micrographs of AuNP-**TOAB** before and after ligand exchange with hydrazone **4**H, after SEC purification. a): TEM (*top*, scale bar 20 nm) and size distribution (*bottom*) of AuNP-**TOAB**: mean diameter 3.76 ± 1.14 nm (30% dispersity). b): TEM (*top*, scale bar 20 nm) and size distribution (*bottom*) of AuNP-**4**: mean diameter 3.71 ± 0.86 nm (23% dispersity).

Following this promising result, the preparation of AuNPs coated with 4-methoxybenzylidene hydrazone **5**H was performed (Scheme **2.6**). A 10 equivalent excess of hydrazone **5**H was used to carry out a ligand exchange with a colloidal gold solution followed by SEC purification as before to give AuNP-**5**.
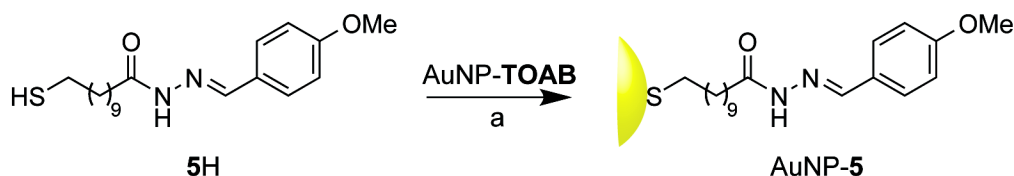
Scheme 2.6   Preparation of AuNP-**5** by ligand exchange with an excess of hydrazone **5**H. a): Toluene, 2 h, rt.

As shown in Figure **2.6**, broad peaks were again observed in the ^{1}H NMR of AuNP-**5** (spectrum b). The peak integration was in good accordance with that expected for hydrazone **5**H. Similar to the ^{1}H NMR of AuNP-**4** (Figure **2.4**), the aromatic peaks were

better resolved than the aliphatic ones. Comparing the chemical shifts of free hydrazone **5**H, the aromatic proton signals shifted upfield (H-*14* $\Delta\delta$ = –0.54 ppm, H-*15* $\Delta\delta$ = –0.42 ppm), consistent with the presence of weak edge-to-face π-π interactions. The imine peak (H-*13*) is also shifted upfield ($\Delta\delta$ = –0.17 ppm). Interestingly, even the NH peak (H-*12*) showed an upfield shift ($\Delta\delta$ = –0.46 ppm). The peak corresponding to the methoxy group (H-*16*) was very well visible in a relatively free region of the spectrum, with an upfield shift compared to the molecular species ($\Delta\delta$ = –0.13 ppm). This peak also appears to be split into a number of components, consistent with chemical shift dispersity representing a major source of peak broadening for NP-bound signals. Finally, the methylene protons of the alkane chain gave rise to a very broad peak between 0.75 and 1.75 ppm, as previously observed for AuNP-**4**.[59]
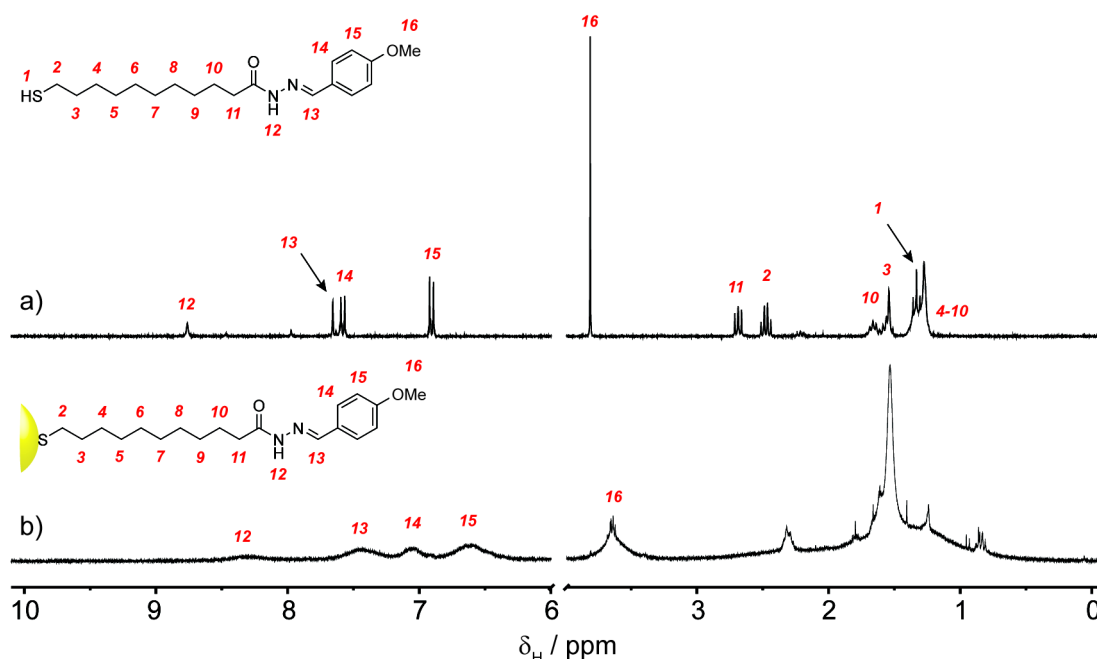
Figure 2.6   Partial ^{1}H NMR spectra (CD$_2$Cl$_2$, 400.1 MHz, 295 K) of hydrazone **5**H (a) and corresponding AuNP-**5** (b).

TEM analysis (Figure **2.7**) revealed a monomodal size distribution with a mean diameter of 2.86 ± 0.65 nm (23% dispersity) comparable to the starting colloidal gold solution (3.07 ± 0.79 nm, 26% dispersity).

According to TEM analysis for both AuNP-**4** and AuNP-**5** obtained pure after SEC purification, no change in NP size was observed after ligand exchange, within the experimental error. This observation is in accordance with the majority of ligand exchange examples reported in the literature.[165]
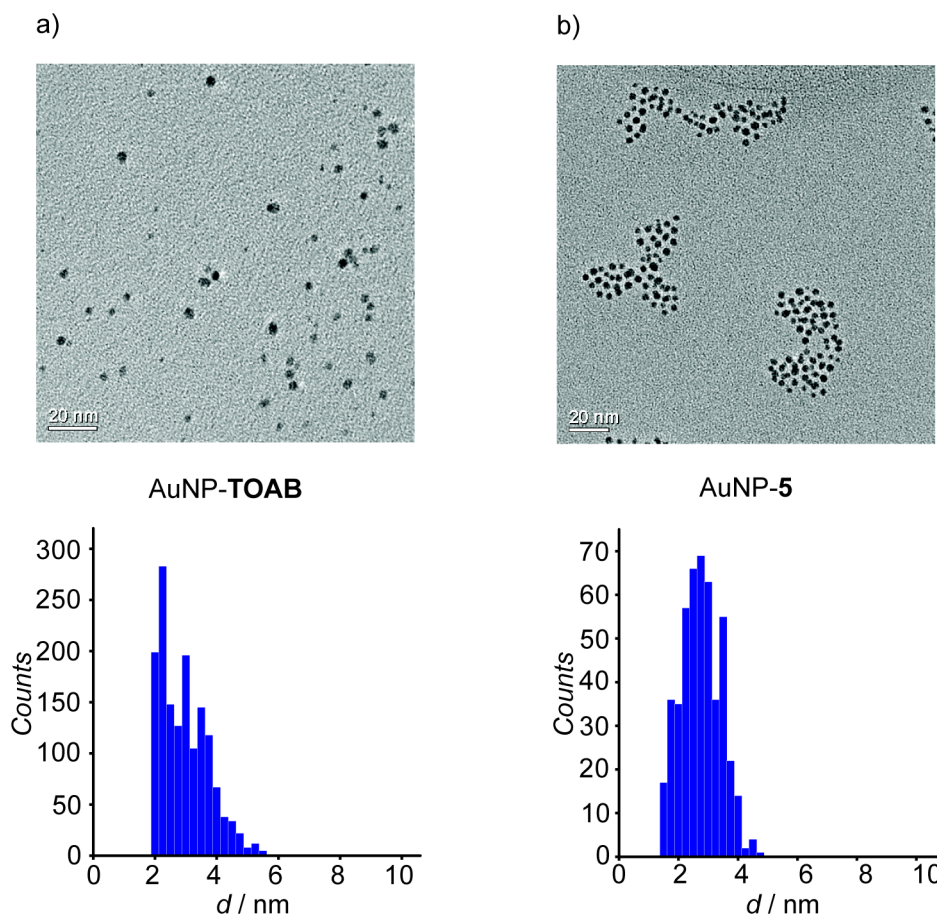
Figure 2.7   TEM micrographs of AuNP-**TOAB** before and after ligand exchange with hydrazone **5**H, after SEC purification. a): TEM (*top*, scale bar 20 nm) and size distribution (*bottom*) of AuNP-**TOAB**: mean diameter 3.07 ± 0.79 nm (26% dispersity). b): TEM (*top*, scale bar 20 nm) and size distribution (*bottom*) of AuNP-**5**: mean diameter 2.86 ± 0.65 nm (23% dispersity).

Despite these positive results, reproducibility of the SEC purification protocol was found to be challenging. A successful purification was achieved only when NPs were contaminated by a small excess of unbound ligand. Higher amounts of thiol and/or disulfide as contaminants frequently resulted in a failed purification. ^{1}H NMR spectra of AuNP-**4** after purification by SEC showed additional sharp peaks not corresponding to thiol **4**H or disulfide **4**$_2$. Further investigations concluded that those peaks correspond to material released from the SEC support itself which required removal by further NP washes with diethyl ether.

Using this method, it was therefore not possible to prepare hydrazone-functionalised AuNP material of sufficient quantity for subsequent investigations of NP-bound dynamic covalent exchange reactions.

2.3 Direct synthesis of *N*-aroyl hydrazone-stabilised gold nanoparticles
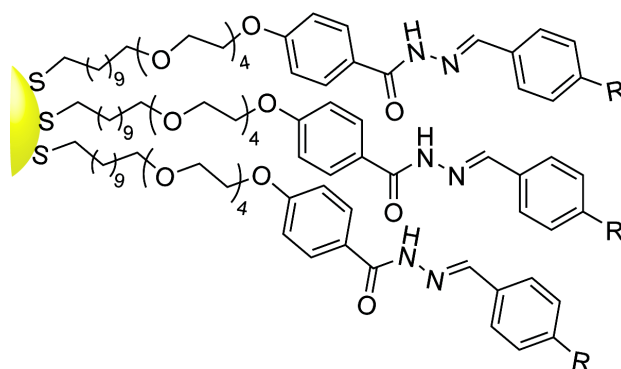
In order to overcome the issues encountered during the preparation of AuNPs functionalised with hydrazones **4**H and **5**H, the ligand design was modified to facilitate the by-product removal after the NP synthesis by solid-solvent extraction.

A tetraethyleneglycol (TEG) unit was included between the alkyl chain and the hydrazone moiety in order to improve solubility of the ligands, and their corresponding disulfides, in polar solvents (e.g. methanol) and to provide further conformational flexibility at the dynamic covalent reactive site.[184,185] Such solvents are also used to achieve AuNP precipitation from the reaction mixture. In this way, it was proposed that the solid ligand-coated AuNPs could be purified from the ligand excess by a series of washing cycles, avoiding the purification step by SEC.

2.3.1   Ligand design and synthetic strategy

To introduce the TEG unit, a procedure already reported in the literature by Rotello was adopted (Scheme **2.7**).[186] To commercially available 11-bromoundecan-1-ol, triphenylmethanethiol was added under basic conditions to afford compound **11**. The hydroxy group was then substituted by conversion to the mesylate **12** followed by alkylation of TEG used in large excess to give the monoalkylated product **13** in 77% yield. The desired trityl-protected precursor **14** was finally obtained by means of a second mesylation step with an overall 28% yield in 4 steps.
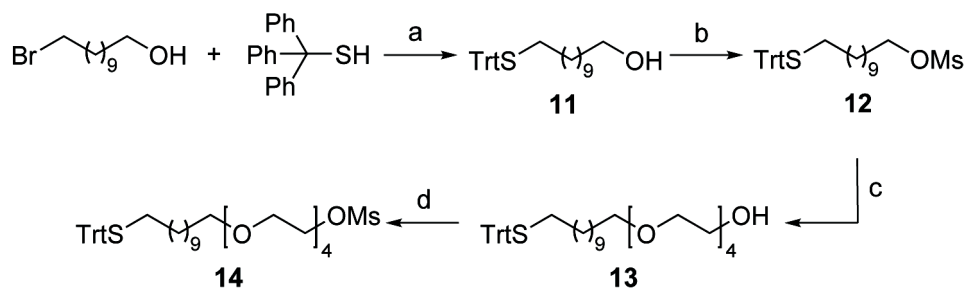
Scheme 2.7   Preparation of trityl protected precursor **14**. a): NaOH, H_2O, 1:1 EtOH/toluene, 3.5 h, rt, 93%. b) MsCl, Et_3N, CH_2Cl_2, 4.5 h, 0 °C to rt, 98%. c): TEG, NaOH, H_2O, 23 h, 90 °C, 77%. d): MsCl, Et_3N, CH_2Cl_2, 4 h, 0 °C to rt, 56%.

The hydrazone moiety was added by means of a further alkylation reaction (Scheme **2.8**). In order to avoid any possible side reaction from the free amino group of commercially available 4-hydroxyphenylhydrazine, it was decided to first prepare hydrazones **17** and **18**, before deprotonating the resulting phenols and treating with a DMF solution of precursor **14** under reflux, to the desired products **19** or **20**. Finally, the thiol group was deprotected and oxidised *in situ* with iodine. The desired disulfides were so obtained in 7 steps with 20% overall yield, for **21**$_2$, and 11% overall yield, for **22**$_2$.
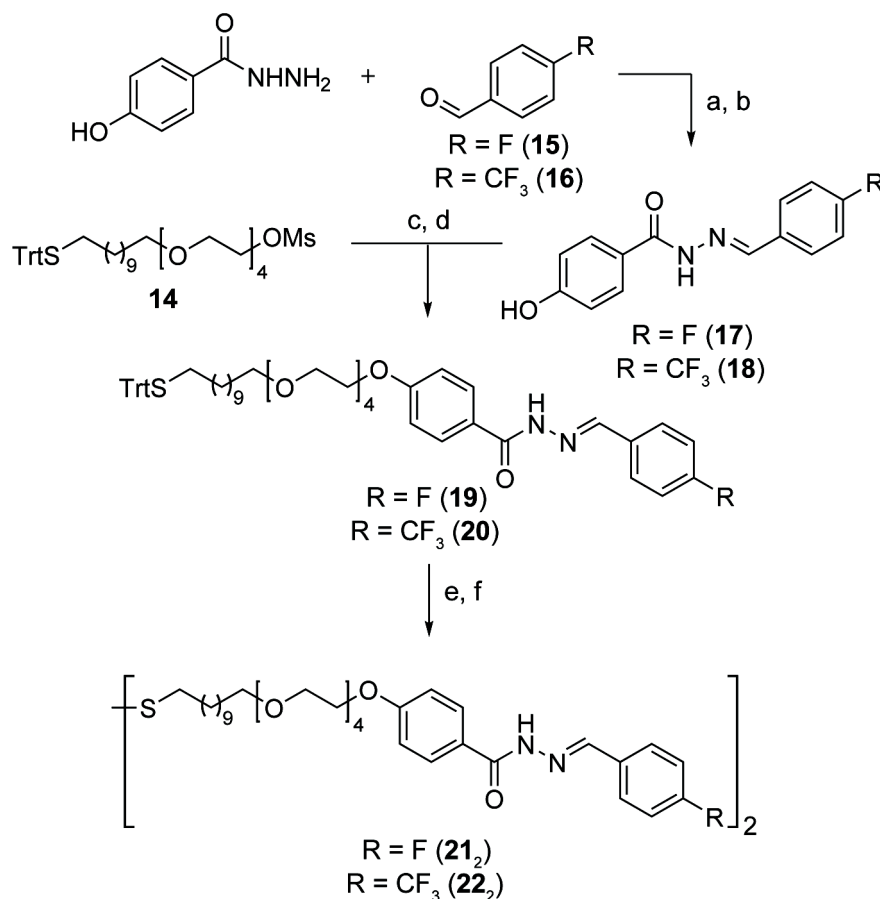
Scheme 2.8   Preparation of ligands **21**$_2$ and **22**$_2$. a): R=F, 4-fluorobenzaldehyde **15** (1 Eq), 6% AcOH, MeOH, 19 h, rt, 95%; or b): R=CF$_3$, 4-(trifluoromethyl)benzaldehyde **16** (2 Eq), 6% AcOH, MeOH, 24 h, rt, 95%. c): R=F, K$_2$CO$_3$ (3 Eq), DMF, 90 °C, 14 h, 52%; or d): R=CF$_3$, K$_2$CO$_3$ (3 Eq), KI (0.5 Eq), DMF, 90 °C, 2 days, 55%. e) R=F, iodine (2 Eq), MeOH, rt, 1 h, 99%; or f): R=CF$_3$, iodine (2 Eq), MeOH, rt, 30 min, 52%.

As discussed in Sections **2.2.2–4**, the two-step variant of the Brust–Schiffrin protocol can be used to obtain ligand-coated AuNPs by ligand exchange from TOAB-stabilised colloidal gold stock solutions.[160] Although a monomodal size distribution could be achieved by this method, the size dispersity was consistently rather large and unsatisfactory.

One of the advantages of preparing functionalised AuNPs by direct synthesis is that the NP growth and the ligand coating occur simultaneously (Chapter **1**). In this way, a better control over size reproducibility is achieved together with lower size dispersity as the stabilising species bind strongly to the NP surface. However, the reducing agent is not physically separated from the organic ligand. Thus, an investigation of the chemical stability of the hydrazone ligands under reducing conditions was necessary.

The method developed by Stucky and co-workers was adopted.[45] For the preparation of functionalised AuNPs, triphenylphosphine gold chloride is employed as gold source, easily prepared from commercially available tetrachloroauric acid and

triphenylphosphine.[187,188] The original procedure consists of the solubilisation of the ligand in a suitable organic solvent with AuPPh₃Cl. *t*-Butylamine borane complex (TBAB) is the reducing agent, which is added as a powder in one portion, under vigorous stirring, to ensure a rapid reduction of Au(I) to Au(0) together with a progressive ligand coverage of the gold surface. The reaction is then quenched by addition of diethyl ether as non-solvent in order to induce NP precipitation. Several washing cycles follow to remove the ligand excess, the TBAB and the by-products of the gold source (Scheme **2.9**).

Although this method was previously optimised only for the preparation of AuNPs in the presence of simple alkane thiols (dodecanethiol, hexanethiol, octanethiol and decanethiol),[45,46] it was proposed that disulfides **21**₂ and **22**₂ would behave in a similar fashion.
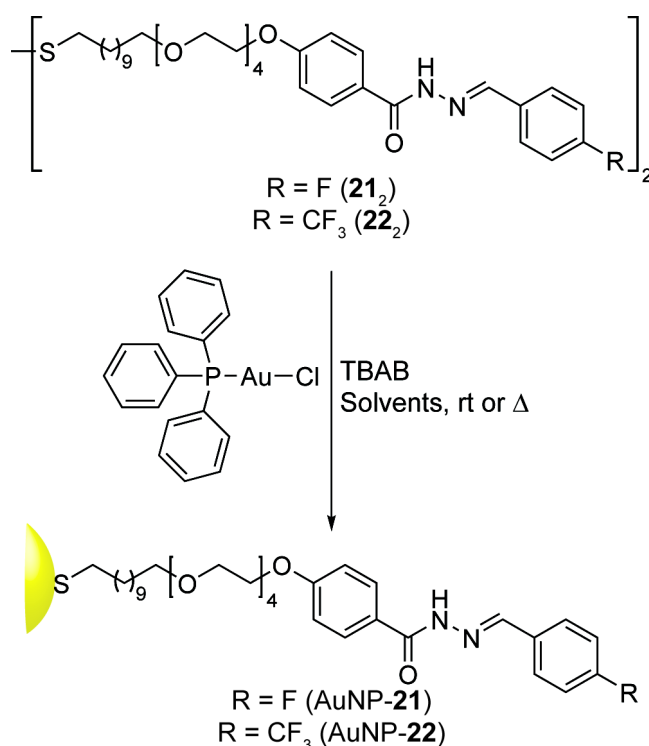
Scheme 2.9   General preparation of AuNP-**21** and AuNP-**22** by direct synthesis with TBAB as reducing agent. Reaction conditions are summarised in Tables **2.3**, **2.5** and **2.6**.

2.3.2   Hydrazone stability under direct synthesis conditions

Before attempting the AuNP functionalisation by direct synthesis, stability of the hydrazone moiety under reducing conditions was investigated using two model compounds (Scheme **2.10**). The hydroxy groups of hydrazones **17** or **18** were

alkylated, under basic conditions, with commercially available 2-chloroethyl methyl ether to afford the desired model compounds **23** and **24**.
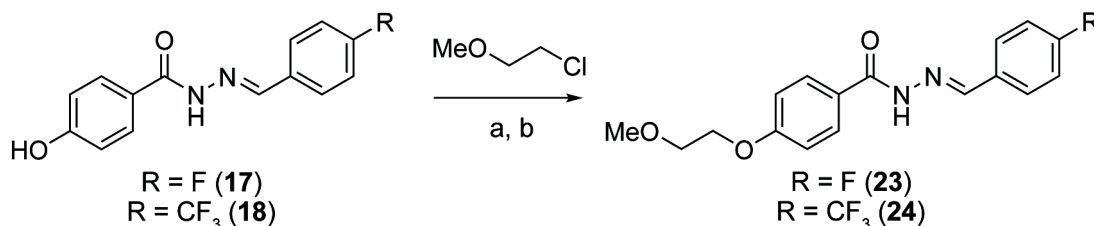
Scheme 2.10   Preparation of the model compounds **23** and **24**. a): R=F, 2-chloroethyl methyl ether (1.2 Eq), K_2CO_3 (3 Eq), DMF, 2 days, 90 °C, 57%; or b): R=CF$_3$, 2-chloroethyl methyl ether (5 Eq), K_2CO_3 (3 Eq), KI (0.5 Eq), DMF, MW 200 W, 30 min, 120 °C, 29%.

Compounds **23** and **24** were, separately, dissolved in an appropriate deuterated solvent mixture and mixed with AuPPh$_3$Cl and TBAB at room temperature. The experiments were monitored by ^{19}F NMR spectroscopy, observing any possible variation of the concentration of compounds **23** and **24**, estimated by means of an internal standard (see Section **5.3.2.1**).

Results showed that compound **23** was stable under these conditions for a period of at least 24 h; the hydrazone concentration did not decrease over that time and no additional ^{19}F peaks were detected. On the contrary, compound **24** was found to be stable for a shorter time (not more than 7 h). This is probably a consequence of the presence of the trifluoromethyl group in the *para* position on the aromatic ring, which makes the C=N bond more electron-poor and so more susceptible to reduction.

2.3.3   Direct synthesis of AuNP-21 from disulfide 21$_2$, purification and characterisation

The premature precipitation of growing functionalised NPs during synthesis (e.g. as observed for AuNP-**TOAB**, Section **2.2.4**) might be correlated with an increased size dispersity. For this reason, a preliminary investigation to find the best solvent to maintain all species in solution during the synthesis was performed.

2.3.3.1   Optimising the conditions for NP direct synthesis, size and dispersity

A series of small-scale experiments was carried out to find a suitable solvent system able to maintain the solubility of both disulfide **21**$_2$ and the growing NPs during the synthesis (Table **2.1**). The concentration of gold was kept constant while the gold/sulfur/TBAB ratio, the temperature and the mixing time were varied. After NP

precipitation with diethyl ether and purification with a methanol/diethyl ether mixture, each sample was characterised by ^{1}H and ^{19}F NMR spectroscopy, UV-Vis and TEM analyses.

Table 2.1   Summary of the preliminary conditions used for the preparation of ligand-coated AuNPs with disulfide **21**$_2$ by direct synthesis with TBAB as reducing agent (d: mean diameter; SPR: surface plasmon resonance).

Entry	Au/S/TBAB ratio	Solvent	T / °C	Time[a] / h	[Au] / mM	d[b] / nm (dispersity)	λ_{max} (SPR) / nm
a	1 : 2 : 10	THF	rt	3	20.0	1.96 ± 0.56 (28%)	None[c]
b	1 : 0.5 : 8.5	MeOH	55, rt	1, 20	20.8	1.99 ± 0.98 (49%)	None[c]
c	1 : 0.5 : 10	H$_2$O/THF 1:9	55, rt	1, 20	20.6	2.19 ± 0.75 (34%)	None[c]
d	1 : 0.5 : 6	THF/MeCN 1:1	rt	2.5	20.7	2.99 ± 0.61 (20%)	489

[a]: The time indicates when Et$_2$O is added to stop the reaction irrespective of when NP precipitation occurred.
[b]: Determined by TEM analysis for a minimum of 100 particle measurements.
[c]: The SPR band is not observed, suggesting a large population of nanoparticles with d < 2 nm.

In a preliminary set of experiments tetrahydrofuran (entry *a*) and methanol (entry *b*) were used. Subsequently, the polarity of the mixture was also varied by adding to tetrahydrofuran either water (entry *c*) or acetonitrile (entry *d*). For entries *a*, *b* and *d* a black precipitate was visible after few minutes from the TBAB addition, indicating that the forming NPs quickly became insoluble. By TEM analysis, the mean diameter of the recovered NPs was estimated to be around 2 nm for entries *a*, *b* and *c*. The large number of NPs with diameter < 2 nm is the reason of the high size dispersity observed for these samples and also explains the lack of observable SPR band.[5]

The presence of small NPs for entry *a*, *b* and *c* is a direct consequence of premature NP precipitation during the synthesis, which did not allow the NP growing process to go to completion. For entry *d*, despite NP precipitation during the synthesis, NPs were obtained a significant larger diameter (around 3 nm) with dispersity around 20%.

After NP precipitation with diethyl ether, the black solid could be easily purified by dispersion of the solid in methanol, followed by sonication and centrifugation, repeating the cycle at least three times, always checking for the presence of UV-active species by TLC. The same operation was then repeated with diethyl ether. After purification by washing, functionalised NPs were analysed by ^{1}H and ^{19}F NMR spectroscopy (Figure **2.8**). The adopted purification protocol provided functionalised AuNP-**21** free from any unbound excess disulfide **21**$_2$ and by-products from TBAB or AuPPh$_3$Cl. Analysis of

both ^{1}H and ^{19}F NMR spectra, provided first evidence of a successful purification because on broad peaks corresponding to NP-bound species were observed.

All ^{19}F NMR spectra show a characteristic broad peak at −111.49 ppm, which is comparable to that for the unbound disulfide **21**$_2$. The absence of any sharp peaks confirmed that the corresponding fluorinated species are strongly bound to the gold surface.

In an ideal situation, only a single fluorine peak would be expected. On the contrary, a second broad peak at −116.50 ppm was also observed with varying intensity across the three experiments (1.2:1 for entry *b*, 2.4:1 for entry *c*, 16:1 for entry *d*). The first obvious hypothesis for the presence of the secondary peak was that a partial reduction of the hydrazone moiety occurred during the NP synthesis.
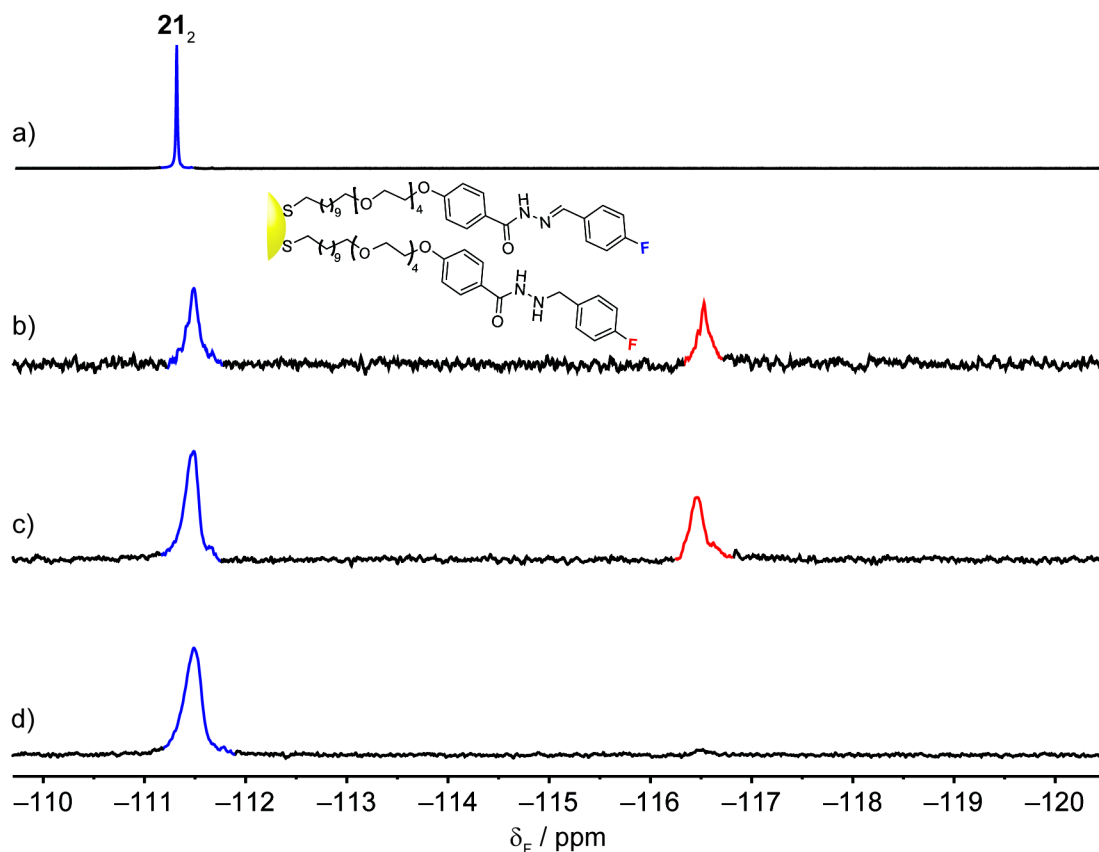
Figure 2.8   Partial ^{19}F NMR spectra ([D$_7$]DMF, 376.4 MHz, 298 K) of AuNP-**21** prepared accordingly to the synthetic conditions summarised in Table **2.3** (spectra b, c and d correspond to entries *b*, *c* and *d*, respectively) compared with disulfide **21**$_2$ (a). 512 scans were recorded for spectra b, c and d. All spectra are referenced to CFCl$_3$ (0.00 ppm).

In order to confirm this hypothesis, model compound **23** was treated with sodium cyanoborohydride (Scheme **2.11**) to selectively reduce the hydrazone moiety. Compound **25** shows one ^{19}F peak (in [D$_7$]DMF) at −116.23 ppm with chemical shift comparable with those observed in Figure **2.8B–C**.

Considering that the hydrazone moiety is stable during test reactions carried out at room temperature as described in Section **2.3.2**, it was concluded that heating at 55 °C was crucial to observe hydrazone reduction under the NP synthesis conditions.
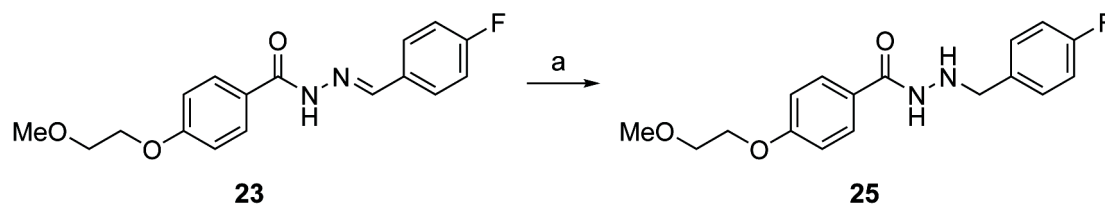
Scheme 2.11   Preparation of model compound **25**. a): NaCNBH$_3$, HCl/MeOH 4:96, 1 h, 0 °C, 57%.

In order to avoid NP precipitation during the synthesis, the colloidal stability of functionalised AuNPs obtained in 1:1 tetrahydrofuran/acetonitrile (Table **2.1**, entry *d*) was investigated. The NPs were found to be soluble only in polar aprotic solvents: *N*,*N*-dimethylformamide (DMF) and dimethyl sulfoxide (DMSO). Colloidal stability was also observed in H$_2$O/DMF mixtures up to 10% v/v. A summary of the solubility properties is presented in Table **2.2**.

Table 2.2   Solubility properties of AuNP-**21** in several solvents. Each test was performed by sonicating 1 mg of AuNP-**21** in 1 mL of solvent or mixture.

Solvent		Solvent	
HexH	NO	MeCN/THF 1:1	NO
Toluene	NO	MeOH/DMF 1:9	YES
Et$_2$O	NO	MeOH/DMF 1:1	Poor
DCM	NO	Water/DMF 1:1	NO
THF	NO	MeCN/MeOH 1:1	NO
EtOAc	NO	MeCN/Water 1:1	NO
Dioxane	NO	1% Water, DMF	YES
Acetone	NO	5% Water, DMF	YES
MeOH	NO	10% Water, DMF	YES
EtOH	NO	20% Water, DMF	NO
MeCN	NO	DMSO	YES
DMF	YES	Water	NO

Since AuNP-**21** showed very good solubility in DMF, further investigations were performed by adding DMF (10% v/v) to tetrahydrofuran and working at room temperature in order to avoid partial reduction of the hydrazone moiety.

Keeping the concentration of gold salt constant (16 mM), a series of small-scale experiments was carried out (Table **2.3**, entries *a–f*). The gold/sulfur/TBAB ratio was varied while the reaction time was kept constant (6 h). A gradual scale up of the synthesis was then performed (entries *g–i*). No NP precipitation was observed for all the experiments, confirming that 10% DMF was able to keep the growing NPs in solution as desired. For each experiment, after diethyl ether addition, a quick work-up was carried out. This involved dispersing the resulting black solid in methanol by sonication, then re-collecting the solid by centrifugation before discarding the colourless supernatant. The same operation was repeated using fresh diethyl ether. After drying under vacuum, each sample was characterised by TEM and UV-Vis analyses.

Table 2.3   Optimisation of the Au/S/TBAB ratio and scale up for the preparation of AuNP-**21** by direct synthesis. General conditions: [Au] 16 mM, DMF/THF 1:9, rt, 6 h.

Entry	Au / μmol	Au/S/TBAB ratio	d^a / nm (dispersity)	λ_{max} (SPR)^b / nm
a	16	1 : 0.5 : 5	2.22 ± 0.34 (15%)	None
b	16	1 : 1 : 5	2.41 ± 0.42 (17%)	None
c	16	1 : 2 : 5	2.32 ± 0.52 (22%)	None
d	16	1 : 0.5 : 10	3.01 ± 0.51 (17%)	509
e	16	1 : 1 : 10	3.06 ± 0.58 (19%)	542
f	16	1 : 1 : 20	2.86 ± 0.76 (27%)	543
g	65	1 : 1 : 10	3.39 ± 0.61 (18%)	509
h	100	1 : 1 : 10	2.79 ± 0.62 (22%)	508
i	192	1 : 1 : 10	2.75 ± 0.54 (20%)	506

^{a}: Size distribution are expressed as mean ± s.d.
^{b}: UV-Vis analysis was performed in DMF.

Some correlations of the NP mean diameter with the experimental conditions were observed. In the first series (entries *a–c*), the amount of TBAB was kept constant (5 equivalents with respect to gold) while the amount of ligand was gradually increased

from 0.5 to 2 equivalents. The mean diameter was found to be comparable, within the experimental error, for all the experiments (around 2.3 nm). By TEM analysis, a large number of small NPs (with diameter around 1 nm) was observed, as also confirmed by UV-Vis analysis, where no SPR band was observed for those samples. In addition, a small increase of the size dispersity was observed (from 15% to 22%, see Section **5.3.2.2** for size distribution histograms). It has to be noted that the dispersity percentages are however lower than those obtained for the preliminary experiments (Table **2.1**, entries *a–c*), suggesting that adding DMF, which keeps the growing NPs in solution, was crucial to obtaining samples with better homogeneity.

Functionalised NPs larger than 2 nm and with a visible SPR band were desirable. For this reason, in a second series of experiments (entries *b*, *e*, and *f*) the amount of ligand was kept constant (equimolar to the amount of the gold). The excess of TBAB instead was increased (5, 10 and 20 equivalents respectively). It was observed that the increase of TBAB from 5 equivalents (entry *b*) to 10 equivalents (entry *e*) led effectively to larger NPs (mean diameter around 3 nm) with no change of the dispersity. On the contrary, a dispersity increase was observed when 20 equivalents of TBAB were used.

It can be concluded that the NP size, specifically when disulfide 21_2 is used, is not affected by the amount of ligand with respect to the amount of gold. On the contrary, the mean NP diameter is affected to some extent by the amount of TBAB. The *optimum* conditions, for this specific ligand and solvent combination, were obtained when the gold/sulfur/TBAB ratio is 1:1:10.

In order to assess the reproducibility of the NP size, a scale up of the synthesis was performed (Table **2.3**, entries *g–i*). Despite a small increase in dispersity (to around 20%), functionalised NPs could be obtained in a reproducible and scalable way with a mean diameter in the range 2.8–3.4 nm.

Each repetition of the synthetic procedure yielded identical molecular characterisation data (see Section **2.3.3.2**). The inherently heterogeneous nature of NP samples, however, means that each batch exhibits small differences in nanoparticulate characteristics. This can be exaggerated by low-sampling methods such as TEM analysis. Nonetheless, the TEM analysis and the UV-Vis spectra of independent batches (Figure **2.9**) demonstrate excellent batch-to-batch consistency for mean NP diameter, size distribution and dispersity from three representative samples of AuNP-**21**.
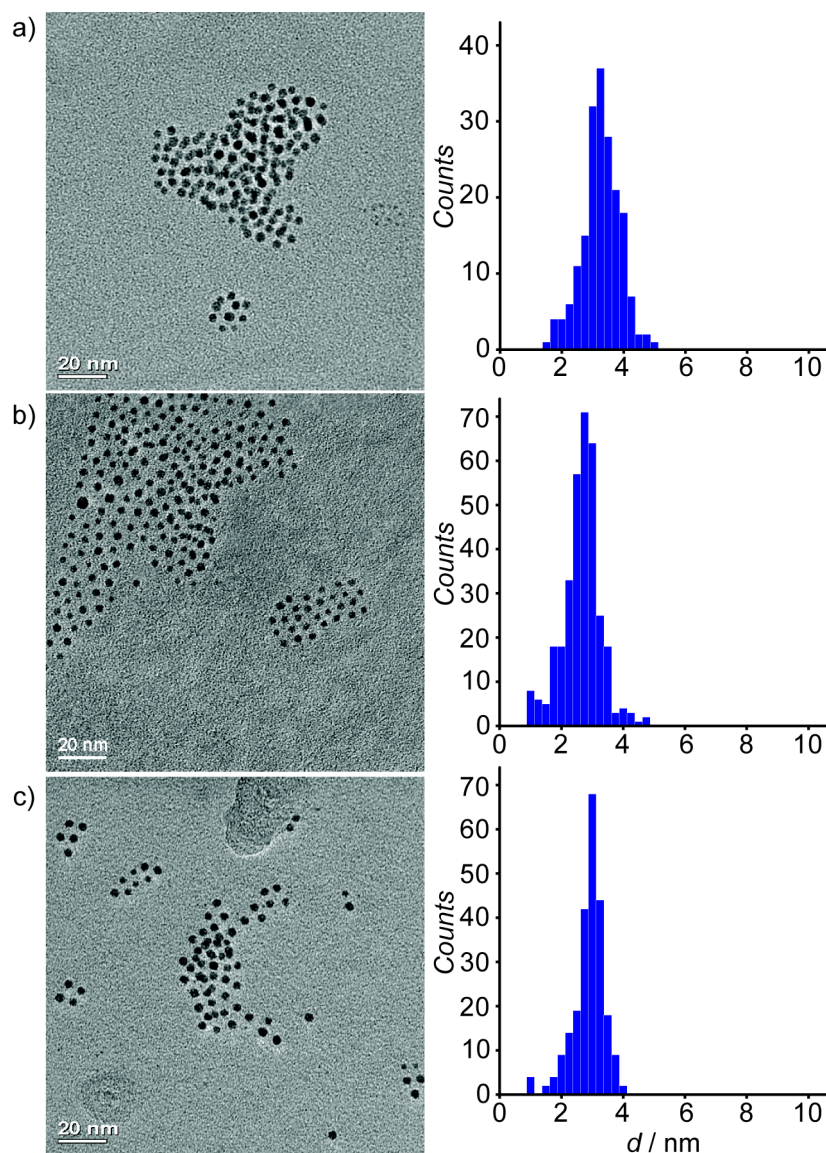
Figure 2.9 Representative TEM micrographs (scale bar 20 nm), size distribution (as determined from several images of each sample) and UV-Vis spectra (solvent: DMF) of AuNP-**21**. a): 3.39 ± 0.61 nm, 18% dispersity, SPR λ_{max} = 509 nm. b): 2.79 ± 0.62 nm, 22% dispersity, SPR λ_{max} = 508 nm. b): diameter 3.01 ± 0.51 nm, 17% dispersity, SPR λ_{max} = 509 nm.

The TEM micrographs show that AuNP-**21** tends to be organised in small aggregates on the TEM grid. This was most likely a drying effect from DMF, whose its high boiling point is sub-optimal for preparing TEM samples.

To verify the colloidal nature of the NP dispersion, an investigation by dynamic light scattering (DLS) was performed (Figure **2.10**). DLS is used to measure the colloid size in a suspension and it is also able to detect the presence of aggregates.[189] If AuNP-**21** existed as aggregates in solution similar to those shown in Figure **2.9**, DLS would show a peak around 100 nm, corresponding to the solvodynamic diameter of these aggregates. On the contrary, the DLS analysis reveals a monomodal size distribution

with an average solvodynamic diameter of 13.9 nm. This value is in good accordance with the theoretical solvodynamic diameter (10.3 nm, without considering the size of the solvation shell, Section **1.3.3**) estimated for AuNP-**21** with a mean diameter of 2.72 nm and functionalised with ligand **21** (3.78 nm[190]). A tilt angle (θ) of 30° for ligand **21** was assumed. The tilt angle is defined as the angle between the ligand and the Z-axis as observed in 2D self-assembled monolayers.[191] Thus, DLS analysis confirmed that the 'aggregates' visible in the TEM pictures are formed during the sample preparation and not during the synthesis.
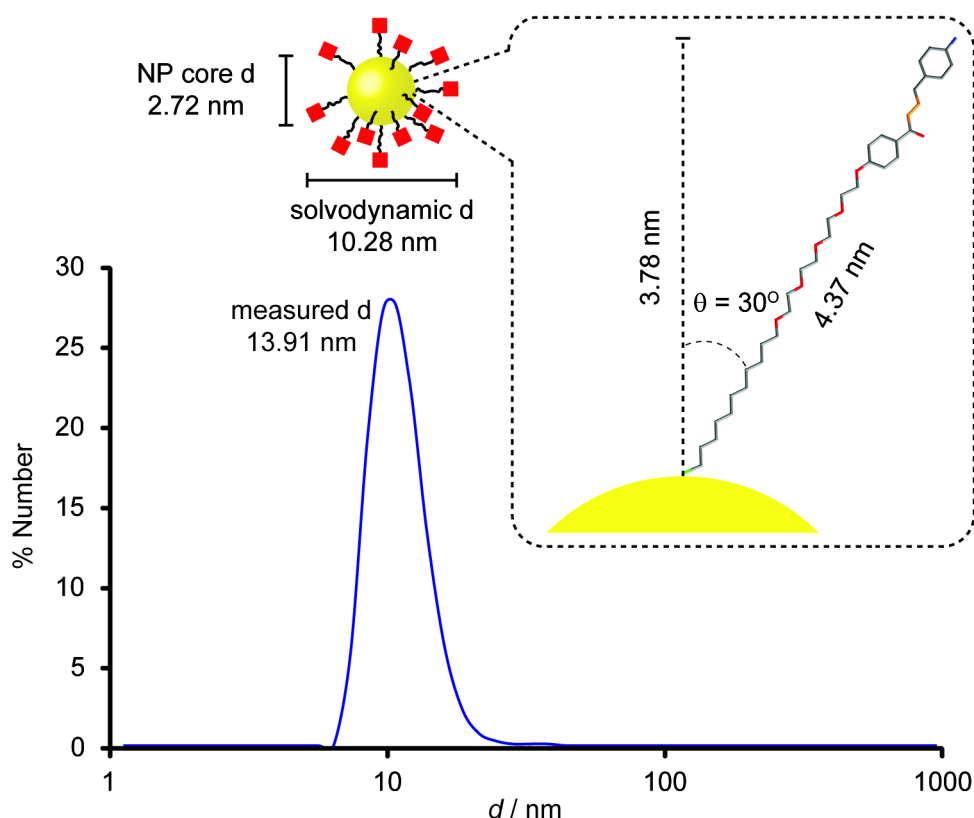
Figure 2.10   Dynamic light scattering analysis of AuNP-**21**. Mean solvodynamic diameter: 13.91 ± 2.73 nm (20% dispersity). Estimated solvodynamic diameter (excluding the solvation shell): 10.28 nm. θ: Tilt angle (30°).[191]

2.3.3.2   *Organic shell characterisation of AuNP-21*

As described in Sections **2.3.3.1**, using the optimised synthetic procedures AuNP-**21** could be obtained with reproducible size, low dispersity and apparently free from unbound disulfide **21**$_2$. Obtaining a pure sample of hydrazone-functionalised AuNPs is essential for following the relatively subtle changes within the monolayer under dynamic covalent exchange conditions. Similarly to AuNP-**4**, AuNP-**21** was then characterised by ^{1}H and ^{19}F NMR spectroscopy (Figure **2.11**). The ^{1}H NMR of AuNP-**21**

(spectrum b) shows the characteristic appearance of broad peaks corresponding to ligands adsorbed on the gold surface. The resonances of the aromatic region are very well resolved and a slight upfield shift of all the aromatic signals was observed when compared to the ^{1}H NMR of disulfide **21**$_2$ (spectrum a). The resonance corresponding to H-*21* is believed to be hidden by the solvent peak of the residual DMF. ^{19}F NMR shows only one broad peak at –111.50 ppm (Figure **2.11D**), slightly upfield shifted ($\Delta\delta$ = –0.16 ppm) when compared to the signal for disulfide **21**$_2$ (Figure **2.11C**), confirming that the hydrazone moiety is not reduced by TBAB at room temperature.
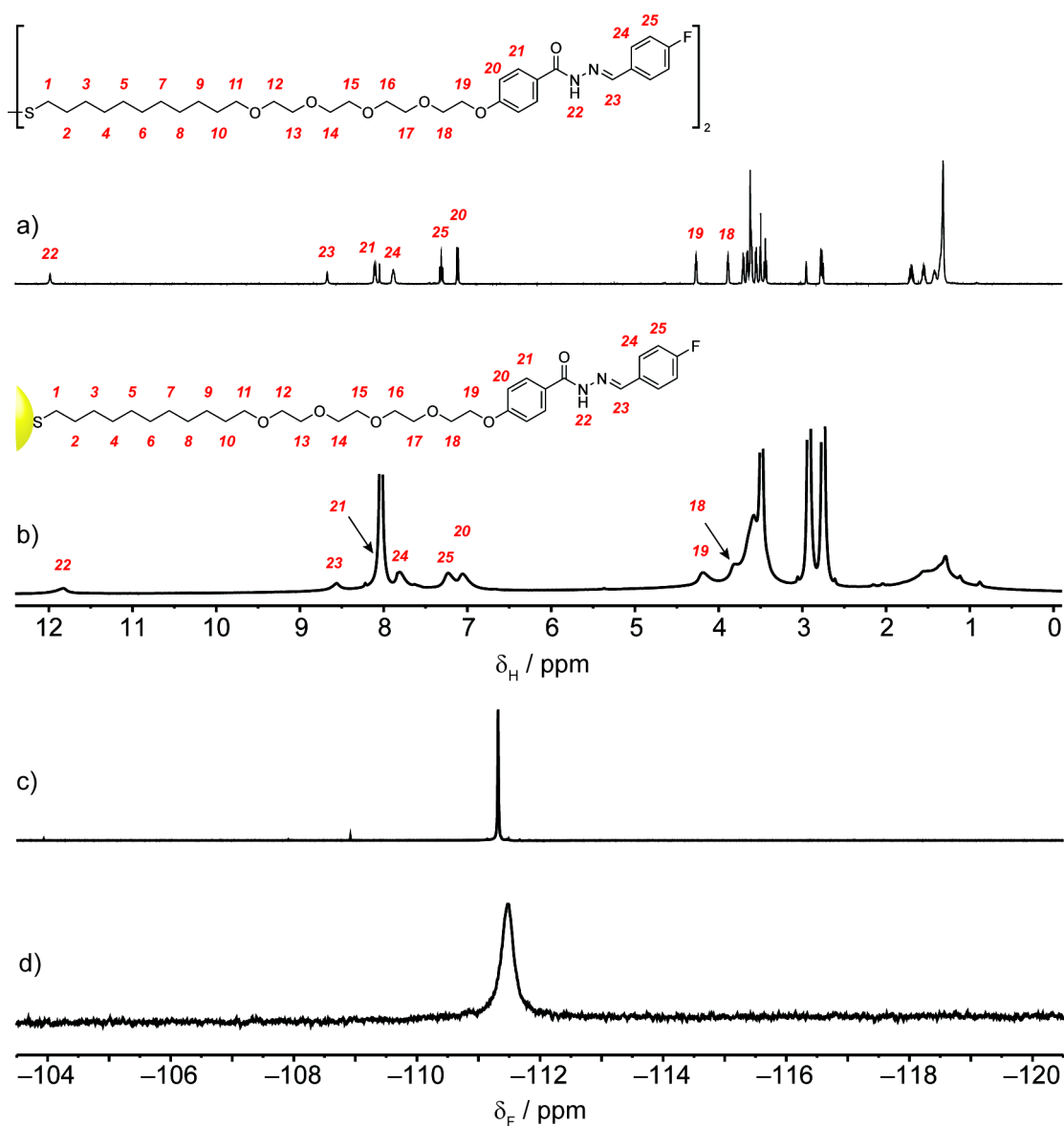
Figure 2.11 Characterisation of AuNP-**21** by NMR spectroscopy. ^{1}H ([D$_7$]DMF, 500.1 MHz, 295 K): a): disulfide **21**$_2$. b): AuNP-**21**. ^{19}F ([D$_7$]DMF, 500.1 MHz, 295 K): c): disulfide **21**$_2$. d): AuNP-**21**. (^{19}F NMR is referenced with CFCl$_3$ at 0.00 ppm).

The absence of sharp peaks suggests that AuNP-**21** is free from unbound species. A more rigorous confirmation of purity is provided by the T_2-filtered NMR analysis of AuNP-**21** (Figure **2.12**). By exploiting the short transverse relaxation times (T_2) for NP-bound nuclei, spin-echo pulse sequences can be used to detect only molecular species which have T_2 times longer than a particular delay time. The CPMG-*z* pulse sequence has been specifically developed to achieve T_2 filtering while avoiding signal distortion due to spin-spin coupling for assessing purity in samples containing NPs.[61] With an appropriate spin echo wait time D21 = 0.1 s, the resulting T_2-filtered ^{1}H NMR should show only resonances corresponding to molecular species, while all the resonances of the NP-bound species are filtered out. As evidenced by the T_2-filtered ^{1}H NMR spectrum of AuNP-**21** (Figure **2.12D**), only signals originating from the non-deuterated DMF and water are observed, confirming the absence of any unbound contaminants. When the same pulse experiment is applied to a 5 mM solution of disulfide **21**₂ (Figure **2.12A**), the resulting spectrum (Figure **2.12B**) is essentially identical to a traditional ^{1}H NMR experiment.
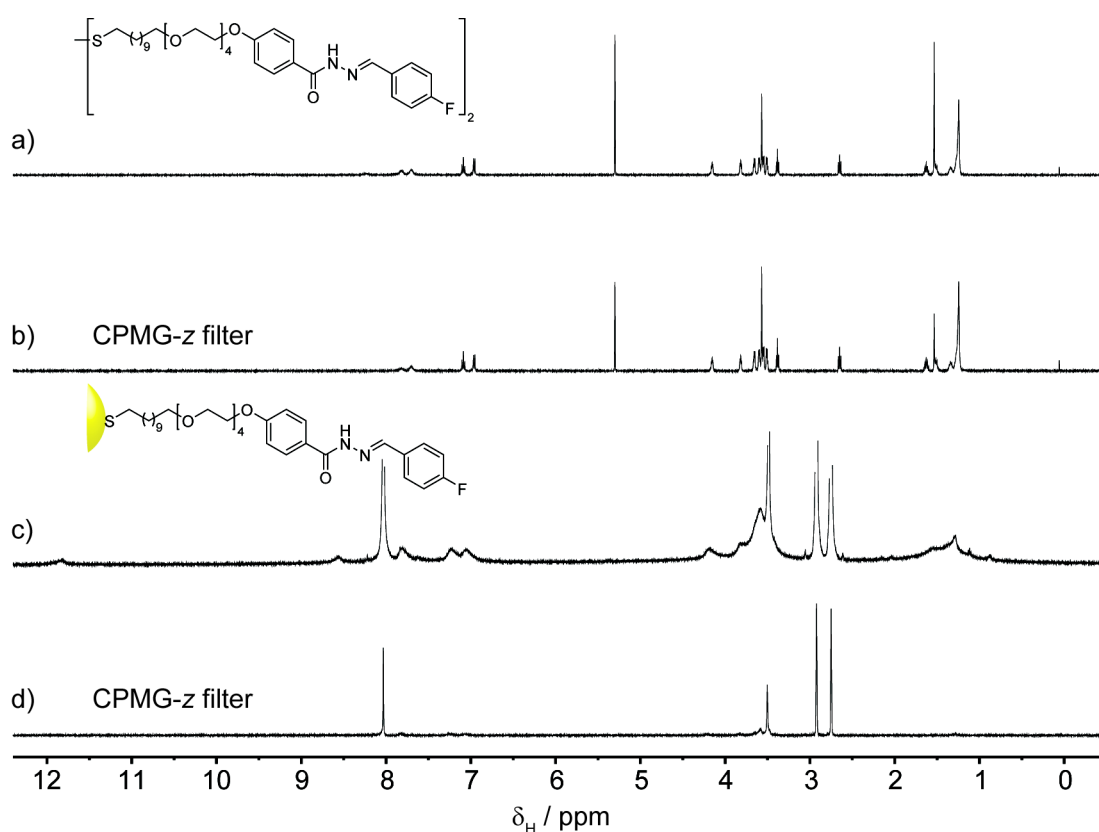
Figure 2.12 ^{1}H NMR (CD$_2$Cl$_2$, 500.1 MHz, 295 K) of disulfide **21**₂ at 5 mM (a) and its corresponding CPMG-*z* filter experiment (b) compared with ^{1}H NMR ([D$_7$]DMF, 500.1 MHz, 295 K) of AuNP-**21** at 5 mM (c) and its corresponding CPMG-*z* filter experiment (d).

The organic ligands bound to the NP core could be also characterised by laser desorption ionisation (LDI) mass spectrometry. AuNPs are able to absorb the excitation energy of the UV laser (355 nm) and for this reason the addition of an external matrix is not required. Such absorption leads to selective desorption and ionisation of the surface-bound molecules which can be detected by a time-of-flight detector. In Figure **2.13**, a LDI mass spectrum of AuNP-**21** is presented together with a proposed fragmentation mechanism.

All the major peaks were assigned. Molecular ions for disulfide **21**$_2$ (peak A) and thiol **21**H (peak D) were observed. Disulfide **21**$_2$ undergoes progressive loss of one and two sulfur atoms (peaks B and C respectively). Thiol **21**H undergoes loss of H_2S (peak E). Peaks with m/z 581.30, 567.31, 553.31 and 539.30 correspond to progressive loss of methylene units from fragment E. Similar behaviour has been reported by Rotello and co-workers for AuNPs stabilised by structurally related monolayers,[76] and matrix-assisted LDI-MS analysis of molecular disulfide **21**$_2$ produced an identical fragmentation pattern.
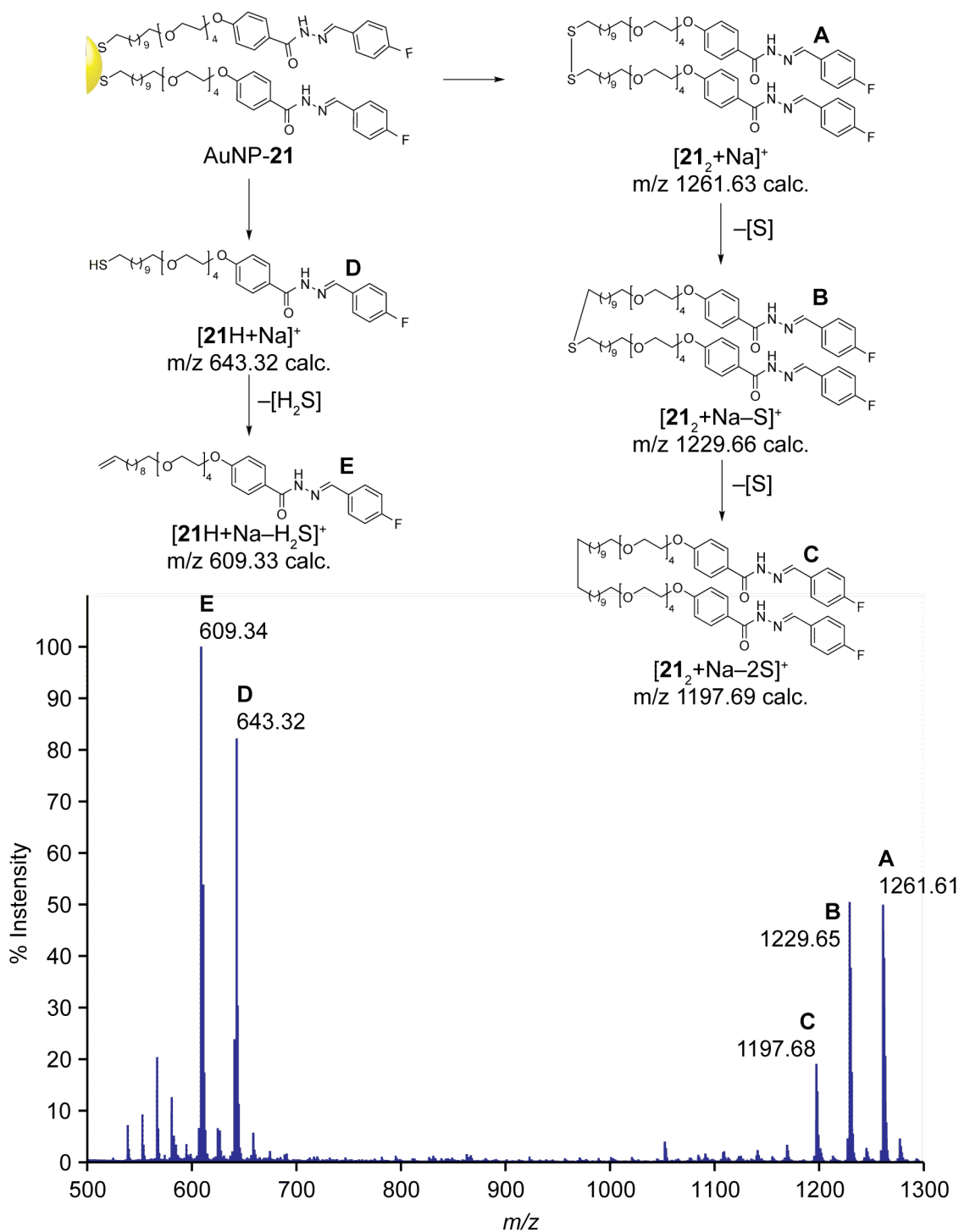
Figure 2.13 LDI mass spectrum and fragmentation pattern for AuNP-**21**. The fragment corresponding to the disulfide **21**$_2$ (peak A, [**21**$_2$+Na]$^+$: m/z 1261.61) undergoes a progressive loss of two sulfur atoms (peak B, [**21**$_2$–S+Na]$^+$: m/z 1229.65; peak C, [**21**$_2$–2S+Na]$^+$: m/z 1197.68). The fragment corresponding to the thiol (peak D, [**21**H+Na]$^+$: m/z 643.32) loses a H$_2$S (peak E, [**21**H–H$_2$S+Na]$^+$: m/z 609.34).

2.3.4   Direct synthesis of AuNP-22 from disulfide 22$_2$, purification and characterisation

Considering the excellent results obtained for the preparation of AuNP-**21** by direct synthesis, the same approach was used to prepare AuNP-**22** starting from disulfide **22**$_2$.

As previously discussed in Section **2.3.2**, model compound **24** was tested under reducing conditions with TBAB and it was concluded that although evidence of reduction was observed, the hydrazone was sufficiently stable at short reaction times up to about 7 h. As for the direct synthesis of AuNP-**21**, preliminary investigations were focussed on finding solvent mixtures able to keep the growing NPs in solution throughout the NP growth process.

In Table **2.4**, a series of small-scale experiments is summarised. The concentration of gold salt was kept constant (16 mM) in equimolar ratio with the amount of ligand. On the contrary, the amount of TBAB was varied from 6 to 15 equivalents. The choice of the solvent mixture was limited to tetrahydrofuran/acetonitrile 1:1 and 10% v/v DMF in tetrahydrofuran because NP precipitation did not occur by using these solvent mixtures. The work-up was carried out with diethyl ether to stop the reaction, followed by several washing cycles of 1:6 methanol/diethyl ether mixture to purify NPs from any unbound species. Characterisation was carried out by TEM and NMR spectroscopy (Figure **2.15**).

Table 2.4   Summary of the conditions used for the preparation of AuNP-**22a–d** by direct synthesis with AuPPh$_3$Cl and TBAB as reducing agent. (SPR: surface plasmon resonance).

Entry	Au[a]/S/TBAB ratio	Solvent	T / °C	Time[b] / h	d[c] / nm (dispersity)	λ$_{max}$ (SPR)[e] / nm
a	1:1:6	THF/MeCN 1:1	30	19	5.24 ± 1.56 —[d]	528
b	1:1:6	THF/MeCN 1:1	rt	6	4.69 ± 1.00 (21%)	516
c	1:1:15	THF/MeCN 1:1	rt	8	4.39 ± 0.98 —[d]	521
d	1:1:10	DMF/THF 1:9	rt	6	5.37 ± 0.86 (16%)	533

[a]: [Au] = 16 mM.
[b]: The time indicates when Et$_2$O is added to stop the reaction.
[c]: Determined by TEM analysis for a minimum of 100 particle measurements.
[d]: Indicative value. A bimodal distribution of the NP sizes was observed.
[e]: UV-Vis analysis was performed in DMF.
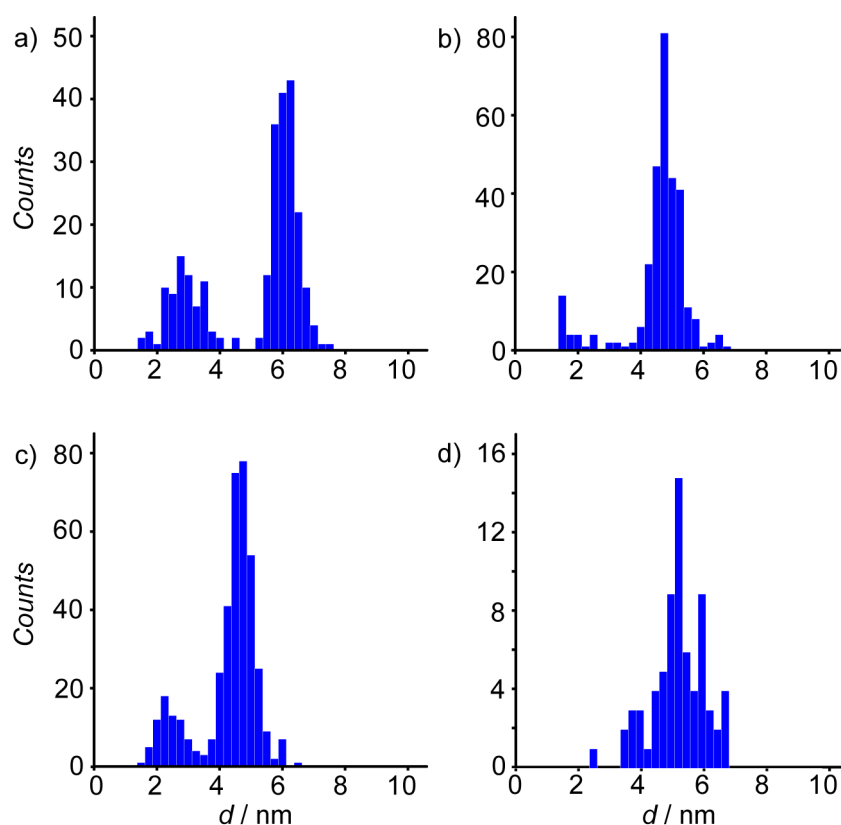
Figure 2.14   Size distribution (as determined from several TEM images of each sample) AuNP-**22a–d** prepared by direct synthesis according to the conditions summarised in Table **2.6** (entries *a–d*). a) Mean diameter 5.24 ± 1.56 nm (bimodal distribution, polydisperse). b): Mean diameter 4.69 ± 1.00 nm (21% dispersity). c): Mean diameter 4.39 ± 0.98 nm (bimodal distribution, polydisperse). d): Mean diameter 5.37 ± 0.86 nm (16% dispersity).

Analysis by TEM showed that AuNP-**22**, independent of the conditions employed, were consistently larger than AuNP-**21** (mean diameter between 4.4 and 5.4 nm, entries *a–d*). In addition, only when DMF was used in the mixture (entry *d*), the size dispersity

was excellent (16%) and a monomodal distribution achieved. On the contrary, the NP synthesis in a tetrahydrofuran/acetonitrile mixture always led to a bimodal size distribution, suggesting that the growth process was not complete when the reaction was stopped.

Moreover, analysis by ^{19}F NMR spectroscopy (Figure **2.15**) suggested that disulfide **22**$_2$ underwent chemical modification during the NP synthesis even at room temperature and at relatively short reaction times. A broad unsymmetrical peak corresponding to ligand **22** on the gold surface was observed in the region between –61.4 and –62 ppm (spectra a–d), slightly upfield shifted ($\Delta\delta$ = –0.09 ppm) when compared to the corresponding peak of disulfide **22**$_2$ (–61.37 ppm, spectrum e). A second peak around –61 ppm was detected in spectra a, b and c. In line with what was observed for AuNP-**21** (see Section **2.3.3.1**), a partial reduction of the hydrazone moiety appears to have occurred during the NP synthesis. This seems to have been minimal in experiment b and essentially eliminated in experiment d.
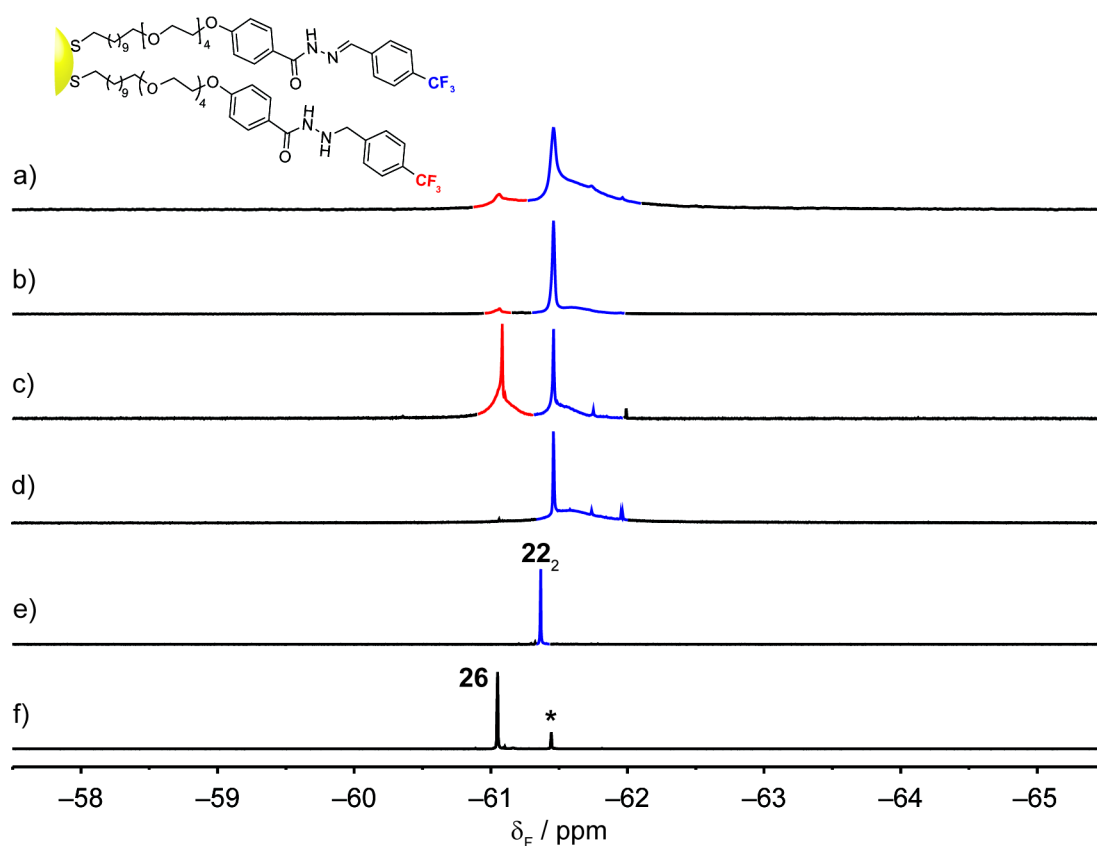
Figure 2.15   Partial ^{19}F NMR spectra ([D$_7$]DMF, 470.5 MHz, 295 K) for preparation of AuNP-**22** by direct synthesis under different synthetic conditions (S/Au 1:1). a): THF/MeCN 1:1, 30 °C, 19 h (6 Eq TBAB). b): THF/MeCN 1:1, rt, 6 h (6 Eq TBAB). c): THF/MeCN 1:1, rt, 8h (15 Eq TBAB). d): DMF/THF 1:9, rt, 6 h (10 Eq TBAB). e): disulfide **22**$_2$. f): model compound **26**. For details, see Table **2.6** (entries *a–d*). *: Residual model compound **24** (< 5%).

In order to confirm this hypothesis, model compound **24** was reduced with sodium cyanoborohydride (Scheme **2.12**) and analysed by ^{19}F NMR spectroscopy (Figure **2.15**, spectrum f). The reduced model compound **26** has a chemical shift (–61.05 ppm) perfectly comparable with that observed from the NP-bound ligands, confirming that a partial reduction of the hydrazone occurred during the synthesis.
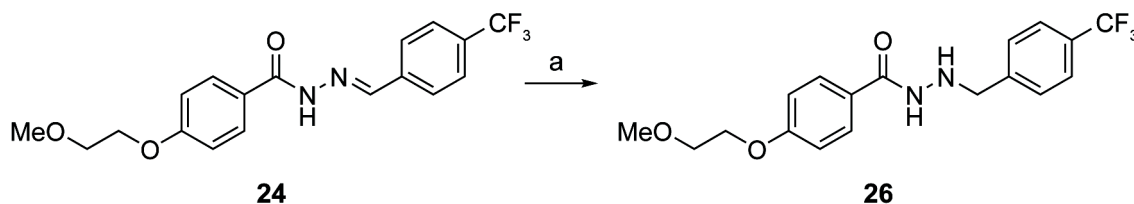
Scheme 2.12   Preparation of model compound **26**. a): NaCNBH$_3$, HCl/MeOH 4:96, 1 h, 0 °C, 37%.

It would appear that maintaining reaction temperature at room temperature and performing the reaction in 10% DMF/THF (experiment d) essentially eliminates the hydrazone reduction side reaction. AuNP-**22** prepared by this method was further characterised by LDI-MS spectrometry (Figure **2.16**) and ^{1}H NMR spectroscopy (Figure **2.17**).

The LDI mass spectrum confirmed the presence of ligand **22** adsorbed on the gold surface. Similarly to AuNP-**21**, the main fragments could be assigned as the result of ligand desorption of the disulfide **22**$_2$ (peaks A, B and C) and the thiol **22**H (peaks D and E). The proposed fragmentation mechanism was comparable with that for AuNP-**21** and previously reported in the literature.[76] No fragments that could be assigned as originating from the reduced ligand were observed, in line with the absence of a signal around –61 ppm in the ^{19}F NMR spectrum (Figure **2.15**). However, signals at m/z 709.29, 764.34 and 782.28 could not be assigned as originating from ligand **22**.
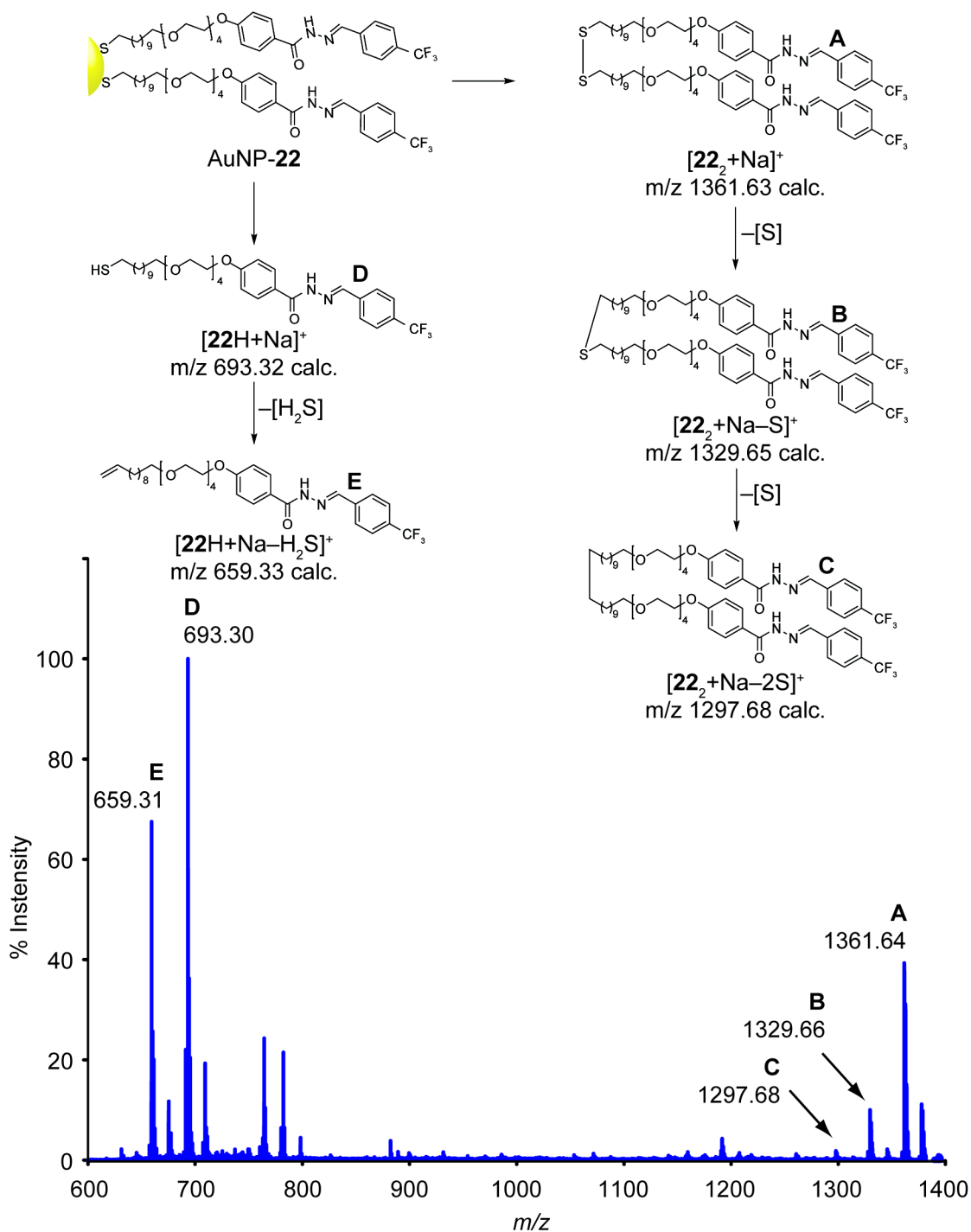
Figure 2.16 LDI mass spectrum and fragmentation pattern for AuNP-**22** prepared by direct synthesis with TBAB (see Table **2.6**, entry *d*). The fragment corresponding to the disulfide **22**$_2$ (peak A, [**22**$_2$+Na]$^+$: m/z 1361.64) undergoes a progressive loss of two sulfur atoms (peak B, [**22**$_2$–S+Na]$^+$: m/z 1329.66; peak C, [**22**$_2$–2S+Na]$^+$: m/z 1297.68). The fragment corresponding to the thiol (peak D, [**22**H+Na]+: m/z 693.30) loses a H2S (peak E, [**22**H–H2S+Na]+: m/z 659.31).

Unfortunately, the ^{1}H NMR spectrum suggested the presence of more than one NP-bound species. Figure **2.17** shows the ^{1}H NMR spectrum of AuNP-**22** prepared under conditions described in Table **2.4** (entry *b*). Broad resonances corresponding to the

methylene peaks of the alkyl and the TEG chain were observed. In particular, H-*18* and H-*19* are well resolved. Resonances corresponding to H-*22* (NH) and H-*23* (CH=) were also visible. On the other hand, many more resonances than expected are observed (particularly between 6 and 8.5 ppm, circled box). An unambiguous assignment of these peaks has not yet been possible, and the presence of a heterogeneous monolayer composed by ligand **22** and other NP-bound unknown species (Figure **2.15D**) was confirmed. This ^{1}H NMR spectrum can be compared to that obtained for AuNP-**22e**, prepared by hydrazone exchange from AuNP-**21** (see Section **3.2.1**). In this case, a homogeneous monolayer of ligand **22** was instead achieved with an excellent correspondence of the broad resonances with molecular disulfide **22**$_2$.
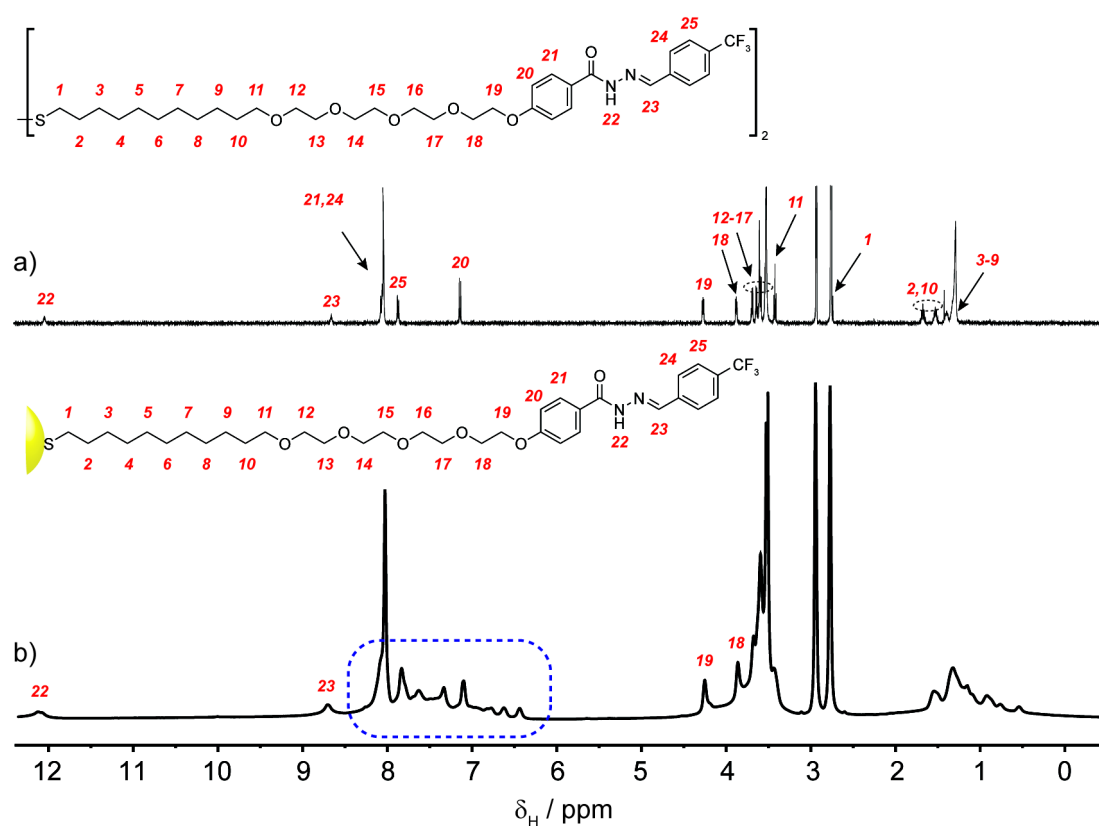
Figure 2.17 ^{1}H NMR ([D$_7$]DMF, 500.1 MHz, 295K). a): disulfide **22**$_2$. b) AuNP-**22b** prepared under conditions described in Table **2.6** (entry *b*).

By combination of NMR spectroscopy and TEM analysis, a connection between the presence of reduced NP-bound ligands **22** (Figure **2.15E**) and the bimodal distribution of the final NP size (Figures **2.14A** and **C** and **2.15A** and **C**) is suggested. From the available data, it seems that the population of small NPs (2–4 nm) obtained under these conditions (Table **2.4**, entries *a* and *c*) appears to correlate with the greater

proportion of reduced hydrazone observed in the NP samples recovered from these experiments.

In order to assess whether this hypothesis is correct, the preparation of NPs functionalised with a homogeneous monolayer of ligand **27** is currently under development (AuNP-**27**, Scheme **2.13**).
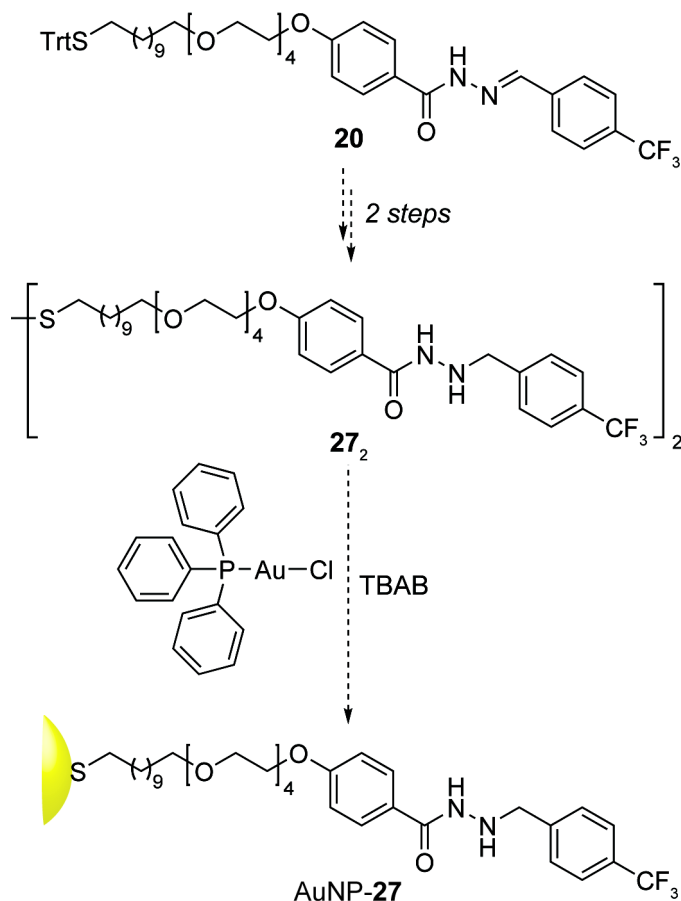
Scheme 2.13   Synthesis of AuNP-**27**. The hydrazone moiety can be reduced with NaCNBH$_3$ before incorporation on the NP surface by direct synthesis (see Schemes **2.11**–**12**).

2.4 Conclusions

Two groups of hydrazone ligands have been designed, synthesised and characterised. AuNPs have been functionalised with hydrazones **4**H and **5**H by ligand exchange. The purification of NP samples after the ligand exchange was challenging. For example, disulfide **4**$_2$ formed during the ligand exchange process showed low solubility in a large variety of organic solvents. This made the purification by solid-solvent extraction impossible to achieve. Eventually, AuNP-**4** and AuNP-**5** were successfully purified by SEC but only when NPs were contaminated by a small excess of unbound ligand.

These practical issues, together with an unsatisfactory polydispersity of the NP samples, were the reason for a change in the ligand design in order to adopt an alternative NP synthetic method. The direct synthesis approach provided much better results in terms of size reproducibility and dispersity, together with an easier and more efficient purification by solid-solvent extraction. Hydrazone 21_2 has more complex structure if compared to those of ligands commonly used in direct synthesis processes, but a reproducible method for the preparation of AuNP-**21** was optimised, leading to good size reproducibility and excellent dispersity. NMR spectroscopy was successfully used to characterise the organic ligands adsorbed on the gold surface. Broad peaks in the NMR spectra confirmed that the ligands were strongly bound to the gold surface and all the resonances could be unambiguously assigned and compared with those of disulfide 21_2. The purity of AuNP-**21** was demonstrated by TLC, ^{1}H and ^{19}F NMR spectroscopy. It was then possible to optimise the synthetic conditions in order to preserve the integrity of the hydrazone moiety under reducing conditions. LDI mass spectrometry further confirmed the chemical structure of the ligand after the NP synthesis.

AuNP-**22** was prepared by direct synthesis similarly to AuNP-**21**. In this case, it was found that disulfide 22_2 was more easily reduced by TBAB than disulfide 21_2. In addition, ^{1}H NMR spectroscopy suggested that other unknown NP-bound species could be also present, resulting in a complex mixed monolayer which also influences the final NP size, as suggested by TEM analysis. The identification of these NP-bound species requires further investigations in order to assess whether ligand **22** undergoes a structural change during the NP synthesis or have a different binding mode on the NP surface.

The presence of a fluorine atom in AuNP-**4**, AuNP-**21** and AuNP-**22** also allowed characterisation by ^{19}F NMR spectroscopy. The simplicity of the ^{19}F NMR spectra could be used as a powerful tool to detect any possible transformation of the fluorinated ligand during the NP synthesis. In addition, ^{19}F NMR spectroscopy shows a great potentiality for monitoring and tracking structural modification of NP-bound fluorinated hydrazone under dynamic covalent exchange conditions.

Chapter 3:
Dynamic covalent chemistry in the nanoparticle monolayer

This chapter demonstrates for the first time that dynamic covalent exchange can take place on the surface of gold nanoparticles (AuNPs) functionalised with a monolayer of hydrazone ligands.

The experimental conditions for the exchange are optimised for the *N*-aroyl hydrazone-functionalised AuNPs prepared in Chapter **2**. The hydrazone monolayer on the NP surface is subjected to dynamic covalent exchange with an excess of a fluorinated benzaldehyde under acidic conditions. In a first stage, the occurrence and the reversibility of the exchange is monitored by ^{19}F nuclear magnetic resonance (NMR) spectroscopy and confirmed by laser desorption ionisation (LDI) mass spectrometry. Subsequently, the reactivity of the monolayer is quantitatively investigated. A series of kinetic profiles is generated under hydrolysis and equimolar exchange conditions and compared with the kinetics for corresponding molecular model compounds treated under identical conditions.

Finally, a comparison between NP-bound dynamic hydrazone exchange and ligand exchange at the NP surface is also reported in order to demonstrate the advantages of the former over the latter.

3.1 Optimising experimental conditions for NP-bound hydrazone hydrolysis and exchange

Dynamic covalent chemistry (DCC) has been successfully applied in supramolecular chemistry, in polymer chemistry and for the preparation of dynamic covalent libraries.[107,109] Examples of dynamic covalent exchange have recently been reported for monolayers confined on two-dimensional flat surfaces,[192–194] and at the surface of self-assembled phospholipid bilayers.[195,196] On the other hand, such an approach on three-dimensional organic-molecule-functionalised NPs has not previously been explored.

In Chapter **2**, the synthesis, purification and characterisation of *N*-aroyl hydrazone functionalised AuNP-**21** was discussed (Figure **3.1**). The organic ligand was designed

to have the sulfur atom, for adsorption on the NP surface by formation of a strong Au–S bond, separated from the hydrazone moiety by a long flexible chain. This chain is composed of an alkyl portion, to ensure appropriate ligand packing on the NP core, as a result of the maximisation of the van der Waals interactions between neighbouring chains.[139] An additional tetraethylene glycol part provides solubility of AuNP-**21** in polar organic solvents.
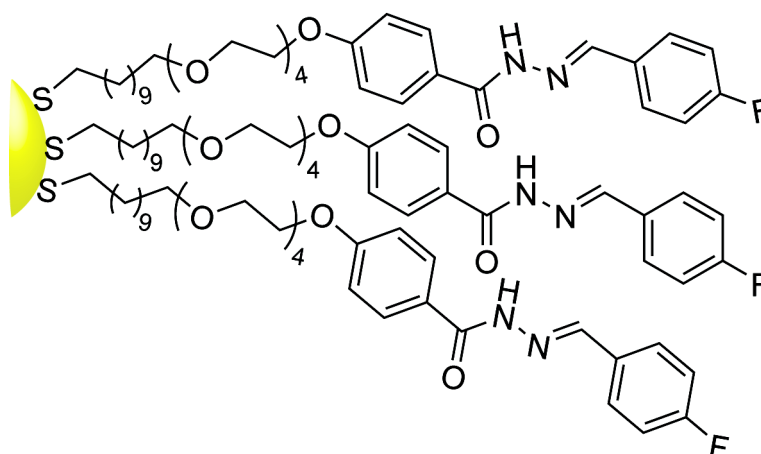
Figure 3.1   *N*-Aroyl hydrazone functionalised gold nanoparticles (AuNP-**21**) employed for performing post-synthetic dynamic covalent chemistry.

As discussed in Chapter **1**, hydrazone exchange can occur at acidic pH *via* hydrolysis and re-condensation,[113,116,197] or at neutral pH by using nucleophilic catalysts (e.g. aniline) *via* transimination.[112,118–121] In order to perform any exchange on AuNPs functionalised with ligand **21** (Figure **3.1**), 4-fluorobenzaldehyde **15** has to be displaced from the NP surface before achieving exchange with another electrophile exchange unit. Exchange *via* transimination requires aniline-type catalysts to be used in large excess (up to 100 equivalents) and would react with any aldehyde species present in the reaction mixture. This would result in a pool of NP-bound and unbound hydrazone and imine species challenging to analytically monitor. In addition, nucleophilic catalysts might interact with the gold surface causing an undesired and uncontrolled ligand displacement. For all these reasons, investigation of the hydrazone NP-bound monolayer reactivity under hydrolysis and exchange conditions was carried out with an acid catalyst.

3.1.1 Colloidal stability of AuNP-21 under acidic conditions

In order to carry out hydrazone exchange in the NP-bound monolayer, the stability of the NP dispersion must be maintained. Considering the limited solvent compatibility of AuNP-**21**, the choice of the solvent was limited to *N,N*-dimethylformamide (DMF) and dimethyl sulfoxide (DMSO) (Chapter **2**). Water attack is also crucial for the formation of the carbinolamine intermediate in the hydrazone hydrolysis/exchange mechanism (Chapter **1**).[111] AuNP-**21** was colloidally stable in 10% H_2O/DMF (Table **2.2**). On the contrary, NP precipitation was observed for higher percentages of water. Trifluoroacetic acid (CF_3CO_2H) was chosen as proton source because it has commonly been used in hydrazone exchange reactions.[107,140] In addition, CF_3CO_2H could be monitored by ^{19}F NMR spectroscopy and conveniently measured as a liquid.

The colloidal stability of AuNP-**21** in 10% H_2O/DMF with CF_3CO_2H was monitored by UV-Vis spectroscopy (Figure **3.2**). By monitoring the surface plasmon resonance (SPR) band, any decrease in the absorbance value or shift in the λ_{max} position would be, respectively, evidence of NP precipitation or aggregation in solution.

The amount of ligand **21** in a dispersion of AuNP-**21** in 10% H_2O/DMSO or 10% H_2O/DMF was estimated by ^{19}F NMR spectroscopy using an internal standard. After dilution to reach suitable UV-Vis concentrations (around 2 mM in terms of **21**), CF_3CO_2H was added (1 or 5 equivalents, with respect to **21**, to the DMSO and DMF mixtures, respectively). As shown in Figure **3.2A**–**B**, a decrease in the absorbance values was observed for the DMSO mixture suggesting NP precipitation from the reaction mixture within 3 hours. The poor stability of AuNP-**21** in the DMSO mixture was also visible by eye as a black NP precipitate formed at the bottom of the cuvette. On the other hand, AuNP-**21** stability in the DMF mixture was satisfactory. UV-Vis spectra recorded over 45 h after CF_3CO_2H addition showed no significant change in absorbance intensity or SPR band shape and position (Figure **3.2C**–**D**). The dispersion was colloidally stable even after incubation at 50 °C for 24 h. Furthermore, transmission electron microscopy analysis (TEM) revealed no significant change in NP mean diameter and size distribution under these conditions and no change to the colloidal dispersion was evident by eye.
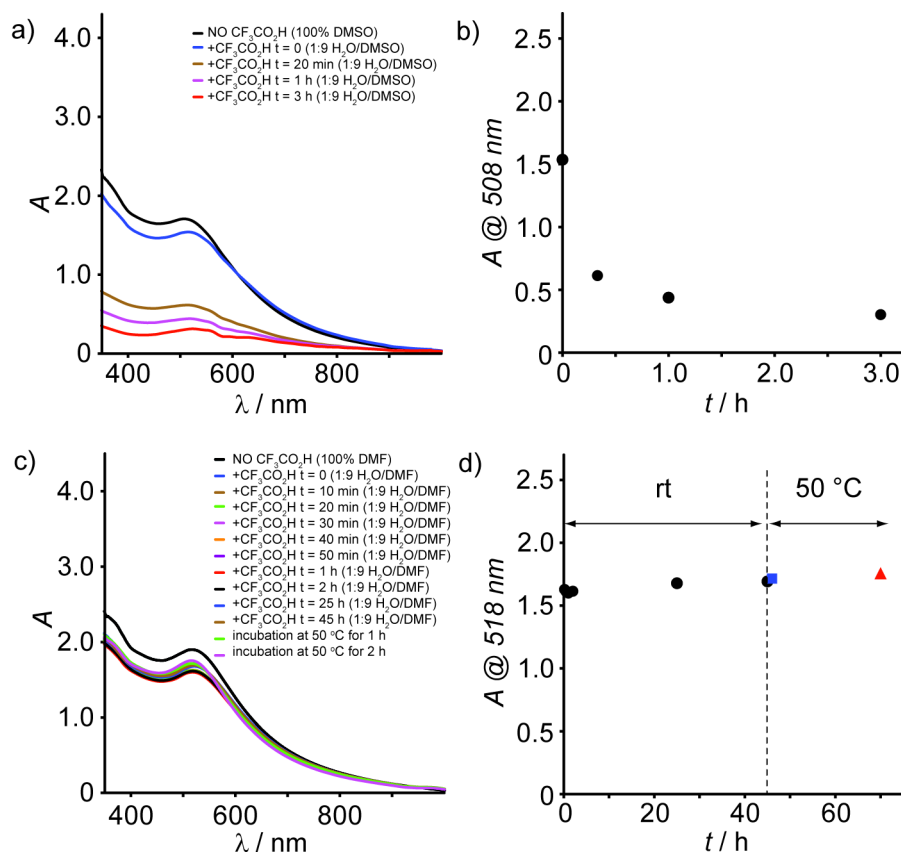
Figure 3.2 Tests of colloidal stability of AuNP-**21**. a): UV-Vis spectra in H_2O/DMSO 1:9 before and after CF_3CO_2H addition at rt (monitored for 3 h). b): Plot of the absorbance values recorded at λ_{max} (SPR) = 508 nm. c): UV-Vis spectra of AuNP-**21** in H_2O/DMF 1:9 before and after CF_3CO_2H addition at rt (monitored for 48 h) and then 50 °C (monitored for a further 24 h). d): Plot of the absorbance values recorded at λ_{max} (SPR) = 518 nm.

3.2 Dynamic covalent exchange in the nanoparticle monolayer: reversible hydrazone exchange between AuNP-21 and AuNP-22

Since AuNP-**21** was stable in 10% H_2O/DMF with 5 equivalents of CF_3CO_2H, the subsequent investigation involved hydrazone exchange with an excess of 4-(trifluoromethyl)benzaldehyde **16** under these conditions. This aldehyde was chosen because the corresponding NP-bound or unbound hydrazones (i.e. disulfide **22**$_2$ and AuNP-**22**, see Chapter **2**) showed ^{19}F NMR resonances around –62 ppm, well removed from the 4-fluorobenzylidene ligands (around –110 ppm). In addition, the hydrazone formed after exchange would have different mass, allowing differentiation by mass spectrometry.

3.2.1   Synthesis of AuNP-22e *via* hydrazone exchange from AuNP-21

A stable colloidal dispersion of AuNP-**21** in 10% D_2O/[D_7]DMF was treated with an excess of aldehyde **16** (20 equivalents with respect to ligand **21**) and CF_3CO_2H (5 equivalents) at 50 °C. The progress of the exchange was monitored by ^{19}F NMR spectroscopy, revealing a gradual decrease of the peak corresponding to NP-bound ligand **21** and a concurrent increase of two new peaks assigned to NP-bound ligand **22** and displaced 4-fluorobenzaldehyde **15**. After 16 h the equilibrium was reached. Hydrazone-functionalised AuNPs were recovered by precipitation with diethyl ether, obtaining a black precipitate which was washed several times with a mixture of methanol and diethyl ether. In this way, unbound molecular species were successfully removed and functionalised NPs were obtained (AuNP-**21**$_{0.1}$**22**$_{0.9}$) with a 1:9 ratio between ligands **21** and **22**, apparent by integration of their respective signals in the ^{19}F NMR spectrum (Figure **3.3**). The sample was then treated again under identical conditions to before and, after purification, a homogeneous monolayer of ligand **22** adsorbed on the NP surface was obtained (AuNP-**22e**) as confirmed by both ^{19}F NMR and LDI-MS analysis of the purified sample (Figure **3.3B**, *middle*). Fragments corresponding to desorbed disulfide **22**$_2$ and thiol **22**H were detected. Furthermore, the fragmentation mechanism was found to be identical to that observed for AuNP-**21** (Chapter **2**).[76] The absence of fragments corresponding to **21**$_2$ or **21**H provided corroboration that the exchange had gone completion (see Section **5.4.4** for full LDI-MS spectrum).
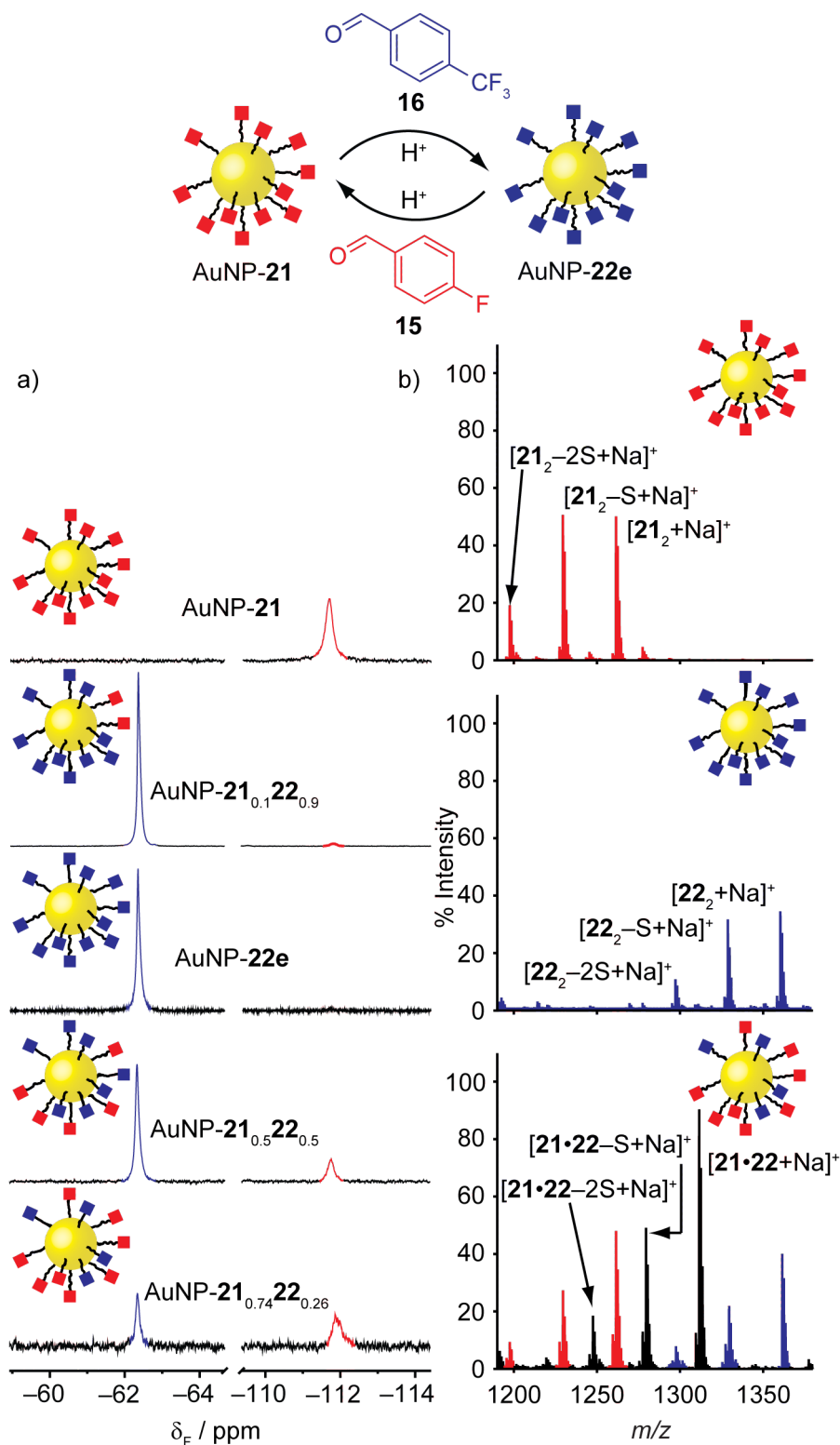
Figure 3.3 Hydrazone exchange between AuNP-**21** and AuNP-**22e**. Conditions: CF_3CO_2H, D_2O/[D_7]DMF 1:9, 50 °C. a) Partial ^{19}F NMR spectra ([D_7]DMF, 470.5 MHz, 295 K), from top to bottom: AuNP-**21**, AuNP-**21**$_{0.1}$**22**$_{0.9}$, AuNP-**22e**, AuNP-**21**$_{0.5}$**22**$_{0.5}$, AuNP-**21**$_{0.74}$**22**$_{0.26}$. b): Partial LDI-MS spectra of AuNP-**21** (*top*), AuNP-**22e** (*middle*) and AuNP-**21**$_{0.74}$**22**$_{0.26}$ (*bottom*). AuNP-**21**: [**21**$_2$+Na]$^+$ m/z 1261.61, [**21**$_2$–S+Na]$^+$ m/z 1229.65, [**21**$_2$–2S+Na]$^+$ m/z 1197.68. AuNP-**22e**: [**22**$_2$+Na]$^+$ m/z 1361.61, [**22**$_2$–S+Na]$^+$ m/z 1329.64, [**22**$_2$–2S+Na]$^+$ m/z 1297.66. AuNP-**21**$_{0.74}$**22**$_{0.26}$: [**21•22**+Na]$^+$ m/z 1311.54, [**21•22**–S+Na]$^+$ m/z 1279.54, [**21•22**–2S+Na]$^+$ m/z 1247.60.

The ^{1}H NMR spectrum of fully exchanged AuNP-**22e** (Figure **3.4B**) shows a pattern of broad peaks, indicating that the hydrazone ligands are strongly adsorbed on the NP surface. The absence of sharp peaks and the T_2-filtered ^{1}H NMR,[61] which shows only the peaks corresponding to the non-deuterated solvent and water (Figure **3.4C**), confirmed that the sample was free from any unbound molecular species.

The ^{1}H NMR of AuNP-**22e** (Figure **3.4B**) shows the aromatic peaks with comparable chemical shifts to those of AuNP-**21** (see Section **5.4.2** for the stacked spectra). In addition, the aromatic peaks are less in number than those of AuNP-**22b** prepared by direct synthesis (see Figure **2.17**). The combination of ^{1}H and ^{19}F NMR analysis suggests therefore the presence of a homogeneous NP-bound hydrazone monolayer. All aromatic chemical shifts related to NP-bound species were slightly upfield shifted when compared to disulfide **22**$_2$ (Figure **3.4A**). Resonances corresponding to H-*20* (Δδ = –0.05 ppm) and H-*25* (Δδ = –0.10 ppm) could be unambiguously assigned while resonances corresponding to H-*21* and H-*24* were found to be obscured by the solvent peak of the residual non-deuterated DMF (8.03 ppm) for both **22**$_2$ and AuNP-**22e**. Resonances corresponding to H-*22* (Δδ = –0.03 ppm) and H-*23* (Δδ = –0.01 ppm) were also assigned. Analysis of the ^{19}F NMR spectrum (Figure **3.4E**) shows only one peak at –61.46 ppm, slightly upfield shifted if compared to that of disulfide **22**$_2$ (Δδ = –0.09 ppm). No ^{19}F peak corresponding to AuNP-**21** was detected (see Section **5.4.3** for full sweep width spectrum), confirming that the hydrazone exchange had gone to completion. It should also be noted that the ^{19}F peak is broad and symmetrical and both ^{1}H and ^{19}F NMR spectra are much better than those obtained when a direct synthesis of AuNP-**22** was attempted.

One of the advantages of DCC is also herein demonstrated. AuNPs with a monolayer of ligand **22** could be successfully obtained as a homogeneous sample by hydrazone exchange from AuNP-**21**, without ligand degradation or reduction. In this way, issues encountered during the direct NP synthesis starting from disulfide **22**$_2$ (Chapter **2**) were circumvented.

Over several repetitions, the analysis of the size histograms before and after hydrazone exchange indicated no statistical change for both NP size and dispersity (Figure **3.5**).
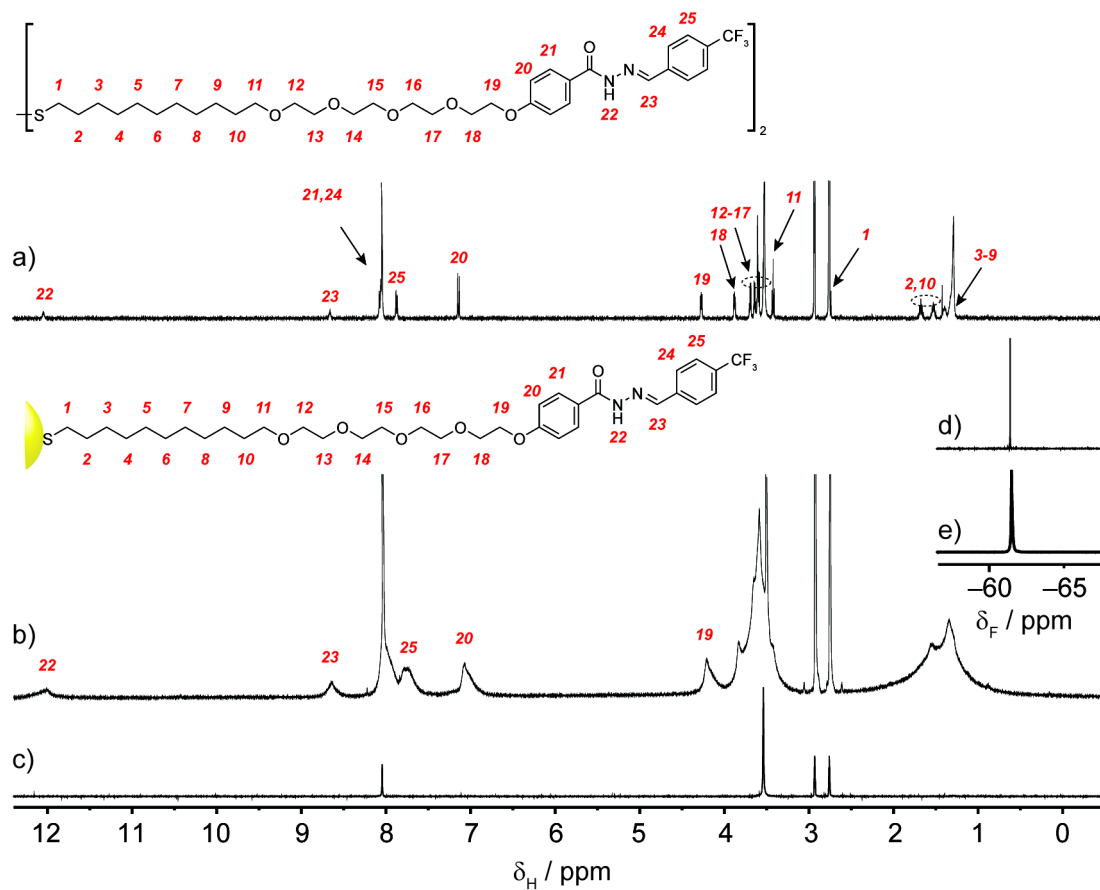
Figure 3.4   Characterisation of AuNP-**22e** by NMR spectroscopy. ^{1}H NMR ([D$_7$]DMF, 500.1 MHz, 295 K): a): disulfide **22**$_2$. b): AuNP-**22e**. c): T_2-filtered NMR of AuNP-**22e**. Partial ^{19}F NMR ([D$_7$]DMF, 470.5 MHz, 295 K): d): disulfide **22**$_2$. e): AuNP-**22e**.
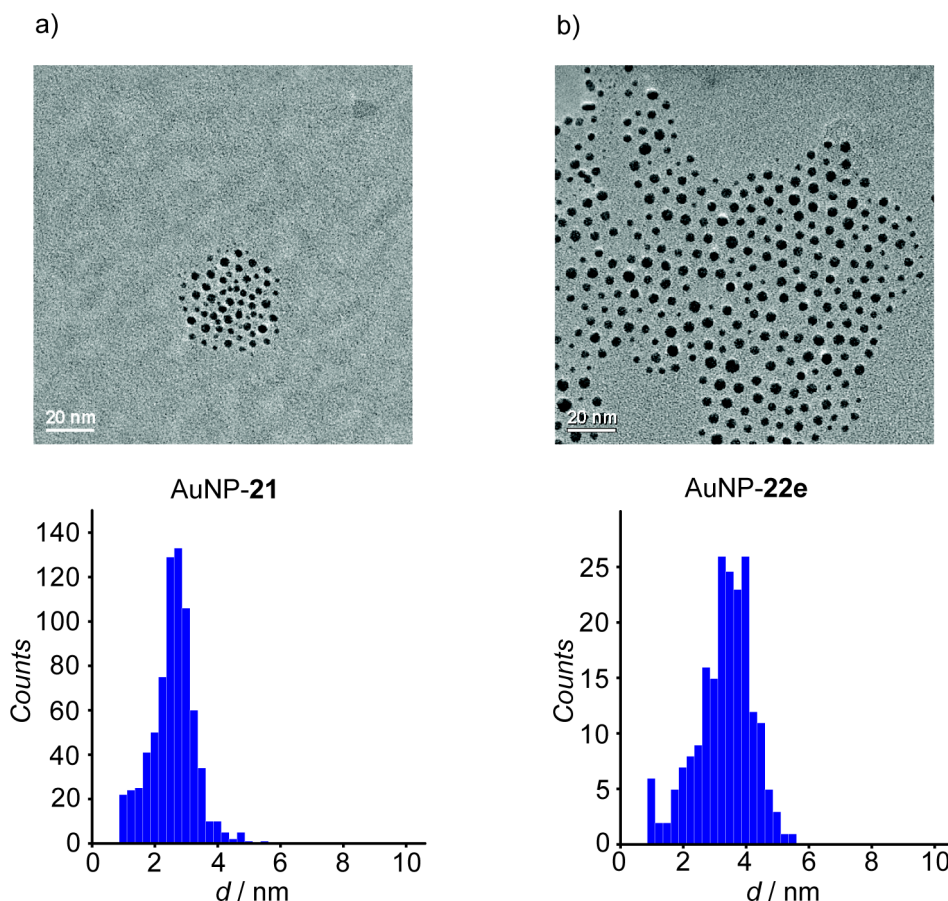
Figure 3.5   TEM micrographs before and after hydrazone exchange. Conditions: 4-(trifluoromethyl)benzaldehyde **16** (20 Eq), CF_3CO_2H (5 Eq), D_2O/[D_7]DMF 1:9, 50 °C, × 2. (a): TEM (*top*, scale bare 20 nm) and size distribution (*bottom*) of AuNP-**21**: mean diameter 2.71 ± 0.68 nm (25% dispersity). (b): TEM (*top*, scale bar 20 nm) and size distribution (*bottom*) of AuNP-**22e**: mean diameter 3.42 ± 0.92 nm (27% dispersity).

After characterisation of fully exchanged AuNP-**22e**, the reversibility of the hydrazone exchange was investigated. AuNP-**22e** was treated with an excess of 4-fluorobenzaldehyde **15** (20 equivalents with respect to ligand **22**) and CF_3CO_2H (5 equivalents) in 10% D_2O/[D_7]DMF. After purification, a clean NP sample (AuNP-**21**$_{0.5}$**22**$_{0.5}$) was obtained with a 1:1 ratio between ligands **21** and **22**, respectively (Figure **3.3A**). The sample was subjected to a further exchange under identical conditions to before and, after purification, a clean NP sample was obtained where the proportion of ligand **21** in the monolayer had increased to 74% (AuNP-**21**$_{0.74}$**22**$_{0.26}$).

The lower extent of exchange in the reverse process (under otherwise identical conditions) is in line with the greater stability for 4-(trifluoromethyl)benzylidene hydrazones (like **22**$_2$ and **24**) when compared to the 4-fluorobenzylidene moiety.[197] The trifluoromethyl group is more electron-withdrawing than the fluorine. This results in a lower electron density on the nitrogen atom which undergoes protonation during

hydrazone hydrolysis and thus in a greater hydrolytic stability of the 4-(trifluoromethyl)benzylidene moiety.

LDI-MS analysis confirmed the observation made by ^{19}F NMR spectroscopy (Section **5.5.3**). The mass spectrum of AuNP-**21**$_{0.74}$**22**$_{0.26}$ showed peaks corresponding homodimers **21**$_2$ and **22**$_2$. In addition, fragments corresponding to heterodisulfide **21•22** were also observed, suggesting an intimate mixing hydrazones on the NP surface.[76] A more detailed analysis of the relative abundance of fragments corresponding to homodimers **21**$_2$ and **22**$_2$ expressed as a ratio 55:45, which is conserved across all pairs of fragments. However, this ratio does not correspond to that suggested by ^{19}F NMR analysis (74% and 26%, respectively). This is not surprising and can be explained by a different ionisation efficiency for ligand **21** and **22** which otherwise undergo, identical fragmentation processes.[76]

3.2.2   Quantitative analysis of monolayer composition by ^{19}F NMR

The utility of ^{19}F NMR spectroscopy for tracking structure modification in the NP-bound monolayer under exchange conditions can be extended for quantitatively monitoring the monolayer reactivity.

However, the ability of ^{19}F NMR spectroscopy to accurately measure the amount of NP-bound fluorinated ligands had to be assessed. For this purpose, AuNP-**21**$_{0.74}$**22**$_{0.26}$ was treated with iodine, resulting in ligand displacement by oxidation (Figure **3.6**). By this way, the desorbed ligands can be analysed as molecular species in solution.

A ^{19}F NMR spectrum was recorded 30 minutes after iodine addition. The resulting spectrum (Figure **3.6B**) showed a pattern of sharp peaks, indicating that the organic species were no longer bound to the NP surface. Peaks corresponding to **21**$_2$ and **22**$_2$ were observed together with those corresponding to hydrolysed aldehydes **15** and **16**. 4-Fluorobenzoic acid, formed by oxidation of **15**, was also observed. Integrating the combined 4-fluoro and 4-(trifluoromethyl) regions indicated the same ratio (74:26) as determined by direct integration of the NP-bound signals.
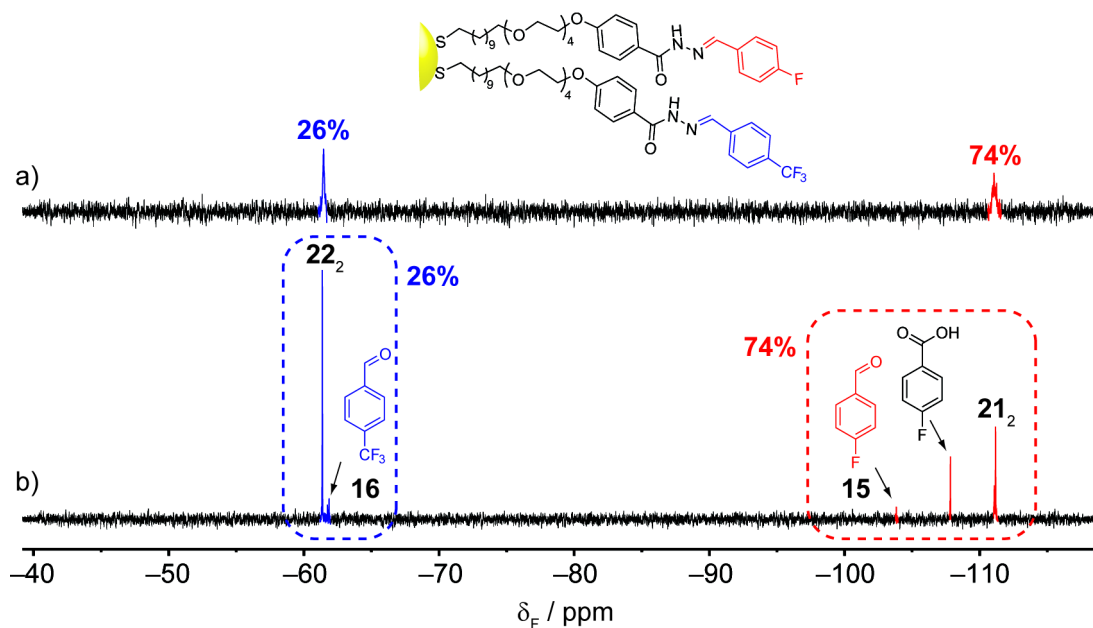
Figure 3.6   Quantification of the relative amount of ligands **21** and **22** by ^{19}F NMR spectroscopy ([D$_7$]DMF, 470.5 MHz, 295 K). a): Spectrum of AuNP-**21**$_{0.74}$**22**$_{0.26}$. b): Spectrum of the same sample recorded 30 min after iodine addition.

Similar experiments were also performed using pure samples of AuNP-**21** (Figure **3.7**) and AuNP-**22e** (Figure **3.8**). The amount of ligand was estimated by integration of the broad NP-bound peak with respect to an internal standard. After iodine addition, several ^{19}F NMR spectra were recorded to monitor the completion of the ligand strip and concurrent hydrolysis and oxidation processes. For both samples AuNP-**21** and AuNP-**22e**, the total concentration of fluorinated species, displaced or not from the NP surface, remained constant over time and was always equal to the amount of ligand estimated before iodine addition.

By this series of experiments, it was therefore demonstrated that ^{19}F NMR spectroscopy provides accurate assessment of both relative and absolute concentrations for NP-bound ligands.

	Time	[**21**] / mM	[**15**+acid]* / mM	[total] / mM
d)	0	6.09		6.09
e)	15 min	3.86	2.28	6.14
f)	2 h	0.82	5.23	6.05
g)	20 h		6.09	6.09

Figure 3.7   ^{19}F NMR ([D7]DMF, 470.5 MHz, 295 K, 16 scans, D1: 22 s) of AuNP-**21** recorded before (d) and after iodine addition at rt (e–g). a) Disulfide **21**2. b): 4-Fluorobenzaldehyde **15**. c): 4-Fluorobenzoic acid. The concentration of 4-fluorobenzoic acid is taken into account together with 4-fluorobenzaldehyde. **IS**: Internal standard (1-fluoro-3-nitrobenzene, 4.95 mM). *: The concentration of 4-fluorobenzoic acid is taken into account together with [**15**].
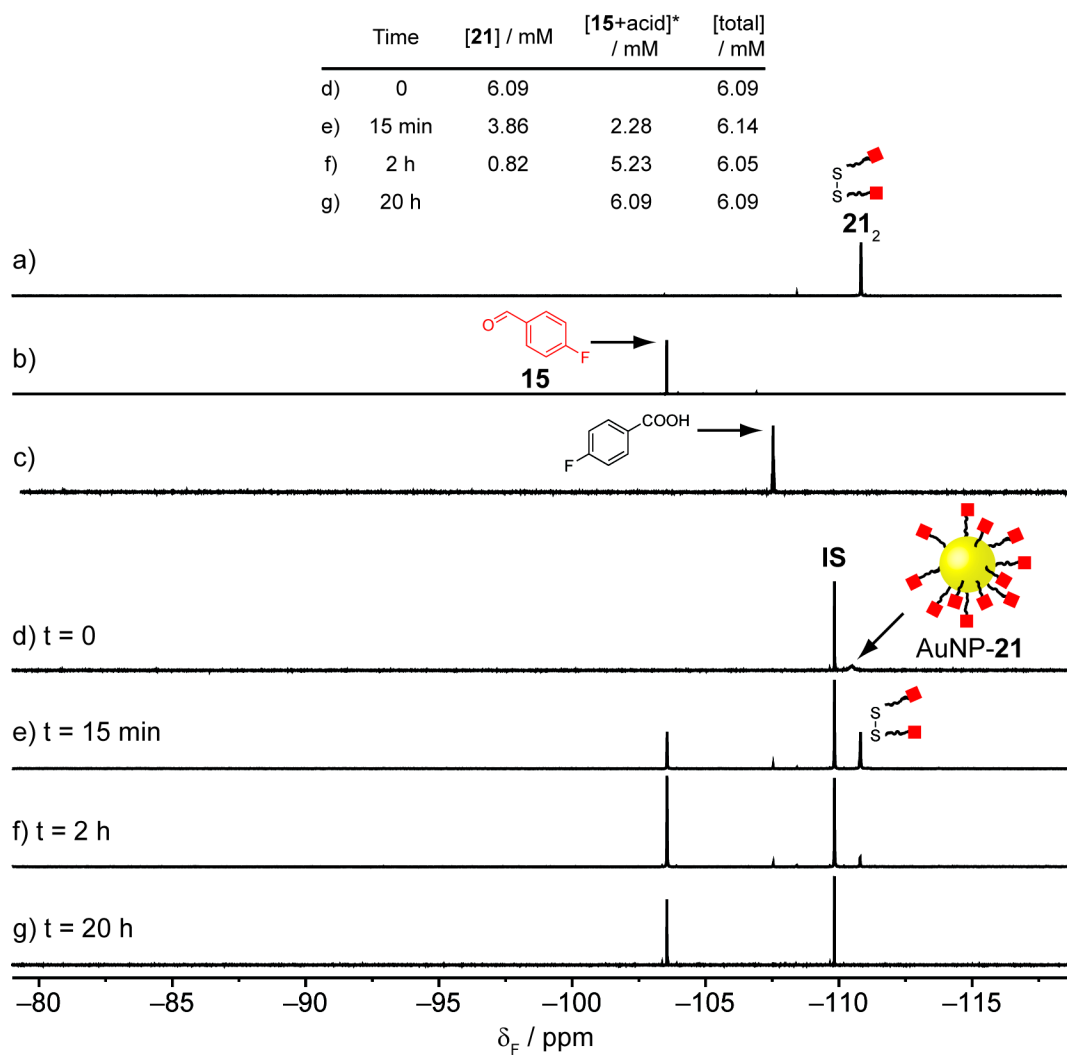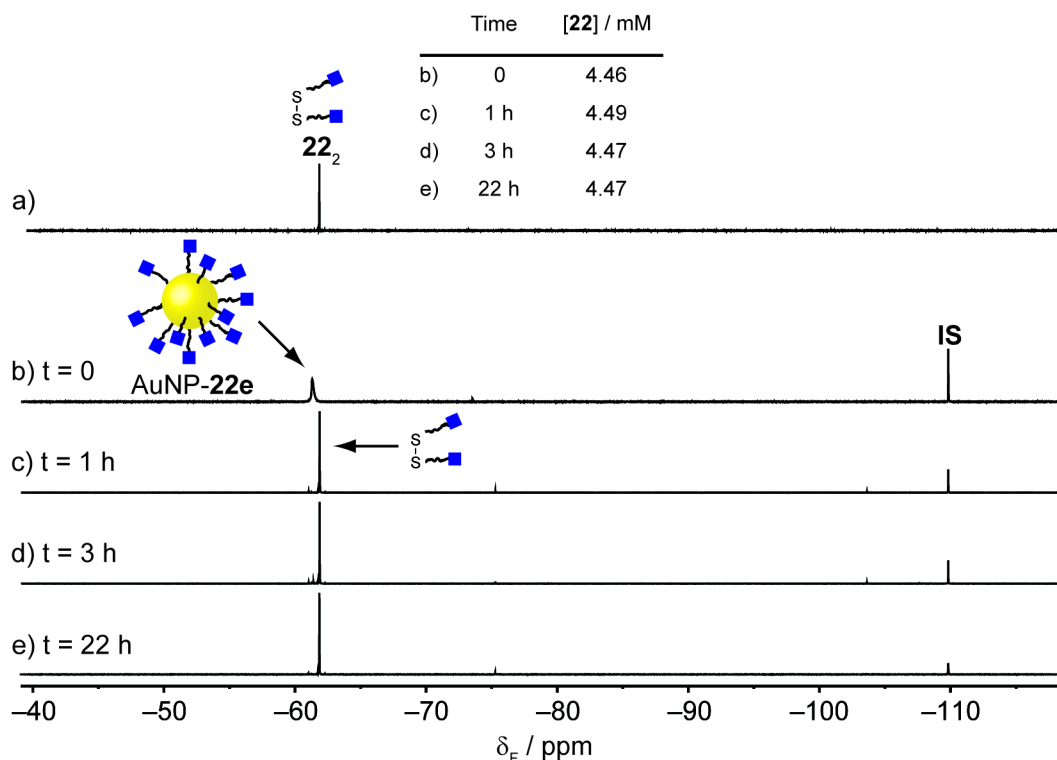
Figure 3.8 ^{19}F NMR ([D$_7$]DMF, 470.5 MHz, 295 K, 16 scans, D1: 22 s) of AuNP-**22e** recorded before (b) and after iodine addition at rt (c–e). a): Disulfide **22**$_2$. **IS**: Internal standard (1-fluoro-3-nitrobenzene, 4.95 mM).

3.3 Kinetics of hydrazone hydrolysis and exchange

In order to gain insight into the effects on reactivity of being bound to the NP surface, AuNP-**21** and AuNP-**22e** were investigated under hydrolysis and equimolar exchange conditions using an excess of CF$_3$CO$_2$H in 10% D$_2$O/[D$_7$]DMF at room temperature, comparing the reactivity of the monolayer with that shown by analogous molecular compounds under the same conditions.

Longitudinal relaxation times (T_1) for ^{19}F signals were determined in order to set appropriate pulse delay times ($\geq$ 5×T_1) for quantitative NMR experiments. T_1 was measured for all the fluorinated species involved in the hydrolysis/exchange process (Section **5.6.1**), finding that T_1 times for NP-bound ligands were slightly shorter than their corresponding free molecular counterparts (0.68 s for AuNP-**21** against 0.92 s for compound **19** and 0.96 s for AuNP-**22e** against 1.18 s for ligand **20**). 4-Fluorobenzaldehyde **15** exhibited the longest T_1 time (3.47 s). Based on the T_1 times measured for every species involved in the hydrolysis/exchange reactions (Table **5.1**), a balance between the delay time (22 s) and number of scans (16), ensured quantitative measurements, sufficient signal-to-noise ratio for the kinetic analyses and a reasonably short overall acquisition time of about 7 minutes. In comparison to the

timescale of the reactions in question, this acquisition time was short enough that the concentrations of reacting species may be considered constant. In addition, the acquisition time becomes less significant when the experiment is performed at room temperature as a result of a slower reaction progress.

3.3.1 Kinetic model for hydrazone hydrolysis

Hydrazone exchange under acidic conditions, in the absence of an excess of nucleophile, occurs *via* preliminary hydrolysis of the hydrazone (Scheme **3.1**).[115,116] In the presence of an acid catalyst, the nitrogen atom in the α position to the sp^2 carbon undergoes protonation, affording a highly electrophilic species. Then, water attack at the sp^2 carbon occurs, forming a carbinolamine intermediate. After a fast proton transfer, breaking of the C–N bond follows resulting in formation of hydrazide and charged aldehyde, which is immediately deprotonated.
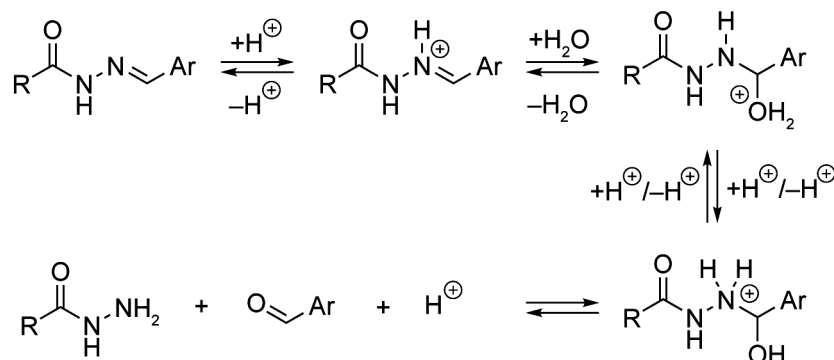
Scheme 3.1   Simplified mechanism for hydrazone hydrolysis and formation.[116]

In order to favour the hydrolysed products (i.e. hydrazide and aldehyde), a high concentration of water is desirable. However, the colloidal stability of AuNP-**21** restricted the maximum amount of water to 10% v/v.

To a first approximation, the reaction can be modelled as a simple reversible process defined by two bimolecular rate constants (k_1 and k_2) as described by Equations **3.1** and **3.2**. The COPASI® software package[198] was used to determine the appropriate set of differential equations to which the experimental data can be fit in order to obtain estimates of the rate constants k_1 and k_2.

$$[\text{Hydrazone}] + [\text{H}_2\text{O}] \underset{k_2}{\overset{k_1}{\rightleftharpoons}} [\text{Hydrazide}] + [\text{Aldehyde}]$$
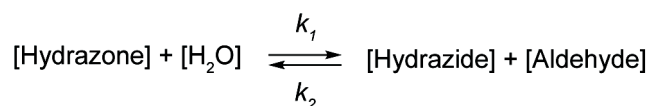
Equation 3.1

$$K_{eq} = \frac{[\text{Hydrazide}][\text{Aldehyde}]}{[\text{Hydrazone}][\text{H}_2\text{O}]} = \frac{k_1}{k_2}$$

Equation 3.2

Hydrolysis experiments were performed using AuNP-**21** and AuNP-**22e** in $\text{D}_2\text{O}/[\text{D}_7]\text{DMF}$ at rt, using 5 equivalents of $\text{CF}_3\text{CO}_2\text{H}$ (with respect to ligand **21** or **22**), comparing the experimental data with corresponding model compounds **23** and **24**, treated under identical conditions.

The reaction progress was monitored by deconvolution of the ^{19}F peaks corresponding to both the NP-bound hydrazone **21** or **22** and released aldehydes **15** or **16** in order to obtain concentration values with respect to an internal standard.

3.3.2 Hydrolysis of molecular compounds 23 and 24

Preliminary investigations on the hydrazone reactivity were carried out with model compounds **23** and **24** (Table **3.1**). From three repeated hydrolysis experiments of **23**, a mean k_1 of 2.75×10^{-9} $\text{mM}^{-1}\text{s}^{-1}$ (s.d. = 30%) and mean k_2 of 2.63×10^{-4} $\text{mM}^{-1}\text{s}^{-1}$ (s.d. = 28%) were calculated. From three repeated hydrolysis experiments of **24**, a mean k_1 of 7.48×10^{-10} $\text{mM}^{-1}\text{s}^{-1}$ (s.d. = 13%) and mean k_2 of 4.43×10^{-4} $\text{mM}^{-1}\text{s}^{-1}$ (s.d. = 39%) were calculated (Table **3.1**).

Table 3.1   Hydrolysis of compounds **23** (entries *a–c*) and **24** (entries *e–g*). Conditions: CF_3CO_2H, D_2O/DMF, rt.

R = F (**23**)   R = F (**15**)
R= CF_3 (**24**)   R= CF_3 (**16**)
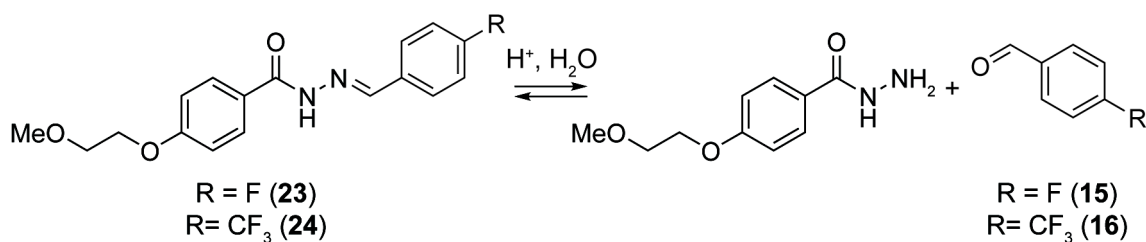
Entry	R	$[Hy]^a$ / mM	$[TFA]^b$ / mM	k_1 / $mM^{-1}s^{-1}$	k_2 / $mM^{-1}s^{-1}$	$K_{eq}^{c,d}$	$K_{eq}(NMR)^{c,e}$
a	F	3.54	19.1	3.89×10^{-9} $(\pm 4\%)^f$	3.50×10^{-4} $(\pm 6\%)^f$	1.11×10^{-5} $(\pm 7\%)^g$	1.10×10^{-5} $(\pm 2\%)^h$
b	F	3.75	16.5	2.33×10^{-9} $(\pm 3\%)^f$	1.70×10^{-4} $(\pm 5\%)^f$	1.37×10^{-5} $(\pm 6\%)^g$	1.91×10^{-5} $(\pm 7\%)^h$
c[i]	F	3.07	18.1	2.02×10^{-9} $(\pm 5\%)^f$	2.68×10^{-4} $(\pm 7\%)^f$	7.52×10^{-6} $(\pm 9\%)^g$	7.31×10^{-6} $(\pm 8\%)^h$
d[j]			*Global fit*	2.50×10^{-9} $(\pm 5\%)^f$	2.40×10^{-4} $(\pm 8\%)^f$	1.04×10^{-5} $(\pm 10\%)^f$	1.25×10^{-5} $(\pm 11\%)^h$
e	CF_3	3.64	19.3	7.99×10^{-10} $(\pm 23\%)^f$	2.13×10^{-4} $(\pm 8\%)^f$	3.75×10^{-6} $(\pm 24\%)^g$	3.58×10^{-6} $(\pm 19\%)^h$
f	CF_3	2.73	19.9	6.38×10^{-10} $(\pm 18\%)^f$	6.80×10^{-4} $(\pm 9\%)^f$	9.39×10^{-7} $(\pm 20\%)^g$	1.03×10^{-6} $(\pm 9\%)^h$
g	CF_3	5.23	25.6	8.08×10^{-10} $(\pm 12\%)^f$	4.37×10^{-4} $(\pm 3\%)^f$	1.85×10^{-6} $(\pm 12\%)^g$	1.81×10^{-6} $(\pm 11\%)^h$
h[j]			*Global fit*	7.59×10^{-10} $(\pm 30\%)^f$	3.85×10^{-4} $(\pm 10\%)^f$	1.97×10^{-6} $(\pm 31\%)^g$	2.14×10^{-6} $(\pm 24\%)^h$

[a]: Concentration in terms of hydrazone **23** or **24**, estimated by ^{19}F NMR with an internal standard.
[b]: Concentration of CF_3CO_2H measured by ^{19}F NMR with an internal standard.
[c]: Dimensionless values.
[d]: $K_{eq} = k_1 / k_2$.
[e]: Determined from Equation **3.2** using the average of the concentration values of the last three data points.
[f]: Coefficient of variation.
[g]: Error propagation calculated from coefficient of variation values of k_1 and k_2.
[h]: ± 1 s.d.
[i]: Hydrolysis performed in 20% D_2O/DMF.
[j]: Global fit of the three data sets for **23** (entries *a–c*) or **24** (entries *e–g*) as determined by COPASI®.

The observed spread of the rate constant values can originate from experimental variation. In fact, deconvolution of NMR peaks has an intrinsic accuracy limitation and the concentration of all the species depends on precise knowledge of the concentration of internal standard.

Another possible reason for the spread of rate constant is that the adopted model (Equation **3.1**) does not take into account the concentration of acid. This would not be a problem if the concentrations of hydrazone and acid were reproduced across the repetitions but this was practically challenging to achieve.

According to the reaction mechanism described in Scheme **3.1**, the acid can affect the reaction in two ways. The hydrazide formed after hydrolysis can be protonated resulting in a reduction of its concentration for the back reaction. On the other hand, the acid can also protonate both the hydrazone and the carbinolamine intermediate in the forward reaction and either the aldehyde or the carbinolamine intermediate in the back reaction, resulting in an increase of the concentration of these protonated intermediates if the concentration of acid, acting as a catalyst, increases.

To investigate if variation in the amount of protonated hydrazide was a significant factor in the spread of rate constant values, the kinetic model was modified by adding the protonation equilibrium for the product hydrazide (Equation **3.3**). Using representative K_a values for hydrazide protonation,[199,200] this modified model did not improve the spread of k_1 and k_2 values for the replicate hydrolysis experiments of **23** and **24**.

$$[HydrazideH]^+ \; \underset{}{\overset{K_a}{\rightleftharpoons}} \; [Hydrazide] + [H]^+$$
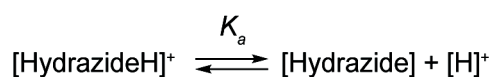
Equation 3.3

To investigate variability between replicate runs as a result of the catalytic action of the acid, the simplest way is to divide k_1 and k_2 by the concentration of CF_3CO_2H, assuming a full dissociation of the acid and equal pK_a values of the key protonated species in both directions. This only gave a small improvement in spread for k_1 and k_2 values for the hydrolysis of **23** (s.d. of 26% and 34%, respectively) and virtually no change in spread of the rate constant values for the hydrolysis of **24** (s.d. of 12% and 40%, respectively).

For all these reasons, the basic model was considered acceptable (Equation **3.1**). To extract accurate fitted parameters from the three repetitions in each case, a global fit to all three data sets at once was carried out (Table **3.1**, entries *d* and *h*). For **23**, this gave excellent results with low coefficients of variation. On the contrary, the global fit for **24** although good by eye, yielded higher errors of coefficient of variation for k_1 but still acceptable. The greater variability in the kinetic parameters determined in this case can perhaps be explained by the extremely low extent of hydrolysis, which proceeds only to 4–8% for **24** so that very small changes in concentration of hydrazone and aldehyde are being measured throughout.

3.3.3   Hydrolysis in the nanoparticle-bound hydrazone monolayer

The kinetic and thermodynamic parameters for the hydrolysis of AuNP-**21** and AuNP-**22e** are presented in Tables **3.2** and **3.3**. Practical challenges in preparing hydrazone-functionalised AuNPs in large scale, the necessity to prepare AuNP-**22e** from AuNP-**21** (Section **3.2.1**) and the requirement to work with a sufficient concentration of NP-bound ligand to attain a reasonable balance of NMR signal-to-noise and acquisition time, made it challenging to perform replicate kinetic experiments from the same batch. Combining the results from different NP batches was considered inappropriate because of the intrinsic variability from batch to batch (e.g. NP size and shape and distribution). Results of replicate runs were therefore considered side-by-side independently and the derived kinetic parameters were not combined.

3.3.3.1 Hydrolysis of AuNP-21

The ^{19}F NMR spectra for the hydrolysis of AuNP-**21** (Section **5.6.2.1**) showed a gradual decrease of the signal corresponding to NP-bound ligand **21** and a concurrent increase of the signal for displaced aldehyde **15**. Except for signals corresponding to CF_3CO_2H and the internal standard, no other ^{19}F peaks (broad or sharp) were detected, confirming that the hydrazone monolayer undergoes hydrolysis without any ligand degradation or displacement.

Concentration values calculated by peak deconvolution for NP-bound ligand **21** and aldehyde **15** were plotted (Figure **3.9**) and compared with a simulated hydrolysis experiment with identical starting concentration using the rate constants determined for the hydrolysis of **23** (Table **3.2**, entry *d*). Slower kinetics were observed for both replicate hydrolysis experiments of AuNP-**21**, while the equilibrium endpoints for NP-bound and unbound reactions were comparable, within the experimental error.
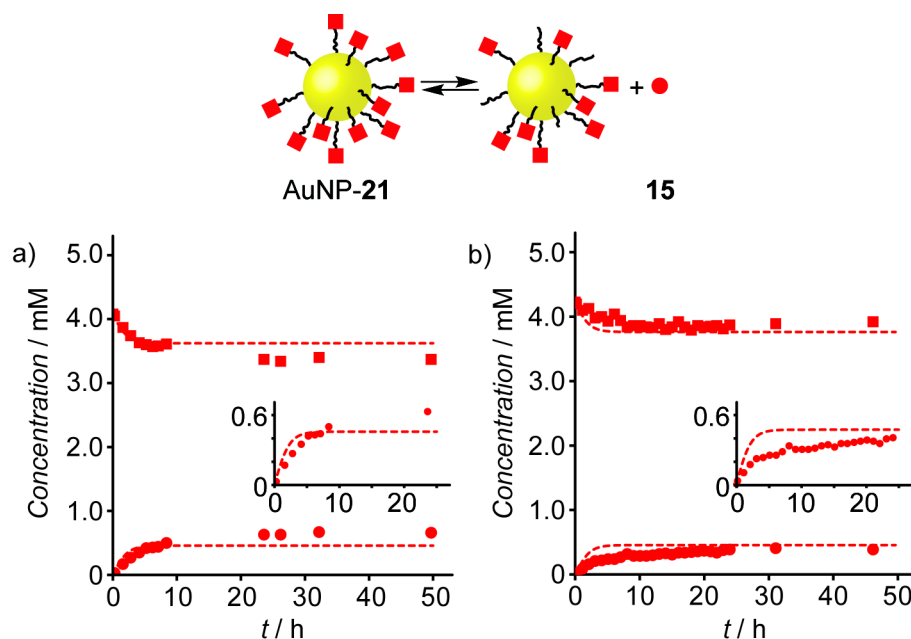
Figure 3.9 Kinetic profiles for replicate hydrazone hydrolysis experiments on independent batches of AuNP-**21**. Conditions: CF_3CO_2H a): 5 Eq; b) 3.2 Eq, with respect to **21**; D_2O/[D_7]DMF 1:9, rt. ■: NP-bound-**21**. ●: 4-Fluorobenzaldehyde **15**. Dashed lines: time course simulation for hydrolysis of **23** under identical conditions (k_1 = 2.50 × 10^{-9} $mM^{-1}s^{-1}$; k_2 = 2.40 × 10^{-4} $mM^{-1}s^{-1}$).

Despite an intrinsic difficulty in deconvoluting the broad peaks corresponding to the NP-bound species, the fitting plot was judged satisfactory (see Section **5.6.3.3**). Table **3.2** summarises the rate constants determined for the hydrolysis of AuNP-**21** (entries *a* and *b*).

The analysis of the hydrolysis for two independent samples of AuNP-**21** showed a small but significant retardation of the hydrolysis in both rate constants when compared to those obtained for **23**. For each experiment, K_{eq} and K_{eq}(NMR) are in close agreement, suggesting that the adopted kinetic model is reliable even for NP-bound experiments. However, the absolute values show some variation between the two replicate experiments lying to either side of the equilibrium position for the hydrolysis of **23**, suggesting that the difference in this value may simply arise from experimental variability. Different binding sites may result in different reactivities and so batch-to-batch variability in the distribution of NP size and shape, and therefore in the relative proportions of different binding sites, could produce variation in ensemble properties such as equilibrium position. Determining the subtle relationships between such intrinsically polydisperse features of NP samples and ensemble reactivity is one of the major challenges facing the development of a rational understanding of NP-bound reactivity.

Table 3.2   Hydrolysis of AuNP-**21**. Conditions: CF_3CO_2H, $D_2O/[D_7]DMF$ 1:9, rt.
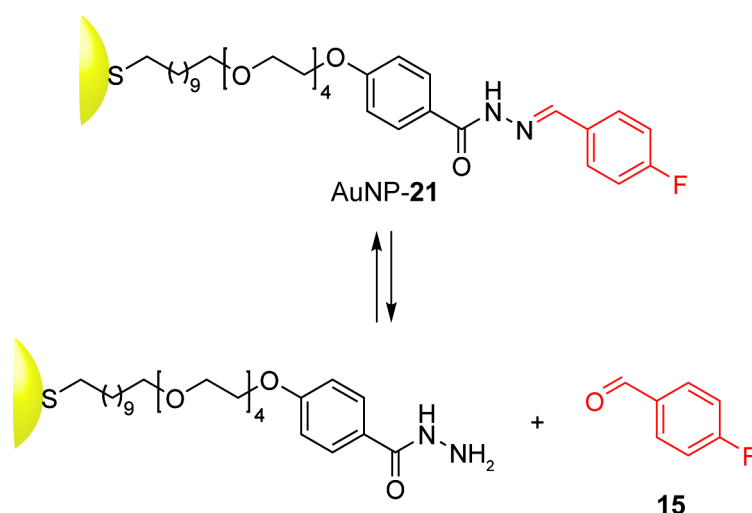
Entry	$[Hy]^a$ / mM	$[TFA]^b$ / mM	k_1 / mM^{-1}s^{-1}	k_2 / mM^{-1}s^{-1}	$K_{eq}^{c,d}$	$K_{eq}(NMR)^{c,e}$
a	4.08	17.1	1.14×10^{-9} $(\pm 2\%)^f$	5.22×10^{-5} $(\pm 3\%)^f$	2.18×10^{-5} $(\pm 4\%)^g$	2.48×10^{-5} $(\pm 2\%)^h$
b	4.27	13.7	7.17×10^{-10} $(\pm 4\%)^f$	1.19×10^{-4} $(\pm 5\%)^f$	6.03×10^{-6} $(\pm 6\%)^g$	6.27×10^{-6} $(\pm 10\%)^h$

[a]: Concentration in terms of ligand **21**, estimated by ^{19}F NMR with an internal standard.
[b]: Concentration of CF_3CO_2H measured by ^{19}F NMR with an internal standard.
[c]: Dimensionless values.
[d]: $K_{eq} = k_1 / k_2$.
[e]: Determined from Equation **3.2** using the average of the concentration values of the last three data points.
[f]: Coefficient of variation.
[g]: Error propagation calculated from coefficient of variation values of k_1 and k_2.
[h]: $\pm$ 1 s.d.

3.3.3.2 Hydrolysis of AuNP-22e

In a similar manner to AuNP-**21**, AuNP-**22e** was dissolved in 10% $D_2O/[D_7]DMF$ and the concentration of NP-bound ligand **22** was estimated with an internal standard. After CF_3CO_2H addition, the hydrolysis was monitored by ^{19}F NMR spectroscopy until equilibrium was achieved. The ^{19}F NMR spectra (Section **5.6.2.2**) show a slight decrease in the peak intensity corresponding to NP-bound ligand **22** and a corresponding gradual increase of the intensity for the peak corresponding to hydrolysed aldehyde **16**. Except for peaks related to CF_3CO_2H and the internal standard, no additional (broad or sharp) peaks were observed, confirming no ligand degradation or displacement as already seen for AuNP-**21**. Concentration values calculated by peak deconvolution for NP-bound ligand **22** and aldehyde **16** are plotted and compared with compound **24** in Figure **3.10**. As observed for AuNP-**21**, a slower

progress to equilibrium is suggested for NP-bound **22** when compared to freely dissolved **24**.
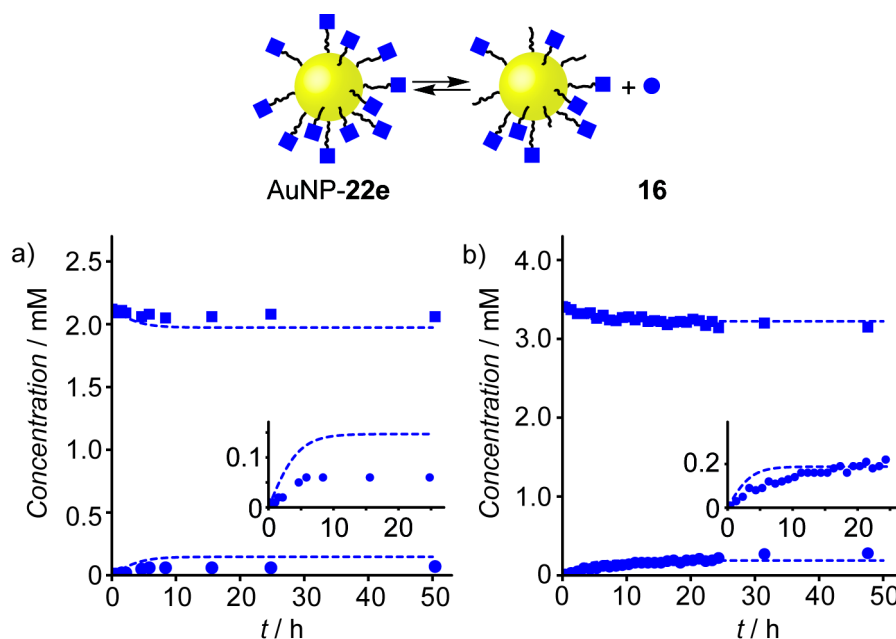

Figure 3.10   Kinetic profiles for replicate hydrazone hydrolysis experiments on independent batches of AuNP-**22e**. Conditions: CF_3CO_2H a): 4.8 Eq; b): 6.0 Eq with respect to **22**, $D_2O/[D_7]DMF$ 1:9, rt. ■: NP-bound-**22**. ●: 4-(Trifluoromethyl)benzaldyde **16**. Dashed lines: time course simulation for hydrolysis of **24** under identical conditions ($k_1 = 7.59 \times 10^{-10}$ mM^{-1}s^{-1}; $k_2 = 3.85 \times 10^{-4}$ mM^{-1}s^{-1}).

The fitted kinetic constant k_1 (Table **3.3**, entries *a* and *b*) is consistently slightly smaller than the global k_1 value determined for molecular model compound **24** (Table **3.1**, entry *h*). On the other hand, the k_2 value for the on-NP reaction appears to be similar or even larger than the molecular model system. It must be noted however, that there is a significant variability in the absolute rate constant values determined for these two experiments, giving us only a rough estimate of these values. A possible reason could be found in the limited extent of hydrolysis observed for NP-bound ligand **22**, which means that all the kinetic data comes from measurements of small absolute changes in the species concentrations. As for AuNP-**21**, variability in the equilibrium positions was again observed. It was concluded that even for AuNP-**22e** there is no difference of equilibrium position when compared to **24**.

Table 3.3   Hydrolysis of AuNP-**22e**. Conditions: CF_3CO_2H, D_2O/[D_7]DMF 1:9, rt.
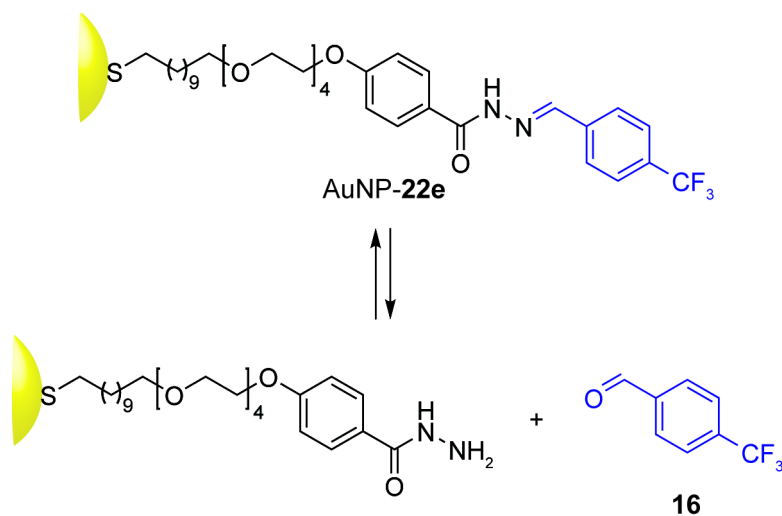
Entry	[Hy]^a / mM	[TFA]^b / mM	k_1 / mM^{-1}s^{-1}	k_2 / mM^{-1}s^{-1}	K_{eq}^{c,d}	K_{eq}(NMR)^{c,e}
a	2.12	10.2	3.18×10^{-10} ($\pm 5\%$)^f	8.77×10^{-4} ($\pm 7\%$)^f	3.63×10^{-7} ($\pm 9\%$)^g	3.57×10^{-7} ($\pm 11\%$)^h
b	3.41	20.5	2.18×10^{-10} ($\pm 3\%$)^f	6.25×10^{-5} ($\pm 8\%$)^f	3.48×10^{-6} ($\pm 9\%$)^g	2.30×10^{-6} ($\pm 13\%$)^h

^{a}: Concentration in terms of ligand **22**, estimated by ^{19}F NMR with an internal standard.
^{b}: Concentration of CF_3CO_2H measured by ^{19}F NMR with an internal standard.
^{c}: Dimensionless values.
^{d}: $K_{eq} = k_1 / k_2$.
^{e}: Determined from Equation **3.2** using the average of the concentration values of the last three data points.
^{f}: Coefficient of variation.
^{g}: Error propagation calculated from coefficient of variation values of k_1 and k_2.
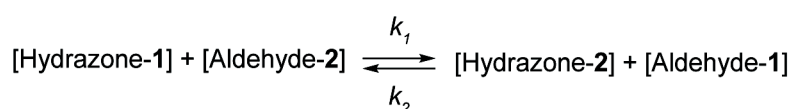^{h}: $\pm$ 1 s.d.

3.3.4   Reversible exchange between AuNP-21 and AuNP-22e

The reactivity of the NP-bound hydrazone monolayer was subsequently investigated under exchange conditions. Equimolar conditions were chosen in order to accurately assess changes in concentration for all exchanging components.

The reaction was triggered by CF_3CO_2H and monitored by ^{19}F NMR spectroscopy until equilibrium was achieved.

To a first approximation, the reaction can be modelled as a reversible process characterised by two bimolecular rate constants, $k_{1(1\rightarrow2)}$ and $k_{2(2\rightarrow1)}$ (Equation **3.4**).

$$[\text{Hydrazone-}\textbf{1}] + [\text{Aldehyde-}\textbf{2}] \underset{k_2}{\overset{k_1}{\rightleftharpoons}} [\text{Hydrazone-}\textbf{2}] + [\text{Aldehyde-}\textbf{1}]$$

Equation 3.4

It should be noted that this simple model assumes all intermediates to be present only at low 'steady state' concentrations (including the free hydrazide, which can be confirmed from the NMR data), while the excess of water and acid catalyst are constant and consistent across all reactions. Furthermore, any difference in pK_a values for the key protonated intermediates between the different reactions is not considered by this simple model. Finally, the concentration of all four fluorinated species (hydrazone starting material and product and aldehydes **15** and **16**) can be used to run the fitting.

Kinetic constants, determined for molecular compounds **23** and **24** treated under equimolar exchange conditions, showed very good reproducibility across three repetitions (Table **3.4**, entries *a–c*), regardless of whether the exchange was started with 100% **23** (entry *a*), 100% **24** (entry *c*) or **23/24** 1:9 (entry *b*). However, a slight increase of the reaction quotient ($Q = k_1 / k_2$) was observed as the amount of **24** at the start is increased (obtaining Q values of 7.85, 10.3 and 11.1 when starting with **23/24** 1:0, 1:9 and 0:1, respectively). By inspecting the ^{19}F NMR spectra at long time points, no additional peaks, which would have suggested decomposition of one of the exchanging species, was observed. The reaction quotient Q calculated from the fitted rate constant is in close agreement with the reaction quotient estimated from the last three data points of the ^{19}F NMR spectra at the equilibrium, Q(NMR) for each experiment. However, species decomposition cannot be excluded completely because some diagnostic peaks could be obscured by those corresponding to hydrazone **24** or aldehyde **16** since the 4-(trifluoromethyl)benzylidene region tends not to be as well-resolved as the 4-fluorobenzylidene one.

Table 3.4   Equimolar hydrazone exchange with molecular compounds **23** and **24**. Conditions: aldehyde **15** or **16**, CF_3CO_2H, D_2O/[D_7]DMF 1:9, rt.
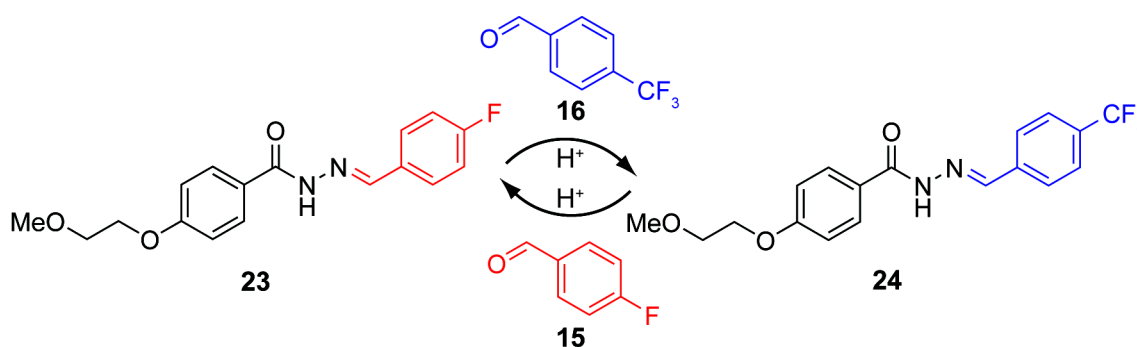
Entry	[Hy]^{a,b} / mM	[Ald]^a / mM	[TFA]^a / mM	k_1 / mM^{-1}s^{-1}	k_2 / mM^{-1}s^{-1}	k_1 / k_2^{c}	Q(NMR)^{c,d}
a	3.61^e	3.35	22.7	7.07×10^{-6} ($\pm$ 2%)^f	9.01×10^{-7} ($\pm$ 5%)^f	7.85 ($\pm$ 5%)^g	7.30 ($\pm$ 2%)^h
b	3.76^i	3.96	19.2	8.02×10^{-6} ($\pm$ 6%)^f	7.80×10^{-7} ($\pm$ 4%)^f	10.3 ($\pm$ 7%)^g	9.05 ($\pm$ 5%)^h
c	3.42^j	3.93	19.2	8.29×10^{-6} ($\pm$ 4%)^f	7.45×10^{-7} ($\pm$ 3%)^f	11.1 ($\pm$ 5%)^g	10.1 ($\pm$ 10%)^h
d^k			Global fit	6.94×10^{-6} ($\pm$ 1%)^f	7.82×10^{-7} ($\pm$ 2%)^f	8.88 ($\pm$ 3%)^g	8.82 ($\pm$ 11%)^h

^{a}: Initial concentration measured with respect to an internal standard.
^{b}: [Hy] = [**23**] + [**24**].
^{c}: Dimensionless values.
^{d} Determined using the average of the concentration values of the last three data points using the Equation Q(NMR) = ([**24**][**15**]) / ([**23**][**16**]).
^{e}: [Hy] = **23** (100%).
^{f}: Coefficient of variation.
^{g}: Error propagation calculated from coefficient of variation values of k_1 and k_2.
^{h}: ± 1 s.d.
^{i}: [Hy] = **23** (10%) + **24** (90%).
^{j}: [Hy] = **24** (100%).
^{k}: Global fit of the three data set (entries *a*–*c*) as determined by COPASI®.

In a similar manner to the hydrolysis reactions (Sections **3.3.3.1–2**), hydrazone exchange of AuNP-**21** and AuNP-**22e** in the presence of an equimolar amount of, **16** and **15** respectively, was carried out. The exchange reactions were monitored until no further changes in component concentration were observed.

For both AuNP-**21** and AuNP-**22e**, ^{19}F NMR spectra (Sections **5.6.2.3–4**) showed a gradual decrease in the intensity of the peaks corresponding to the NP-bound hydrazone starting material and the exchanging aldehyde. At the same time, a gradual increase in the intensity of the peaks corresponding to the displaced benzaldehyde and the NP-bound hydrazone product was observed.

A clear kinetic inhibition is apparent for the NP-bound hydrazone exchange starting with AuNP-**21** (Figure **3.11**) when compared to **23** treated under identical conditions. Furthermore, a difference in reaction quotient is also now clearly observed, with the

NP-bound equilibrium favouring the 4-fluorobenzylidene hydrazone more than corresponding molecular system. However, such conclusions must be taken in the context of the variability observed for the equilibrium endpoint in the molecular control experiments.
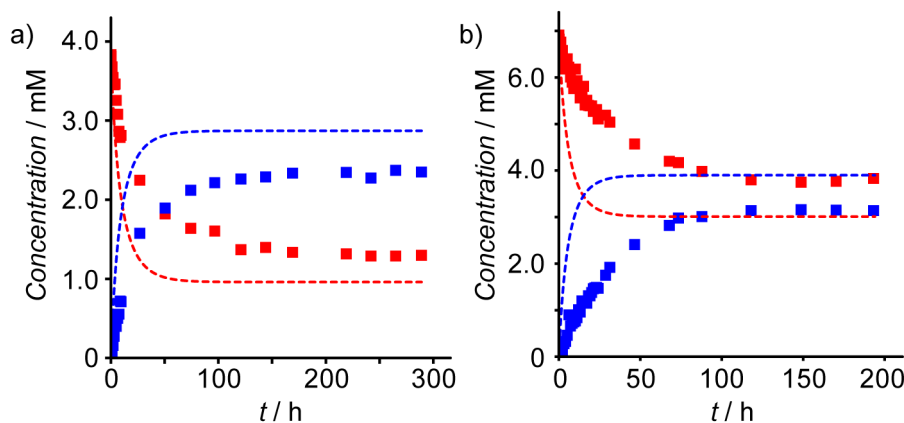

Figure 3.11 Kinetic profiles for equimolar hydrazone exchange from AuNP-**21** to AuNP-**22e**. Conditions: 4-(trifluoromethyl)benzaldehyde **16** (1.0 Eq with respect to **21**), CF$_3$CO$_2$H (5.0 Eq with respect to **21**), D$_2$O/[D$_7$]DMF 1:9, rt. ■: NP-bound-**21**. ■: NP-bound-**22**. Concentration of aldehydes **15** and **16** were also measured but are omitted here for clarity. Dashed lines: time course simulation by COPASI® for equimolar exchange with molecular compounds **23** and **24** under identical conditions (Table **3.4**, entry *d*: $k_1 = 6.94 \times 10^{-6}$ mM^{-1}s^{-1}; $k_2 = 7.82 \times 10^{-7}$ mM^{-1}s^{-1}).

Rate constants for two independent equimolar exchange experiments, starting with AuNP-**21**, were fitted using the kinetic mechanism in Equation **3.4** using COPASI® (Table **3.5**, entries *a* and *b*) and compared with those estimated from the global fitting of the experiments carried out with molecular compounds (Table **3.4**, entry *d*). Both rate constants were found to be smaller than those corresponding to molecular compounds, confirming slower kinetics for NP-bound hydrazone ligands as already observed for the hydrolysis experiments. In order to verify the retardation observed for NP-bound **21**, the inhibition factor (IF), defined as the ratio between the kinetic constant determined for NP-bound **21** ($k_{(NP)}$) and that calculated for the molecular model ($k_{(MOL)}$), can be calculated. Interestingly, the inhibitory effect is stronger in the forward reaction (IF$_{1\rightarrow2}$ = $k_{1(NP)}$ / $k_{1(MOL)}$ = 0.28 and 0.13 for entries *a* and *b*, respectively) than the back reaction (IF$_{2\rightarrow1}$ = $k_{2(NP)}$ / $k_{2(MOL)}$ = 0.91 and 0.47 for entries *a* and *b*, respectively).

Table 3.5   Equimolar hydrazone exchange from AuNP-**21** to AuNP-**22e**. Conditions: aldehyde **16**, CF$_3$CO$_2$H, D$_2$O/[D$_7$]DMF 1:9, rt.
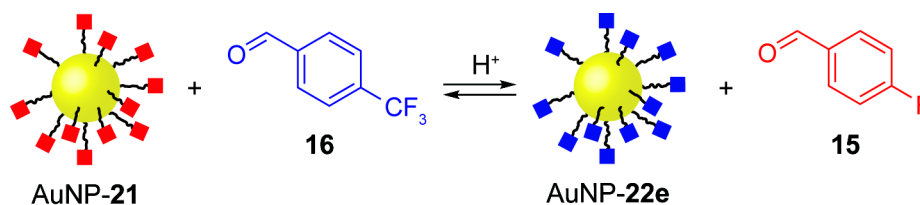
Entry	[Hy]^a / mM	[Ald]^a / mM	[TFA]^a / mM	k_1 / mM^{-1}s^{-1}	k_2 / mM^{-1}s^{-1}	k_1 / k_2^{b}	Q(NMR)^{b,c}
a	3.83	3.84	18.4	1.93×10^{-6} ($\pm$ 2%)^d	7.13×10^{-7} ($\pm$ 4%)^d	2.70 ($\pm$ 4%)^e	3.34 ($\pm$ 4%)^f
b	6.91	4.47	20.7	9.24×10^{-7} ($\pm$ 1%)^d	3.71×10^{-7} ($\pm$ 3%)^d	2.49 ($\pm$ 3%)^e	2.45 ($\pm$ 5%)^f

^{a}: Initial concentration measured with respect to an internal standard.
^{b}: Dimensionless values.
^{c}: Determined using the average of the concentration values of the last three data points using the Equation Q(NMR) = ([AuNP-**22**][**15**]) / ([AuNP-**21**][**16**]).
^{d}: Coefficient of variation.
^{e}: Error propagation calculated from coefficient of variation values of k_1 and k_2.
^{f}: $\pm$ 1 s.d.

Equimolar hydrazone exchange was investigated starting also from AuNP-**22e**. Due to the fact that AuNP-**22e** could only be prepared by hydrazone exchange from AuNP-**21**, material could only be obtained in relatively small quantities. However, two preliminary experiments were run from two independent batches (see Section **5.6.2.4** for stacked ^{19}F NMR spectra). Preliminary results (Figure **3.12**) indicated a very slight suppression of the kinetics for NP-bound **22** (Table **3.6**, entries *a* and *b*) compared to molecular experiments.

A reaction endpoint that favoured NP-bound **22** more strongly than the corresponding molecular system was also observed. Differences in equilibrium endpoint are currently more difficult to rationalise as they appear to be confounded by significant run-to-run variability. There does however appear to be a suggestion that some proportion of starting hydrazones is not available to exchange. The source of variability in equilibrium endpoint for the molecular system must first be determined to fully understand this effect. Starting with AuNP-**22e**, it seems that equilibrium is not achieved under equimolar conditions. This was already observed for the molecular compounds (Table **3.4**, entries *a–c*), showing that the reaction quotient increases as the amount of 4-(trifluoromethyl)benzylidene hydrazone **24** increases from 0% to 100%. Interestingly, this effect is exacerbated on the NP surface (Table **3.6**). As a result of this, the hydrazone exchange on the NP surface favours the 4-fluorobenzylidene moiety more than the molecular experiment. These observations seem to be related to the specific experimental conditions used (equimolar exchange

at room temperature). In fact, results discussed in Section **3.2.1** indicate that under more forcing conditions (e.g. 40 equivalents of **15** at 50 °C) exchange of the NP-bound hydrazone **22** does proceed to higher extent. This suggests that either the population of 'unexchangeable' hydrazones is not irreversible or that the kinetic trap is a slow side reaction, not observed at higher temperatures.

Table 3.6   Equimolar hydrazone exchange from AuNP-**22e** to AuNP-**21**. Conditions: aldehyde **15**, CF$_3$CO$_2$H, D$_2$O/[D$_7$]DMF 1:9, rt.
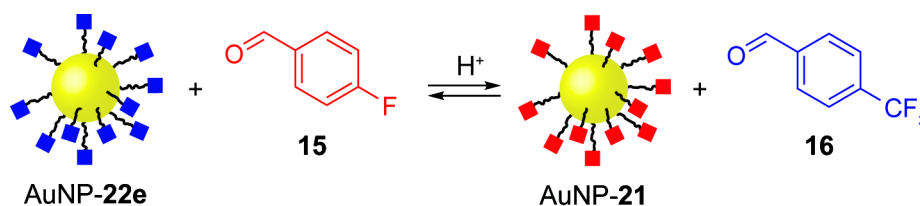
Entry	[Hy][a] / mM	[Ald][a] / mM	[TFA][a] / mM	k_1 / mM^{-1}s^{-1}	k_2 / mM^{-1}s^{-1}	k_1 / k_2[b]	K_{eq}(NMR)[b,c]
a	1.97	1.89	8.47	1.88×10^{-5} ($\pm$ 5%)[d]	6.44×10^{-7} ($\pm$ 3%)[d]	29.2 ($\pm$ 6%)[e]	16.2 ($\pm$ 3%)[f]
b	3.18	3.83	19.7	6.78×10^{-6} ($\pm$ 4%)[d]	4.41×10^{-7} ($\pm$ 2%)[d]	15.4 ($\pm$ 4%)[e]	14.7 ($\pm$ 6%)[f]

[a]: Initial concentration measured with respect to an internal standard.
[b]: Dimensionless values.
[c]: Determined using the average of the concentration values of the last three data points using the Equation Q(NMR) = ([AuNP-**22**][**15**]) / ([AuNP-**21**][**16**]).
[d]: Coefficient of variation.
[e]: Error propagation calculated from coefficient of variation values of k_1 and k_2.
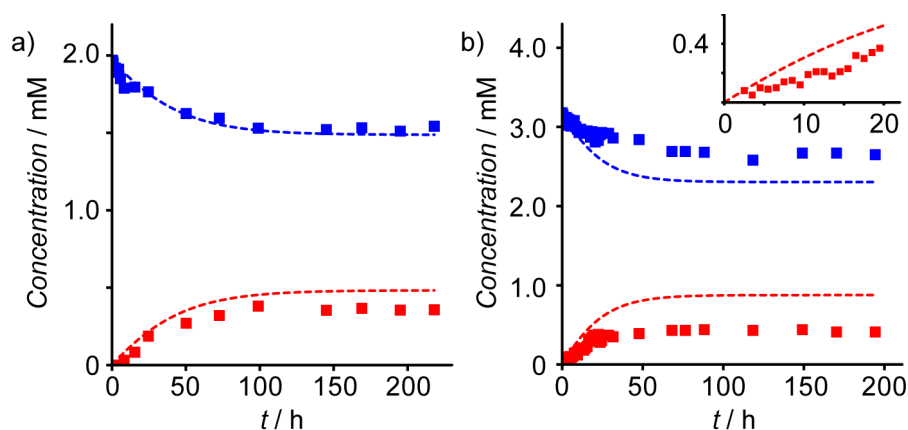[f]: $\pm$ 1 s.d.

Figure 3.12   Kinetic profiles for equimolar hydrazone exchange from AuNP-**22e** to AuNP-**21**. Conditions: 4-(trifluoromethyl)benzaldehyde **15** (1.0 Eq with respect to **22**), CF$_3$CO$_2$H (5.0 Eq with respect to **22**), D$_2$O/[D$_7$]DMF 1:9, rt. ■: NP-bound-**21**. ■: NP-bound-**22**. Concentration of aldehydes **15** and **16** were also measured but are omitted here for clarity. Dashed lines: time course simulation by COPASI® for equimolar exchange with molecular compounds **23** and **24** under identical conditions (Table **3.4**, entry *d*: $k_1 = 6.94 \times 10^{-6}$ mM^{-1}s^{-1}; $k_2 = 7.82 \times 10^{-7}$ mM^{-1}s^{-1}).

Slower kinetics for the NP-bound reaction might be expected on the basis of simple steric arguments, yet presumably the relatively high surface curvature of the small NPs

employed here, together with the conformationally flexible tetraethylene glycol spacer, play a role in minimizing any intra-monolayer effects on reactivity so that the effects observed are relatively small. Indeed, even for potentially much more crowded 2D monolayers, dynamic covalent reactions have been shown to behave in a similar manner to their solution-based analogues,[194] while the kinetic inhibition for dynamic covalent thioester exchange on the surface of liposomes displayed similarly moderate inhibition.[195] It therefore appears that dynamic covalent hydrazone exchange may be transferred onto NP-bound monolayers without qualitatively affecting the behaviour of the equilibration process, yet there are significant quantitative differences. The potential for differential inhibition for exchange in each direction is interesting, and it is unclear whether intra-monolayer interactions or local concentration effects can influence the inhibition. The suggestion of subtle surface-bound effects raises intriguing questions as to how changes in nanoscale features and intra-monolayer interactions will affect the kinetics and thermodynamics for these processes. Deeper insight into such questions as how the NP-bound environment affects each step in hydrazone hydrolysis and re-formation, or the pK_a values for key protonated intermediates in the NP-bound monolayer, will require detailed study of these processes and their constituent hydrazone hydrolysis/formation 'half-reactions'.

3.4 Comparison of dynamic covalent hydrazone exchange with monolayer ligand exchange

Replacing the NP-stabilising surface species in a 'ligand exchange' process has long been established as a viable method for modifying the as-synthesised surface functionality of AuNPs (Chapter **1**).[165,201] This process might also be considered as a dynamic covalent exchange of the Au–S bond that anchors the organic monolayer to the NP surface.

To compare the dynamic covalent exchange process with an analogous ligand exchange process, AuNP-**21** was treated with disulfide **22**₂. Whereas the hydrazone exchange reaction occurs readily at room temperature in the presence of only one equivalent of aldehyde exchange unit (Figure **3.11**), < 3% exchange was observed for the ligand exchange process under analogous conditions, even after an extended reaction time of 48 hours. Under heating, the ligand exchange process eventually proceeded to about 19% after 5 days.

The two processes were then compared in the presence of 20 equivalents exchange species at 50 °C. A much slower rate and lower efficiency for the ligand exchange

process was again observed (Figure **3.13**). The slow rate of ligand exchange and inability to approach complete exchange is in agreement with literature reports on similar systems.[165,202]
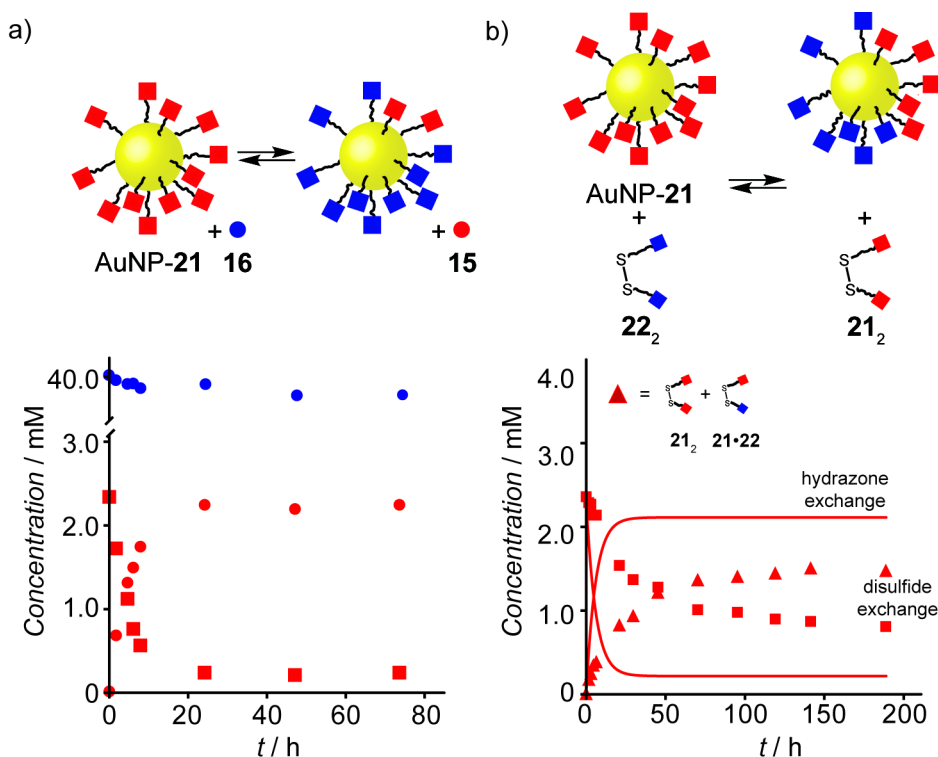

Figure 3.13   Kinetic profiles for hydrazone exchange and disulfide exchange of AuNP-**21**. a) Hydrazone exchange: aldehyde **16** (20 Eq with respect to **21**), CF_3CO_2H (5 Eq with respect to **21**), D_2O/DMF 1:9, 50 °C. ■: NP-bound-**21**. ●: displaced aldehyde **15**. ●: aldehyde **16**. Concentration of NP-bound-**22** was also quantified, but is omitted here for clarity. b) Disulfide exchange: disulfide **22**₂ (10 Eq with respect to **21**), D_2O/DMF 1:9, 50 °C. ■: NP-bound-**21**. ▲: displaced ligand **21** (as thiol/disulfide). Concentrations of disulfide **22**₂ and NP-bound-**22** could not be independently measured because their corresponding ^{19}F peaks show the same chemical shift in D_2O/DMF 1:9. The combined peak showed constant concentration over time, as would be expected. Lines correspond to hydrazone exchange (see Figure **3.13A**) under analogous experimental conditions.

The two exchange processes occur via quite different mechanisms, making quantitative comparison of kinetics challenging. In addition, the mechanism of the ligand exchange is still under debate, and most probably corresponds to a complex and system dependent process that can not satisfactorily be described by simple kinetic models.[165] A crude but practically revealing comparison between the two processes is provided by the reaction half-life (Table **3.7**), which is defined as the time taken to progress half-way to the equilibrium position. It should be noted that for a bimolecular process, this only allows comparison between reactions at the same starting concentration. With a starting concentration of 2.3 mM (in terms of ligand **21**, Figure **3.13B**), at 50 °C in the presence of 20 equivalents of disulfide **22**₂ (in terms of

sulfur), ligand exchange proceeds to 63% exchange with a half-life of 17.9 h, compared to hydrazone exchange, which proceeds to 86% exchange with a half-life of 4.1 h in the presence of 20 equivalents aldehyde **16** (Figure **3.13A**).

Table 3.7   Comparison of rate and efficiency of hydrazone exchange and ligand exchange processes for AuNP-**21**.

	Extent of exchange from AuNP-21	$t_{\frac{1}{2}}^{a}$ / h
Hydrazone exchange AuNP-**21** + **16**	86%	4.1
Ligand exchange AuNP-**21** + **22**$_2$	63%	17.9

^{a}: Estimated from ^{19}F NMR by determination of reaction endpoint then interpolation between points closest to 50% of final conversion. All reaction carried out at starting concentration of AuNP-**21** = 2.3 mM in D_2O/DMF 1:9 at 50 °C.

By exchanging simple molecular units at the periphery of the NP-stabilising monolayer using well-established reversible covalent reactions, DCC represents a mild and flexible approach to reversibly manipulating NP-bound functionality, with several advantages over replacing the entire ligand at the NP surface:

- Dynamic covalent exchange can take place at significantly higher rates and under milder conditions (e.g. lower temperatures and/or lower equivalents of exchange units) than ligand exchange. In addition, dynamic covalent exchange exploits simple and readily accessible exchange units (e.g. simple aromatic aldehydes), whereas ligand exchange requires the multi-step synthesis of relatively complex surface-active ligands for each new exchange process.

- Introducing large excesses of thiol exchange units leads to complex mixtures of high molecular weight thiols and disulfides, which must be purified away from ligand exchanged NPs. This is often a challenging and time-consuming process, as discussed in Chapter **2**.

- As demonstrated in Figure **3.3**, the dynamic covalent exchange process may be readily and predictably employed to achieve mixed monolayers of a given composition. By comparison, the control of monolayer composition under ligand exchange is poorly understood.[165] Such a control may be system dependent or may involve kinetically trapped states. The rate and extent of the ligand exchange process can even depend on the NP batch age.[203]

- DCC does not involve disruption of the monolayer–NP linkage, preserving the NP colloidal stability during the exchange and reducing the risks of surface etching, reconstruction or NP decompositions.[165,204]

- Typically, ligand exchange protocols take advantage of a designed increase in monolayer stability (e.g. by replacing weakly bound tetraalkyl ammonium bromide ligands or phosphine ligands by thiols,[184,205] or by replacing short-chain alkyl thiols with longer chain alkyl thiols[206]). In such cases, the exchange process becomes effectively irreversible or a reduction in exchange efficiency may occur.[139] DCC is inherently reversible and can be used to switch surface functionality many times over (Figure **3.3**).

- As the dynamic covalent bonds are independent of the NP–molecule bonds, the dynamic covalent approach should be generalizable to virtually any monolayer-stabilized NP system, including those for which ligand exchange has not been demonstrated or has been shown to lead to degradation of NP properties.

3.5 Conclusions

A post-synthetic approach for manipulating hydrazone-functionalised AuNPs exploiting dynamic covalent exchange has been demonstrated for the first time.

The occurrence of hydrazone exchange in the NP-bound monolayer was monitored by ^{19}F NMR spectroscopy and confirmed by LDI-MS analysis. A pure sample of AuNP-**21** could undergo hydrazone exchange with an excess of aldehyde **16** under acidic conditions, obtaining a homogeneous monolayer of ligand **22** adsorbed on the NP surface, without any observed ligand displacement. The exchange was demonstrated to be reversible, since NP-bound **22** could undergo reverse exchange by using an excess of aldehyde **15** under identical exchange conditions. One of the potential applications of dynamic covalent chemistry performed in the NP-bound monolayer was here demonstrated. AuNP-**22e** could be obtained pure and with a homogeneous monolayer by hydrazone exchange, avoiding the partial reduction occurred when preparing AuNP-**22a**–**d** by a direct synthesis approach (see Chapter **2**).

Despite the broad resonances associated with NP-bound species, it was possible to quantitatively measure the concentration of NP-bound fluorinated ligands and to track in real time modification of the NP monolayer composition under hydrolysis and exchange conditions using ^{19}F NMR spectroscopy. Observed data were compared with freely dissolved molecular analogues. Slower kinetics, for both hydrolysis and exchange experiments, were observed for NP-bound hydrazones. Under hydrolysis

conditions, the endpoint for reaction of NP-bound and unbound hydrazones is comparable within the accuracy of the current methods. On the contrary, small differences in equilibrium endpoint have been observed for the exchange reactions, suggesting that the 4-fluorobenzylidene moiety is favoured at the equilibrium on the NP surface more than analogous molecular experiments.

By a direct comparison of dynamic covalent hydrazone exchange and Au–S ligand exchange, under analogous conditions, it was demonstrated that the former process is quicker and more efficient than the latter.

Dynamic covalent exchange shows great promise for performing post-synthetic manipulations on ligand-functionalised NPs and furthermore provides insight about the molecular reactivity when confined to a NP-bound monolayer. By reversible modification of the functionality of NP-bound small molecules, DCC could become a powerful method for tuning a wide range of NP properties by modifying the properties of the NP-bound organic ligands and could also offer a promising approach for the covalent assembly of ligand-functionalised NPs.

Chapter 4:
Exploiting hydrazone exchange for tuning nanoparticle properties

This Chapter reports a simple but powerful strategy for the post-synthetic manipulation of gold nanoparticle (AuNP) properties by dynamic hydrazone exchange. A reversible switching of NP solvophilicity was achieved allowing colloidal stability in different solvents by simply choosing an appropriate aldehyde exchange unit. After exchange and purification, hydrazone-functionalised AuNPs are characterised by nuclear magnetic resonance (NMR) spectroscopy, laser desorption ionisation mass spectrometry (LDI-MS), UV-Vis and transmission electron microscopy (TEM).

In addition, a solvent-dependent aggregation process, driven by non-covalent interactions, is monitored by dynamic light scattering (DLS) analysis by observing variations in the solvodynamic diameter.

Hydrazone-functionalised AuNPs were also assembled with each other by means of a bifunctional aldehyde linker. Early stage experiments analysed by TEM displayed interesting NP superstructures with a dendritic-like organisation.

Finally, further studies required for investigating the potential use of NP reversible solvophilicity switching and dynamic covalent assembly of hydrazone-functionalised AuNPs is reported.

4.1 Solubility switching of hydrazone-functionalised gold nanoparticles

Tuning NP solvent compatibility is often required in order to match a specific NP synthetic route with a specific end application.[207] For example, preparation of ligand-functionalised metal NPs has seen a dramatic increase in recent years for applications in biology and medicine.[23] However, the currently available synthetic methods for the preparation of water-soluble NPs[33,34] often do not guarantee good reproducibility in terms of size and dispersity when compared to alternative methods for NP preparation in organic solvents.[40,45,46] Thus, developing strategies to change the NP solubility from organic to aqueous solvents, or *vice versa*, is an important challenge.

Both non-covalent and covalent approaches have been adopted in numerous strategies for achieving NP solubility switching. Non-covalent methods include host-guest interactions (e.g. by using cyclodextrins[208–210] or calixarenes[211]) and strategies based on NP encapsulation with polymers[212,213] or dendrimers.[214–217] Alternatively, approaches based on electrostatic interactions, which allow modification of the charge density on the NP surface and result in phase transfer, are also available.[218–221] Covalent strategies for NP solubility switching are based on ligand exchange[222–224] or covalent post-synthetic modifications of the NP-bound organic monolayer, including amide coupling[225,226] or ester hydrolysis.[227]

However, all the above mentioned examples reported NP phase transfer only in an irreversible fashion and, in many cases, require large and complex species (e.g. cyclodextrins, polymers, dendrimers etc.) to achieve the solubility change. One of the few examples of reversible transfer between aqueous and organic solvents exploits counterion exchange on ruthenium complexes adsorbed on the NP surface.[228] Other reversible strategies include NP functionalisation with a spiropyran polymer which undergoes reversible switching between hydrophobic and hydrophilic states upon UV-Vis irradiation[229] or NPs functionalised with mercaptocarboranes, which exhibit redox-dependent solubility properties.[230]

From the cited examples it can be concluded that NP solubility switching may be achieved by modifying the solvophilicity properties of the NP-bound organic ligands, independently from the nature of the metal core. For this reason, post-synthetic modification of the NP-bound monolayer based on dynamic hydrazone exchange, as investigated in Chapter **3**, could be a new and powerful approach for tuning NP solubility and indeed NP physicochemical properties more generally.

As discussed in Chapter **2**, solvent compatibility of AuNP-**21** was limited to polar protic solvents like *N,N*-dimethylformamide (DMF, Scheme **4.2**, *top*) and dimethyl sulfoxide (DMSO), or mixtures of these solvents with water up to a maximum of 10% v/v (Table **2.4**). To demonstrate the potential of dynamic covalent exchange for reversible solubility control under mild conditions, alkyl aldehyde **28** (Scheme **4.1**) was designed in order to achieve improved NP solubility in hydrophobic solvents, while commercially available 2-formylbenzenesulfonic acid sodium salt **29** was employed to achieve solubility in polar solvents.

By using these components, the reversible switching of NP solubility properties between three distinct states could therefore be explored (Scheme **4.2**)
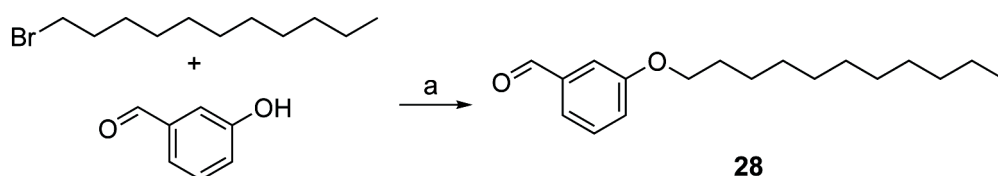
**Scheme 4.1**   Synthesis of aldehyde **28**. a): K$_2$CO$_3$, KI, MeCN, 19 h, reflux, 84%.
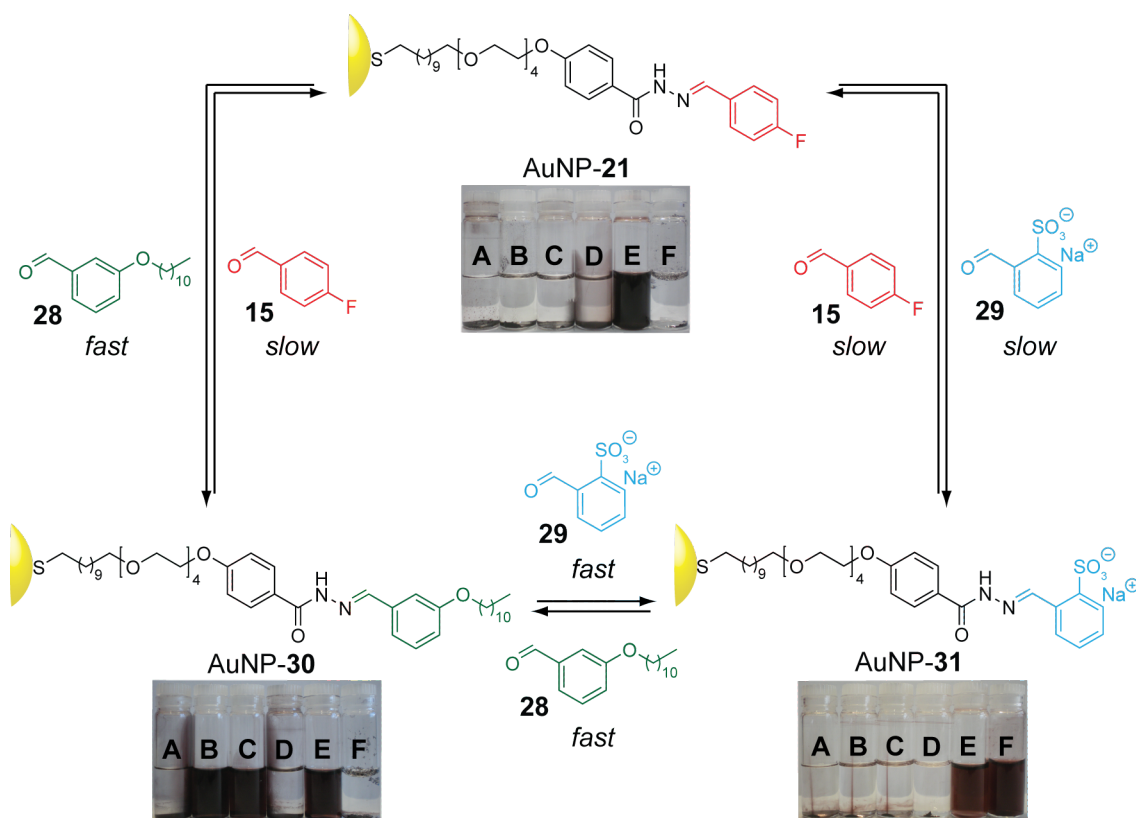
Scheme 4.2   Reversible switching of AuNP solvophilicity *via* hydrazone exchange. AuNP-**21** to AuNP-**30**: **28**, CF$_3$CO$_2$H, D$_2$O/[D$_7$]DMF 1:9, 1.5 h, 50 °C. AuNP-**30** to AuNP-**21**: **15**, CF$_3$CO$_2$H, D$_2$O/[D$_7$]DMF 1:99, 16 h, 50 °C, repeat × 1. AuNP-**30** to AuNP-**31**: **29**, CF$_3$CO$_2$H, D$_2$O/[D$_8$]THF 5:95, 1 h, 50 °C. AuNP-**31** to AuNP-**30**: **28**, CF$_3$CO$_2$H, D$_2$O/[D$_8$]THF 1:9, 1 h, 50 °C. AuNP-**21** to AuNP-**31**: **29**, CF$_3$CO$_2$H, D$_2$O/[D$_7$]DMF 1:9, 16 h, 50 °C. AuNP-**31** to AuNP-**21**: **15**, CF$_3$CO$_2$H, D$_2$O/[D$_7$]DMF 1:9, 16 h, 50 °C. Solvents in the inset pictures: **A** = hexane, **B** = chloroform, **C** = tetrahydrofuran, **D** = methanol, **E** = DMF, **F** = water.

4.1.1   Solubility switching between polar organic and apolar organic solvents

AuNP-**21**, whose ligand concentration was estimated by ^{19}F NMR spectroscopy with respect to an internal standard, was treated with an excess of aldehyde **28** (20 equivalents) and CF$_3$CO$_2$H (5 equivalents) in 10% D$_2$O/[D$_7$]DMF at 50 °C (Scheme **4.3**). After one hour, all NPs had precipitated from the reaction mixture (Figure **4.1B**). Under identical conditions, but in the absence of CF$_3$CO$_2$H, AuNP-**21** proved to be

entirely stable, suggesting that NP precipitation was the result of dynamic hydrazone exchange with aldehyde **28**.
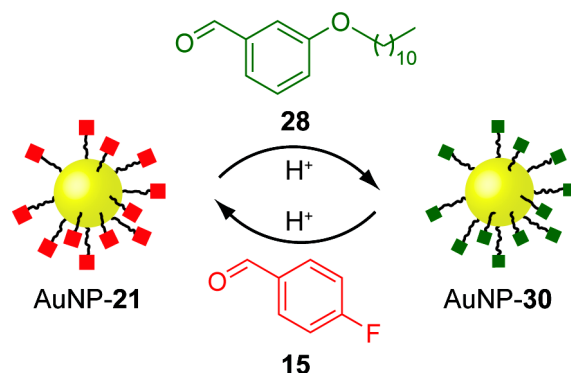
Scheme 4.3   Reversible switching between AuNP-**21** and AuNP-**30** *via* hydrazone exchange under acidic conditions. For details see Scheme **4.2**.

^{19}F NMR analysis of the heterogeneous sample (Figure **4.1B**) revealed that the broad peak corresponding to NP-bound ligand **21** had completely disappeared, as expected after NP precipitation. In addition, a peak corresponding to displaced 4-fluorobenzaldehyde **15** was observed. Excluding peaks corresponding to CF_3CO_2H and the internal standard, no additional peaks were detected. The extent of reaction could be estimated by measuring the quantity of released **15** and was consistently determined to be ≥ 95%.
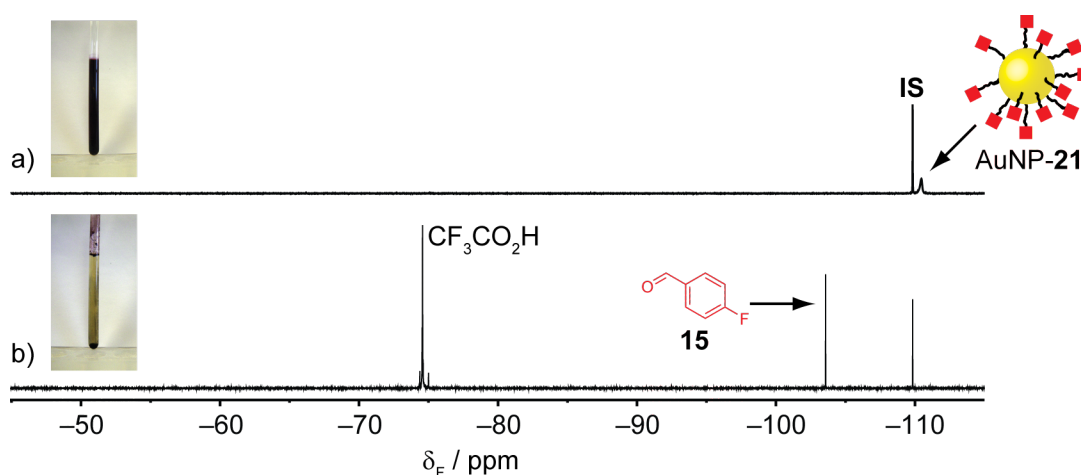
Figure 4.1   ^{19}F NMR (D$_2$O/[D$_7$]DMF 1:9, 470.5 MHz, 295 K, D1: 22 s) of AuNP-**21**. a): Before addition of aldehyde **15** and CF_3CO_2H for the hydrazone exchange. b): ^{19}F NMR of the supernatant solution after NP precipitation showing the presence of the exchanged 4-fluorobenzaldehyde **15**. The extent of the exchange was estimated to be ≥ 95%. **IS**: 1-Fluoro-3-nitrobenzene (4.95 mM).

Subsequently, the supernatant solution was discarded and the black solid recovered and purified by re-dispersing in methanol, followed by precipitation with hexane, sonication and centrifugation. This operation was repeated at least three times, monitoring the presence of unbound aldehydes **15** and **28** by thin layer chromatography (TLC) until the black solid was assessed to be free of molecular contaminants.

The sample (AuNP-**30**) showed markedly different solubility properties to AuNP-**21**, exhibiting colloidal stability in organic solvents of intermediate polarity, such as chloroform and tetrahydrofuran (Figure **4.2A**).
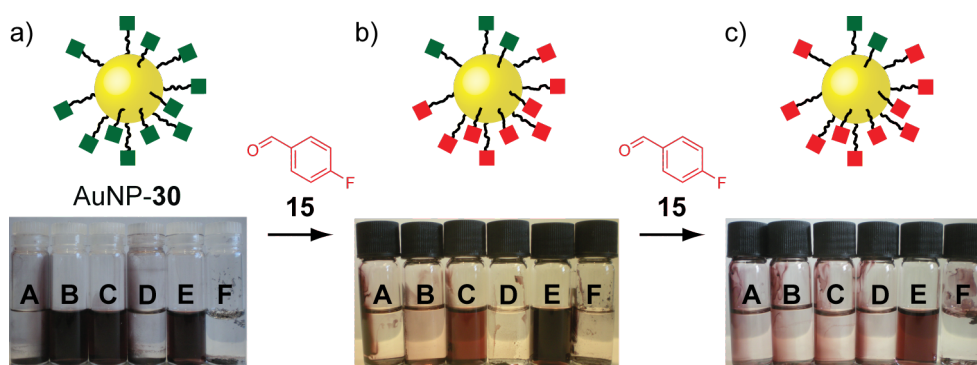
Figure 4.2   Solvent compatibility from AuNP-**30** to AuNP-**21** *via* hydrazone. From a) to b) and from b) to c): **15** (20 Eq), CF_3CO_2H (5 Eq), $D_2O/[D_7]DMF$ 1:99, overnight, 50 °C. Solvents in the inset pictures: **A** = hexane, **B** = chloroform, **C** = tetrahydrofuran, **D** = methanol, **E** = DMF, **F** = water.

The ^{1}H NMR spectrum of AuNP-**30** showed a pattern of broad peaks, suggesting that all the organic species detected were strongly adsorbed on the NP surface (Figure **4.3A**). This was further confirmed by T_2-filtered NMR (see Chapter **2** for details) in which only the peak of the non-deuterated solvent was detected.[61] Resonances corresponding to H-*1* (NH) and H-*2* (CH=) could be unambiguously assigned.

A small amount of NP-bound ligand **21** was detected by ^{19}F NMR spectroscopy (Figure **4.3**, *inset*). LDI-MS analysis (Figure **4.4**) confirmed that NP-bound **30** had formed by hydrazone exchange by observation of the peaks corresponding to disulfide **30**$_2$ and thiol **30**H. In addition, LDI-MS analysis confirmed the presence of non-exchanged NP-bound **21** because of the presence of small fragments related to thiol **21**H and heterodisulfide **21**•**30**.[76]
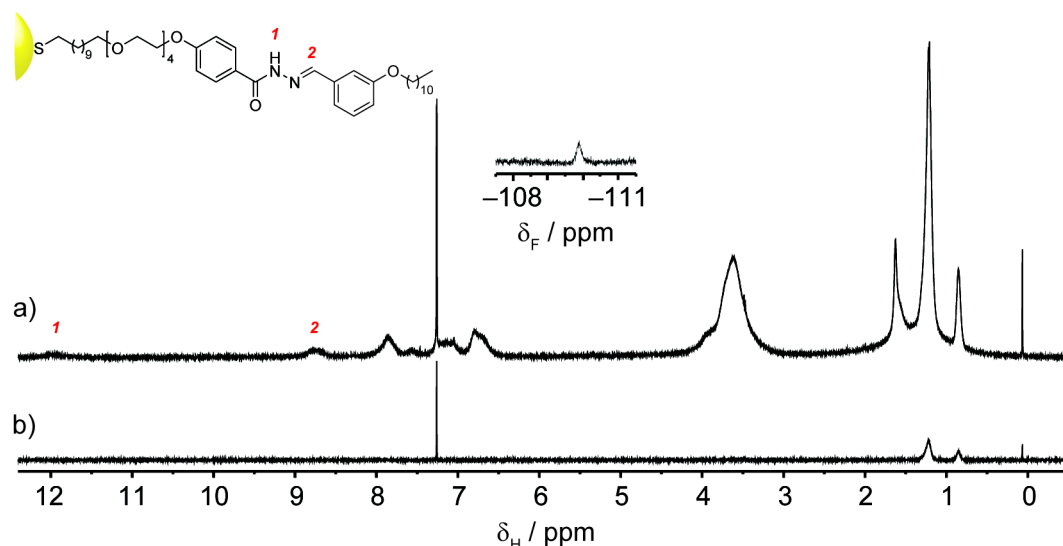
Figure 4.3 Characterisation of AuNP-**30** by NMR spectroscopy. ^{1}H (CDCl$_3$, 500.1 MHz, 295 K). a): AuNP-**30**. b): T_2-filtered spectrum (D21: 0.1 s). Inset: ^{19}F NMR (CDCl$_3$, 470.5 MHz, 295 K) showing the presence of NP-bound **21** not exchanged (≤ 5%).
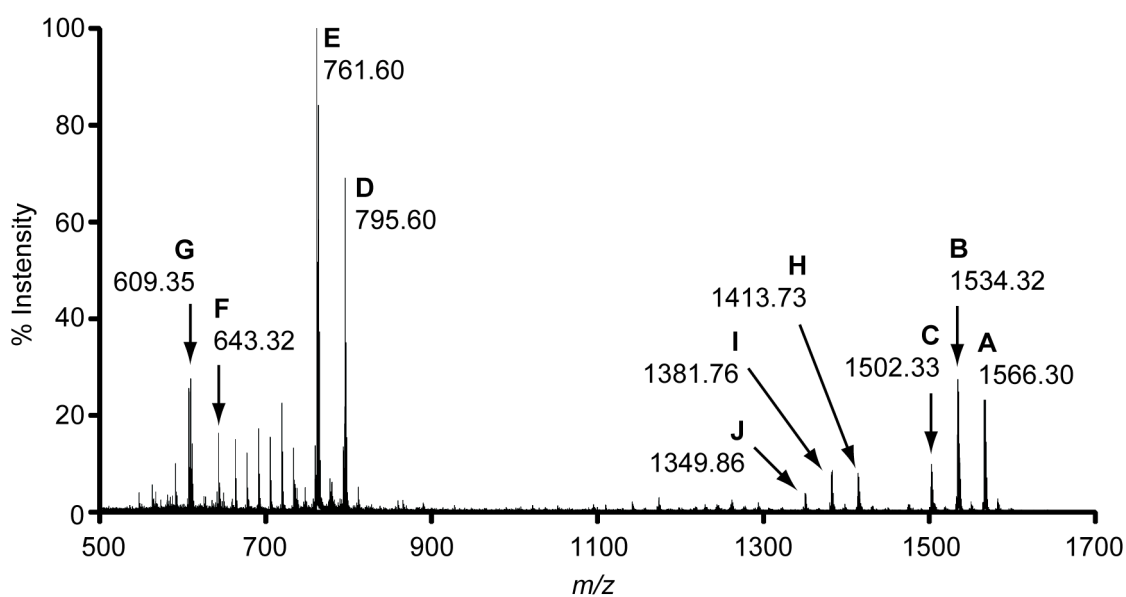

Figure 4.4 LDI mass spectrum of AuNP-**30**. The ion corresponding to the disulfide of ligand **30** (peak A, [**30**$_2$+Na]$^+$: m/z 1566.30) undergoes a progressive loss of two sulfur atoms (peak B, [**30**$_2$–S+Na]$^+$: m/z 1534.32; peak C, [**30**$_2$–2S+Na]$^+$: m/z 1502.33). The ion corresponding to thiol **30**H (peak D, [**30**H+Na]$^+$: m/z 795.60) loses H$_2$S (peak E, [**30**H–H$_2$S+Na]$^+$: m/z 761.60), followed by progressive loss of CH$_2$ units. F): [**21**H+Na]$^+$: m/z 643.32. G): [**21**H–H$_2$S+Na]$^+$: m/z 609.35. H): [**21**•**30**+Na]$^+$: m/z 1413.73. I): [**21**•**30**–S+Na]$^+$: m/z 1381.76. J): [**21**•**30**–2S+Na]$^+$: m/z 1349.86.

In order to demonstrate the reversibility of the process, AuNP-**21** was also obtained *via* hydrazone exchange from AuNP-**30**. As a result of the increased hydrophobicity of AuNP-**30**, the proportion of water in the reaction solvent was reduced from 10% to 1% v/v. This was necessary in order to provide sufficient colloidal stability to AuNP-**30**, which had precipitated in 10% D$_2$O/[D$_7$]DMF and, at the same time, ensure the

presence of water, which is crucial for the occurrence of the hydrazone exchange under acidic conditions (see Section **3.3.1**). Due to the lack of a fluorine tag and the absence of suitably well-resolved signals in the ^{1}H NMR spectrum of AuNP-**30**, a quantitative recovery of AuNP-**30** prepared from AuNP-**21** was assumed in estimating the hydrazone concentration in the sample.

An excess of aldehyde **15** (20 equivalents) and CF_3CO_2H (5 equivalents) was therefore added and the mixture was heated at 50 °C overnight. Under these conditions, no NP precipitation was observed. Before purification, analysis by ^{19}F NMR spectroscopy (Figure **4.5**) revealed successful hydrazone exchange, as the resonance of NP-bound **21** at around –110 ppm had increased in intensity (Figure **4.5B**). Assuming the concentration of CF_3CO_2H to be constant throughout the exchange, integration of the ^{19}F peaks indicated a 4.47% decrease of the peak area corresponding to **15**. No aldehyde oxidation occurred, as observed by integrating the peak corresponding to 4-fluorobenzoic acid before and after the exchange. Approximately, 90% exchange was calculated under these conditions.
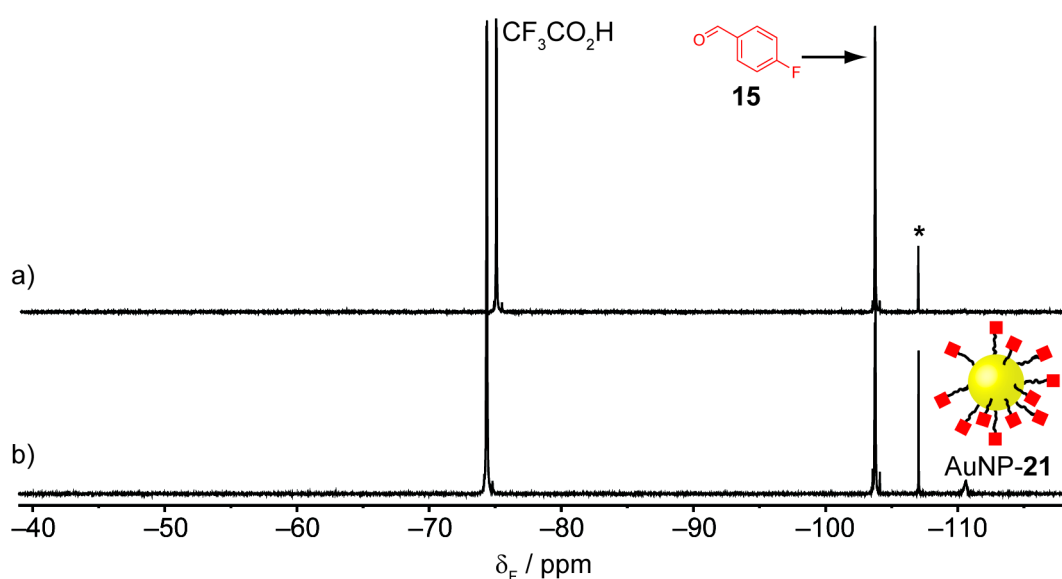
Figure 4.5 ^{19}F NMR (D$_2$O/[D$_7$]DMF 1:99, 470.5 MHz, 295 K) for the hydrazone exchange from AuNP-**30** to AuNP-**21**. a): AuNP-**30** under hydrazone exchange after 1 h from the beginning of the experiment. b): AuNP-**30** exchanged to AuNP-**21** after 22 h from the beginning of the exchange before purification. *: 4-Fluorobenzoic acid.

The sample prepared as described above (AuNP-**21**$_{0.9}$**30**$_{0.1}$) was no longer colloidally stable in chloroform but maintained stability in tetrahydrofuran (Figure **4.2B**). These intermediate solubility properties between a homogeneous NP-bound monolayer of **21** and **30** suggested therefore the presence of a mixed monolayer composed by both ligands **21** and **30**. LDI-MS analysis confirmed the hypothesis, revealing the presence

of fragments corresponding to ligands **21** and **30** (Figure **4.6**). It should be noted that the exchange from AuNP-**30** to AuNP-**21** had gone almost to completion (about 90%). However, it seems that even small amounts of ligand **30** in the NP-bound monolayer (≤ 10%) are able to determine NP solubility in solvents less polar than DMF.
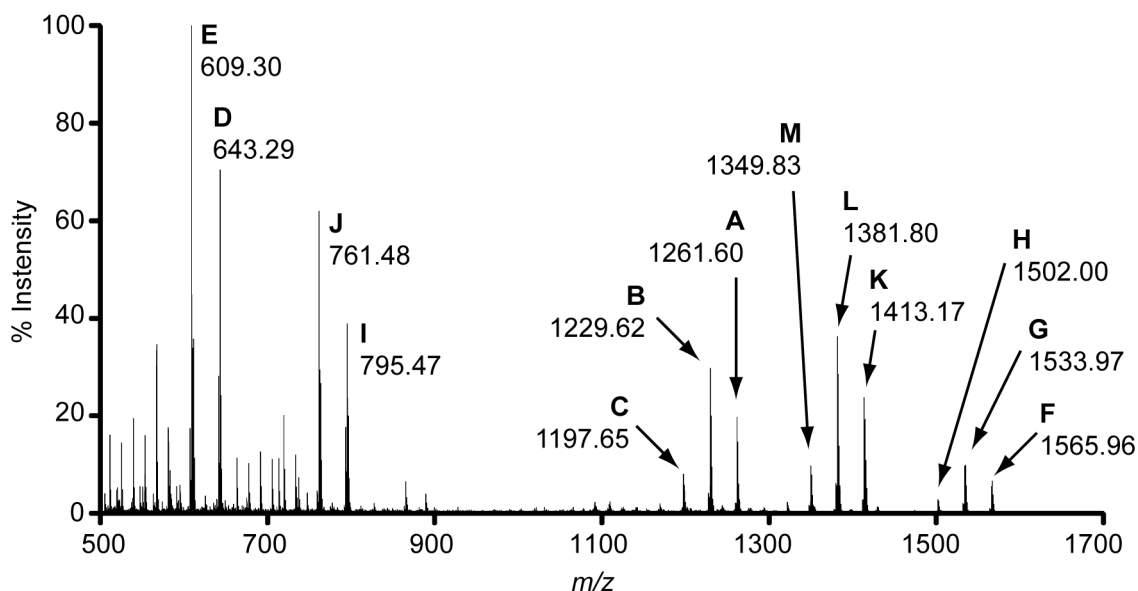

Figure 4.6   LDI-MS of the intermediate exchange product from AuNP-**30** to AuNP-**21**. A): [**21**$_2$+Na]$^+$: m/z 1261.60. B): [**21**$_2$–S+Na]$^+$: m/z 1229.62. C): [**21**$_2$–2S+Na]$^+$: m/z 1197.65. D): [**21**H+Na]$^+$: m/z 643.29. E): [**21**H–H$_2$S+Na]$^+$: m/z 609.30. F): [**30**$_2$+Na]$^+$: m/z 1565.96. G): [**30**$_2$–S+Na]$^+$: m/z 1533.97. H): [**30**$_2$–2S+Na]$^+$: m/z 1502.00. I): [**30**H+Na]$^+$: m/z 795.47. J): [**30**H–H$_2$S+Na]$^+$: m/z 761.48. K): [**21**•**30**+Na]$^+$: m/z 1413.17. L): [**21**•**30**–S+Na]$^+$: m/z 1381.80. M): [**21**•**30**–2S+Na]$^+$: m/z 1349.83. A further round of exchange with aldehyde **15** produced a spectrum identical to Figure **2.12** (see Section **5.8.1.3** for related NMR spectra).

AuNP-**21**$_{0.9}$**30**$_{0.1}$ was then recovered, purified and subjected to a second cycle of hydrazone exchange under identical conditions. After precipitation and purification as before, the sample showed this time identical solubility properties (Figure **4.2C**) to those shown by a sample of AuNP-**21** prepared as discussed in Section **2.2.3**. Analysis by ^{19}F and ^{1}H NMR spectroscopy (Section **5.8.1.3**) was consistent with a homogenous NP-bound monolayer of ligand **21** and indistinguishable from NMR spectra corresponding to AuNP-**21** prepared by direct synthesis (Section **2.3.3.2**).

Dynamic hydrazone exchange in the NP-bound monolayer therefore not only allows NP solubility switching between solvents of markedly different polarity, but can also be used to prepare AuNPs with mixed hydrazone monolayers, which correspondingly display solubility properties that are intermediate between the two extremes.

4.1.2   Solubility switching between apolar organic and aqueous solvents

Initial attempts to prepare water-soluble NPs by treating AuNP-**30** with water soluble aldehyde **29** were carried out using a biphasic water/chloroform system (1:9) to achieve both colloidal stability of hydrophobic AuNP-**30** and complete solubilisation of hydrophilic aldehyde **29** (Scheme **4.4**).
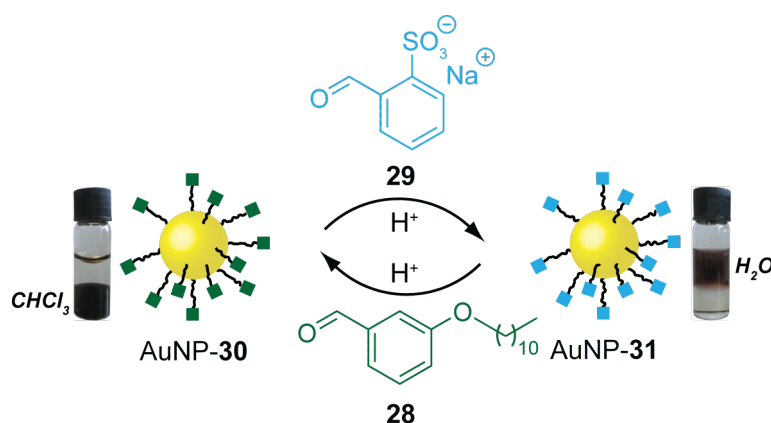
Scheme 4.4   Reversible preparation and AuNP-**30** and AuNP-**31** *via* hydrazone exchange under acidic conditions. For details see Scheme **4.2**.

As before, the amount of NP-bound ligand **30** was approximated assuming a quantitative recovery from the exchange starting from AuNP-**21** (Section **4.1.1**). Aldehyde **29** (20 equivalents) and CF_3CO_2H (5 equivalents) were dissolved in water, added to AuNP-**30** in chloroform, and the biphasic mixture was heated at 50 °C under vigorous stirring. Within ten minutes, full NP precipitation was observed (AuNP-**30**$_x$**31**$_y$). The black solid exhibited poor solubility in water and insufficient dissolved sample was obtained for NMR analysis in water or in other solvents. However, TEM analysis confirmed the presence of AuNPs in the aqueous phase (Figure **4.7**). Interestingly, the AuNPs looked to be organised in small aggregates, with a mean diameter of 14.7 ± 2.86 nm (19% dispersity). This could be the result of hydrophobic interactions between ligands **30** in order to minimise contact with water. Unfortunately, it was not possible to push the exchange to a higher extent under these conditions, probably because only partial hydrazone exchange occurred when NPs precipitated from the reaction mixture.
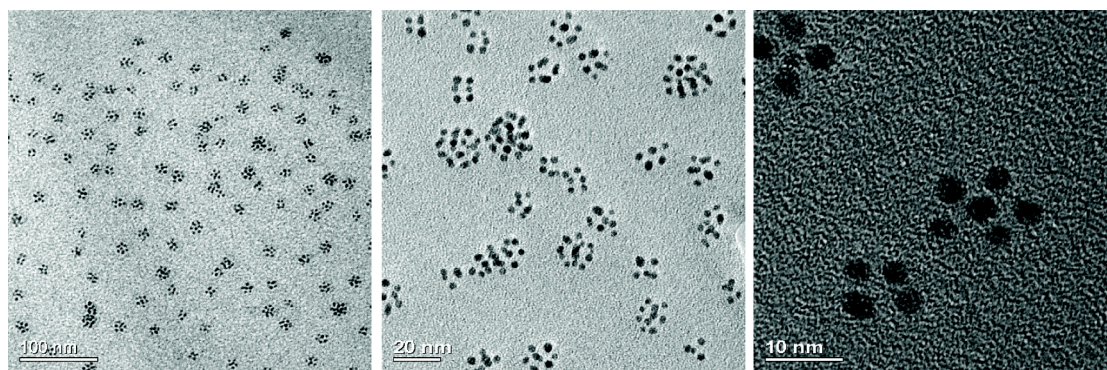
Figure 4.7   TEM micrographs (scale bars from left to right: 100, 20 and 10 nm) of AuNP-$\mathbf{30}_x\mathbf{31}_y$ (incomplete exchange). Conditions: aldehyde **29** (20 Eq), CF_3CO_2H (5 Eq), $H_2O/CHCl_3$ 1:9, 50 °C.

In order to improve control over the exchange process, a solvent mixture was sought that could balance the solubility of the hydrophobic AuNP-**30** starting material with the poor solubility of aldehyde **29** in solvents other than water, while also maintaining the colloidal stability of the NPs as they become increasingly hydrophilic. A good compromise was found to be 5% water/tetrahydrofuran. By using this solvent system, hydrazone exchange from AuNP-**30** was attempted again as before (20 equivalents of **29** and 5 equivalents of CF_3CO_2H at 50 °C). NP precipitation occurred also under these conditions. However, NPs remained soluble for a longer period of time achieving, presumably, a higher extent of exchange. Before purification, ^{1}H NMR analysis of the supernatant confirmed the presence of displaced hydrophobic aldehyde **28**. The supernatant was then discarded, and the black solid was washed with 1% water/tetrahydrofuran to remove any NP-unbound species, obtaining AuNP-**31** as a pure sample. AuNP-**31** maintained solvent compatibility with DMF but it was no longer soluble in chloroform and tetrahydrofuran and showed full colloidal stability in water (Scheme **4.2**).

By comparing ^{1}H NMR spectra of AuNP-**30** (Figure **4.3A**) and AuNP-**31** (Figure **4.8A**), it is possible to assess that the exchange is almost complete. The broad peaks corresponding to the *m*-alkoxy substituent of NP-bound **30** are barely visible after the exchange. In addition, AuNP-**31** is free from any unbound species as confirmed by the T_2-filter experiment (Figure **4.8B**) where only the peak corresponding to the residual non-deuterated solvent is detected.[61]
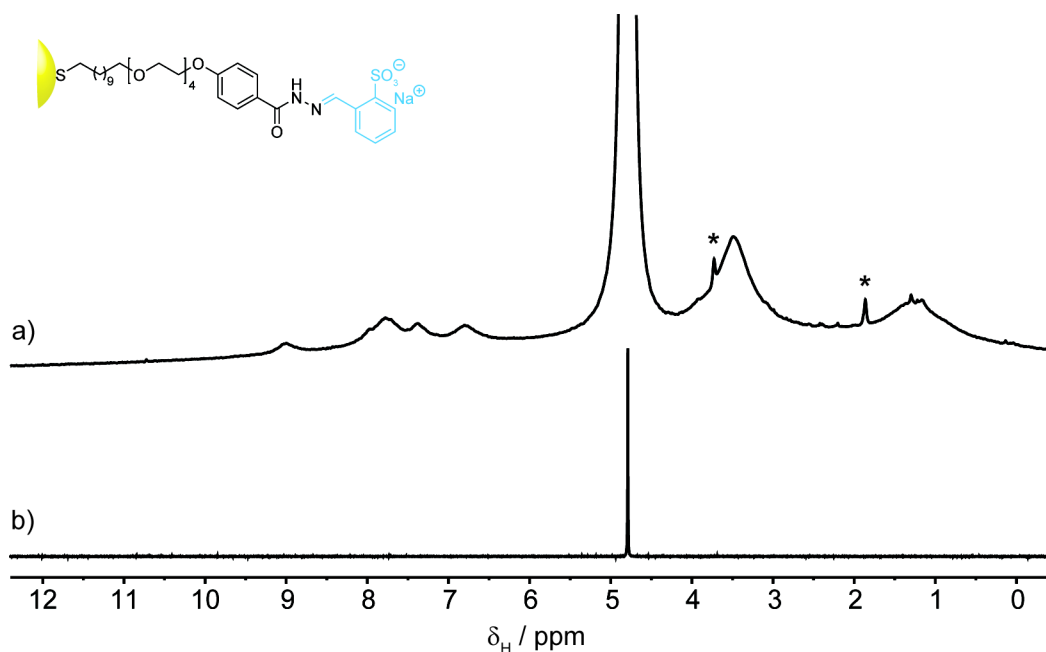
Figure 4.8   ^{1}H NMR (D$_2$O, 500.1 MHz, 295 K) analysis of AuNP-**31**. a): AuNP-**31**. b): T_2-filtered spectrum (D21: 0.1 s). *: Residual non-deuterated THF.

LDI-MS analysis further confirmed the hydrazone exchange. Mass spectra were obtained in both positive and negative ionisation mode (Figures **4.9–10**). In positive mode, diagnostic peaks corresponding to thiol **31**H and related fragment resulting from loss of H$_2$S were detected. In addition, fragments corresponding to ligand **30** confirmed that the exchange was not complete although the NMR evidence (*vide supra*) suggests only a small proportion of NP-bound **30** remains. The negative ion mode spectrum (Figure **4.10**) further confirmed the successful preparation of AuNP-**31** by hydrazone exchange. Signals corresponding to the thiolate (peak A), or fragments formed by β-elimination from the disulfide (peak C) were observed together their corresponding loses of H$_2$S (peaks B and D, respectively). This characteristic pattern in negative mode matrix assisted LDI analysis was previously reported for small disulfide molecules.[231]
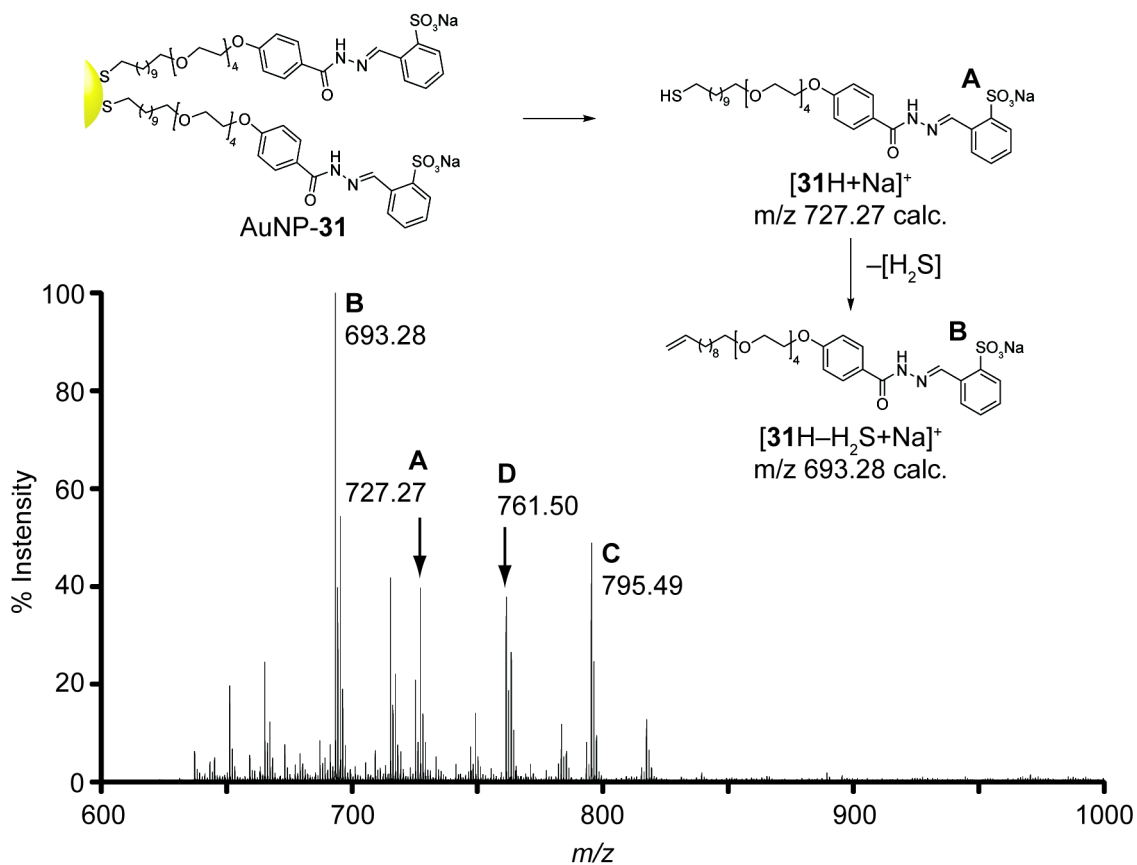
Figure 4.9 LDI mass spectrum and fragmentation pattern for AuNP-**31** (positive mode). The ion corresponding to thiol **31**H (peak A, [**31**H+Na]$^+$: m/z 727.27) loses H$_2$S (peak B, [**31**H–H$_2$S+Na]$^+$: m/z 693.28). C): [**30**H+Na]$^+$: m/z 795.49. D): [**30**H–H$_2$S+Na]$^+$: m/z 761.50.
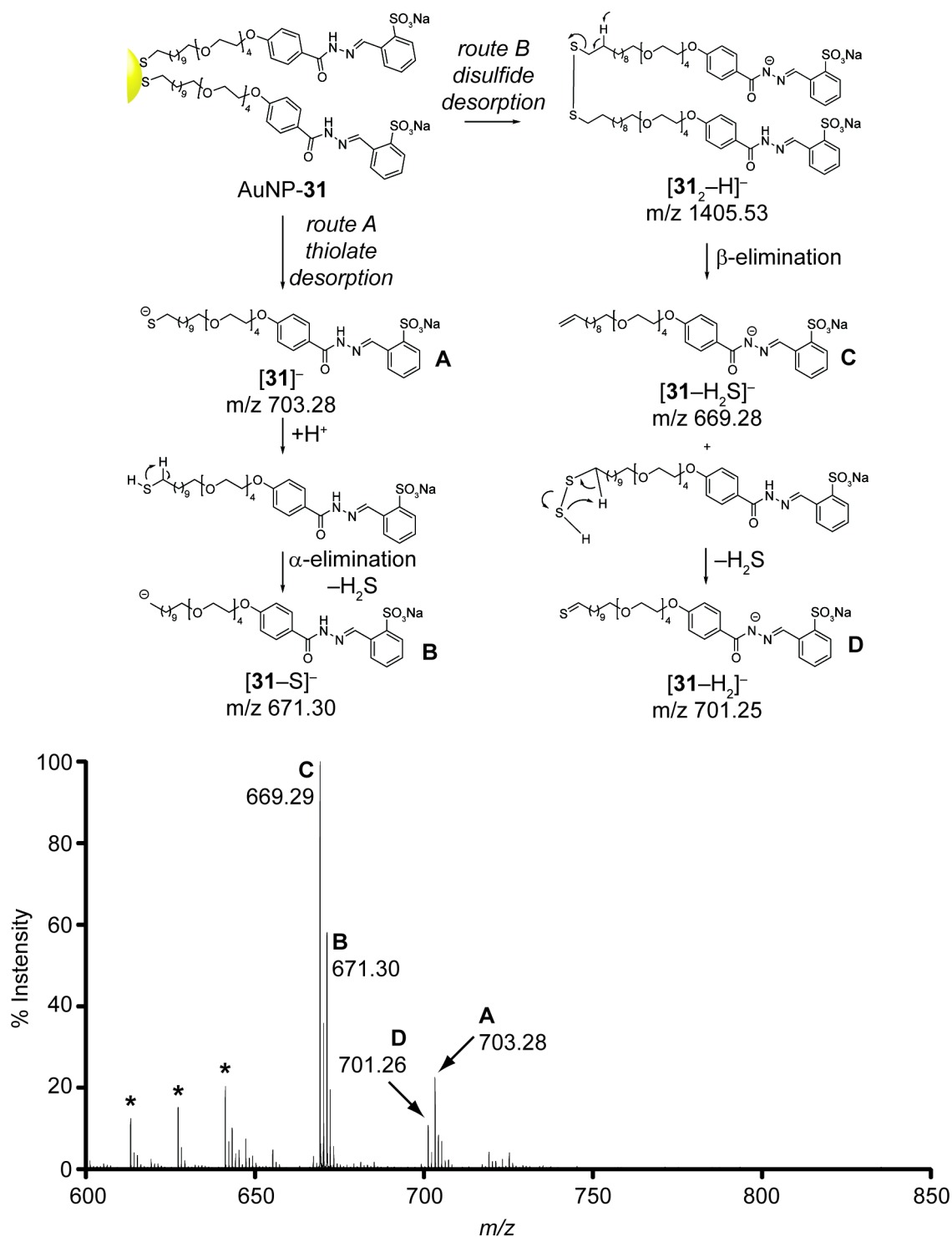
Figure 4.10   LDI mass spectrum and fragmentation pattern for AuNP-**31** (negative mode). The ion corresponding to the thiolate (peak A, [**31**]⁻: m/z 703.28) loses H_2S via α-elimination (peak B, [**31**–S]⁻: m/z 671.30). The disulfide of ligand **31** undergoes a rearrangement via β-elimination forming two fragments: peak C, [**31**–H_2S]⁻: m/z 669.29, peak D, [**31**–H_2]⁻: m/z 701.26.[231] *: Progressive loss of CH_2 units from fragment with m/z 669.29 (peak C).

The reversibility of the hydrazone exchange was confirmed by treating AuNP-**31** with aldehyde **28** (20 equivalents) and CF_3CO_2H (5 equivalents) in 10% $D_2O/[D_8]THF$ at 50 °C. After 20 minutes, partial NP precipitation was observed. The sample was kept at

50 °C for an additional 40 minutes after which all NP material had precipitated. The crude black material showed identical solubility properties and LDI-MS fragmentation pattern to AuNP-**30** prepared from AuNP-**21** (see Section **4.1.1**).

4.1.3 Solubility switching between polar organic and aqueous solvents

Reversible hydrazone exchange between AuNP-**21** and AuNP-**31** (Scheme **4.5**) was also investigated to demonstrate that each NP system (AuNP-**21**, AuNP-**30** and AuNP-**31**) could be obtained independently from either one of the other two NP systems (Scheme **4.2**).
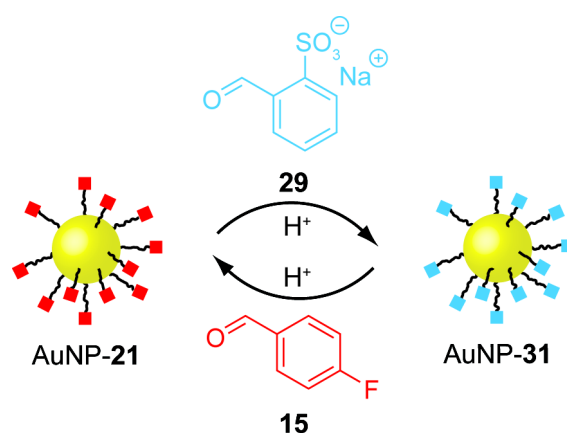
Scheme 4.5   Reversible preparation of AuNP-**21** and AuNP-**31** *via* hydrazone exchange under acidic conditions. For details see Scheme **4.2**.

An excess of aldehyde **29** (20 equivalents) and CF_3CO_2H (5 equivalents) was added to AuNP-**21** dissolved in 10% D_2O/DMF. On heating to 50 °C, no NP precipitation was observed even after 2 days under these conditions. ^{1}H NMR analysis of the crude reaction mixture revealed the presence of displaced aldehyde **15** and, by integration of the ^{19}F peaks corresponding to **15** and NP-bound **21**, the extent of hydrolysis was estimated (as previously shown for AuNP-**30**, Figure **4.1**) and found to be 76% after 18 h from CF_3CO_2H addition. No further aldehyde **15** was released after 42 h, thus equilibrium achievement was confirmed. NP precipitation was induced by addition of diethyl ether and the recovered black material was then purified.

Despite presumably the presence of up to 24% ligand **21** within the monolayer, the resulting NPs showed identical solvent compatibility to AuNP-**31** prepared starting from AuNP-**30**. ^{19}F NMR analysis confirmed the presence of non-exchanged NP-bound ligand **21** (Figure **5.30**, *inset*), as did LDI-MS, which detected fragments related to both ligands **21**H and **31**H together with heterodisulfide **21•31** (Figure **5.31**).

The reversibility of the exchange was assessed by treating AuNP-$21_{0.24}31_{0.76}$ with an excess of aldehyde **15** (20 equivalents) and CF_3CO_2H (5 equivalents) in 10% $D_2O/[D_7]DMF$ at 50 °C overnight. Analysis by ^{19}F NMR spectroscopy before any purification confirmed an increase in intensity of the broad peak corresponding to NP-bound ligand **21**. After NP precipitation by diethyl ether addition and purification with a mixture of DMF and diethyl ether, the recovered black material was no longer soluble in water and was only soluble in DMF. Although LDI-MS analysis (Figure **5.35**) indicated the presence of some residual NP-bound ligand **31** alongside ligand **21**, the recovered material was no longer soluble in water and was only soluble in DMF, identical to the initial sample of AuNP-**21**.

4.1.4   Non-covalent aggregation of AuNP-30

Of all the samples prepared by hydrazone exchange with simple aldehydes **15**, **28** and **29**, AuNP-**30** showed colloidal stability in the widest range of solvents (including chloroform, tetrahydrofuran and DMF). It was also observed that by varying the composition of the NP-bound monolayer starting from 100% NP-bound ligand **30**, AuNPs with intermediate solubility properties could be obtained (Figure **4.2B**). Furthermore, the observation of small aggregates on TEM analysis of AuNPs functionalised with a mixed monolayer composed of ligands **30** and **31** (Figure **4.7**) is suggestive of a non-covalent NP assembly process driven by hydrophobic effects. In order to further explore the balance of solubilising and aggregative forces for NPs bearing hydrophobic ligands, colloidal dispersions of pure AuNP-**30** in a variety of solvents were analysed by DLS by which variations of the solvodynamic diameter could be indicative of NP aggregation processes.[53]

AuNP-**30**, prepared *via* hydrazone exchange starting from AuNP-**21** (Section **4.1.1**), was re-dissolved in chloroform. The dispersion was sonicated and gently centrifuged to physically remove any non-dissolved NP aggregates. In order to exclude from the dispersion any irreversibly formed aggregates larger than 100 nm, the solution was passed through a 100 nm filter and divided into several aliquots. Samples for DLS analysis were then prepared by evaporating the solvent under vacuum, followed by re-dispersion of the residue to a final concentration of about 0.3 mg mL^{-1} in 100% chloroform, 100% tetrahydrofuran and in several mixtures of the two solvents (Figure **4.11A**). In a separate experiment, the extent of aggregation was also investigated in tetrahydrofuran mixtures with increasing amounts of water (Figure **4.11B**).
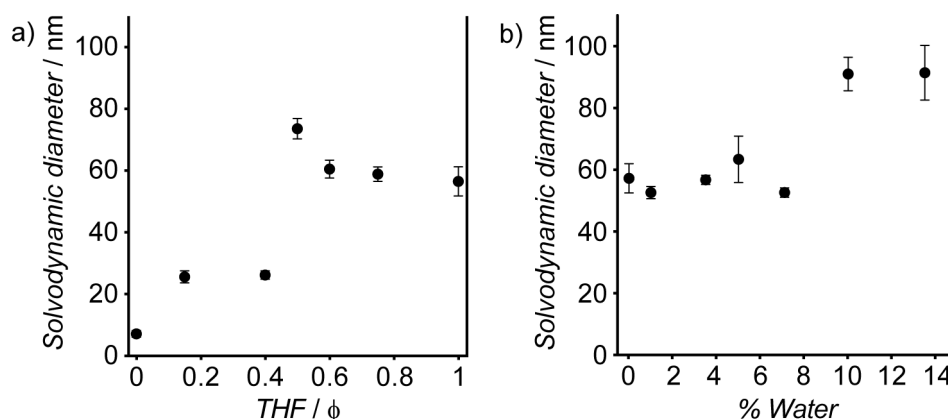
Figure 4.11   Variation of the solvodynamic diameter of AuNP-**30** monitored by dynamic light scattering. a): AuNP-**30** dissolved in CHCl$_3$/THF mixtures. b): AuNP-**30** dissolved in THF with increasing amount of water. Error bars: ± 1 s.d. of the mean diameter estimated from at least six independent measurements.

As evidenced in Figure **4.11A**, the measured solvodynamic diameter in 100% chloroform (7.52 ± 1.09 nm), corresponding approximately to the diameter of one NP, was largely smaller if compared to that measured in 100% tetrahydrofuran (56.9 ± 4.62 nm). For increasing volume fractions of tetrahydrofuran (ϕ_{THF}), two discontinuous increases of the solvodynamic diameter were observed, the first for ϕ_{THF} from 0 to 0.15 and the second for ϕ_{THF} from 0.4 to 0.5. A maximum diameter was observed for ϕ_{THF} = 0.5 (70.2 ± 3.31 nm). The increase of the solvodynamic diameter suggested NP aggregation as the polarity of the mixture increases. For ϕ_{THF} from 0.5 to 0.6, DLS analysis indicated a small decrease of the solvodynamic diameter. For 0.6 ≤ ϕ_{THF} ≤ 1.0, no further changes were observed, within the experimental error.

The maximum at ϕ_{THF} = 0.5 may be indicative of the presence of solvent molecules included in the NP aggregates. As the polarity of the solvent increases (ϕ_{THF} > 0.5), the *m*-alkoxy chains of NP-bound **30** are induced to minimise their interaction with the solvent. The result is a solvent displacement from the NP aggregates and subsequent slight decrease of the measured solvodynamic diameter of the NP aggregate, as a result the contraction of the average interparticle distance within the assembly.

TEM analysis (Figure **4.12**) further confirmed a different degree of NP aggregation depending on the solvent mixture. In order to minimise the effect of a slow solvent evaporation during the preparation of TEM samples, the TEM grid was directly dipped into the NP dispersion and immediately dried under high vacuum. When the TEM sample was prepared from a 100% chloroform dispersion, NPs looked to be quite well distributed on the grid (Figure **4.12**, *left*). On the other hand, when the sample was

prepared from 1:1 chloroform/tetrahydrofuran mixture, TEM pictures showed that NPs were organised in large aggregates with diameter ≥ 50 nm (Figure **4.12**, *right*).
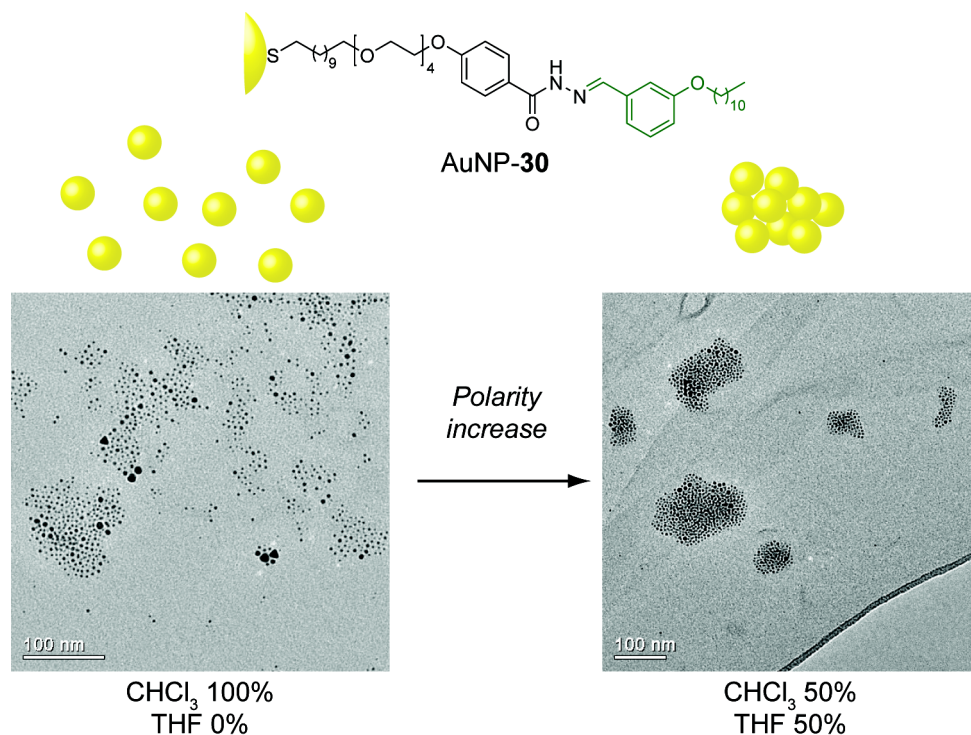

AuNP-30

Figure 4.12   Representative TEM micrographs of AuNP-**30** (scale bar 100 nm). Samples were prepared by dipping the TEM grid in the NP dispersion followed by solvent evaporation under high vacuum. Solvent systems: CHCl$_3$ (*left*), CHCl$_3$/THF 1:1 (*right*). For additional TEM micrographs, see Section **5.9**.

In tetrahydrofuran/water mixtures (Figure **4.11B**), no further aggregation of AuNP-**30** occurred from 0% to 7% water v/v. On the contrary, a sharp increase of the solvodynamic diameter (up to about 90 nm) was observed for higher amounts of water (10% and 13% v/v). For higher percentages of water, AuNP-**30** was not colloidally stable and NP precipitation occurred.

The preliminary results, which have to be however repeated with a more homogeneous sample of AuNP-**30**, interestingly show that the aggregation process appears to be self-limiting within the range of solvents employed, producing NP aggregates of well defined size, within the boundaries of the experimental error.

4.1.5   Nanoparticle solubility switching: conclusions and perspectives

Reversible AuNP solubility switching based on dynamic hydrazone exchange within the NP-bound monolayer has been successfully achieved, providing undoubted advantages of this strategy over other approaches.

The conditions employed for the hydrazone exchange are mild and the NP switching was achieved by using very simple exchange units. In addition, NP solubility switching driven by hydrazone exchange within the NP-bound monolayer allows the nanoscale features such as NP size to be maintained unlike, for example, other approaches (e.g. polymer encapsulation). NP solubility switching can be successfully achieved between three distinct states where ligand-functionalised NPs are indefinitely stable over time.

Clearly, in some cases hydrazone exchange did not reach completion before NP precipitation quenched the reaction. Although further optimisation of the reaction solvent composition, or subjecting part-exchanged material to a further round of exchange, could be used to attain complete exchange in these cases, this was not necessary to achieve a radical change in AuNP solvent compatibility. On the other hand, the results obtained on exchanging from AuNP-**30** to AuNP-**21** indicate that, at appropriate proportions, mixed monolayers can give access to AuNP samples with solubility properties that are intermediate between the extremes defined by the two homoligand samples. The ability to reversibly and repeatedly switch between distinct states, and more subtly tune monolayer composition across a continuum of compositions, suggests a powerful and flexible approach for controlling a variety of NP properties that are governed by the surface monolayer molecular structure.

Further investigation will be required to establish the precise relationship between the composition of the NP-bound monolayer and any given property such as solubility, and the appropriate conditions for achieving a given composition by design. By this way, it could be investigated whether the solvent switching occurs gradually or sharply by achievement of a 'critical composition' of the mixed monolayer.

4.2 Assembly of AuNP-21 *via* hydrazone exchange

Reversible AuNP self-assembly driven by non-covalent oligonucleotide hybridisation has been successfully developed for preparing highly ordered functionalised nanomaterials.[25,85] As discussed in Chapter **3** and further confirmed in Section **4.1**, post-synthetic covalent modification of ligand-functionalised AuNPs *via* hydrazone exchange has been successfully demonstrated. It was then reasonable to exploit dynamic hydrazone covalent exchange for assembling NPs with each other, exploiting the reversibility and the stability of hydrazone covalent bonds. Covalent NP assembly *via* hydrazone exchange has also the potentiality to be performed in a wider range of experimental conditions when compared to oligonucleotide-based NP assembly, which

is efficient only in aqueous solutions within small window of temperature and salt concentration.

Preliminary investigations using AuNP-**21** and commercially available bifunctional terephthalaldehyde (Figure **4.13**) were carried out. AuNP-**21** was dissolved in 10% D_2O/DMF and the ligand concentration was measured by ^{19}F NMR spectroscopy with respect to an internal standard. The dispersion was further diluted reaching a final concentration of about 20 μM in terms of ligand **21**. The so obtained sample was analysed by TEM (Figure **4.14A**), observing that NPs were uniformly distributed on the grid. This starting NP dispersion was divided into aliquots to which different amounts of bifunctional aldehyde (0.1, 1 and 5 equivalents with respect to **21**) and CF_3CO_2H (5 equivalents) were added, working at room temperature. In addition, two control experiments were performed. In the first, AuNP-**21** was treated with terephthalaldehyde (0.1 equivalents) without adding CF_3CO_2H while, in the second, only CF_3CO_2H (5 equivalents) was added to AuNP-**21**. After one day, a small amount of precipitate was observed only in the vials where both CF_3CO_2H and aldehyde were present. After 21 days, complete precipitation was observed in the vial containing 5 equivalents of terephthalaldehyde (Figure **4.13C**), while in the vials with fewer equivalents of the linker (Figure **4.13A**–**B**) NP precipitation was not complete and the dispersion was still deeply red-coloured. On the contrary, no NP precipitation was observed in the two vials where only aldehyde or CF_3CO_2H were added (Figure **4.13D**–**E**).
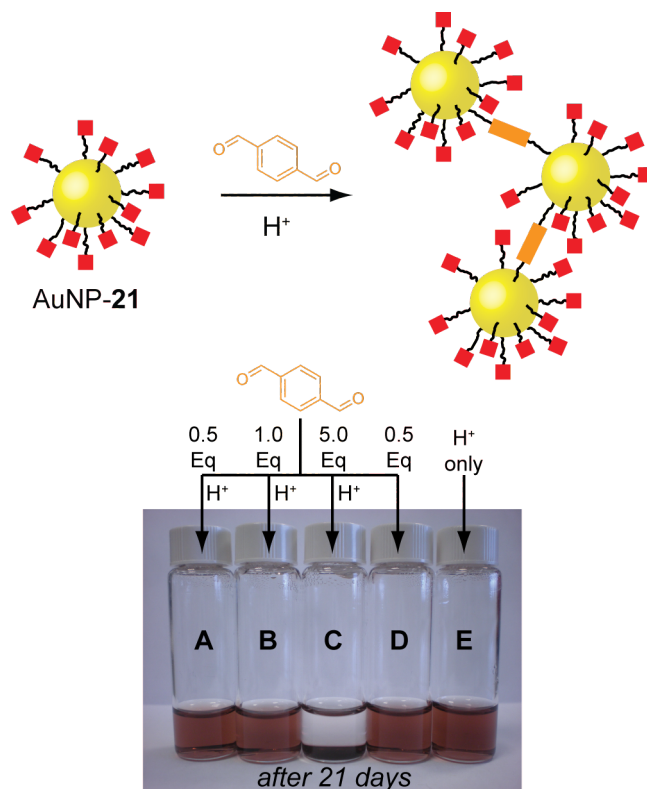
Figure 4.13   Pictures of aggregation experiments of AuNP-**21** with terephthalaldehyde taken after 21 days. Conditions: CF_3CO_2H (5 Eq with respect to **21**), H_2O/DMF 1:9, rt. Aldehyde: a) 0.5 Eq, b) 1 Eq, c) 5 Eq (with respect to **21**). d): same conditions of a) without CF_3CO_2H. e): same conditions of a), b) and c) without aldehyde.

Analysis by TEM was then carried out (Figure **4.14B**–**D**). For vials where NP precipitation was not complete, the TEM sample was prepared by simply dipping the TEM grid into the dispersion followed by quick evaporation under high vacuum to avoid misleading observations due to the water/DMF slow evaporation process. On the contrary the vial shown in Figure **4.13C** was extensively sonicated in order to re-disperse the insoluble black material and the preparation of the TEM grid was done in the same way. As shown in Figure **4.14** (additional TEM pictures are included in Section **5.10**), for the samples where only partial precipitation occurred, even the supernatant showed presence of aggregates after 21 days (Figure **4.14B**–**C**). In both experiments where 0.1 or 1 equivalents of aldehyde were employed, NPs are organised in relatively small aggregates (< 100 nm) with a good colloidal stability in H_2O/DMF 1:9. TEM analysis of the dispersion after full NP precipitation (Figure **4.14D**) shows an interesting NP organisation in dendritic-like superstructures, which is consistent over the whole TEM grid (see Section **5.10** for additional TEM images). A further characterisation of these insoluble NP aggregates was performed by using scanning tunnelling microscopy, which is able to provide information about the sample surface (Figure **4.14E**),[232] and suggests a porous architecture. TEM analysis of the

two control experiments (Section **5.10**) gave further confirmation that the so described NP superstructures were formed as a result of hydrazone exchange. In the absence of bifunctional aldehyde or CF_3CO_2H, TEM analysis reveals that the NPs remain well-separated and evenly distributed on the TEM grid, similarly to those shown in Figure **4.14A**. A very few small amorphous aggregates were also observed as, very likely, the result of solvent slow evaporation processes during the preparation of the TEM grid.
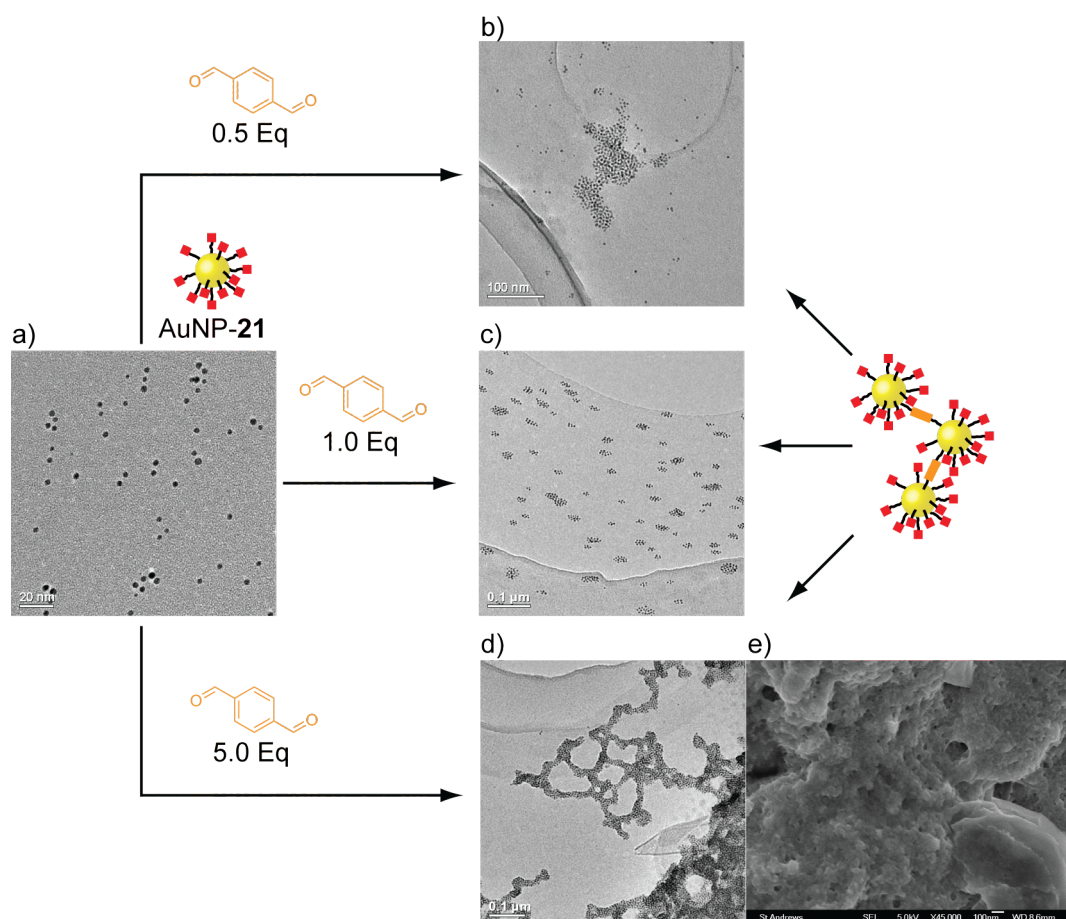
Figure 4.14   Aggregation of AuNP-**21** with terephthalaldehyde *via* hydrazone exchange. Conditions: CF_3CO_2H (5 Eq in terms of ligand **21**), H_2O/DMF 1:9. TEM micrographs before (*a*) and after CF_3CO_2H addition (21 days, *b, c, d*) a): AuNP-**21** before hydrazone exchange (scale bar 20 nm). b): AuNP-**21** with 0.5 Eq of aldehyde (scale bar 100 nm). c): AuNP-**21** with 1.0 Eq of aldehyde (scale bar 100 nm). d): AuNP-**21** with 5.0 Eq of aldehyde (scale bar 100 nm). e): Scanning tunnelling microscopy analysis of the insoluble NP aggregates (scale bar 100 nm), suggesting a porous architecture. For additional images, see Section **5.10**.

4.2.1   Nanoparticle assembly by dynamic hydrazone chemistry: perspectives

The above described observations provide preliminary evidence that NP self-assembly may be achieved by dynamic covalent hydrazone exchange under acidic conditions. For this purpose, the assembly process should be more closely monitored by UV-Vis

spectroscopy and DLS analysis. These techniques should be able to detect modifications of the NP dispersion, as the exchange proceeds, by observing shifts in the position of the surface plasmon resonance band or decrease in its intensity on NP precipitation (for UV-Vis, see Section **1.2.2**) or an increase of the solvodynamic diameter over time (for DLS, see Sections **1.2.3** and **4.1.4**). In addition, it would be interesting to investigate possible modifications of the NP superstructure by modifying experimental conditions such as solvent and temperature in order to keep the growing aggregates stable in solution for a longer time and to assess whether greater order in the superstructure can be achieved. Alternatively, the number of NP-bound active ligands that undergo hydrazone exchange could be reduced. This may be studied by preparing heterogeneously-functionalised NPs with an inert ligand (e.g. 1-dodecanethiol).

A logical and unexplored route for connecting NPs to each other *via* hydrazone exchange would be to employ ligand functionalised AuNPs which are complementary to each other (Figure **4.15**) in order to obtain 'colloidal molecules' where NPs can be considered like atoms connected by the organic ligands which work as bonds.
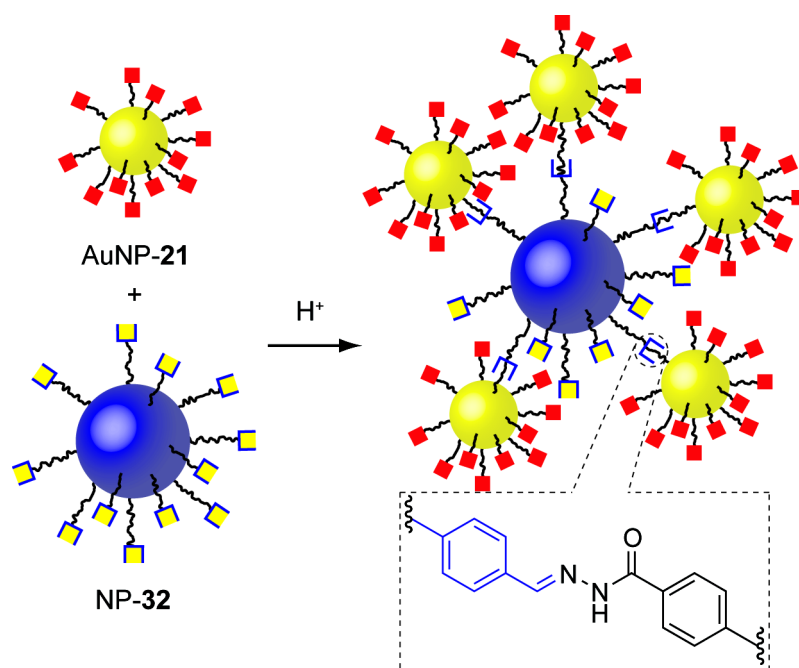
Figure 4.15   Aggregation of complementary ligand-functionalised AuNPs *via* hydrazone exchange.

As discussed in Chapters **3** and **4**, the NP-bound monolayer can be efficiently and reversibly modified employing small aldehyde units *via* hydrazone exchange. Ideally, the same concept could be used by using aldehyde-functionalised NPs (e.g. NP-**32**) where the aldehyde group is now at the end of the thiol ligand adsorbed on the NP

surface. The aldehyde group is sensitive to reduction, so its insertion on the NP-bound ligand might be problematic in terms of compatibility with the available methods for preparing metal NPs under reducing conditions.[40,45,46] In addition, even in the case of a successful preparation of aldehyde-functionalised AuNPs, their stability over time must be assessed because the aldehyde group could undergo oxidation. Ensuring aldehyde stability is known to represent a particular challenge in the presence of AuNPs which can act as efficient redox catalysts for aerobic oxidations.[233–236] One solution could be the synthesis of a ligand where the aldehyde is protected as hydrazone. This would overcome the possible issues mentioned before and provide a new class of hydrazone-functionalised NPs (see Figure **4.15**, dashed box). Early investigations on this new class of hydrazone ligands have revealed that such hydrazone moieties are stable under reducing conditions suggesting they can be effectively used in direct NP synthesis methods (see Sections **1.2.1.3** and **2.3.3**).[45,46] Once this new class of hydrazone-functionalised AuNPs becomes available, it will be possible not only to attempt the preparation of aggregates with complementary NPs (Figure **4.15**) but also to widen the knowledge on the hydrazone exchange performed within the NP-bound monolayer. In fact, such ligand-functionalised AuNPs would undergo hydrazone exchange with small hydrazide exchange units, allowing the study of the exchange mechanism not only in acidic conditions but also at neutral pH by using nucleophilic catalysts (see Section **1.5.1**).[117–123]

General conclusion

This Thesis reports, for the first time, investigations on the dynamic covalent reactivity of organic ligands immobilised as a monolayer adsorbed on the surface of gold nanoparticles (AuNPs).

Two classes of ligands have been prepared for NP functionalisation: *N*-acyl and *N*-aroyl hydrazones. The choice of the strategy for NP functionalisation (i.e. ligand exchange or direct synthesis) is strictly connected to the relative stability of the hydrazone moiety under the NP synthetic conditions. *N*-Acyl hydrazone ligands were adsorbed on pre-synthetized AuNPs stabilised with a weakly bound temporary ligand. On the other hand, a synthetic method has been developed and optimised for the preparation of *N*-aroyl hydrazone-functionalised AuNPs with reproducible size and dispersity by direct synthesis. In addition, the direct synthesis approach, compared to ligand exchange, provided undoubtedly advantages in terms of NP purification from by-products.

A range of analytical techniques, including ^{1}H and ^{19}F nuclear magnetic resonance (NMR) spectroscopy, transmission electron microscopy (TEM) and laser desorption mass spectrometry, has been employed to confirm that *N*-aroyl hydrazone-functionalised AuNPs can be prepared with a high degree of purity from any unbound species with reproducible size and low dispersity. This is an essential requirement in order to establish full characterisation of the NP-bound molecular structure, in a similar manner to molecular systems, and to assess that the integrity of the hydrazone ligand is preserved during the NP synthesis. Further investigations by TEM revealed that the mean size of functionalised AuNPs prepared by direct synthesis is affected by the nature of the ligand and even subtle changes in the ligand structure can result in non-negligible variations of the NP size distribution.

Using *N*-aroyl hydrazone-functionalized AuNPs, dynamic covalent exchange of the surface-bound hydrazones has been demonstrated and characterised. The exchange has been achieved by employing small aldehydes as exchange species under mild acid-catalysed conditions. This novel strategy for the manipulation of ligand-functionalised NPs uniquely combines the reversibility of a thermodynamically controlled process with the stability of covalent bonds. A variety of analytical techniques confirmed that the exchange involves transformation of the NP-bound monolayer while the integrity of the metal core is preserved. By employing ^{19}F NMR spectroscopy, the reactivity of the NP-bound hydrazone has been quantitatively probed

and the variations in the concentration of the NP-bound and unbound species involved in the hydrolysis and exchange processes were tracked in real time. This allowed the kinetic study of the monolayer reactivity which could be fitted to simple models for hydrazone hydrolysis and exchange. A comparison with structurally similar molecular compounds under analogous conditions revealed slower kinetics when hydrazone molecules are immobilised in a monolayer for both hydrazone hydrolysis and exchange. Further investigations confirmed that the optimised dynamic exchange approach is simple to perform and is more efficient than analogous strategies involving manipulations of the NP-bound monolayer based on ligand exchange.

The investigation on the reactivity of the hydrazone monolayer can be extended in the future to explore the occurrence of the dynamic exchange under neutral conditions (i.e. by means of a nucleophilic catalyst). In addition, the investigation protocols developed in this Thesis can be opportunely modified in order to study the reactivity of other dynamic bonds (e.g. boronic esters and acetals) when incorporated in a NP-bound monolayer and, potentially, further extended to other types of functionalised NPs.

By reversible modification of the functionality of NP-bound small molecules, DCC could become a powerful strategy for tuning those NP properties that are dependent on the way in which the NP-bound monolayer interacts with the surrounding environment. Early stage qualitative studies involved the colloidal stability of *N*-aroyl hydrazone-functionalised AuNPs in several solvents. By choosing an appropriate aldehyde as exchange unit, it has been demonstrated that the solvophilicity of the monolayer, and hence of the functionalised NPs, can be modified as the result of dynamic hydrazone exchange under mild conditions. The exchange process was confirmed to be reversible and NP solubility switching could be successfully achieved between three distinct states where hydrazone-functionalised NPs are indefinitely stable over time. More subtle changes in NP colloidal behaviour on dynamic covalent exchange were also observed, such as the formation of colloidally stable solvent-sensitive aggregates, which were detected by dynamic light scattering analysis.

Further investigations revealed that hydrazone exchange can be used to provide NPs functionalised with a mixed monolayer, which results in intermediate solubility properties between the extremes produced by homogeneous monolayers of the two components. The ideal goal would be the possibility to predict the NP solubility properties depending on the composition of the NP-bound monolayer. This dynamic, reversible approach could be a promising strategy in order to develop powerful and scalable methods for controlling a variety of NP properties that are governed by the surface monolayer molecular structure. Investigations to establish the precise

relationship between the monolayer composition and the NP solubility properties are currently in progress.

Finally, it has been shown that dynamic hydrazone exchange is a very promising candidate for achieving NP assemblies under thermodynamic control. Preliminary investigations revealed that hydrazone-functionalised NPs aggregate over time to form 'dendritic-like' structures in the presence of a bifunctional aldehyde linker under acidic conditions. Control experiments suggest that these structures are the result of hydrazone exchange between the ligand-functionalised NPs and the linker. However, further investigations are certainly required in order to achieve NP assemblies in a controlled and predictable fashion. Yet, understanding the factors governing these assemblies in order to potentially exhibit reversibility and adaptability are intriguing challenges to be addressed.

Performing dynamic covalent chemistry within the NP-bound monolayer and, moreover, monitoring in real-time the monolayer reactivity is indeed a promising new strategy which can, potentially, start to fill the gap for a detailed comprehension of the processes occurring at the nanoscale. However, such an approach is still challenging and further investigations are certainly required in order to achieve full understanding and, potentially, predict the reactivity of a NP-bound monolayer. In addition, early stage studies on the post-synthetic modification of NP properties and self-assembly could provide, in the future, new tools for the development of bottom-up synthetic strategies for the preparation of an entire new class of nanomaterials which can potentially have countless applications in many fields including optics, electronics, catalysis and medicine.

Chapter 5:
Experimental and synthetic procedures

5.1 General experimental procedures

Unless stated otherwise, all reagents were purchased from commercial sources and used without further purification. Dry solvents were obtained by means of a MBBRAUN MB SPS-800[TM]. Column chromatography was carried out using Geduran® Si60 (40-63 μm, Merck, Germany) as the stationary phase, and thin-layer chromatography (TLC) was performed on pre-coated silica gel plates (0.25 mm thick, 60F$_{254}$, Merck, Germany) and observed under UV light. AuNP micrographs were obtained using a JEM 2010 TEM on samples prepared by deposition of one drop of nanoparticle suspension on Holey Carbon Films on 300 mesh Cu grids (Agar Scientific®). Scanning tunnelling microscopy analysis was performed by Mr Ross Blackley. UV-Vis spectroscopy was performed using a Thermo Scientific Evolution Array UV-Visible Spectrophotometer. ^{1}H, ^{13}C, ^{19}F and ^{31}P NMR spectra were recorded on Bruker AV 300, 400 and 500 instruments, at a constant temperature of 25 °C. ^{1}H and ^{13}C chemical shifts are reported in parts per million (ppm) from high to low field and referenced to the literature values for chemical shifts of residual non-deuterated solvent, with respect to tetramethylsilane.[237] ^{19}F NMR chemical shifts are referenced with respect to CFCl$_3$ (0.00 ppm) using an internal standard as reported. ^{31}P NMR chemical shifts are referenced to PPh$_3$ (–6.00 ppm) as external standard. Standard abbreviations indicating multiplicity are used as follows: bs (broad singlet), d (doublet), dd (doublet of doublets), m (multiplet), q (quartet), s (singlet), t (triplet), J (coupling constant). Quantitative NMR experiments were run with a pulse delay time $\geq 5 \times T_1$ for the slowest relaxing signal to be observed. Relaxation times for all quantified species are listed in Section **5.6.1**. All melting points were determined using a Stuart SMP30 Melting Point Apparatus.

Laser desorption ionization mass spectrometry (LDI-MS) was performed by applying a NP solution (0.5 μL) to a MALDI target followed by air drying. The spectrum was then acquired using a 4800 MALDI TOF/TOF Analyser (ABSciex, Foster City, CA) equipped with a Nd:YAG 355 nm laser and calibrated using a mixture of peptides. Samples were

analysed in positive and negative MS mode over the appropriate *m/z* range, by averaging 1000 laser spots. On-NP LDI-MS measurements were performed by Dr Catherine Botting and Dr Sally Shirran. DLS measurements were performed on a Malvern Zetasizer μV instrument. As a first approximation, viscosity, refractive index and dielectric constant values for binary mixtures were calculated according to equations reported in the literature.[238–240]

5.2 Synthesis of organic compounds

Methyl 11-mercaptoundecanoate (1)[141]
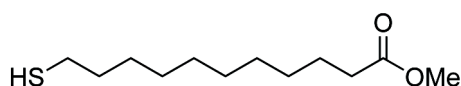
11-Mercaptoundecanoic acid (5.01 g, 22.9 mmol) was dissolved in MeOH (100 mL) and concentrated H_2SO_4 (5 mL) was added. The reaction mixture was refluxed for 3 h and monitored by TLC. The solvent was then removed under reduced pressure, H_2O (50 mL) was added and the aqueous layer was extracted with CH_2Cl_2 (3 × 50 mL). The combined organic layers were dried over $MgSO_4$ and the solvent was evaporated under reduced pressure to afford ester **1** (5.38 g, 99%) as a yellow oil.

^{1}H NMR (400.1 MHz, $CDCl_3$): δ 1.21–1.41 (m, 12H, 6 × CH_2), 1.30–1.34 (t, *J* = 7.5 Hz, 1H, SH), 1.55–1.65 (m, 4H, 2 × CH_2), 2.25–2.32 (t, *J* = 8.0 Hz, 2H, CH_2CO), 2.47–2.55 (q, *J* = 7.5 Hz, 2H, CH_2S), 3.70 (s, 3H, OMe) ppm.

^{13}C NMR (125.8 MHz, $CDCl_3$): δ 25.4, 25.7, 29.1, 29.8, 29.9, 30.0, 30.1, 30.2, 34.8, 34.9, 52.2, 175.1 ppm.

Methyl 11-mercaptoundecanoate hydrazide (2)[142]
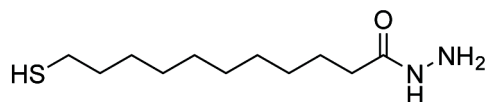
Hydrazine monohydrate (10.6 mL, 219 mmol) and methyl ester **1** (5.09 g, 21.9 mmol) were dissolved in MeOH (50 mL). The reaction mixture was refluxed for 3 h. The solvent was then removed under reduced pressure, the crude product was dissolved in H_2O (50 mL) and extracted with CH_2Cl_2 (4 × 30 mL). The combined organic layers were then washed with saturated aqueous NH_4Cl solution, dried with $MgSO_4$, filtered and

concentrated at reduced pressure to afford hydrazide **2** (4.06 g, 80%) as white solid. Mp: 94–95 °C.

^{1}H NMR (400.1 MHz, CDCl$_3$): δ 1.22–1.41 (m, 12H, 6 × CH$_2$), 1.30–1.34 (t, J = 7.6 Hz, 1H, SH), 1.54–1.68 (m, 4H, 2 × CH$_2$), 2.10–2.17 (t, J = 7.6 Hz, 2H, CH$_2$CO), 2.47–2.55 (q, J = 7.2 Hz, 2H, CH$_2$S), 3.92 (bs, 2H, NH$_2$), 6.82 (bs, 1H, NH) ppm.

^{13}C NMR (125.8 MHz, CDCl$_3$): δ 24.8, 25.6, 28.5, 29.2, 29.4, 29.5, 29.6, 34.2, 34.7, 39.4, 174.1 ppm.

1-(4-Formylphenyl)-*N,N,N*-trimethylmethanammonium iodide (3)[144]
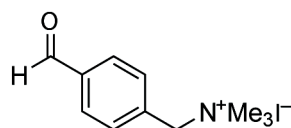
Compound **10** (984 mg, 2.82 mmol) was dissolved in a mixture CH$_3$CO$_2$H/H$_2$O 1:1 (20 mL) and stirred for 23 h at rt. After solvent removal under reduced pressure, aldehyde **3** (736 mg, 85%) was obtained pure after crystallisation from EtOH/Et$_2$O 1:1 with HexH as pale yellow solid. Mp: 208–212 °C (lit[144]: 205–206 °C).

^{1}H NMR (500.1 MHz, [D$_6$]DMSO): δ 3.07 (s, 9H, 3 × CH$_3$), 4.66 (s, 2H, CH$_2$N), 7.74–7.83 (d, J = 8.0 Hz, 2H, H$_{Ar}$), 8.02–8.08 (d, J = 8.0 Hz, 2H, H$_{Ar}$), 10.11 (s, 1H, CHO) ppm.

^{13}C NMR (499.9 MHz, [D$_6$]DMSO): δ 52.0, 66.7, 129.8, 133.7, 134.4, 137.1, 139.0 ppm.

HRMS (ES$^+$) *m/z* calculated for C$_{11}$H$_{16}$NO [M–I]$^+$ 178.1226, found 178.1224.

N'-(4-Fluorobenzylidene)-11-mercaptoundecanehydrazide (4H)
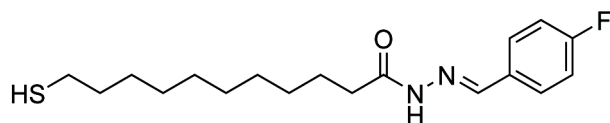
Hydrazide **2** (2.00 g, 8.61 mmol) was dissolved in EtOH (60 mL) to which CH$_3$CO$_2$H (50 µL, 0.86 mmol) was added. Then, 4-fluorobenzaldehyde (0.92 mL, 8.61 mmol) was added and the reaction mixture was stirred for 17 h at rt. The white suspension was filtered, washed with Et$_2$O and dried under vacuum to afford hydrazone **4**H (2.83 g, 97%) as white solid. Mp: 90–93 °C.

^{1}H NMR (500.1 MHz, CD$_2$Cl$_2$): δ 1.21–1.51 (m, 12H, 6 × CH$_2$), 1.32–1.35 (t, J = 7.8 Hz, 1H, SH), 1.52–1.60 (m, J = 7.2 Hz, 2H, CH$_2$), 1.64–1.71 (m, J = 7.7 Hz, 2H, CH$_2$),

2.44–2.50 (q, *J* = 7.4 Hz, 2H, CH$_2$S), 2.68–2.74 (t, *J* = 7.6 Hz, 2H, CH$_2$CO), 7.05–7-12 (t, *J* = 8.7 Hz, 2H, H$_{Ar}$), 7.62–7.69 (dd, *J* = 8.7, 5.5 Hz, 2H, H$_{Ar}$), 7.74 (s, 1H, CH=), 9.43 (bs, 1H, NH) ppm.

^{13}C NMR (100.6 MHz, CD$_2$Cl$_2$): δ 24.9, 25.2, 25.8, 28.8, 29.5, 29.77, 29.86, 29.89, 33.0, 34.5, 116.0–116.3 (d, *J* = 22 Hz), 129.2–129.3 (d, *J* = 8.6 Hz), 130.89–130.93 (d, *J* = 3.0 Hz), 142.2, 162.8–165.3 (d, *J* = 249 Hz), 176.6 ppm.

^{19}F NMR (470.5 MHz, CD$_2$Cl$_2$): δ −111.14 ppm (s, 1F).

HRMS (ES$^+$) *m/z* calculated for C$_{18}$H$_{27}$FN$_2$NaOS [M+Na]$^+$ 361.1726, found 361.1712.

11,11'-Disulfanediylbis(*N'*-(4-fluorobenzylidene)undecanehydrazide) (4$_2$)
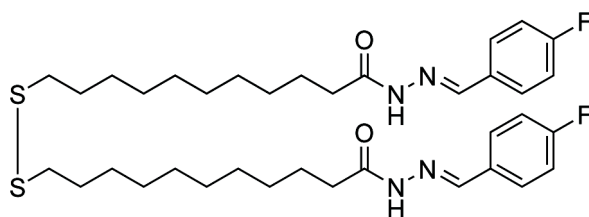
Iodine (149 mg, 0.59 mmol) was added to a solution of hydrazone **4**H (99.1 mg, 0.29 mmol) in CH$_2$Cl$_2$ (10 mL). The mixture was stirred at rt for 30 min. Then, the solution was decoloured with sodium sulfite saturated solution and diluted with brine. The organic phase was separated and the aqueous phase was further extracted with CH$_2$Cl$_2$ (2 × 20 mL). The combined organic layers were dried over magnesium sulfate and evaporated under reduced pressure to afford disulfide **4**$_2$ as a clean product (73.4 mg, 75%). Mp: 118–119 °C.

^{1}H NMR (500.1 MHz, CDCl$_3$ + 2 drops of CD$_3$OD): δ 1.11–1.37 (m, 32H, 16 × CH$_2$), 2.55–2.62 (t, *J* = 7.5 Hz, 4H, 2 × CH$_2$S), 2.63–2.69 (t, *J* = 7.5 Hz, 4H, 2 × CH$_2$CO), 6.91–7.07 (m, 4H, H$_{Ar}$), 7.53–7.67 (m, 4H, H$_{Ar}$), 7.76 (s, 2H, 2 × CH=), 10.08 (bs, 2H, 2 × NH) ppm.

^{13}C NMR (125.8 MHz, CDCl$_3$ + 2 drops of CD$_3$OD): δ 24.8, 25.7, 28.5, 29.2, 29.3, 29.40, 29.43, 32.6, 34.9, 39.1, 115.7–115.9 (d, *J* = 22 Hz), 128.8–128.9 (d, *J* = 8.5 Hz), 130.25–130.28 (d, *J* = 3.3 Hz), 142.9, 162.8–164.8 (d, *J* = 251 Hz), 176.9.

^{19}F NMR (470.5 MHz, CDCl$_3$ + 2 drops of CD$_3$OD): δ −110.52 (s, 1F) ppm.

HRMS (ES$^+$) *m/z* calculated for C$_{36}$H$_{53}$F$_2$N$_4$O$_2$S$_2$ [M+H]$^+$ 675.3573, found 675.3571.

11-Mercapto-*N'*-(4-methoxybenzylidene)undecanehydrazide (5H)
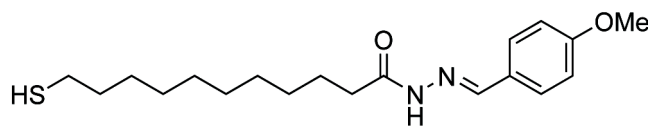
Hydrazide **2** (306 mg, 1.32 mmol) was dissolved in EtOH (30 mL) to which CH_3CO_2H (7.5 μL, 0.13 mmol) was added. Then, *p*-anisaldehyde (0.16 mL, 1.32 mmol) was added and the reaction mixture was stirred for 3 h at rt. The solvent was removed under reduced pressure, H_2O was added (30 mL) followed by extraction with CH_2Cl_2 (3 × 25 mL). The combined organic layers were dried over $MgSO_4$, filtered and evaporated under vacuum and the crude product was purified by chromatography (SiO$_2$, *c*-Hex/EtOAc 4:1) to afford hydrazone **5**H as pale yellow solid (415 mg, 89%). Mp: 100–104 °C.

^{1}H NMR (400.1 MHz, CDCl$_3$): δ 1.21–1.46 (m, 12 H, 6 × CH$_2$), 1.29–1.35 (t, *J* = 7.7 Hz, 1H, SH), 1.54–1.63 (m, *J* = 7.2 Hz, 2H, CH$_2$), 1.68–1.77 (m, *J* = 7.7 Hz, 2H, CH$_2$), 2.46–2.54 (q, *J* = 7.5 Hz, 2H, C*H*$_2$SH), 2.71–2.79 (t, *J* = 7.5 Hz, 2H, C*H*$_2$CO), 3.84 (s, 3H, OMe), 6.89–6.94 (d, *J* = 8.8 Hz, 2H, H$_{Ar}$), 7.57–7.63 (d, *J* = 8.8 Hz, 2H, H$_{Ar}$), 7.76 (s, 1H, CH), 9.91 (bs, 1H, NH) ppm.

^{13}C NMR (75.5 MHz, CDCl$_3$): δ 24.8, 24.9, 26.0, 28.8, 29.5, 29.7, 29.84, 29.88, 33.0, 34.5, 55.8, 114.6, 127.2, 176.5, 128.9, 129.4, 143.6 ppm.

HRMS (ES$^+$) *m/z* calculated for C$_{19}$H$_{30}$N$_2$NaO$_2$S [M+Na]$^+$ 373.1926, found 373.1909.

***N'*-Benzylidene-11-mercaptoundecanehydrazide (6H)**
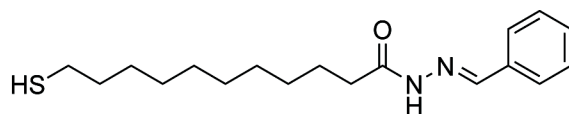
Hydrazide **2** (300 mg, 1.29 mmol) was dissolved in EtOH (30 mL) to which CH_3CO_2H (7.4 μL, 0.1 Eq) was added. Then, benzaldehyde (131 μL, 1.29 mmol) was added and the reaction mixture was stirred for 3 h at rt. The solvent was removed under reduced pressure, H_2O (25 mL) was added to the crude product followed by extraction with CH_2Cl_2 (3 × 25 mL). The combined organic layers were dried over $MgSO_4$, filtered and evaporated under reduced pressure to afford hydrazone **6**H (386 mg, 93%) as white solid. Mp: 65–69 °C.

^{1}H NMR (400.1 MHz, CD$_2$Cl$_2$): δ 1.21–1.44 (m, 12H, 6 × CH$_2$), 1.31–1.35 (t, *J* = 7.6 Hz, 1H, SH), 1.51–1.61 (m, 2H, CH$_2$), 1.64–1.75 (m, 2H, CH$_2$), 2.43–2.52 (q, *J* = 7.2 Hz,

2H, CH_2S), 2.69–2.76 (t, *J* = 7.6 Hz, 2H, CH_2CO), 7.33–7.43 (m, 3H, H$_{Ar}$), 7.62–7.70 (m, 2H, H$_{Ar}$), 7.80 (s, 1H, CH=), 9.79 (bs, 1H, NH) ppm.

^{13}C NMR (75.5 MHz, CD$_2$Cl$_2$): δ 25.0, 25.2, 28.8, 29.5, 29.8, 29.9, 30.0, 30.3, 33.1, 34.5, 127.4, 129.1, 130.3, 134.6, 143.4, 176.5 ppm.

HRMS (ES$^+$) *m/z* calculated for C$_{18}$H$_{28}$N$_2$NaOS [M+Na]$^+$ 343.1820, found 343.1805.

1-(4-((2-(11-Mercaptoundecanoyl)hydrazono)methyl)phenyl)-*N,N,N*-trimethylmethanammonium iodide (7H)
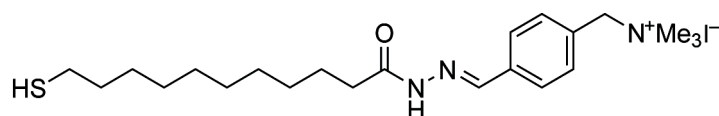
Aldehyde **3** (500 mg, 1.64 mmol) was dissolved in MeOH (10 mL) to which CH$_3$CO$_2$H (10 μL, 0.16 mmol) was added. Then, a solution of hydrazide **2** (381 mg, 1.64 mmol) in MeOH (10 mL) was added to the reaction mixture and it was stirred for 17 h at rt. The solvent was then removed under reduced pressure and hydrazone **7**H (815 mg, 96%) was obtained after crystallisation from Et$_2$O/EtOH 1:1 with HexH as white solid. Mp: 158–162 °C.

^{1}H NMR (400.1 MHz, [D$_6$]DMSO): δ 1.16–1.29 (m, 13H, 6 × CH$_2$ + SH), 1.42–1.64 (m, 4H, 2 × CH$_2$), 2.38–2.48 (m, 2H, CH$_2$S), 2.58–2.65 (m, 2H, CH$_2$CO), 3.05 (s, 9H, 3 × CH$_3$), 4.57 (s, 2H, CH$_2$N), 7.54–7.65 (m, 2H, H$_{Ar}$), 7.72–7.81 (m, 2H, H$_{Ar}$), 8.02 (s, 1H, CH=), 11.32 (bs, 1H, NH) ppm.

^{13}C NMR (75.5 MHz, [D$_6$]DMSO): δ 23.7, 24.2, 24.9, 27.7, 28.5, 28.7, 28.8, 28.9, 31.8, 33.4, 51.8, 67.3, 126.9, 129.3, 133.2, 136.1, 141.2, 168.8 ppm.

HRMS (ES$^+$) *m/z* calculated for C$_{22}$H$_{38}$N$_3$OS [M–I]$^+$ 392.2730, found 392.2718.

4-(1,3-Dioxolan-2-yl)benzonitrile (8)[143]
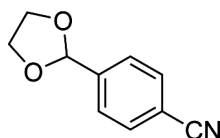
To a solution of 4-cyanobenzaldehyde (2.28 g, 17.4 mmol) in dry toluene (20 mL), ethylene glycol (3.87 mL, 69.5 mmol) and *p*-toluenesulfonic acid (1.65 mg, 0.01 mmol) were added. The mixture was refluxed for 5 h and H$_2$O was removed by Dean-Stark apparatus. The solution was then cooled at rt and 5% NaHCO$_3$ solution (10 mL) was added. An extraction with CH$_2$Cl$_2$ (3 × 20 mL) followed. The combined organic layers

were then washed with H_2O (2 × 20 mL), dried over $MgSO_4$ and evaporated under reduced pressure. Pure colourless hygroscopic compound **8** (1.63 g, 53%) was crystallised from the residual oil in $HexH/Et_2O$ 6:4. Mp: 45–46 °C (lit[143]: 40 °C).

^{1}H NMR (400.1 MHz, $CDCl_3$): δ 4.03–4.14 (m, 4H, 2 × CH_2), 5.85 (s, 1H, CH), 7.57–7.61 (d, J = 8.0 Hz, 2H, H_{Ar}), 7.66–7.70 (d, J = 8.4 Hz, 2H, H_{Ar}) ppm.

(4-(1,3-Dioxolan-2-yl)phenyl)methanamine (9)[143]
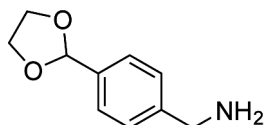
To a solution of $LiAlH_4$ (490 mg, 12.9 mmol) in dry Et_2O (15 mL), a solution of compound **8** (1.13 g, 6.46 mmol) was added dropwise at 0 °C. The mixture was stirred for 1 h and then gently warmed to rt and stirred for further 18 h. The reaction was then quenched with EtOH (1 mL) and a mixture $EtOH/H_2O$ 1:1 (1 mL). After 30 min stirring, it was filtered over $MgSO_4$ and the resulting filtrate was washed with diethyl ether. The organic solvent was removed under vacuum to afford **9** (989 mg, 85%) as yellow oil.

^{1}H NMR (400.1 MHz, $CDCl_3$): δ 2.69 (bs, 2H, NH_2), 3.83 (s, 2H, CH_2N), 3,94–4.14 (m, 4H, 2 x CH_2O), 5.77 (s, 1H, CH), 7.28–7.32 (d, J = 8.1 Hz, 2H, H_{Ar}), 7.41–7.44 (d, J = 8.2 Hz, 2H, H_{Ar}) ppm.

1-(4-(1,3-Dioxolan-2-yl)phenyl)-*N,N,N*-trimethylmethanammonium iodide (10)[144]
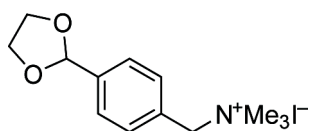
A solution of compound **9** (1.58 g, 8.84 mmol) and Bu_3N (4.21 mL, 17.7 mmol) in DMF (11 mL) was cooled at 0 °C, and MeI (2.75 mL, 44.2 mmol) was added dropwise. The solution was warmed to rt and stirred for further 20 h. EtOAc (100 mL) was then added to the mixture and the so obtained precipitate was filtered and washed with Et_2O to afford compound **10** (1.96 g, 63%) as pale yellow solid. Mp: 197–200 °C (lit:[144] 196–198 °C).

^{1}H NMR (400.1 MHz, $[D_6]DMSO$): δ 3.04 (s, 9H, 3 × CH_3), 3.91–4.11 (m, 4H, 2 × CH_2O), 4.57 (s, 2H, CH_2N), 5.79 (s, 1H, CH), 7.57 (m, 4H, H_{Ar}) ppm.

11-(Tritylthio)undecan-1-ol (11)[186]
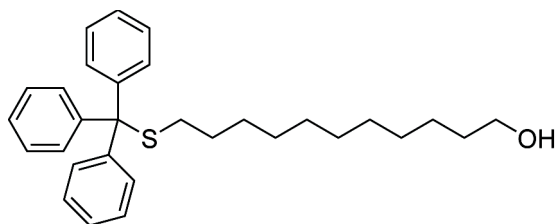
A solution of NaOH (1.12 g, 28.1 mmol) in H_2O (10 mL) was added to a solution of triphenylmethanethiol (5.51 g, 19.9 mmol) in 1:1 EtOH/toluene (50 mL). Then, a solution of 11-bromoundecan-1-ol (5.01 g, 20.0 mmol) in 1:1 EtOH/toluene (50 mL) was added and the reaction mixture was stirred at rt for 3.5 h. The mixture was poured into a saturated solution of $NaHCO_3$ (25 mL) and extracted with Et_2O (3 × 20 mL). The combined organic layers were washed with brine (2 × 20 mL), dried over $MgSO_4$ and evaporated under reduced pressure. The crude product was purified by flash chromatography (SiO_2, HexH/EtOAc 8:1 to 1:1) to afford alcohol **11** as pale yellow oil (8.28 g, 93%, spectral data in agreement with the literature[186]).

^1H NMR (500.1 MHz, $CDCl_3$): δ 1.08–1.49 (m, 16H, 8 × CH_2), 1.52–1.59 (m, 2H, CH_2), 2.10–2.16 (t, J = 6.9 Hz, 2H, CH_2S), 3.61–3.66 (t, J = 7.0 Hz, 2H, CH_2O), 7.18–7.23 (m, 3H, H_{Ar}), 7.25–7.30 (m, 6H, H_{Ar}), 7.39–7.43 (m, 6H, H_{Ar}) ppm.

^{13}C NMR (125.8 MHz, $CDCl_3$): δ 25.8, 28.3, 28.7, 29.1, 29.3, 29.5, 29.6, 29.7, 32.1, 32.9, 34.2, 63.1, 126.6, 127.9, 129.7, 145.2 ppm.

11-(Tritylthio)undecyl methanesulfonate (12)[186]
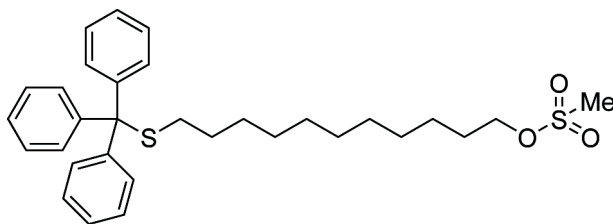
A solution of alcohol **11** (5.16 g, 11.5 mmol) and Et_3N (2.41 mL, 17.3 mmol) in CH_2Cl_2 (30 mL) was cooled at 0 °C. Methanesulfonyl chloride (1.79 mL, 23.1 mmol) in CH_2Cl_2 (15 mL) was then added dropwise. The solution was stirred for 30 min at 0 °C and then warmed to rt and stirred for a further 4 h. The solvent was then removed under reduced pressure and the crude oil was re-dissolved in CH_2Cl_2 (50 mL) and washed with 0.1 M HCl (2 × 50 mL), saturated $NaHCO_3$ solution (2 × 50 mL) and brine (100 mL). The organic phase was dried over $MgSO_4$ and evaporated under vacuum to afford

compound **12** as yellow oil (5.94 g, 98%, spectral data in agreement with the literature[186]).

¹H NMR (400.1 MHz, CDCl₃): δ 1.09–1.33 (m, 14H, 7 × CH₂), 1.34–1.45 (m, 2H, CH₂), 1.70–1.78 (m, 2H, CH₂), 2.09–2.16 (t, *J* = 7.3 Hz, 2H, CH₂S), 3.00 (s, 3H, CH₃), 4.18–4.24 (t, *J* = 6.6 Hz, 2H, CH₂O), 7.18–7.23 (m, 3H, H_Ar), 7.25–7.31 (m, 6H, H_Ar), 7.39–7.43 (m, 6H, H_Ar) ppm.

¹³C NMR (75.5 MHz, CDCl₃): δ 25.5, 28.7, 29.1, 29.2, 29.3, 29.5, 29.5, 32.1, 32.9, 34.2, 37.5, 66.5, 70.3, 126.6, 127.9, 129.7, 145.2 ppm.

1,1,1-Triphenyl-14,17,20,23-tetraoxa-2-thiapentacosan-25-ol (13)[186]
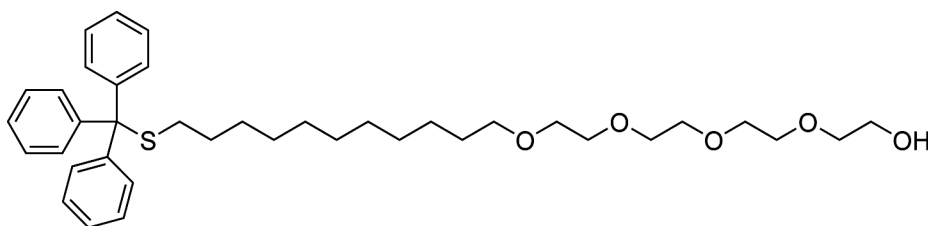
A solution of NaOH (1.75 g, 43.8 mmol) in H₂O (2 mL) was mixed with tetraethylene glycol (84 mL) and heated to 90 °C for 1 h. Then, compound **12** (15.3 g, 29.2 mmol) was added to the mixture and stirred at 90 °C for 23 h. The reaction mixture was then cooled to rt, poured into H₂O (200 mL) and extracted with EtOAc (2 × 200 mL). The organic phase was washed with a saturated NaHCO₃ solution (3 × 100 mL) and brine (3 × 100 mL), dried over MgSO₄ and evaporated under reduced pressure to afford alcohol **13** as yellow oil (14.0 g, 77%, spectral data in agreement with the literature[186]).

¹H NMR (400.1 MHz, CDCl₃): δ 1.06–1.42 (m, 16H, 8 × CH₂), 1.51–1.60 (m, 2H, CH₂), 2.08–2.16 (t, *J* = 6.9 Hz, 2H, CH₂S), 3.39–3.46 (t, *J* = 6.8 Hz, 2H, CH₂O), 3.48–3.68 (m, 16H, 8 × CH₂O), 7.15–7.20 (m, 3H, H_Ar), 7.22–7.31 (m, 6H, H_Ar), 7.36–7.43 (m, 6H, H_Ar) ppm.

¹³C NMR (75.5 MHz, CDCl₃): δ 28.7, 29.15, 29.28, 29.32, 29.48, 29.54, 29.61, 29.63, 29.69, 29.73, 32.2, 45.3, 61.9, 66.5, 70.2, 70.5, 70.7, 70.8, 71.7, 72.7, 126.6, 127.9, 129.7, 145.2 ppm.

1,1,1-Triphenyl-14,17,20,23-tetraoxa-2-thiapentacosan-25-yl methanesulfonate (14)[186]
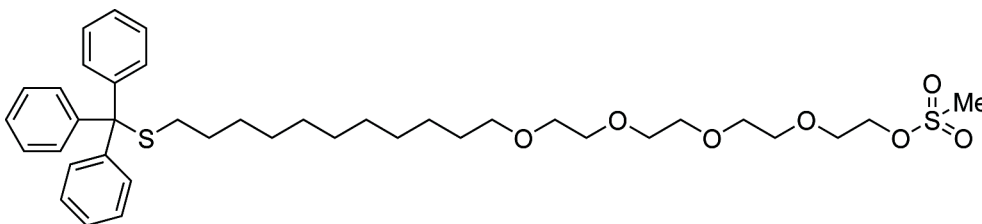
Under an atmosphere of Ar, alcohol **13** (4.09 g, 6.57 mmol) was dissolved in dry CH_2Cl_2 (60 mL) and Et_3N (2.75 mL, 19.7 mmol) was added. The reaction mixture was cooled to 0 °C and methanesulfonyl chloride (0.76 mL, 9.85 mmol) was added and the mixture stirred at 0 °C for a further 10 min and then allowed to warm to rt and stir for 4 h. The reaction was quenched with 0.1 M HCl (2 × 50 mL) and the organic layer was washed with saturated $NaHCO_3$ solution (2 × 50 mL) and brine (2 × 50 mL), dried over $MgSO_4$ and evaporated under reduced pressure. The crude product was purified by chromatography (SiO$_2$, HexH/EtOAc 1:2) to afford **14** as a yellow oil (3.47 g, 75%, spectral data in agreement with the literature[186]).

^{1}H NMR (500.1 MHz, CDCl$_3$): δ 1.06–1.44 (m, 16H, 8 × CH$_2$), 1.51–1.60 (m, 2H, CH$_2$), 2.08–2.15 (t, *J* = 8.1 Hz, 2H, CH$_2$S), 3.06 (s, 3H, CH$_3$), 3.40–3.46 (t, *J* = 6.7 Hz, 2H, CH$_2$O), 3.49–3.68 (m, 12H, 6 × CH$_2$O), 3.73–3.72 (m, 2H, CH$_2$O), 4.34–4.39 (m, 2H, CH$_2$O), 7.16–7.22 (m, 3H, H$_{Ar}$), 7.23–7.31 (m, 6H, H$_{Ar}$), 7.37–7.43 (m, 6H, H$_{Ar}$) ppm.

^{13}C NMR (125.7 MHz, CDCl$_3$): δ 26.2, 27.0, 28.7, 29.0, 29.2, 29.3, 29.5, 29.6, 29.7, 29.8, 32.2, 37.9, 45.3, 69.2, 69.4, 70.2, 70.3, 70.65, 70.72, 70.77, 71.7, 126.6, 127.9, 129.7, 145.2 ppm.

N'-(4-Fluorobenzylidene)-4-hydroxybenzohydrazide (17)
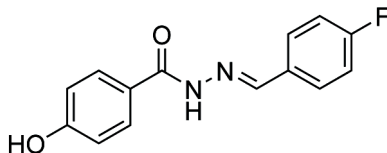
To a solution of 4-hydroxybenzhydrazide (1.25 g, 8.24 mmol) in MeOH (150 mL), CH_3CO_2H (10 mL) and 4-fluorobenzaldehyde (0.88 mL, 8.24 mmol) were added. The reaction mixture was stirred for 19 h at rt, monitored by TLC. The mixture was then evaporated under reduced pressure obtaining a white solid which was re-dissolved in

hot EtOH and precipitated with cold water, affording clean hydrazone **17** as a white solid (2.02 g, 95%). Mp: 247–248 °C.

^{1}H NMR (500.1 MHz, [D$_6$]DMSO): δ 6.80–6.93 (d, *J* = 8.5 Hz, 2H, H$_{Ar}$), 7.21–7.36 (t, *J* = 8.7 Hz, 2H, H$_{Ar}$), 7.69–7.88 (m, 4H, H$_{Ar}$), 8.43 (s, 1H, CH=), 10.14 (bs, 1H, OH), 11.67 (bs, 1H, NH) ppm.

^{13}C NMR (75.5 MHz, [D$_6$]DMSO): δ 115.0, 115.7–116.0 (d, *J* = 22 Hz), 123.8, 129.0–129.1 (d, *J* = 8.6 Hz), 129.7, 131.13–131.17 (d, *J* = 2.8 Hz), 145.7, 160.7, 161.3–164.6 (d, *J* = 248 Hz), 162.8 ppm.

^{19}F NMR (470.5 MHz, [D$_6$]DMSO): δ −110.45 (s, 1F) ppm.

HRMS (ES$^-$) *m/z* calculated for C$_{14}$H$_{10}$FN$_2$O$_2$ [M−H]$^-$ 257.0732, found 257.0733.

4-Hydroxy-*N'*-(4-(trifluoromethyl)benzylidene)benzohydrazide (18)
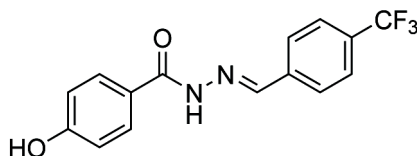
4-(Trifluoromethyl)benzaldehyde (2.7 mL, 19.7 mmol) was added to a solution of 4-hydroxybenzhydrazide (1.50 g, 9.84 mmol) in 6% CH$_3$CO$_2$H in MeOH (70 mL). The reaction was monitored by TLC and the mixture was left stirring at rt for 24 h. The mixture was then evaporated under reduced pressure and white crystals of hydrazone **18** were obtained by recrystallization from hot MeOH/EtOH 1:1 with HexH (2.89 g, 95%). Mp: 266–267 °C.

^{1}H NMR (500.1 MHz, [D$_6$]DMSO): δ 6.81–6.96 (d, *J* = 8.5 Hz, 2H, H$_{Ar}$), 7.72–7.81 (d, *J* = 8.0 Hz, 2H, H$_{Ar}$), 7.82–7.92 (d, *J* = 8.5 Hz, 2H, H$_{Ar}$), 7.93–8.02 (m, 2H, H$_{Ar}$), 8.50 (s, 1H, CH=), 10.18 (bs, 1H, OH), 11.86 (bs, 1H, NH) ppm.

^{13}C NMR (125.7 MHz, [D$_6$]DMSO): δ 115.1, 123.1, 123.6, 125.2, 125.71–125.74 (d, *J* = 3.5 Hz), 127.5, 129.4–129.6 (d, *J* = 32 Hz), 129.8, 138.6, 145.0, 160.9–163.0 (d, *J* = 259 Hz) ppm.

^{19}F NMR (470.3 MHz, [D$_6$]DMSO): δ −60.74 (s, 3F) ppm.

HRMS (ES$^+$) *m/z* calculated for C$_{15}$H$_{11}$F$_3$N$_2$NaO$_2$ [M+Na]$^+$ 331.0670, found 331.0658.

### *N'*-(4-Fluorobenzylidene)-4-((1,1,1-triphenyl-14,17,20,23-tetraoxa-2-thiapentacosan-25-yl)oxy)benzohydrazide (19)
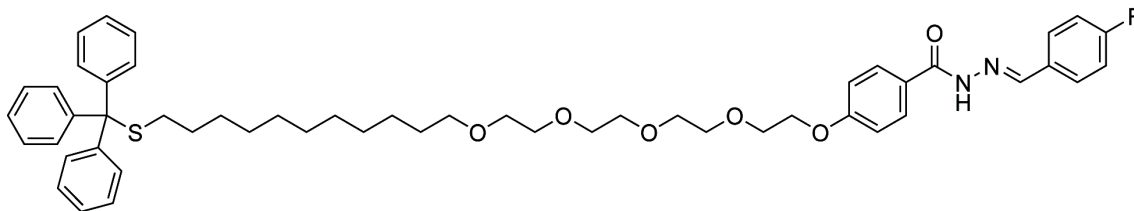
Under an atmosphere of Ar, K_2CO_3 (1.26 g, 9.12 mmol) was added to a solution of hydrazone **17** (785 mg, 3.04 mmol) in dry DMF (25 mL) and stirred for 20 min at rt. Then a solution of alcohol **14** (1.77 g, 2.52 mmol) in dry DMF (25 mL) was added and the reaction mixture was heated at 90 °C for 14 h. The reaction progress was monitored by TLC. The mixture was then allowed to cool to rt before brine (50 mL) was added. The aqueous layer was extracted with CH_2Cl_2 (3 × 100 mL). The combined organic layers were dried over $MgSO_4$, filtered and evaporated under reduced pressure. The crude oil was purified by chromatography (SiO_2, CH_2Cl_2/MeCN 1:1) to afford **19** as a colourless oil (1.13 mg, 52%).

^{1}H NMR (500.1 MHz, CD_2Cl_2): δ 1.05–1.30 (m, 14H, 7 × CH_2), 1.32–1.46 (m, 2H, CH_2), 1.56–1.59 (m, 2H, CH_2), 2.04–2.14 (t, *J* = 8.5 Hz, 2H, CH_2S), 3.33–3.42 (t, *J* = 8.5 Hz, 2H, CH_2O), 3.46–3.71 (m, 12H, 6 × CH_2O), 3.77–3.88 (m, 2H, CH_2O), 4.10–4.22 (m, 2H, CH_2O), 6.88–6.99 (d, *J* = 7.4 Hz, 2H, H_{Ar}), 7.00–7.10 (t, *J* = 8.0 Hz, 2H, H_{Ar}), 7.15–7.21 (m, 3H, H_{Ar}), 7.23–7.29 (m, 6H, H_{Ar}), 7.35–7.41 (m, 6H, H_{Ar}), 7.56–7.76 (m, 2H, H_{Ar}), 7.77–7.94 (m, 2H, H_{Ar}), 8.20 (s, 1H, CH=), 9.34 (bs, 1H, NH) ppm.

^{13}C NMR (100.6 MHz, CD_2Cl_2): δ 26.5, 28.9, 29.4, 29.5, 29.76, 29.85, 29.86, 29.9, 30.1, 32.2, 60.6, 66.6, 68.0, 69.8, 70.4, 70.85, 70.87, 70.91, 71.1, 71.7, 79.5, 114.7, 116.0–116.2 (d, *J* = 22 Hz), 116.6, 125.80, 125.81, 126.8, 128.1, 129.6–129.7 (d, *J* = 8.1 Hz), 129.9, 130.74–130.76 (d, *J* = 2.8 Hz), 145.4, 162.2, 163.0–165.5 (d, J = 250 Hz) ppm.

^{19}F NMR (470.6 MHz, CD_2Cl_2): δ −110.42 (s, 1F) ppm.

HRMS (ES$^+$) *m/z* calculated for $C_{52}H_{63}FN_2NaO_6S$ [M+Na]$^+$ 885.4289, found 885.4278.

N'-(4-(Trifluoromethyl)benzylidene)-4-((1,1,1-triphenyl-14,17,20,23-tetraoxa-2-thiapentacosan-25-yl)oxy)benzohydrazide (20)
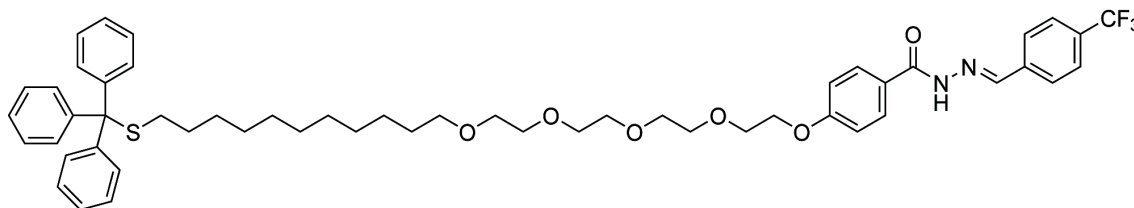
Under an atmosphere of Ar, hydrazone **18** (771 mg, 2.50 mmol), K_2CO_3 (865 mg, 6.26 mmol) and KI (173 mg, 1.04 mmol) were dissolved in dry DMF (20 mL) and stirred for 20 min at rt. Then, a solution of alcohol **14** (1.46 g, 2.09 mmol) in dry DMF (20 mL) was added and the reaction mixture was heated to 90 °C and stirred for 2 days. After cooling to rt, EtOAc (100 mL) was added and the organic phase was washed with water (100 mL), brine (3 × 100 mL), dried over $MgSO_4$, filtered and evaporated under reduced pressure. The crude product was then purified by chromatography (SiO_2, HexH/EtOAc 1:3) to afford **20** as a yellow oil (1.06 g, 55%).

^{1}H NMR (400.1 MHz, CD_2Cl_2): δ 1.07–1.42 (m, 16H, 8 × CH_2), 1.47–1.58 (m, 2H, CH_2), 2.08–2.17 (t, *J* = 7.6 Hz, 2H, CH_2S), 3.34–3.44 (t, *J* = 6.8 Hz, 2H, CH_2O), 3.49–3.73 (m, 12H, 6 × CH_2O), 3.74–3.88 (m, 2H, CH_2O), 4.03–4.14 (m, 2H, CH_2O), 6.83–6.99 (d, *J* = 8.4 Hz, 2H, H_{Ar}), 7.17–7.24 (m, 3H, H_{Ar}), 7.25–7.33 (m, 6H, H_{Ar}), 7.38–7.46 (m, 6H, H_{Ar}), 7.49–7.58 (d, *J* = 8.0 Hz, 2H, H_{Ar}), 7.67–7.76 (d, *J* = 8.0 Hz, 2H, H_{Ar}), 7.89–7.98 (d, *J* = 8.8 Hz, 2H, H_{Ar}), 8.45 (s, 1H, CH=), 10.96 (bs, 1H, NH) ppm.

^{13}C NMR (100.6 MHz, CD_2Cl_2): δ 26.5, 28.9, 29.4, 29.5, 29.79, 29.87, 29.89, 30.0, 30.1, 32.3, 66.7, 68.0, 68.6, 69.8, 70.4, 70.88, 70.92, 71.1, 71.8, 114.6, 120.3, 120.9, 123.0, 125.6, 125.85–125.88 (d, *J* = 3.3 Hz), 126.9, 127.9, 128.2, 129.9, 131.4–131.7 (d, *J* = 32 Hz), 132.5, 138.2, 145.5, 146.8, 162.3–164.5 (d, *J* = 220 Hz) ppm.

^{19}F NMR (376.5 MHz, CD_2Cl_2): δ –63.37 (s, 3F) ppm.

HRMS (ES$^+$) *m/z* calculated for $C_{53}H_{63}F_3N_2NaO_6S$ [M+Na]$^+$ 935.4257, found 935.4235.

4,4′-(3,6,9,12,37,40,43,46-Octaoxa-24,25-dithiaoctatetracontane-1,48-diylbis(oxy))bis(*N′*-(4-fluorobenzylidene)benzohydrazide) (21₂)
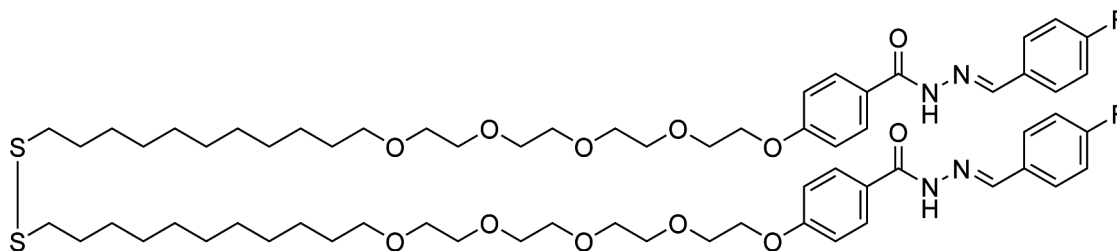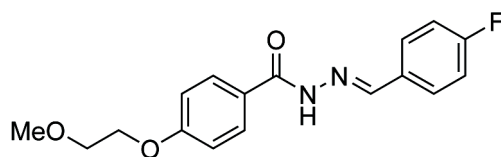

Iodine (162 mg, 0.64 mmol) was added to a solution of compound **19** (275 mg, 0.32 mmol) in MeOH (20 mL). The mixture was stirred at rt for 1 h. Then, the solution was decoloured by addition of a saturated solution of $NaHSO_3$, and extracted with CH_2Cl_2 (3 × 20 mL), dried over $MgSO_4$ and evaporated under reduced pressure. The crude oil was purified by chromatography (SiO_2, CH_2Cl_2/MeOH 20:1) to afford **21₂** as a colourless oil (222 mg, 99%).

^{1}H NMR (500.1 MHz, CD_2Cl_2): δ 1.16–1.40 (m, 28H, 14 × CH_2), 1.45–1.55 (m, 4H, 2 × CH_2), 1.58–1.68 (m, 4H, 2 × CH_2), 2.60–2.70 (t, *J* = 7.5 Hz, 4H, 2 × CH_2S), 3.31–3.41 (t, *J* = 6.5 Hz, 4H, 2 × CH_2O), 3.45–3.68 (m, 24H, 12 × CH_2O), 3.72–3.86 (m, 4H, 2 × CH_2O), 3.98–4.15 (m, 4H, 2 × CH_2O), 6.77–7.02 (m, 8H, H_{Ar}), 7.50–7.58 (dd, *J* = 7.6, 5.5 Hz, 4H, H_{Ar}), 7.86–8.03 (d, *J* = 8.0 Hz, 4H, H_{Ar}), 8.39 (s, 2H, 2 × CH=), 11.01 (bs, 2H, 2 × NH) ppm.

^{13}C NMR (125.8 MHz, CD_2Cl_2): δ 26.5, 28.8, 29.56, 29.57, 29.84, 29.86, 29.90, 29.94, 30.0, 39.5, 67.9, 69.8, 70.4, 70.83, 70.89, 70.90, 71.1, 71.7, 114.6, 115.9–116.1 (d, *J* = 22 Hz), 125.8, 129.58–129.64 (d, *J* = 8.1 Hz), 130.0, 130.94–130.95 (d, *J* = 1.9 Hz), 147.5, 162.1, 163.1–165.1 (d, *J* = 250 Hz), 164.3 ppm.

^{19}F NMR (376.4 MHz, CD_2Cl_2): δ −110.50 (s, 2F) ppm.

HRMS (ES⁺) *m/z* calculated for $C_{66}H_{96}F_2N_4NaO_{12}S_2$ [M+Na]⁺ 1261.6326, found 1261.6297.

MALDI-MS (positive mode): [**21₂**+Na]⁺ calc. 1261.63, found 1261.55; [**21₂**–S+Na]⁺ calc. 1229.66, found 1229.52; [**21**H+Na]⁺ calc. 643.32, found 643.24; [**21**H–H_2S+Na]⁺ calc. 609.33, found 609.26. In order to analyse **21** by MALDI-MS, the sample was mixed with matrix α-cyano-4-hydroxycinnamic acid.

4,4′-(3,6,9,12,37,40,43,46-Octaoxa-24,25-dithiaoctatetracontane-1,48-diylbis(oxy))bis(*N′*-(4-(trifluoromethyl)benzylidene)benzohydrazide) (22$_2$)
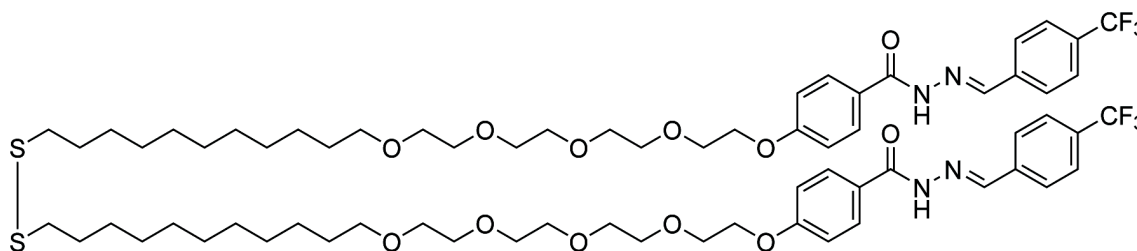
Iodine (587 mg, 2.31 mmol) was added to a solution of compound **20** (1.06 g, 1.16 mmol) in MeOH (40 mL). The mixture was stirred at rt for 30 min. The solution was decoloured by addition of a saturated solution of sodium sulfite then the volume was partially reduced under reduced pressure. Brine (50 mL) was then added, the aqueous phase was extracted with CH_2Cl_2 (3 × 50 mL), dried over $MgSO_4$ and evaporated under reduced pressure. The crude oil was purified by chromatography (SiO$_2$, CH_2Cl_2/MeOH 20:1) to afford **22$_2$** as a white foam (404 mg, 52%).

^{1}H NMR (500.1 MHz, CD_2Cl_2): δ 1.19–1.38 (m, 28H, 14 × CH_2), 1.45–1.54 (m, 4H, 2 × CH_2), 1.58–1.67 (m, 4H, 2 × CH_2), 2.61–2.68 (t, *J* = 7.2 Hz, 4H, 2 × CH_2S), 3.33–3.40 (t, *J* = 7.0 Hz, 4H, 2 × CH_2O), 3.47–3.67 (m, 24H, 12 × CH_2O), 3.75–3.82 (m, 4H, 2 × CH_2O), 4.04–4.13 (m, 4H, 2 × CH_2O), 6.84–6.95 (d, *J* = 7.5 Hz, 4H, H$_{Ar}$), 7.51–7.60 (d, *J* = 7.5 Hz, 4H, H$_{Ar}$), 7.69–7.77 (d, *J* = 8.0 Hz, 4H, H$_{Ar}$), 7.85–7.95 (d, *J* = 8.0 Hz, 4H, H$_{Ar}$), 8.41 (s, 2H, 2 × CH=), 10.67 (bs, 2H, 2 × NH) ppm.

^{13}C NMR (125.7 MHz, CD_2Cl_2): δ 26.5, 28.9, 29.6, 29.86, 29.89, 29.90, 29.94, 29.95, 30.1, 39.5, 68.0, 69.8, 70.4, 70.86, 70.88, 70.91, 70.92, 71.1, 71.7, 114.7, 121.1, 123.3, 125.6, 125.88–125.90 (d, *J* = 3.4 Hz), 127.9, 129.92–129.94 (d, *J* = 2.5 Hz), 131.4–131.7 (d, *J* = 32 Hz), 138.1, 146.6, 162.3 ppm.

^{19}F NMR (470.3 MHz, CD_2Cl_2): δ –62.92 (s, 6F) ppm.

HRMS (ES$^+$) *m/z* calculated for $C_{68}H_{96}F_6N_4NaO_{12}S_2$ [M+Na]$^+$ 1361.6263, found 1361.6248.

N'-(4-Fluorobenzylidene)-4-(2-methoxyethoxy)benzohydrazide (23)

Under an atmosphere of Ar, K_2CO_3 (667 mg, 4.83 mmol) was added to a solution of compound **17** (509 mg, 1.97 mmol) in dry DMF (22 mL) and stirred for 20 min at rt. Then, 2-chloroethyl methyl ether (0.18 mL, 1.84 mmol) was added and the reaction mixture was heated to 90 °C for 2 days. The reaction progress was monitored by TLC. The mixture was then allowed to cool to rt, before brine (20 mL) was added and the aqueous phase then extracted with CH_2Cl_2 (2 × 20 mL). The combined organic layers were dried over $MgSO_4$ and evaporated under reduced pressure. The crude was purified by chromatography (SiO_2, CH_2Cl_2/MeOH 20:1), followed by precipitation from hot ethanol with cold water to give **23** as a pale green solid (248 mg, 42%). Mp: 168–169 °C.

^1H NMR (400.1 MHz, [D$_6$]DMSO): δ 3.32 (s, 3H, CH$_3$), 3.64–3.73 (m, 2H, CH$_2$O), 4.12–4.23 (m, 2H, CH$_2$O), 7.00–7.14 (d, *J* = 8.4 Hz, 2H, H$_{Ar}$), 7.23–7.37 (t, *J* = 7.3 Hz, 2H, H$_{Ar}$), 7.71–7.84 (m, 2H, H$_{Ar}$), 7.85–7.95 (d, *J* = 8.4 Hz, 2H, H$_{Ar}$), 8.44 (s, 1H, CH=), 11.75 (bs, 1H, NH) ppm.

^{13}C NMR (100.6 MHz, [D$_6$]DMSO): δ 58.2, 67.1, 70.2, 114.2, 115.8–116.0 (d, *J* = 22 Hz), 125.4, 129.1–129.2 (d, *J* = 8.1 Hz), 129.5, 131.06–131.09 (d, *J* = 2.2 Hz), 146.0, 161.3, 161.8–164.3 (d, *J* = 247 Hz), 162.5 ppm.

^{19}F NMR (376.5 MHz, [D$_6$]DMSO): δ −110.85 (s, 1F) ppm.

HRMS (ES$^+$) *m/z* calculated for $C_{17}H_{17}FN_2NaO_3$ [M+Na]$^+$ 339.1121, found 339.1110.

4-(2-Methoxyethoxy)- N'-(4-(trifluoromethyl)benzylidene)benzohydrazide (24)
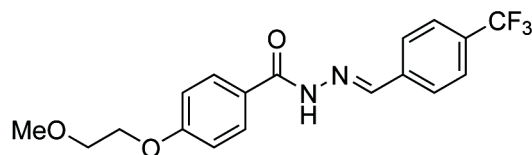
2-Chloroethyl methyl ether (0.76 mL, 8.32 mmol), hydrazone **18** (513 mg, 1.66 mmol), K_2CO_3 (690 mg, 4.99 mmol) and KI (138 mg, 0.83 mmol) were dissolved in dry DMF (10 mL). The mixture was heated under microwave irradiation (200 W) at 120°C for 30 min. Then, EtOAc (50 mL) was added and the organic phase was washed with H_2O

(50 mL) and brine (2 x 50 mL), dried over $MgSO_4$, filtered and evaporated under reduced pressure. Product **24** was obtained by recrystallization from hot MeOH/EtOH with H_2O as a pale yellow solid (177 mg, 29%). Mp: 201–202 °C.

^1H NMR (500.1 MHz, [D_6]DMSO): δ 3.32 (s, 3H, CH_3), 3.63–3.76 (m, 2H, CH_2O), 4.12–4.26 (m, 2H, CH_2O), 7.03–7.14 (d, *J* = 8.0 Hz, 2H, H_{Ar}), 7.75–7.86 (d, *J* = 7.0 Hz, 2H, H_{Ar}), 7.87–8.02 (m, 4H, H_{Ar}), 8.51 (s, 1H, CH=), 11.94 (bs, 1H, NH) ppm.

^{13}C NMR (125.7 MHz, [D_6]DMSO): δ 58.2, 67.2, 70.2, 114.2, 123.1, 125.2, 125.7–125.8 (d, *J* = 3.5 Hz), 127.6, 129.4, 129.7, 138.5, 145.3, 161.4, 162.7 ppm.

^{19}F NMR (470.3 MHz, [D_6]DMSO): δ –60.71 (s, 3F) ppm.

HRMS (ES$^+$) *m/z* calculated for $C_{18}H_{17}F_3N_2NaO_3$ [M+Na]$^+$ 389.1089, found 389.1074.

N'-(4-Fluorobenzyl)-4-(2-methoxyethoxy)benzohydrazide (25)
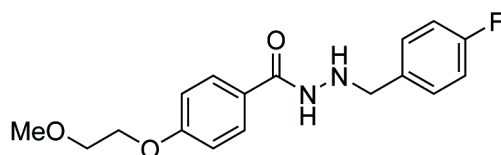
Under an atmosphere of Ar, compound **23** (109 mg, 0.34 mmol) was dissolved in MeOH (10 mL) and cooled to 0 °C. $NaCNBH_3$ (53.9 mg, 0.85 mmol) was then added and the reaction mixture was acidified with HCl (0.5 mL). After 1 h, the reaction was neutralised with saturated $NaHCO_3$ (10 mL) and the aqueous phase was extracted with CH_2Cl_2 (3 × 20 mL). The combined organic layers were dried over $MgSO_4$, and evaporated under reduced pressure. The crude was purified by chromatography (SiO_2, CH_2Cl_2/MeCN 1:1) to afford **25** as a white solid (62.2 mg, 57%). Mp: 115–116 °C.

^1H NMR (500.1 MHz, [D_6]DMSO): δ 3.30 (s, 3H, CH_3), 3.63–3.67 (m, 2H, CH_2O), 3.92–3.96 (d, *J* = 5.0 Hz, 2H, CH_2N), 4.11–4.15 (m, 2H, CH_2O), 5.36–5.44 (m, 1H, CH_2NH), 6.95–7.00 (d, *J* = 8.5 Hz, 2H, H_{Ar}), 7.11–7.17 (t, *J* = 9.0 Hz, 2H, H_{Ar}), 7.37–7.43 (m, 2H, H_{Ar}), 7.72–7.77 (d, *J* = 9.0 Hz, 2H, H_{Ar}), 9.87–9.92 (m, 1H, CON*H*) ppm.

^{13}C NMR (125.8 MHz, [D_6]DMSO): δ 54.0, 58.2, 67.1, 70.3, 114.0, 114.8–115.0 (d, *J* = 21 Hz), 125.4, 128.9, 130.5–130.6 (d, *J* = 8.1 Hz), 134.84–134.86 (d, *J* = 2.8 Hz), 160.4–162.3 (d, J = 242 Hz), 160.9, 162.3 ppm.

^{19}F NMR (470.5 MHz, [D_6]DMSO): δ –115.49 (s, 1F) ppm.

HRMS (ES$^+$) *m/z* calculated for $C_{17}H_{19}FN_2NaO_3$ [M+Na]$^+$ 341.1277, found 341.1264.

4-(2-Methoxyethoxy)-*N'*-(4-(trifluoromethyl)benzyl)benzohydrazide (26)
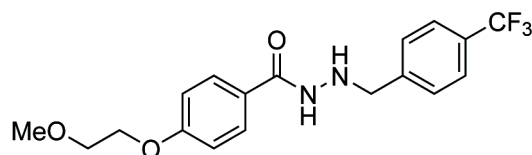
Under an atmosphere of Ar, compound **24** (23.7 mg, 0.06 mmol) was dissolved in MeOH (5 mL) and cooled to 0 °C. NaCNBH$_3$ (10.2 mg, 0.16 mmol) was then added and the reaction mixture was acidified with HCl (0.25 mL). After 40 min, the reaction was neutralised with saturated NaHCO$_3$ (20 mL) and the aqueous phase was extracted with CH$_2$Cl$_2$ (3 × 20 mL). The combined organic layers were dried over MgSO$_4$, filtered and evaporated under reduced pressure. The crude was purified by chromatography (SiO$_2$, HexH/EtOAc 1:3) to afford **26** as a white solid (8.10 mg, 37%). Mp: 160–161 °C.

^{1}H NMR (500.1 MHz, [D$_6$]DMSO): δ 3.29 (s, 3H, C*H*$_3$), 3.63–3.68 (m, 2H, C*H*$_2$O), 4.04–4.09 (m, 2H, C*H*$_2$N), 4.12–4.15 (m, 2H, C*H*$_2$O), 5.58 (m, 1H, CH$_2$N*H*), 6.94–7.00 (d, *J* = 9.0 Hz, 2H, *H*$_{Ar}$), 7.58–7.63 (d, *J* = 8.0 Hz, 2H, *H*$_{Ar}$), 7.66–7.71 (d, *J* = 8.0 Hz, 2H, *H*$_{Ar}$), 7.72–7.75 (d, *J* = 9.0 Hz, 2H, *H*$_{Ar}$), 9.89 (m, 1H, CON*H*) ppm.

^{13}C NMR (125.7 MHz, [D$_6$]DMSO): δ 54.1, 58.2, 67.1, 70.2, 114.0, 115.5, 118.2, 124.93–124.96 (d, *J* = 3.6 Hz), 127.4–127.7 (d, *J* = 32 Hz), 128.9, 129.2, 143.8, 160.9, 165.4 ppm.

^{19}F NMR (470.5 MHz, [D$_6$]DMSO): δ –60.30 (s, 3F) ppm.

HRMS (ES$^+$) *m/z* calculated for C$_{18}$H$_{19}$F$_3$N$_2$NaO$_3$ [M+Na]$^+$ 391.1245, found 391.1232.

3-(Undecyloxy)benzaldehyde (28)
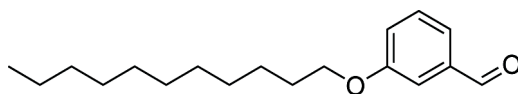
Under an atmosphere of Ar, 3-hydroxybenzaldehyde (1.25 g, 10.3 mmol), K$_2$CO$_3$ (4.26 g, 30.8 mmol) and KI (852 mg, 5.13 mmol) were dissolved in dry MeCN (50 mL) and stirred at rt for 30 min. Then, 1-bromoundecane (3.06 mL, 12.3 mmol) was added and the reaction mixture was refluxed for 19 h, monitoring the reaction by TLC. The solvent was then partially evaporated under reduced pressure, EtOAc (50 mL) was added and the organic phase was washed with H$_2$O (50 mL) and brine (2 × 50 mL), dried over MgSO$_4$, filtered and evaporated. The crude product was then purified by

chromatography (SiO$_2$, HexH/EtOAc 19:1) to afford pure aldehyde **28** as a yellow oil (2.40 g, 84%).

^{1}H NMR (500.1 MHz, CDCl$_3$): δ 0.84–0.91 (t, J = 7.0 Hz, 3H, CH$_3$), 1.20–1.50 (m, 16H, 8 × CH$_2$), 1.76–1.84 (m, 2H, CH$_2$), 3.98–4.03 (t, J = 6.5 Hz, 2H, CH$_2$O), 7.14–7.20 (m, 1H, H$_{Ar}$), 7.37–7.39 (m, 1H, H$_{Ar}$), 7.41–7.46 (m, 2H, H$_{Ar}$), 9.97 (s, 1H, CHO) ppm.

^{13}C NMR (125.7 MHz, CDCl$_3$): δ 14.28, 22.8, 26.1, 29.3, 29.49, 29.51, 29.71, 29.74, 29.8, 32.1, 68.5, 112.9, 122.1, 123.5, 130.1, 137.9, 159.9, 192.4 ppm.

HRMS (ES$^+$) *m/z* calculated for C$_{19}$H$_{32}$NaO$_3$ [M+Na+MeOH]$^+$ 331.2249, found 331.2241.

Chloro(triphenylphosphine)gold(I) (AuPPh$_3$Cl)[187,188]
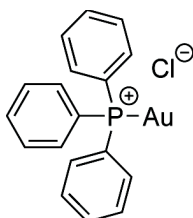
A solution of triphenylphosphine (2.69 g, 10.3 mmol) in Et$_2$O (35 mL) was added dropwise over 15 min to a solution of gold(III) chloride trihydrate (2.02 g, 5.12 mmol) in Et$_2$O (100 mL) at 0 °C. The reaction mixture was stirred at 0 °C for 3 h and then allowed to warm to rt. The white precipitate was recovered by filtration, washed with cold Et$_2$O then recrystallized from CH$_2$Cl$_2$/HexH to give AuPPh$_3$Cl as a white solid (2.24 g, 89%). Mp: 236–237 °C.

^{1}H NMR (500.1 MHz, CDCl$_3$): δ 7.45–7.55 (m, 15H, H$_{Ar}$) ppm.

^{13}C NMR (125.8 MHz, CDCl$_3$): δ 129.1–128.4 (d, *J* = 96.7 Hz), 129.5–129.3 (d, *J* = 11.8 Hz), 132.3–132.0 (d, *J* = 2.5 Hz), 134.4–134.1 (d, *J* = 13.7 Hz) ppm.

^{31}P NMR (202.5 MHz, CDCl$_3$): δ 33.31 (s, 1P) ppm (in agreement with the literature values[187,188]).

HRMS (ES$^+$) *m/z* calculated for C$_{18}$H$_{15}$AuClNaP [M+Na]$^+$ 517.0163, found 517.1602.

5.3 Procedures for nanoparticle synthesis and functionalisation

5.3.1 Preparation of TOAB-stabilised gold nanoparticles and functionalisation by ligand exchange

5.3.1.1 *Gold colloid solution (AuNP-TOAB)*[160]
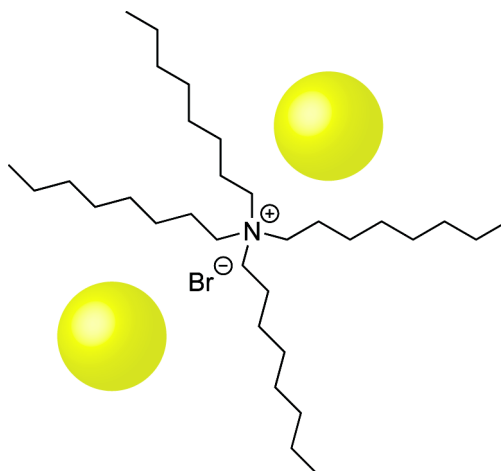
All batches were made following the same general procedure.[160] The preparation of AuNP-**TOAB***g* (see Table **5.6**) is described as an explanatory example.

To a solution of gold(III) chloride trihydrate (0.3 mmol) in H_2O (10 mL), a solution of TOAB (1.4 mmol) in toluene (28 mL) was added. The biphasic mixture was vigorously stirred for 15 min, while the yellow aqueous solution turned into deep red. Then, a fresh solution of $NaBH_4$ (3.2 mmol) in H_2O (5 mL) was added dropwise. After 1 h stirring, phases were separated, the aqueous layer was discarded and the organic solution was kept refrigerated under Ar for further use. Mean diameter: 3.01 ± 0.92 nm (31% dispersity). SPR λ_{max} = 520 nm (in toluene).

^{1}H NMR (400.1 MHz, $CDCl_3$): δ 0.84–0.96 (t, *J* = 7.2 Hz, 3H, CH_3), 1.20–1.48 (m, 10H, 5 × CH_2), 1.61–1.75 (m, 2H, CH_2), 3.30–3.42 (m, 2H, CH_2N) ppm.
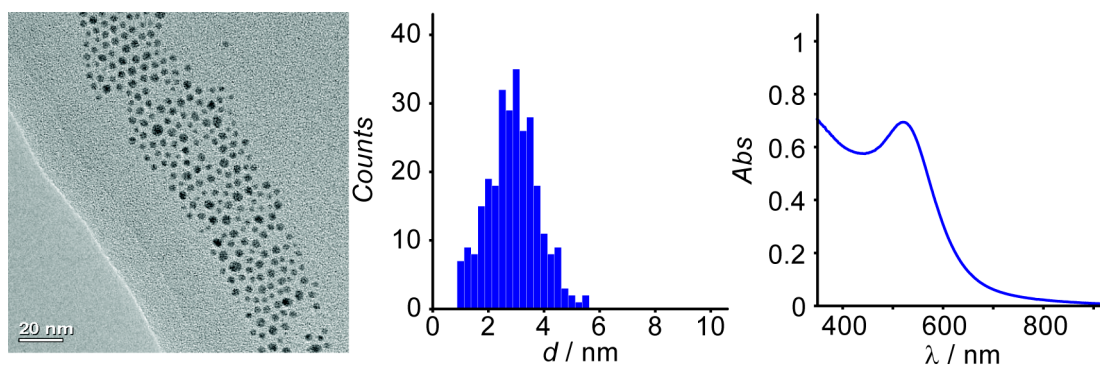
Figure 5.1   AuNP-**TOAB**: TEM micrograph (scale bar 20 nm), size distribution (diameter 3.01 ± 0.92 nm, 31% dispersity) and UV-Vis spectrum (SPR λ_{max} = 520 nm).

5.3.1.2 Preparation of AuNP-4 by the ligand exchange method
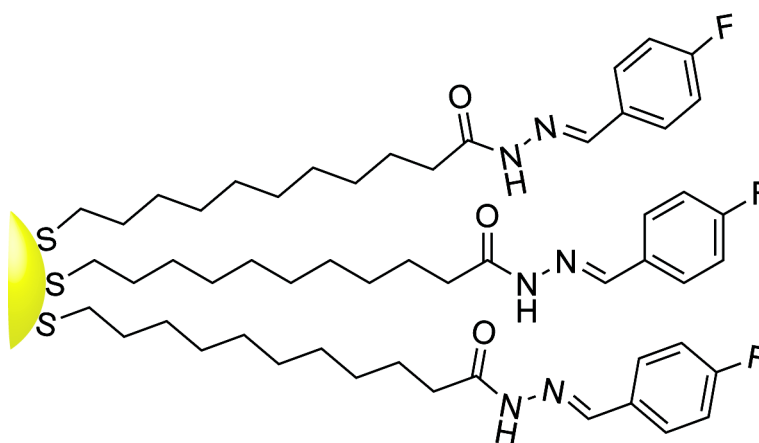
Under Ar, to a degassed solution of gold colloid solution AuNP-**TOAB** (45 mL), a solution of hydrazone **4**H (133 mg, 393 μmol) in CH$_2$Cl$_2$ (5 mL) was added. The reaction mixture was vigorously stirred for 2 h at rt. An excess of MeOH was then added in order to induce NP precipitation. The supernatant solution was then decanted and the solid was transferred into a centrifuge tube, washed with methanol (40 mL), sonicated (10 min) and centrifuged (10 min, 6000 rpm, 5 °C). The precipitate was then dissolved in THF and purified by size exclusion chromatography (100% THF).[176] The clean fractions were then collected and evaporated under reduced pressure. A pure black solid was obtained (65.3 mg). Mean diameter: 3.71 ± 0.86 nm (23% dispersity).

^{1}H NMR (499.9 MHz, CD$_2$Cl$_2$): δ 0.12–3.19 (m, 20H, 10 × CH$_2$), 6.80 (m, 2H, H$_{Ar}$), 7.45 (m, 2H, H$_{Ar}$), 8.40 (bs, 1H, CH=) ppm.

^{19}F NMR (470.3 MHz, CD$_2$Cl$_2$): δ from −110.68 (bs, 1F) ppm.

5.3.1.3 Preparation of AuNP-5 by the ligand exchange method
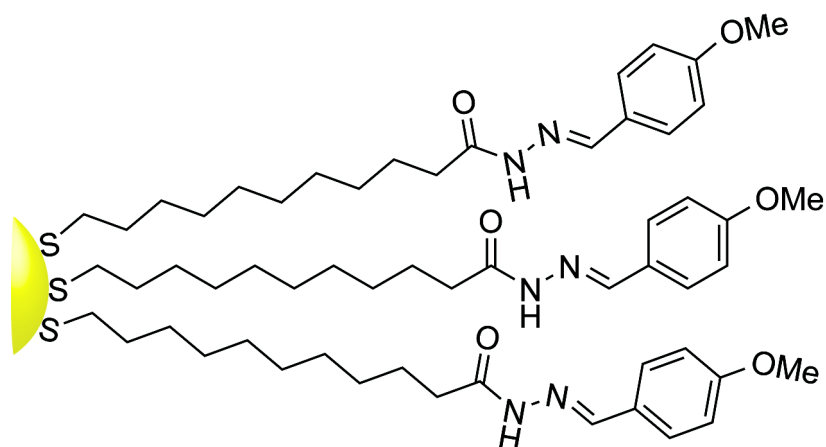
Under Ar, to a degassed solution of gold colloid solution AuNP-**TOAB** (50 mL), a solution of hydrazone **5**H (291 mg, 831 μmol) in CH$_2$Cl$_2$ (5 mL) was added. The reaction mixture was vigorously stirred for 2 h at rt. An excess of MeOH was then added in order to induce NP precipitation. The supernatant solution was then decanted and the solid was transferred into a centrifuge tube, washed with methanol (40 mL), sonicated (10 min) and centrifuged (10 min, 6000 rpm, 5 °C). The precipitate was then dissolved in THF and purified by size exclusion chromatography (100% THF).[176] The clean fractions were then collected and evaporated under reduced pressure. A pure black solid was obtained (65.3 mg). Mean diameter: 2.86 ± 0.65 nm (23% dispersity).
^{1}H NMR (400.1 MHz, CD$_2$Cl$_2$): δ 0.52–2.97 (m, 20H, 10 × CH$_2$), 3.63 (bs, 3H, CH$_3$), 6.61 (m, 2H, H$_{Ar}$), 7.06 (m, 2H, H$_{Ar}$), 7.45 (bs, 1H, CH=), 8.32 (bs, 1H, NH) ppm.

5.3.2 Preparation of functionalised gold nanoparticles by direct synthesis

5.3.2.1 Hydrazone stability under the reducing conditions used for nanoparticle synthesis

In order to investigate the stability of the hydrazone moiety under reducing conditions, model hydrazones **23** or **24** (8 μmol), AuPPh$_3$Cl (3.95 mg, 8 μmol) and *tert*-butylamine borane complex (6.96 mg, 80 μmol) were dissolved in DMF/[D$_8$]THF 1:9 (0.5 mL) at rt. The stability of the hydrazone moiety was monitored by ^{19}F NMR over 24 h (Figures **5.2** and **5.3**) by calculating its concentration against the internal standard (4-fluorotoluene, 16.0 mM). Hydrazone **23** was confirmed to be stable for at least 24 h at rt since its concentration did not change over time (Figure **5.2**). On the other hand,

hydrazone **24** was stable only for 7 h. After 24 h, about 20% of hydrazone **24** was found to be reduced under the chosen conditions (Figure **5.3**).

	Time / h	[23] / mM
a)	0.3	13.7
b)	2.1	14.3
c)	4.1	14.3
d)	7.2	14.3
e)	23.7	13.5
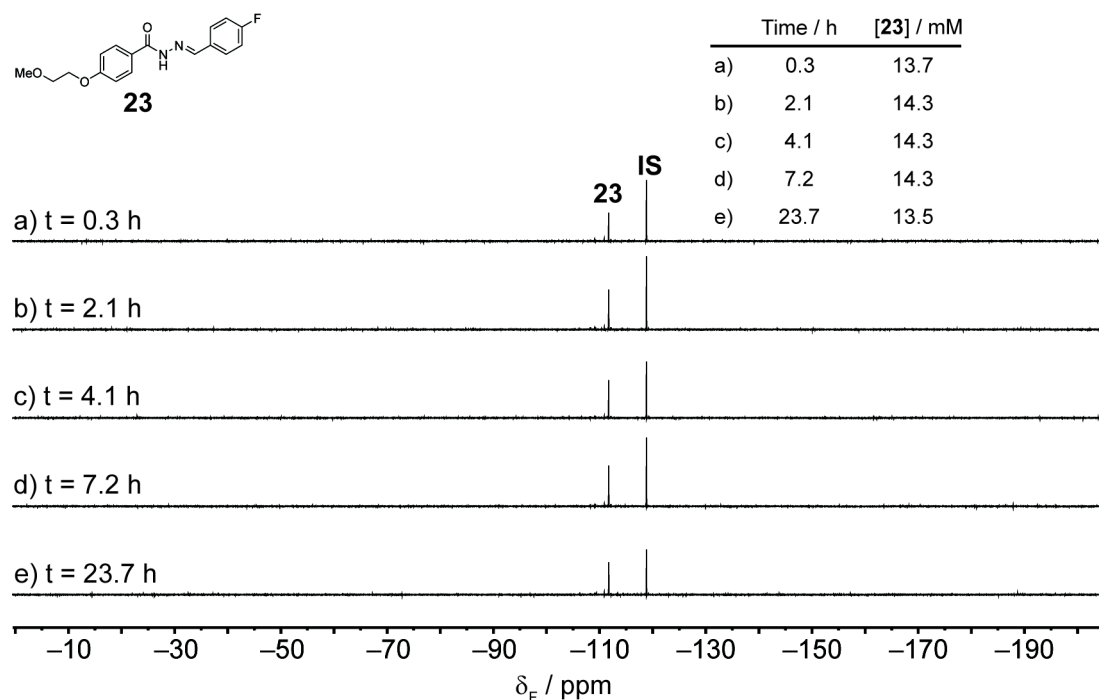
Figure 5.2 ^{19}F NMR (DMF/[D$_8$]THF 1:9, 470.5 MHz, 295 K) of compound **23** recorded after TBAB addition at rt (a–e). **IS**: internal standard (4-fluorotoluene, 16.0 mM). Conditions: AuPPh$_3$Cl (1 Eq), TBAB (10 Eq), DMF/[D$_8$]THF 1:9, rt.

	Time / h	[24] / mM
a)	0.4	20.0
b)	2.3	20.5
c)	4.3	20.9
d)	7.4	20.4
e)	23.9	16.4
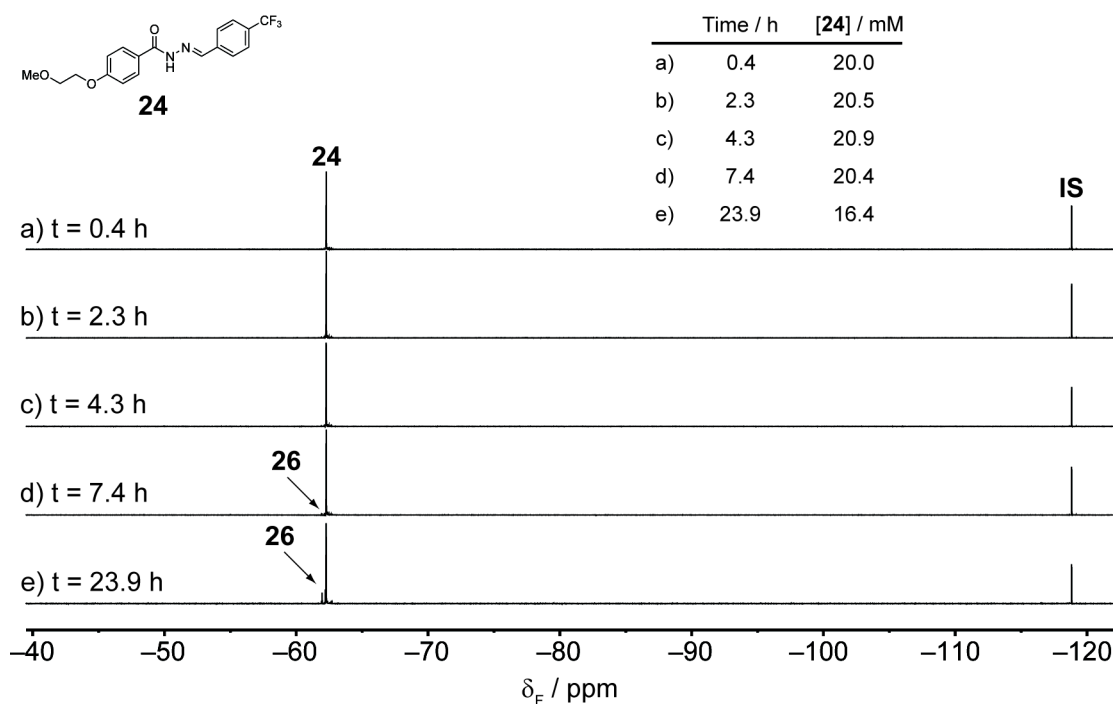
Figure 5.3 ^{19}F NMR (DMF/[D$_8$]DMSO 1:9, 470.5 MHz, 295 K) of compound **24** after TBAB addition (a–e). **IS**: internal standard (4-fluorotoluene, 16.0 mM). Conditions: AuPPh$_3$Cl (1 Eq), TBAB (10 Eq), DMF/[D$_8$]THF 1:9, rt.

5.3.2.2 Preparation of AuNP-21 by direct synthesis method
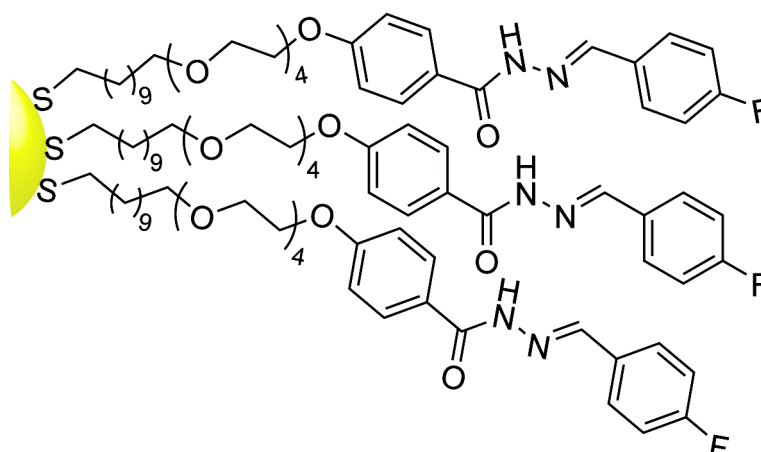
Representative procedure as summarised in Table **2.5** (entry *g*): Disulfide **21**$_2$ (40.0 mg, 32.2 µmol) and AuPPh$_3$Cl (31.9 mg, 64.5 µmol) were dissolved in DMF/THF 1:9 (4.0 mL). *tert*-Butylamine borane complex (56.1 mg, 645 µmol) was then added as a powder and the reaction mixture was vigorously stirred for 6 h at rt. The reaction was then quenched with Et$_2$O (5 mL) in order to achieve NP precipitation. The black solid was then washed with MeOH using the following procedure: NPs were dispersed in MeOH and Et$_2$O (7 mL), sonicated for 15 min, and centrifuged (4000 rpm, 5 °C, 10 min). The operation was repeated 3 times for each solvent. Evaporation under vacuum afforded AuNP-**21** as a black solid (9.73 mg). Mean diameter: 3.39 ± 0.61 nm (18% dispersity). SPR λ_{max} = 509 nm (in DMF).

^{1}H NMR (500.1 MHz, [D$_7$]DMF): δ 0.49–2.28 (m, 22H, CH$_2$), 3.31–3.94 (m, 14H, CH$_2$O), 4.04–4.34 (m, 2H, CH$_2$O), 6.79–7.41 (m, 4H, H$_{Ar}$), 7.63–7.91 (m, 2H, H$_{Ar}$), 8.56 (bs, 1H, CH=), 11.84 (bs, 1H, NH) ppm.

^{19}F NMR (470.5 MHz, [D$_7$]DMF): δ −111.49 (s, 1F) ppm.

The histograms corresponding to all the conditions employed for the synthesis of AuNP-**21** (Table **2.5**, entries *a–i*) are summarised in Figure **5.4**.
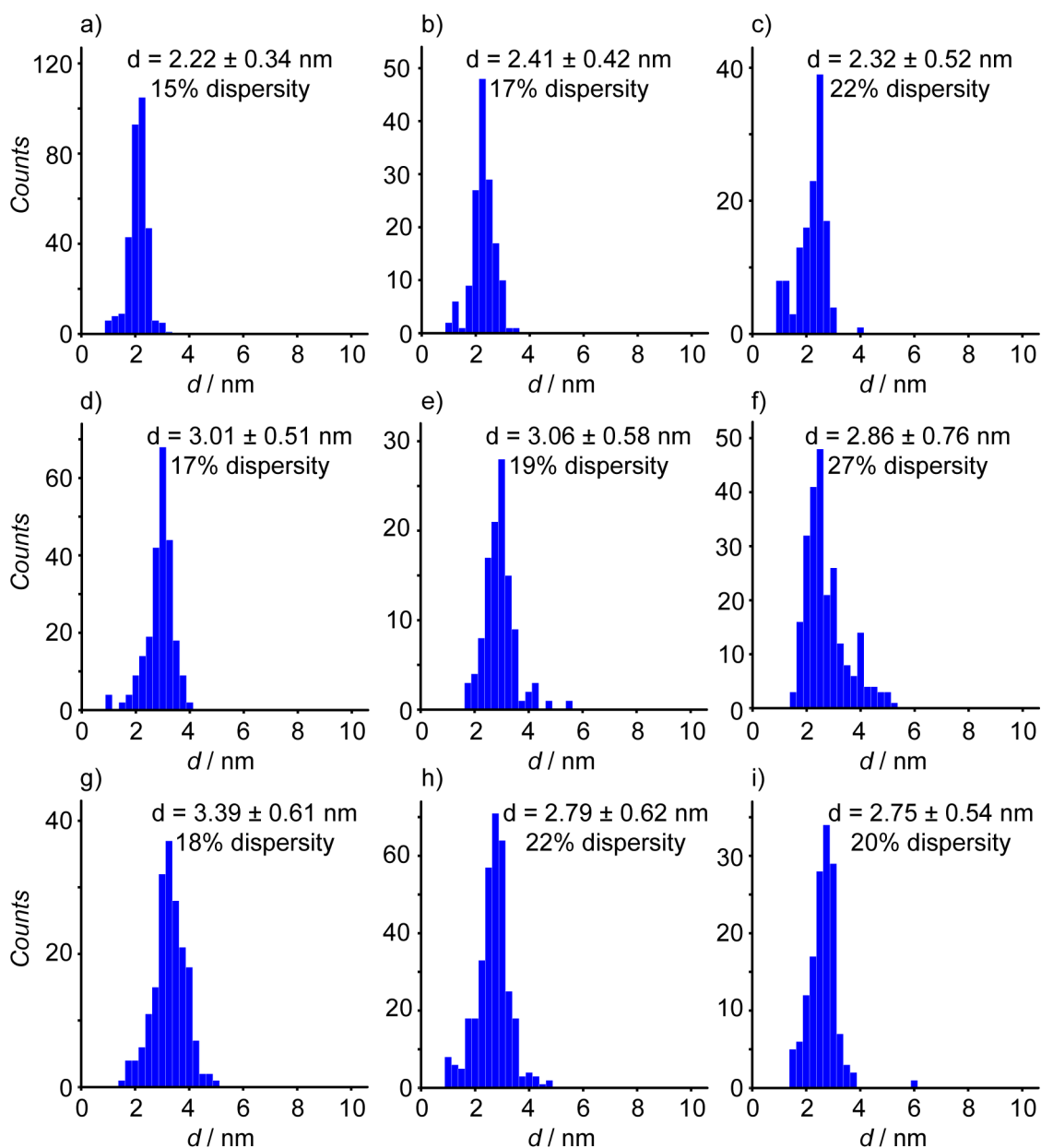
Figure 5.4   Size distribution of AuNP-**21** prepared as summarised in Table **2.5**.

5.3.2.3   Preparation of AuNP-22d by direct synthesis method

Representative procedure as summarised in Table **2.6** (entry *d*): disulfide **22**$_2$ (50.0 mg, 37.3 μmol) and AuPPh$_3$Cl (36.9 mg, 74.7 μmol) were dissolved in DMF/THF 1:9 (4.7 mL). *tert*-Butylamine borane complex (32.5 mg, 373 μmol) was then added as a powder and the reaction mixture was vigorously stirred for 6 h at rt. The reaction was then quenched with an excess of Et$_2$O in order to achieve full NP precipitation. The black solid was recovered by centrifugation and then washed with MeOH using the following procedure: NPs were dispersed in MeOH/Et$_2$O 1:6 (7 mL), sonicated for

15 min, and centrifuged (4000 rpm, 5 °C, 10 min). The operation was repeated 3 times. Evaporation under vacuum afforded a black solid (42.8 mg). Mean diameter: 5.37 ± 0.86 nm (16% dispersity). SPR λ_{max} = 533 nm (in DMF).

5.4 Synthesis of AuNP-22e via hydrazone exchange from AuNP-21: preparation, purification and characterisation
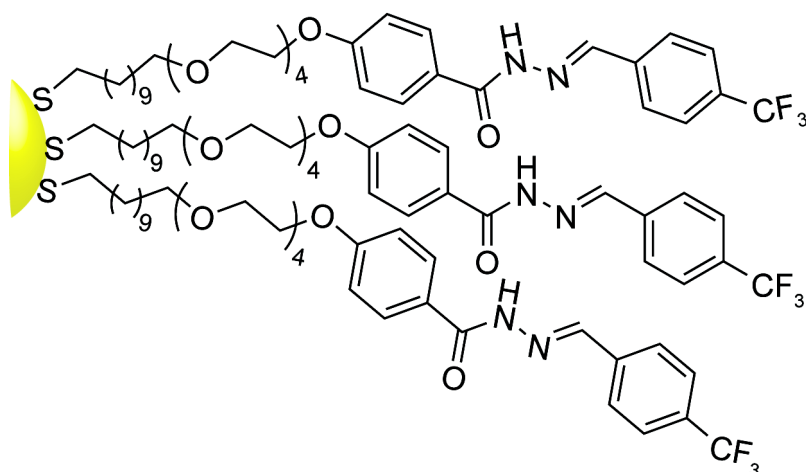
5.4.1 Synthetic procedure

To a solution of AuNP-**21** (2.69 μmol in terms of ligand **21**, 500 μL) in D$_2$O/[D$_7$]DMF 1:9, a solution of 4-(trifluoromethyl)benzaldehyde **16** (53.7 μmol, 20 Eq, 50 μL) in D$_2$O/[D$_7$]DMF 1:9 and a solution of CF$_3$CO$_2$H (13.4 μmol, 5 Eq, 50 μL) in D$_2$O/[D$_7$]DMF 1:9 were added. The reaction mixture was heated at 50 °C overnight. After 16 h the equilibrium was achieved and Et$_2$O (5 mL) was added in order to achieve NP precipitation. The black solid was then washed with MeOH/Et$_2$O 1:6 using the following procedure: NPs were dispersed in the solvent mix (7 mL), sonicated for 15 min, and centrifuged (4000 rpm, 5 °C, 10 min). Intermediate ^{19}F NMR analysis revealed a 1:9 ratio between ligands **21** and **22**. The black solid was then re-dissolved in D$_2$O/[D$_7$]DMF 1:9 (500 mL) and fresh aldehyde **16** (53.7 μmol, 20 Eq, 50 mL) and CF$_3$CO$_2$H (13.4 μmol, 5 Eq, mL) in D$_2$O/[D$_7$]DMF 1:9 were added. The reaction mixture was heated at 50 °C overnight and the full conversion was monitored by ^{19}F NMR. The reaction was then quenched with Et$_2$O (5 mL) in order to achieve NP precipitation. The black solid was then washed with MeOH using the same procedure described above. Evaporation under vacuum afforded pure AuNP-**22e** (32.3 mg, Figures **5.5** and **5.6**).

^{1}H NMR (500.1 MHz, [D$_7$]DMF): δ 0.52–2.37 (m, 22H, 11 × CH$_2$), 3.19–3.98 (m, 14H, 7 × CH$_2$O), 4.01–4.35 (m, 2H, CH$_2$O), 6.80–7.24 (m, 4H, H$_{Ar}$), 7.48–7.88 (m, 4H, H$_{Ar}$), 8.64 (bs, 1H, CH=), 12.01 (bs, 1H, NH) ppm.

^{19}F NMR (470.5 MHz, [D$_7$]DMF): δ –61.46 (s, 3F) ppm.

5.4.2 Full sweep width ^{1}H NMR spectra for dynamic covalent hydrazone exchange from AuNP-21 to AuNP-22e
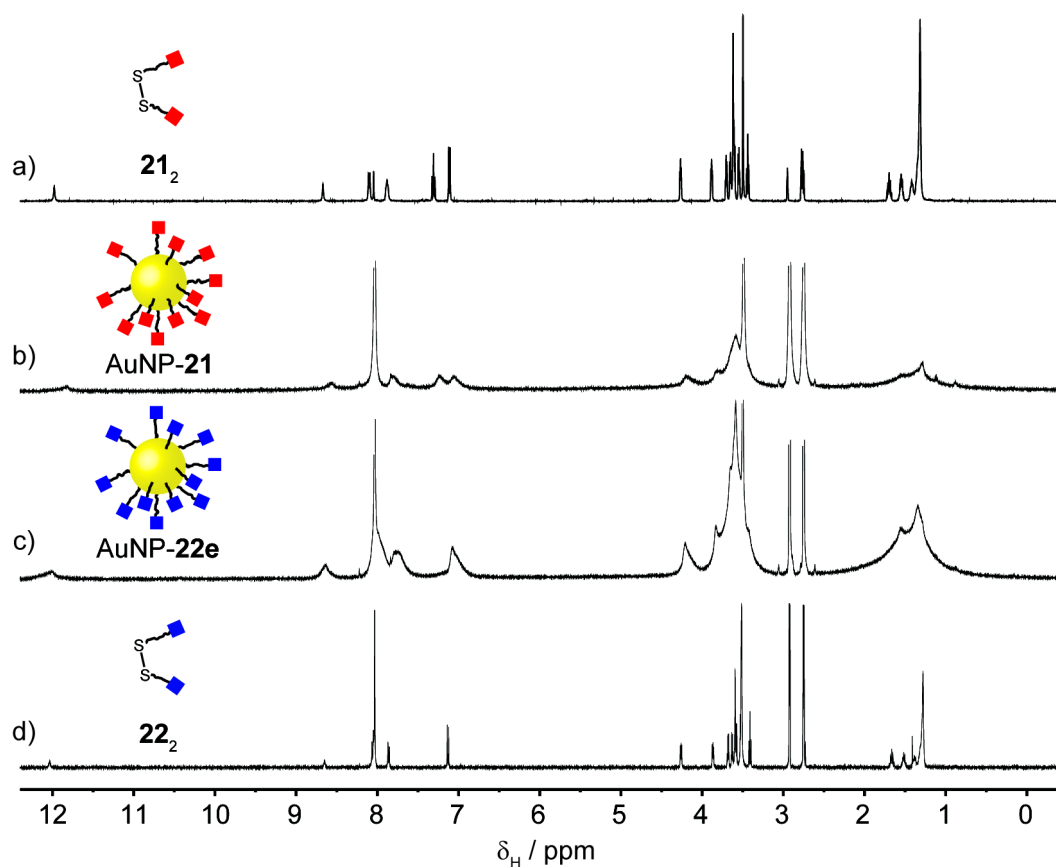
Figure 5.5 ^{1}H NMR ([D$_7$]DMF, 500.1 MHz, 295 K) for hydrazone exchange from AuNP-**21** to AuNP-**22e**. a): disulfide **21**$_2$. b): AuNP-**21**. c): AuNP-**22e**. d): disulfide **22**$_2$.

5.4.3 Full sweep width ^{19}F NMR spectra for dynamic covalent hydrazone exchange from AuNP-21 to AuNP-22e
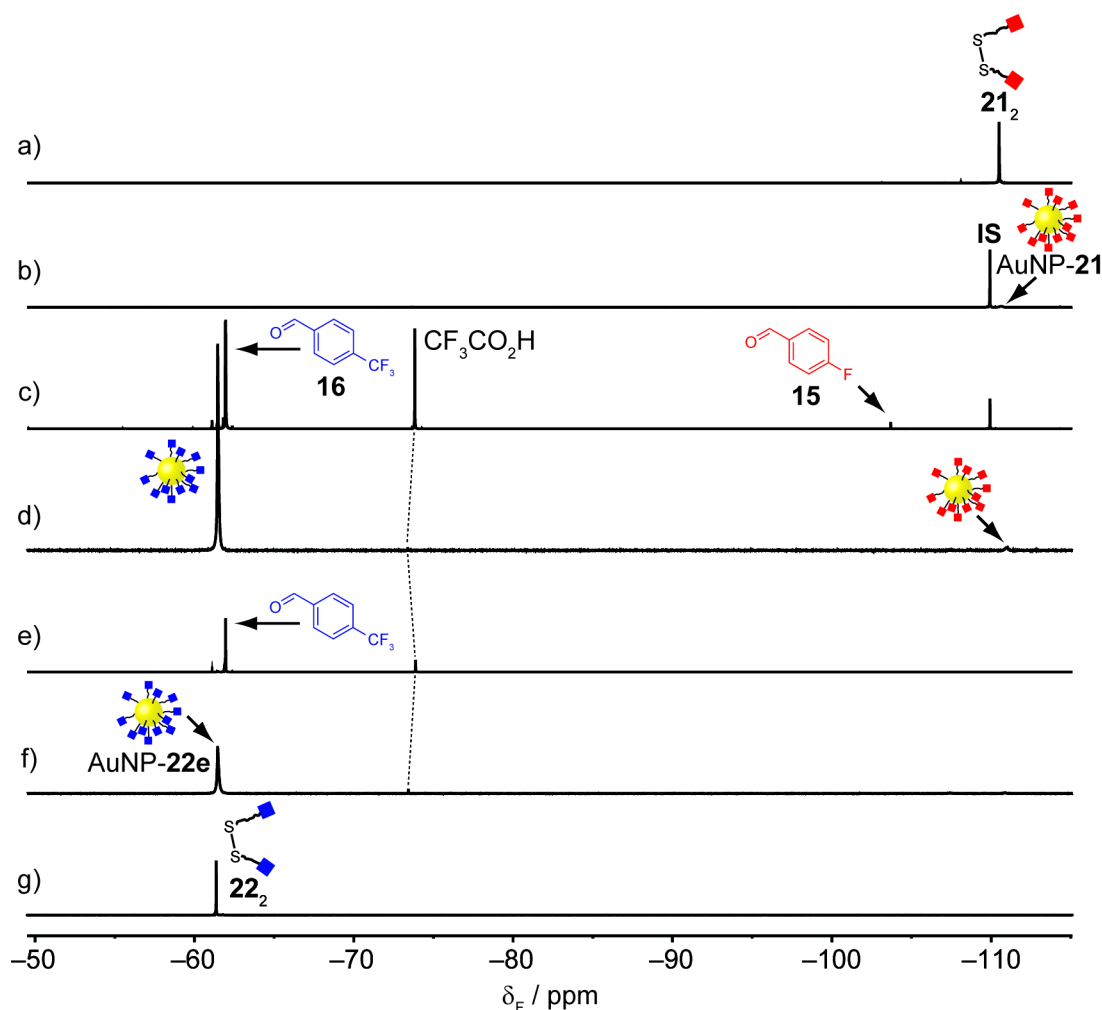
Figure 5.6 ^{19}F NMR (a, d, f, g: [D$_7$]DMF; b, c, e: D$_2$O/[D$_7$]DMF 1:9; 470.5 MHz, 295 K) for hydrazone exchange from AuNP-**21** to AuNP-**22e**. a): Disulfide **21**$_2$. b): AuNP-**21**. c): Crude sample after exchange with 4-(trifluoromethyl)benzaldehyde **16** (20 Eq). d): Purified sample after exchange: AuNP-**21**$_{0.1}$**22**$_{0.9}$. e): Crude sample after a second round of exchange with 4-(trifluoromethyl)benzaldehyde **16** (20 Eq). f): Purified AuNP-**22e** displaying complete hydrazone exchange. g): Disulfide **22**$_2$. **IS**: 3-fluoronitrobenzene.

5.4.4 LDI-MS of AuNP-22e prepared by dynamic covalent exchange from AuNP-21

AuNP surface-bound molecular species can be detected by LDI-MS.[76] Direct absorption of the UV laser excitation energy (355 nm) by the AuNPs leads to desorption and ionisation of surface-bound molecules without requiring addition of an external matrix. The surface desorbed ions formed from similar thiolate-protected AuNPs have previously been characterised,[76] and the same ionisation and fragmentation pattern was observed for desorbed ligand **22** (Figure **5.7**). Molecular

ions for the disulfide **22**$_2$ (peak A) and thiol **22**H (peak D) were both observed. In addition, progressive loss of one and two sulfur atoms from the disulfide (peaks B and C, respectively) and the loss of H_2S from the thiol (peak E) were also observed.
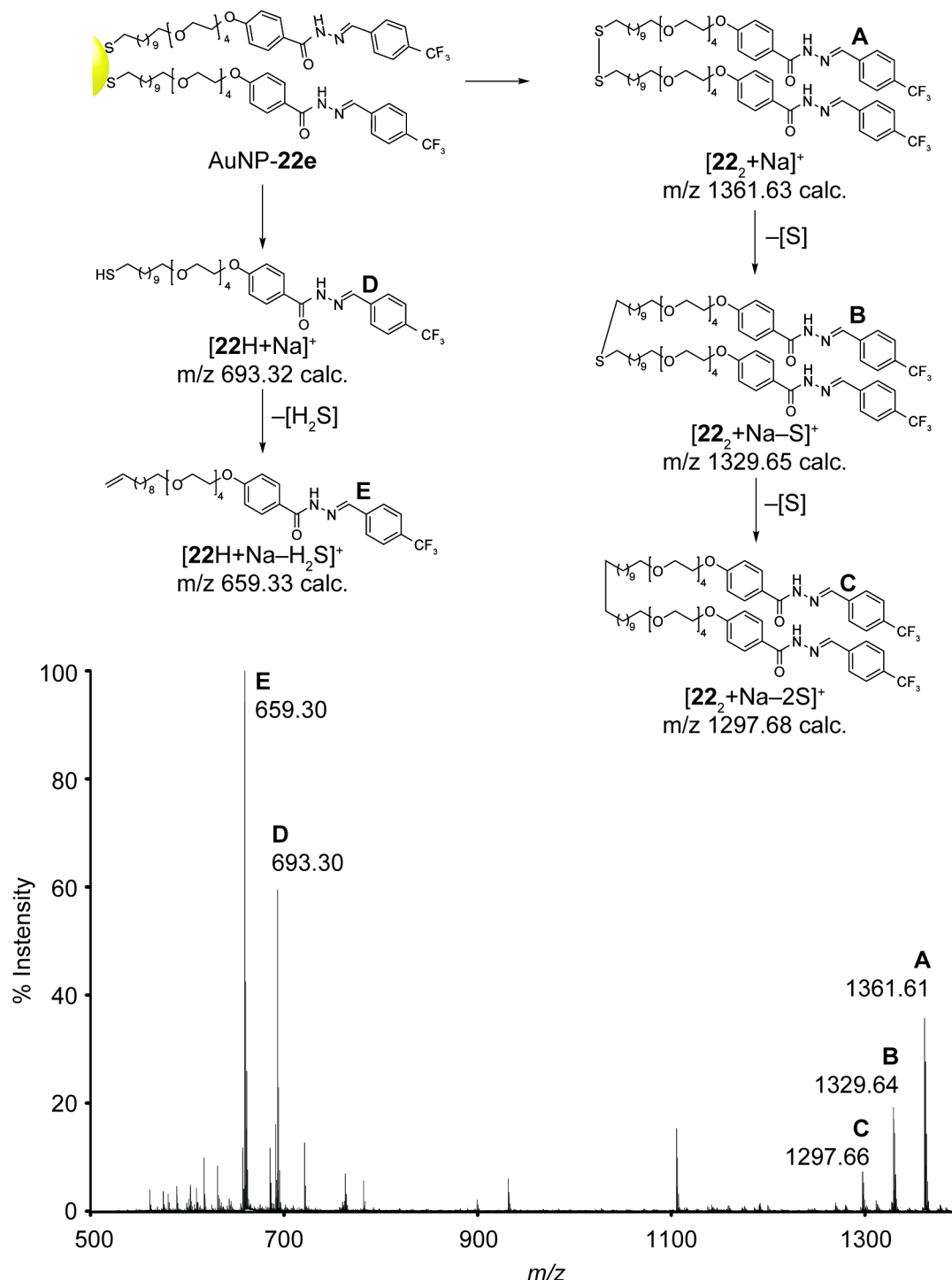
Figure 5.7   LDI mass spectrum and fragmentation pattern for AuNP-**22e**. The ion corresponding to disulfide **22**$_2$ (peak A, [**22**$_2$+Na]$^+$: m/z 1361.61) undergoes a progressive loss of two sulfur atoms (peak B, [**22**$_2$–S+Na]$^+$: m/z 1329.64; peak C, [**22**$_2$–2S+Na]$^+$: m/z 1297.66). The ion corresponding to thiol **22**H (peak D, [**22**H+Na]$^+$: m/z 693.30) loses H_2S (peak E, [**22**H–H$_2$S+Na]$^+$: m/z 659.30).

5.5 Reverse direction dynamic covalent exchange from AuNP-22e to AuNP-21

5.5.1 Synthetic procedure

To a solution of AuNP-**22e** (1.32 μmol in terms of ligand **22**, 500 μL) in D_2O/[D_7]DMF 1:9, a solution of 4-fluorobenzaldehyde **15** (13.2 μmol, 10 Eq, 50 μL) in D_2O/[D_7]DMF 1:9 and a solution of CF_3CO_2H (6.58 μmol, 5 Eq, 50 μL) in D_2O/[D_7]DMF 1:9 were added. The reaction mixture was heated at 50 °C for 2 days and then Et_2O (5 mL) was added in order to achieve NP precipitation. The black solid was washed with MeOH/Et_2O 1:6 using the following procedure: NPs were dispersed in the solvent mix (7 mL), sonicated for 15 min and centrifuged (4000 rpm, 5 °C, 10 min). ^{19}F NMR analysis revealed a 1:1 ratio between ligands **21** and **22**. The black solid was then re-dissolved in D_2O/[D_7]DMF 1:9 (500 μL) and fresh 4-fluorobenzaldehyde **15** (39.5 μmol, 30 Eq, 50 μL) and CF_3CO_2H (6.58 μmol, 5 Eq, 50 μL) in D_2O/[D_7]DMF 1:9 were added. The reaction mixture was heated at 50 °C for 3 days and the full conversion was monitored by ^{19}F NMR. The reaction was then quenched with Et_2O (5 mL) in order to achieve NP precipitation. The black solid then was washed with MeOH/Et_2O 1:6 using the same procedure described above. A sample of pure NPs (8.8 mg) was obtained after evaporation under vacuum.

5.5.2 Full sweep width ^{19}F NMR spectra of the exchange from AuNP-22e to AuNP-21
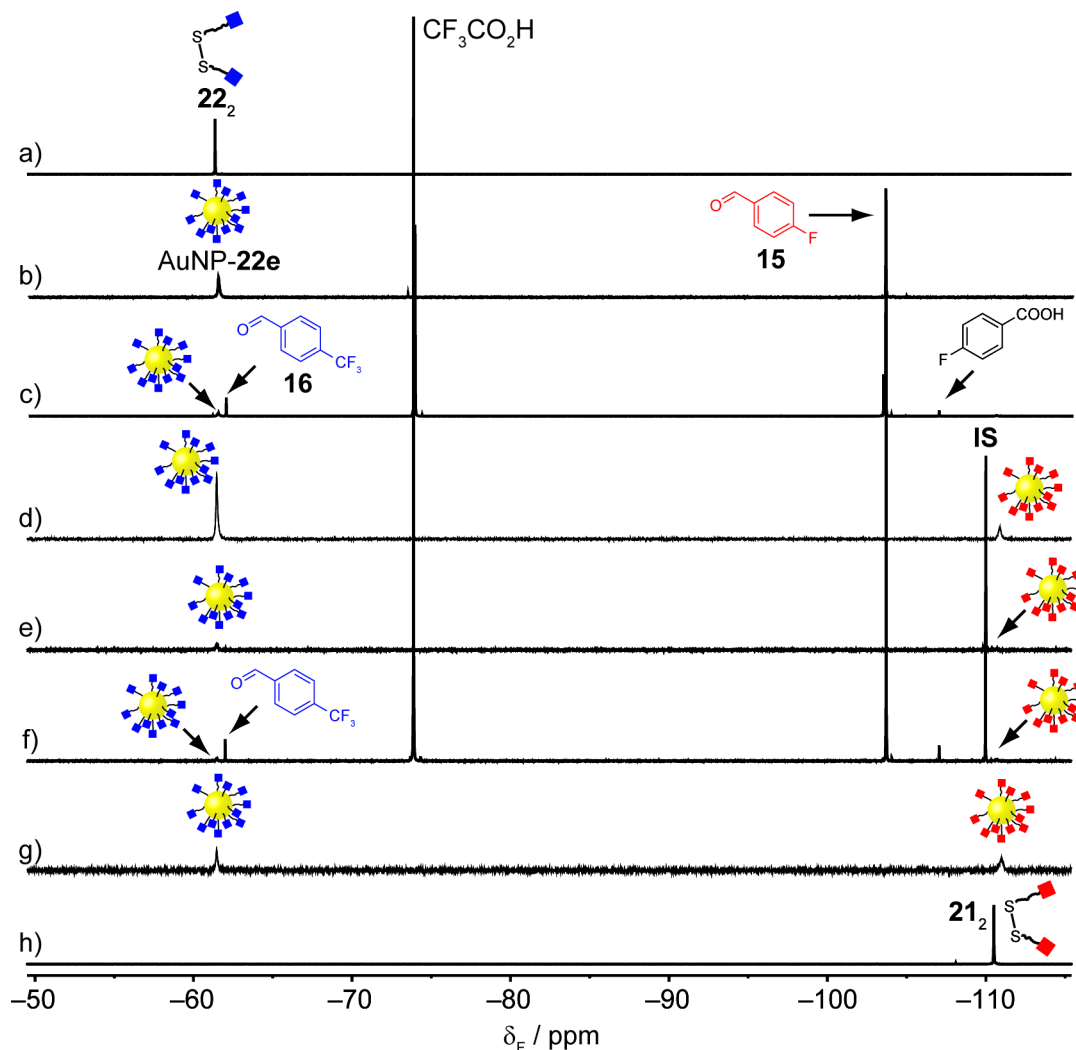
Figure 5.8 ^{19}F NMR (a, d, g, h: [D$_7$]DMF; b, c, e, f D$_2$O/[D$_7$]DMF 1:9, 470.5 MHz, 295 K) for hydrazone exchange from AuNP-**22e** to AuNP-**21**. a): Disulfide **22**$_2$. b): AuNP-**22e**. c): Crude sample after exchange with 4-fluorobenzaldehyde **15** (10 Eq). d): Purified sample after exchange: AuNP-**21**$_{0.5}$**22**$_{0.5}$. e): Crude sample after a second round of exchange with 4-fluorobenzaldehyde **15** (30 Eq). f): Purified sample after the second exchange, before NP precipitation. g): Purified sample after second round of exchange: AuNP-**21**$_{0.74}$**22**$_{0.26}$ h): Disulfide **21**$_2$. **IS**: 3-fluoronitrobenzene.

5.5.3 LDI-MS analysis: AuNP-21$_{0.74}$22$_{0.26}$

For fragmentation pattern of AuNP-**21** and AuNP-**22e** see Figures **2.12** and **5.7**.[76] The formation of a mixed monolayer for AuNP-**21**$_{0.74}$**22**$_{0.26}$ was confirmed by observation of ions corresponding to each of the parent thiolates (**21**H and **22**H), homodisulfides (**21**$_2$ and **22**$_2$) and mixed disulfide (**21**•**22**).
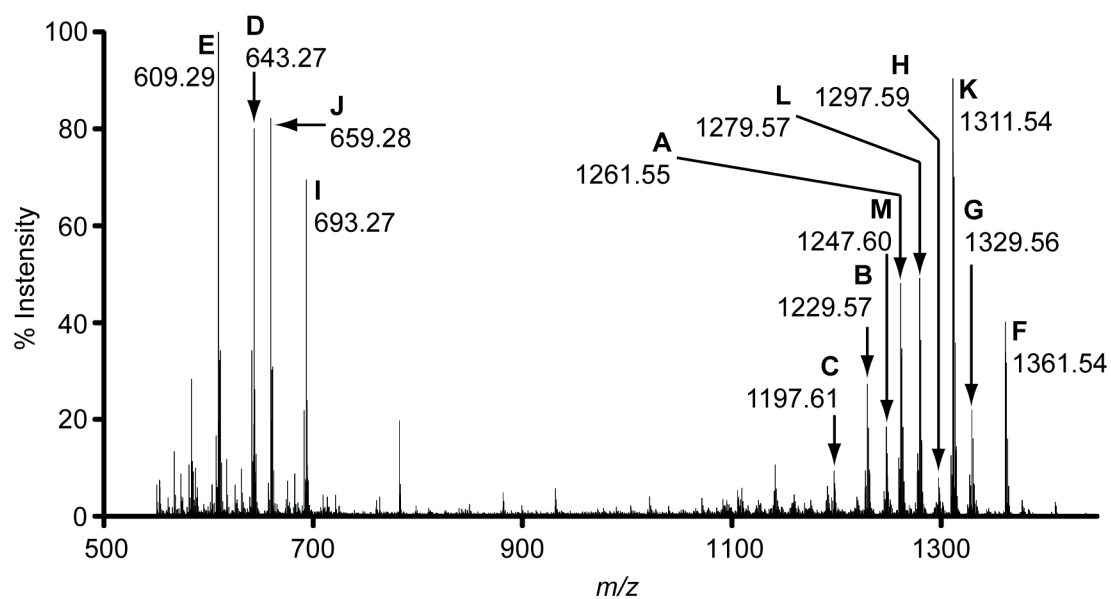
Figure 5.9 LDI mass spectrum of AuNP-$21_{0.74}22_{0.26}$. A): $[21_2+Na]^+$: m/z 1261.55. B): $[21_2–S+Na]^+$: m/z 1229.57. C): $[21_2–2S+Na]^+$: m/z 1197.61. D): $[21H+Na]^+$: m/z 643.27. (E): $[21H–H_2S+Na]^+$: m/z 609.29. F): $[22_2+Na]^+$: m/z 1361.54. G): $[22_2–S+Na]^+$: m/z 1329.56. H): $[22_2–2S+Na]^+$: m/z 1297.59. I): $[22H+Na]^+$: m/z 693.27. J): $[22–H_2S+Na]^+$: m/z 659.28. K): $[21•22+Na]^+$: m/z 1311.54. L): $[21•22–S+Na]^+$: m/z 1279.57. M): $[21•22–2S+Na]^+$: m/z 1247.60.

5.5.4   Nanoparticulate structural characterisation: AuNP-21$_{0.74}$22$_{0.26}$
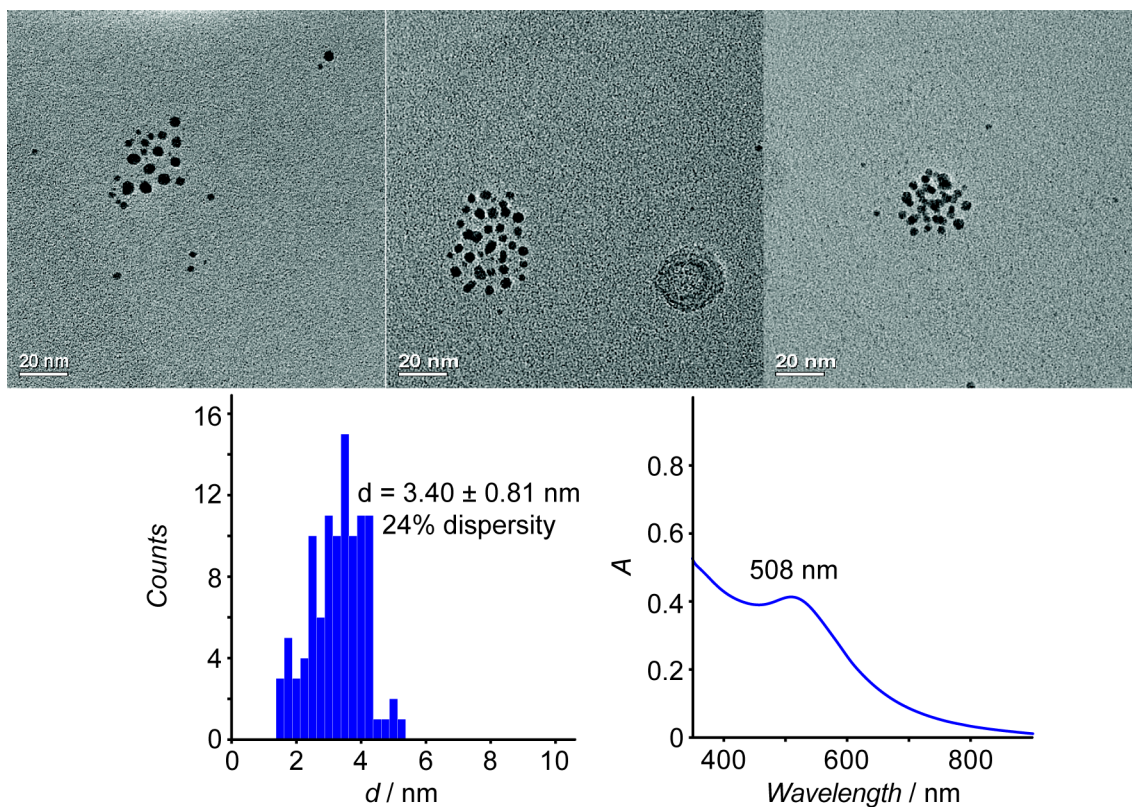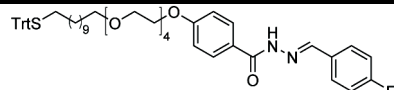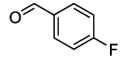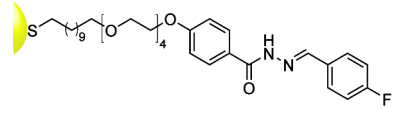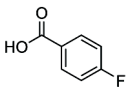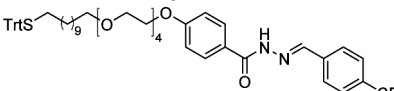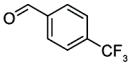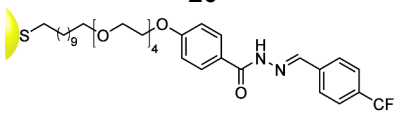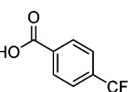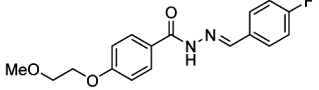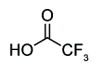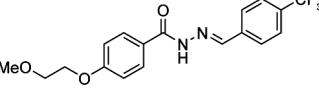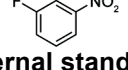

Figure 5.10   Representative TEM micrographs of AuNP-**21**$_{0.74}$**22**$_{0.26}$ (scale bar 20 nm), size distribution (diameter 3.40 ± 0.81, 24% dispersity) and UV-Vis spectrum (SPR λ_{max} = 508 nm).

5.6 Kinetic studies by ^{19}F NMR spectroscopy

5.6.1 Relaxation times

Longitudinal relaxation times (T_1) for ^{19}F signals were determined by inversion-recovery method in order to set appropriate pulse delay times ($\geq 5 \times T_1$) for quantitative NMR experiments.

Table 5.1   Relaxation times for quantitative ^{19}F NMR experiments in D_2O/[D_7]DMF 1:9 at rt.

Compound	T_1 / s	Compound	T_1 / s
19	0.92	**15**	3.47[a]
AuNP-**21**	0.68		2.47
20	1.18	**16**	1.73
AuNP-**22e**	0.96		3.04
23	1.07		2.33
24	0.91	**Internal standard**	3.24

[a]: Longest T_1. The ^{19}F NMR quantitative experiment was set with a delay time of 22 s.

5.6.2 Kinetic measurements and deconvolution data

5.6.2.1 Hydrolysis of AuNP-21

Hydrazone hydrolysis was examined starting from AuNP-**21** in 10% D_2O/[D_7]DMF. The concentration of **21** was assessed by ^{19}F NMR in the presence of 1-fluoro-3-nitrobenzene (internal standard), then the reaction triggered by addition of CF_3CO_2H (5 Eq with respect to **21**). Reaction progress was assessed by deconvoluting

signals corresponding to both the NP-bound hydrazone **21** and released 4-fluorobenzaldehyde **15** (Figure **5.11**).
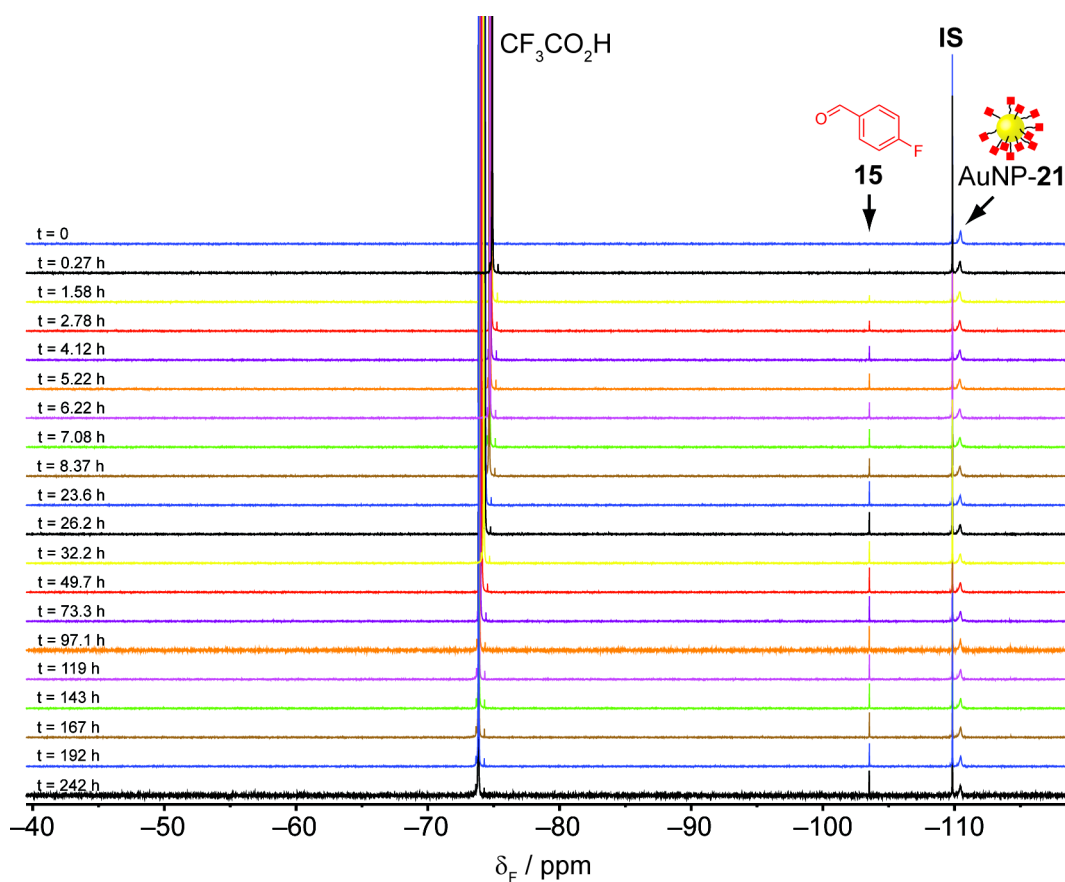

Figure 5.11   Stacked ^{19}F NMR spectra (D$_2$O/[D$_7$]/DMF 1:9, 470.5 MHz, 295 K, 16 scans, D1: 22 s) of the hydrolysis of AuNP-**21** at rt recorded for 242 h. Conditions: CF$_3$CO$_2$H (5 Eq), D$_2$O/[D$_7$]/DMF 1:9, rt. **IS**: 1-fluoro-3-nitrobenzene (4.95 mM).

5.6.2.2 Hydrolysis of AuNP-22e

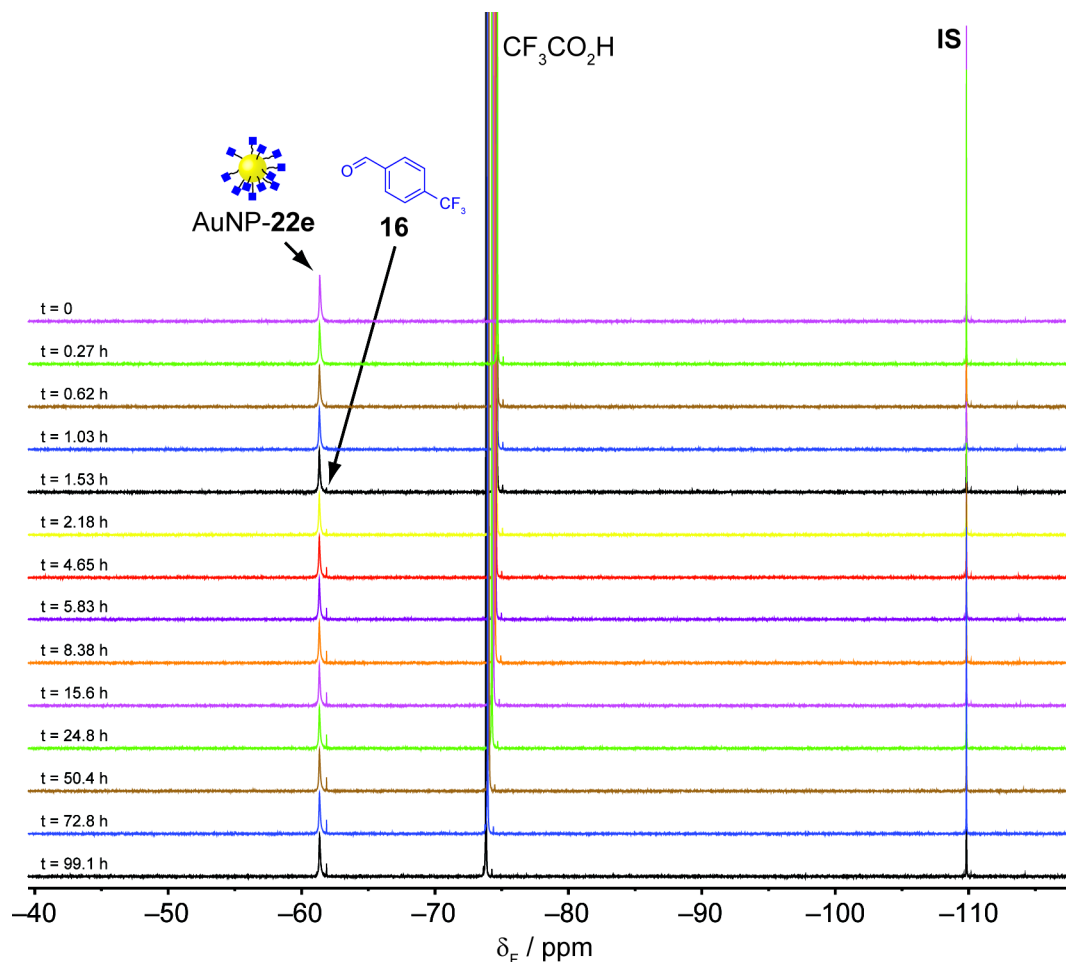Hydrolysis of AuNP-**22e** was examined with the same procedure adopted for AuNP-**21** (see Section **5.6.2.1**).

Figure 5.12   Stacked ^{19}F NMR spectra (D$_2$O/[D$_7$]/DMF 1:9, 470.5 MHz, 295 K, 16 scans, D1: 22 s) of the hydrolysis of AuNP-**22e** at rt recorded for 99 h. Conditions: CF$_3$CO$_2$H (5 Eq), D$_2$O/[D$_7$]/DMF 1:9, rt. **IS**: 1-fluoro-3-nitrobenzene (4.95 mM).

5.6.2.3 Equimolar exchange from AuNP-21 to AuNP-22e

In a similar manner to the hydrolysis reactions (Sections **5.6.2.1**–**2**), hydrazone exchange in the presence 4-(trifluoromethyl)benzaldehyde **16** (1 Eq) was tracked in real time for AuNP-**21**. Figure **5.13** shows the ^{19}F NMR spectra for a characteristic equimolar exchange experiments from AuNP-**21**. After the addition of **16** and CF$_3$CO$_2$H, a gradual decrease in intensity of the peaks corresponding to NP-bound **21** and free **16** was observed, together with an associated increase in the peaks corresponding to NP-bound **22** and displaced 4-fluorobenzaldehyde **15**.
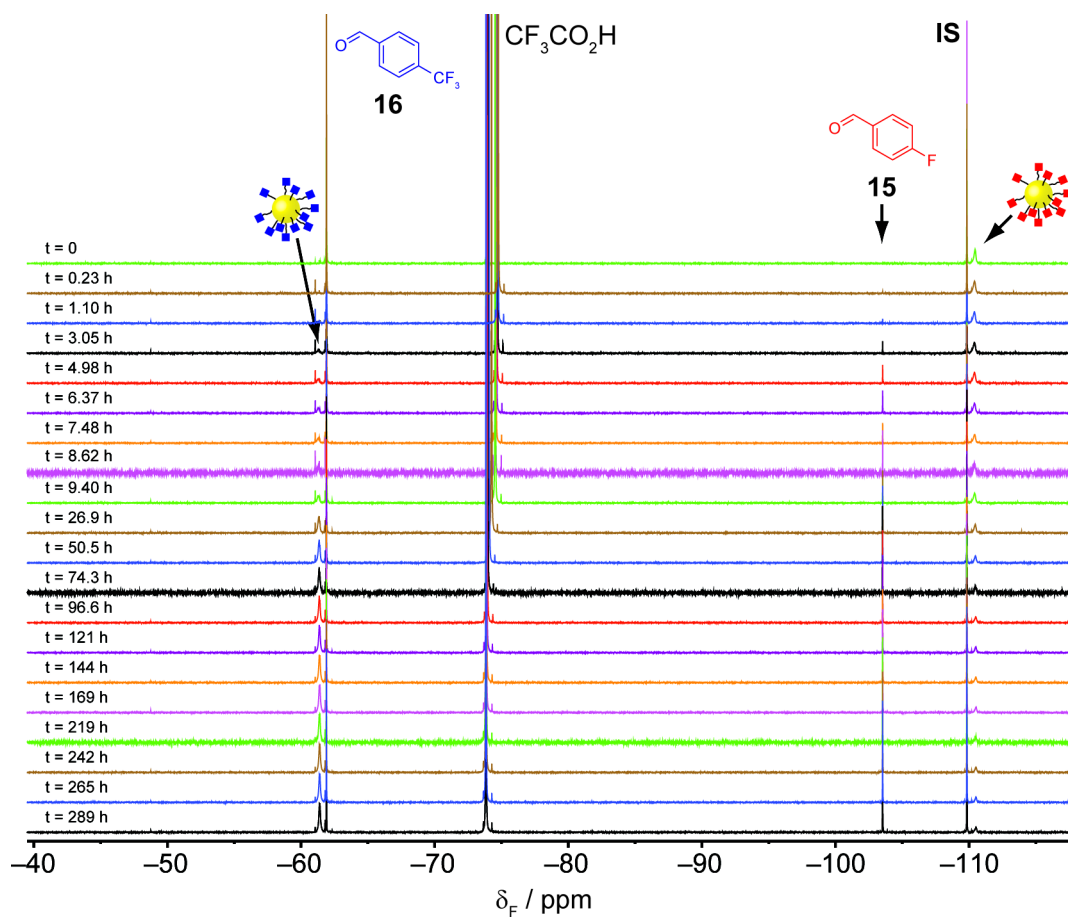
Figure 5.13   Stacked ^{19}F NMR spectra (D$_2$O/[D$_7$]DMF 1:9, 470.5 MHz, 295 K, 16 scans, D1: 22 s) of the exchange of AuNP-**21** at rt recorded for 289 h. Conditions: **16** (1 Eq), CF$_3$CO$_2$H (5 Eq), D$_2$O/[D$_7$]DMF 1:9, rt. **IS**: 1-fluoro-3-nitrobenzene (4.95 mM).

5.6.2.4 Equimolar exchange from AuNP-22e to AuNP-21

Equimolar exchange starting from AuNP-**22e** was examined with the same procedure adopted for AuNP-**21** (Section **5.6.2.3**).
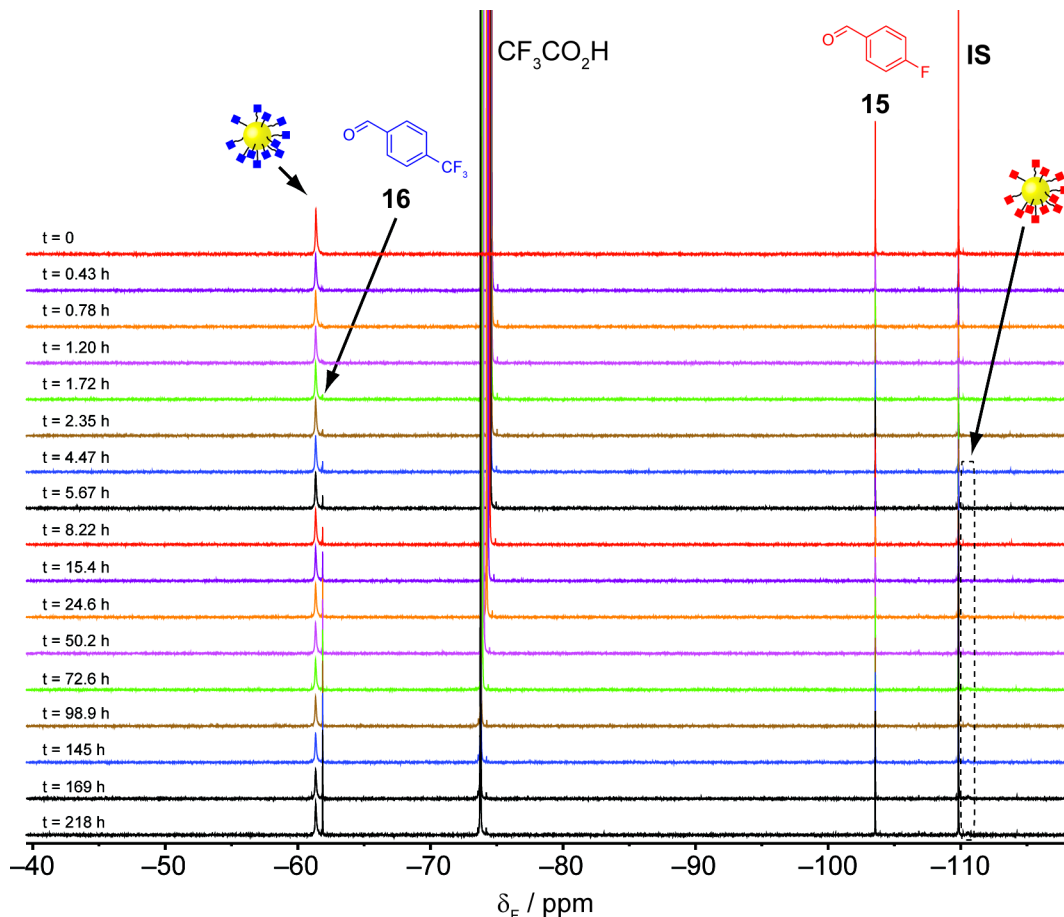

Figure 5.14   Stacked ^{19}F NMR spectra (D$_2$O/[D$_7$]DMF 1:9, 470.5 MHz, 295 K, 16 scans, D1: 22 s) of the exchange of AuNP-**22e** at rt recorded for 218 h. Conditions: **15** (1 Eq), CF$_3$CO$_2$H (5 Eq), D$_2$O/[D$_7$]DMF 1:9, rt. **IS**: 1-fluoro-3-nitrobenzene (4.95 mM).

5.6.3   Fitting of the hydrolysis experiments by COPASI®[198]

The COPASI® software package was used to determine the appropriate set of differential equations to which the experimental data could be fit in order to obtain estimates of the rate constants k_1 and k_2.[198]

Hydrolysis experiments were fit using Equation **3.1** (see Sections **5.6.3.1**–**4**). The kinetic constant values are summarised in Tables **3.1**–**3**.
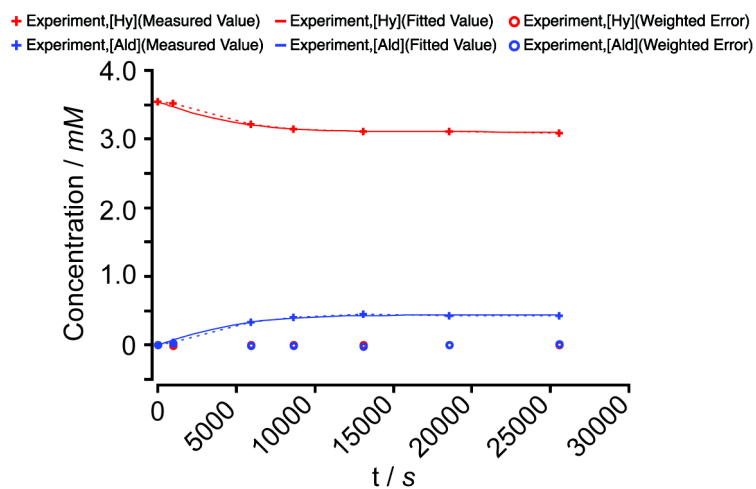
5.6.3.1 Hydrolysis of hydrazone 23

Figure 5.15   Representative example of the experimental data for the hydrolysis of model hydrazone **23** (Table **3.1**, entry *a*) fitted with COPASI®.

Figure 5.16   Global fitting by COPASI® for the hydrolysis of model hydrazone **23** (Table **3.1**, entries *a–c*). The calculated *k* values are shown in Table **3.1**, entry *d*.

5.6.3.2 Hydrolysis of model hydrazone 24

Figure 5.17   Representative example of the experimental data for the hydrolysis of model hydrazone **24** (Table **3.1**, entry *e*) fitted with COPASI®.
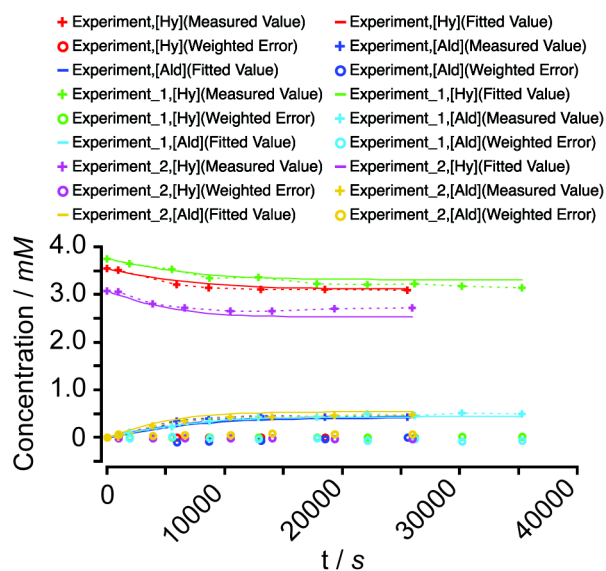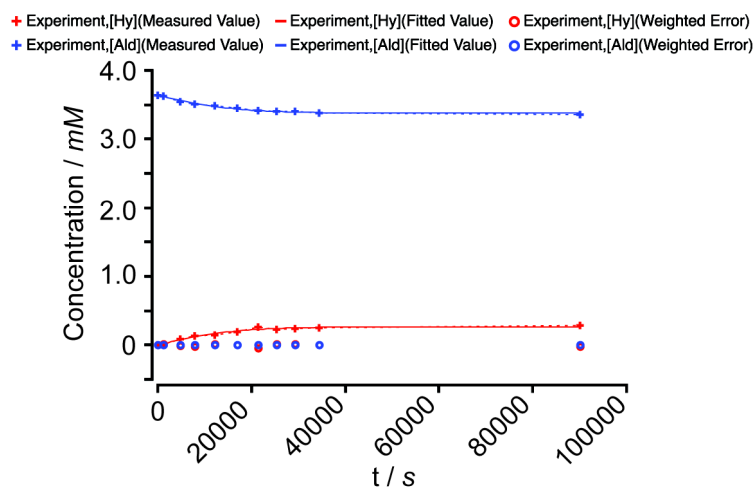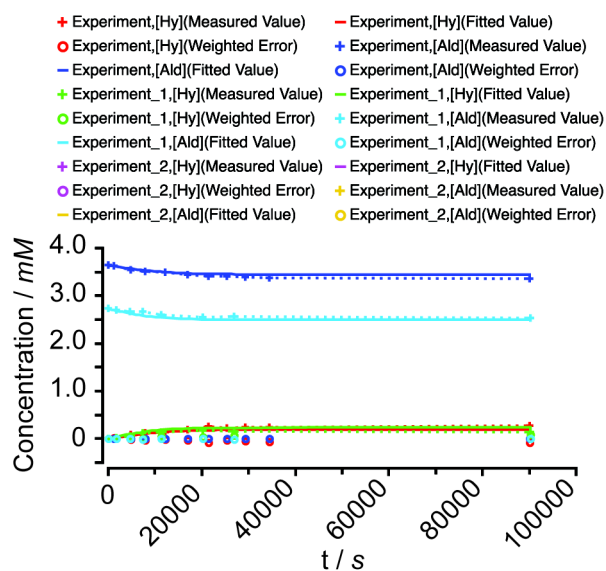

Figure 5.18   Global fitting by COPASI® for the hydrolysis of model hydrazone **24** (Table **3.1**, entries *e*–*g*). The calculated *k* values are shown in Table **3.1**, entry *h*.

5.6.3.3 Hydrolysis of AuNP-21
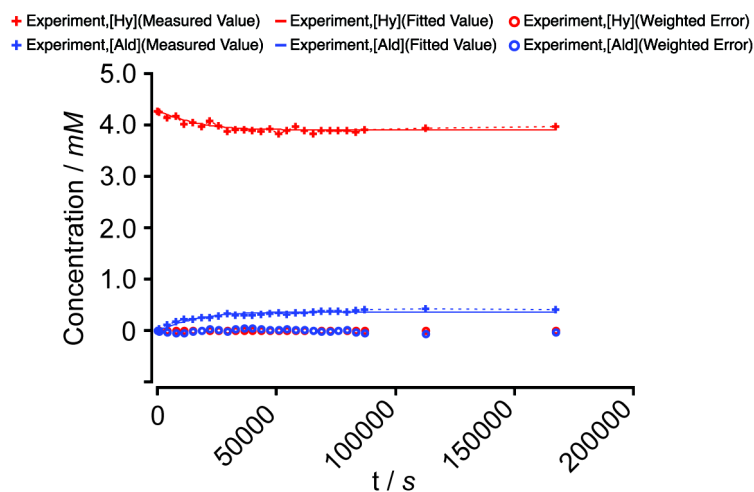
Figure 5.19   Representative example of the experimental data for the hydrolysis of AuNP-**21** (Table **3.2**, entry *b*) fitted with COPASI®.

5.6.3.4 Hydrolysis of AuNP-22e
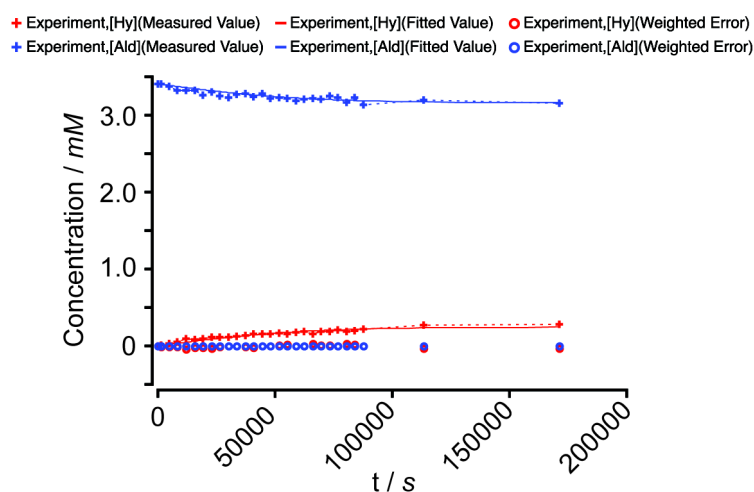
Figure 5.20   Representative example of the experimental data for the hydrolysis of AuNP-**22e** (Table **3.3**, entry *b*) fitted with COPASI®.

5.6.4 Fitting of the exchange experiments

In a preliminary stage, the rate constants calculated for the individual hydrolysis experiments of molecular compounds **23** and **24** (Table **3.1**, entries *d* and *h*) were used for generating a model with Equations **5.1** and **5.2**. In fact, the general hydrazone mechanism could be described as the combination of two reversible hydrolysis reactions for the hydrazone starting material and product.
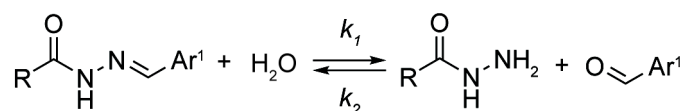
Equation 5.1
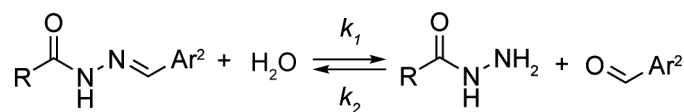
Equation 5.2

Ideally, the rate constants would have described the hydrazone exchange. Surprisingly, it was observed that the model was able to simulate the experimental data only for the first ten hours from the CF_3CO_2H triggering (Figure **5.21**). After, a deviation from the experimental data was consistently observed for both NP-bound and unbound hydrazones.

For this reason, exchange experiments were fit according to the mechanism of Equation **3.4** (see Sections **5.6.4.1**–**3**).

The kinetic constant values are summarised in Tables **3.4**–**6**.
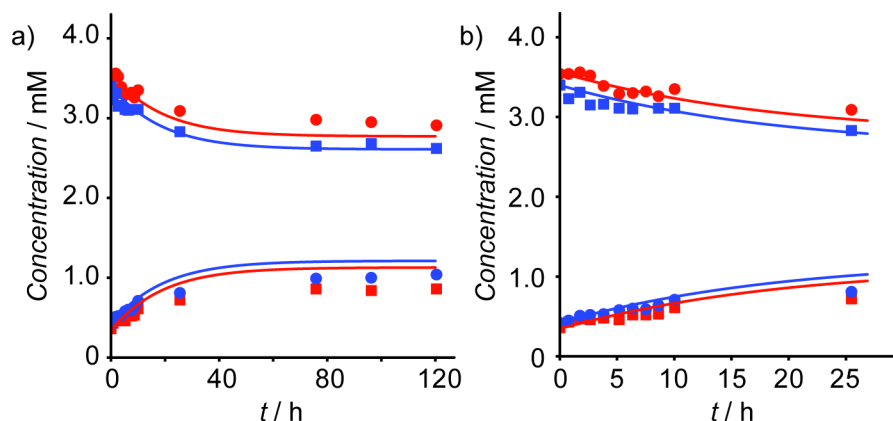
Figure 5.21   Kinetic profile for hydrazone exchange with compound **23** and **24**. Conditions: **23** (0.1 Eq), **24** (0.9 Eq), 4-fluorobenzaldehyde **15** (0.9 Eq), 4-(trifluoromethyl)benzaldehyde **16** (0.1 Eq), CF_3CO_2H (5.1 Eq), D_2O/DMF 1:9, rt. ■ : **23**. ■ : **24**. ● : 4-Fluorobenzaldehyde **15**. ● : 4-(Trifluoromethyl)benzaldehyde **16**. Full lines: fitting by COPASI®: hydrolysis of **23**: $k_1 = 2.50 \times 10^{-9}$ $mM^{-1}s^{-1}$ and $k_2 = 2.40 \times 10^{-4}$ $mM^{-1}s^{-1}$; hydrolysis of **24**, $k_1 = 7.59 \times 10^{-10}$ $mM^{-1}s^{-1}$ and $k_2 = 3.85 \times 10^{-4}$ $mM^{-1}s^{-1}$.

5.6.4.1 Equimolar exchange with molecular hydrazones 23 and 24
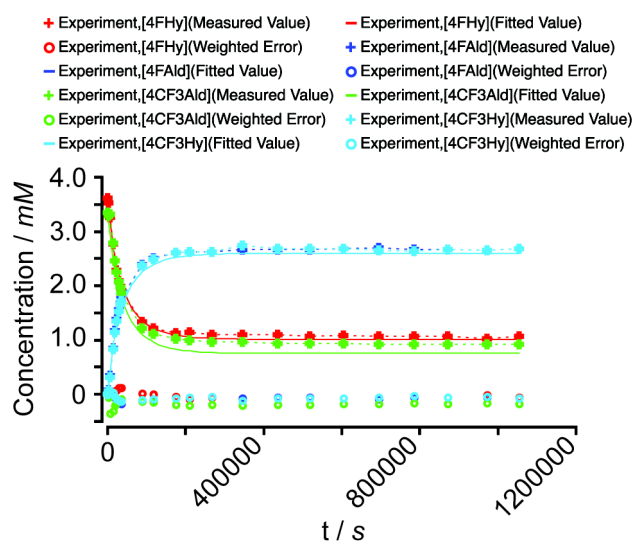
Figure 5.22   Global fitting by COPASI® for the equimolar exchange between **23** and **24** from three repeated experiments (Table **3.4**, entries *a–c*). The calculated *k* values are shown in Table **3.4**, entry *d*).

5.6.4.2 Equimolar exchange from AuNP-21 to AuNP-22e
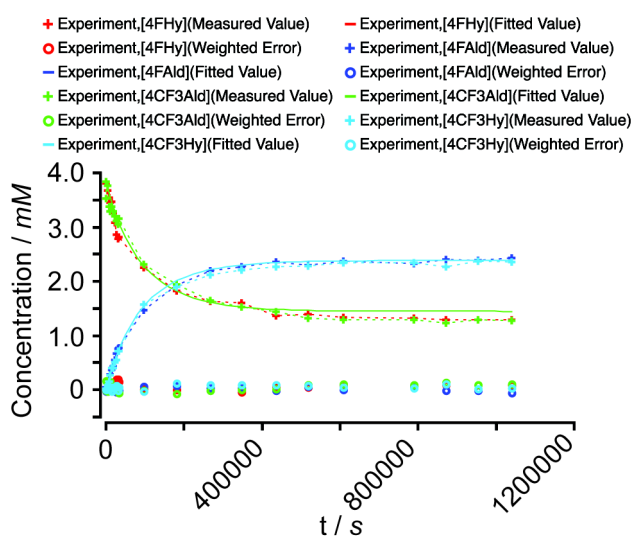
Figure 5.23   Equimolar exchange from AuNP-**21** to AuNP-**22e** (Table **3.5**, entry *a*) fitted with COPASI®.

5.6.4.3 Equimolar exchange from AuNP-22e to AuNP-21
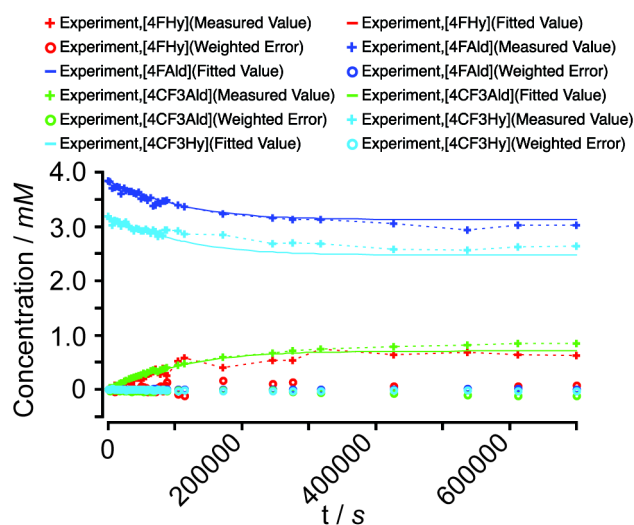
Figure 5.24   Equimolar exchange from AuNP-**22e** to AuNP-**21** (Table **3.6**, entry *b*) fitted with COPASI®.

5.7 Comparison of dynamic covalent hydrazone exchange with monolayer ligand exchange

Dynamic hydrazone exchange and monolayer ligand exchange in the NP monolayer occur *via* quite different mechanisms, making quantitative comparison of kinetics challenging. For this reason, the two processes were analysed under analogous conditions (same starting concentration of the NP-bound ligand **21** and same excess of the exchange unit, aldehyde **16** or disulfide **22**$_2$) at 50 °C. For an additional comparison, a further exchange experiment using molecular compound **24** at 50 °C was also performed. The experiments were monitored by ^{19}F NMR spectroscopy as described in Section **5.6**.

Experimental conditions:

- Ligand exchange: AuNP-**21** (1.95 μmol with respect to **21**, 500 μL), **22**$_2$ (19.5 μmol, 50 μL, 20 Eq excess with respect to **21**), D$_2$O/DMF 1:9, 50 °C.

- Hydrazone exchange: AuNP-**21** (2.01 μmol with respect to **21**, 500 μL), **16** (40.2 μmol, 50 μL, 20 Eq excess), CF$_3$CO$_2$H (10.1 μmol, 50 μL, 5.0 Eq), D$_2$O/DMF 1:9, 50 °C.

- Hydrazone exchange with molecular compound: **24** (1.52 μmol, 500 μL), **16** (30.3 μmol, 50 μL, 20 Eq excess), CF$_3$CO$_2$H (7.58 μmol, 50 μL, 5.0 Eq excess), D$_2$O/DMF 1:9, 50 °C.

The two processes where compared by using the half-life, calculated in, respectively, 17.9, 4.1 and 2.1 h, confirming that ligand exchange is slower when compared to hydrazone exchange (both for NP-bound and unbound species). In addition, ligand exchange is also less efficient since it proceeds to 63% exchange while hydrazone exchange (in the NP-bound monolayer) proceeds to 86% exchange.

The ligand exchange process using 1 Eq of ligand **22** at rt in D_2O/DMF 1:9 provides < 3% exchange, even after an extended reaction time of 48 h.

5.8 Solubility switching between AuNP-21, AuNP-30 and AuNP-31

Switching between each of AuNP-**21**, AuNP-**30** and AuNP-**31** could be achieved in either direction. The solvent compatibility properties of each species were independent from the route to produce it (Scheme **5.1**).
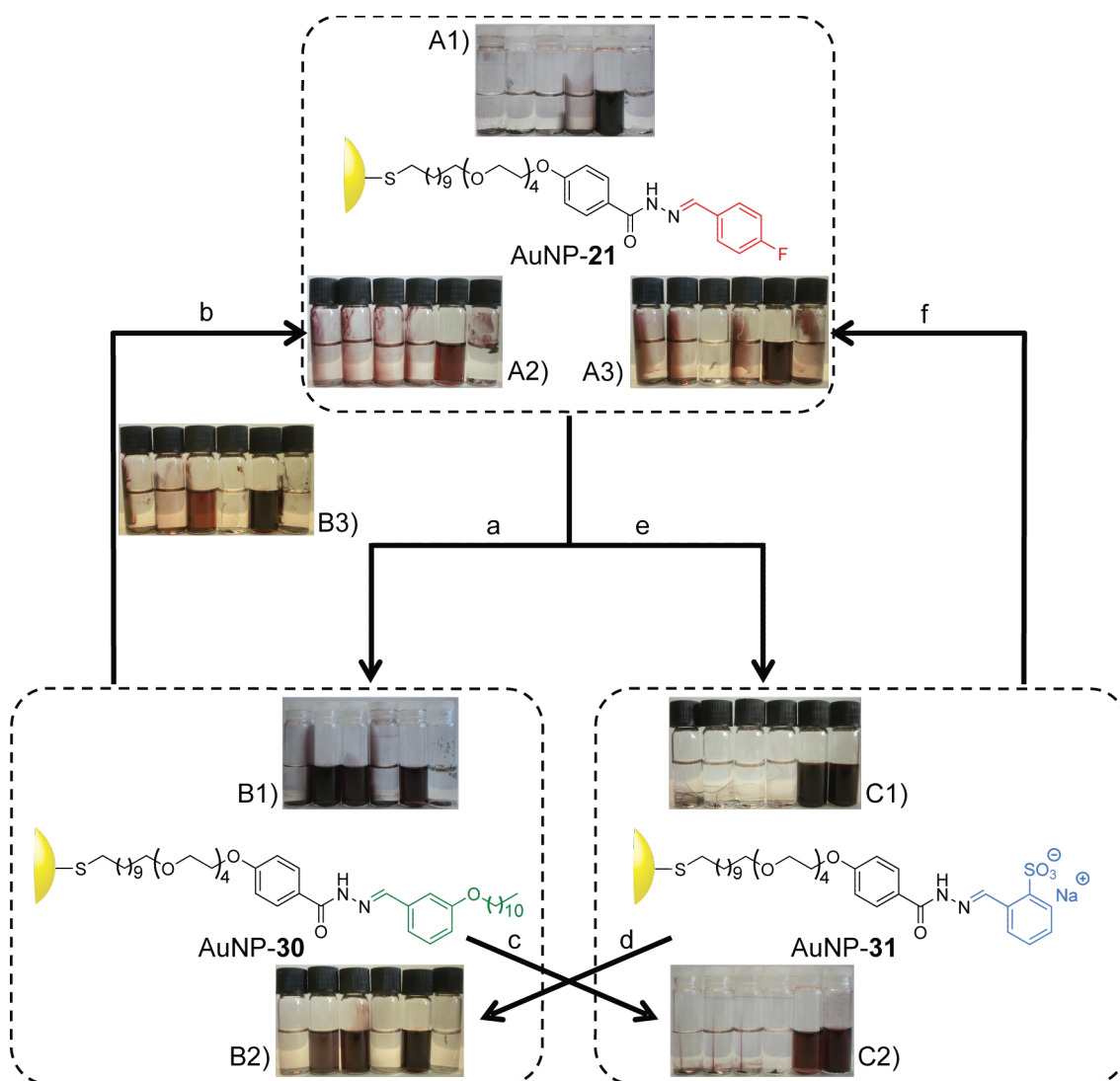
Scheme 5.1   a): 3-(Undecyloxy)benzaldehyde **28** (20 Eq), CF$_3$CO$_2$H (5 Eq), D$_2$O/[D$_7$]DMF 1:9, 1.5 h, 50 °C. b): 4-Fluorobenzaldehyde **15** (20 Eq), CF$_3$CO$_2$H (5 Eq), D$_2$O/[D$_7$]DMF 1:99, overnight, 50 °C, purify, repeat. c): 2-Formylbenzene sulfonic acid sodium salt **29** (20 Eq), CF$_3$CO$_2$H (5 Eq), D$_2$O/[D$_8$]THF 5:95, 1 h, 50 °C. d): 3-(Undecyloxy)benzaldehyde **28** (20 Eq), CF$_3$CO$_2$H (5 Eq), D$_2$O/[D$_8$]THF 1:9, 1 h, 50 °C. e): 2-Formylbenzene sulfonic acid sodium salt **29** (20 Eq), CF$_3$CO$_2$H (5 Eq), D$_2$O/[D$_7$]DMF 1:9, overnight, 50 °C. f): 4-Fluorobenzaldehyde **15** (20 Eq), CF$_3$CO$_2$H (5 Eq), D$_2$O/[D$_7$]DMF 1:9, overnight, 50 °C. Solvents (from left to right) in the inset pictures: hexane, CHCl$_3$, THF, MeOH, DMF, water.

5.8.1 Solubility switching between AuNP-21 (polar organic) and AuNP-30 (apolar organic)
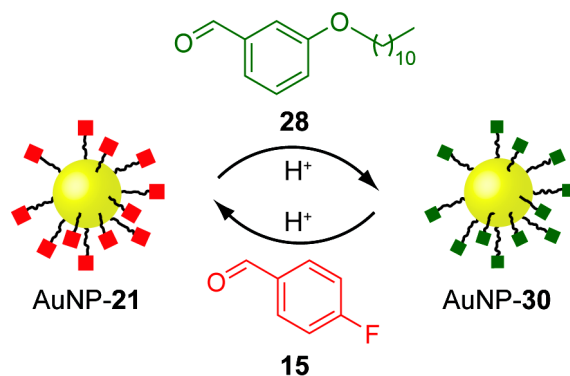
Aldehyde **28** (91.6 μmol, 20 Eq, 50 μL) and CF_3CO_2H (22.9 μmol, 5 Eq, 50 μL) were added to a solution of AuNP-**21** (4.58 μmol in terms of ligand **21**, 500 μL) in D_2O/[D_7]DMF 1:9. The reaction mixture was heated at 50 °C for 1.5 h after which full precipitation of NPs had resulted. The supernatant was analysed by ^{19}F NMR to determine unbound molecular species before removal (Figure **4.1**). The resulting black solid was then re-suspended in MeOH (1 mL), HexH (7 mL) was added to induce NP flocculation and the resulting suspension was sonicated for 15 min. Precipitated NPs were recovered by centrifugation (4000 rpm, 5 °C, 10 min). This operation was repeated three times and pure AuNP-**30** was afforded. Mean diameter: 2.82 ± 0.48 nm (18% dispersity). SPR λ_{max} = 508 nm (in $CHCl_3$).

^1H NMR (500.1 MHz, $CDCl_3$): δ 0.46–2.33 (m, CH_2), 2.92–4.55 (m, CH_2O), 6.40–6.93 (m, H_{Ar}), 6.96–7.49 (m, H_{Ar}), 7.45–8.24 (m, H_{Ar}), 8.75 (bs, 1H, CH=), 11.94 (bs, 1H, NH) ppm.

5.8.1.1 LDI-MS analysis of AuNP-30

LDI-MS analysis was performed as discussed in Section **5.4.4**.[76] Peaks corresponding to AuNP-**21** are barely visible, while the relative abundance of the peaks corresponding to the heterodisulfide **21•30** is not more than 10% (Figure **5.25**). LDI-MS analysis further confirms that the exchange is almost complete.
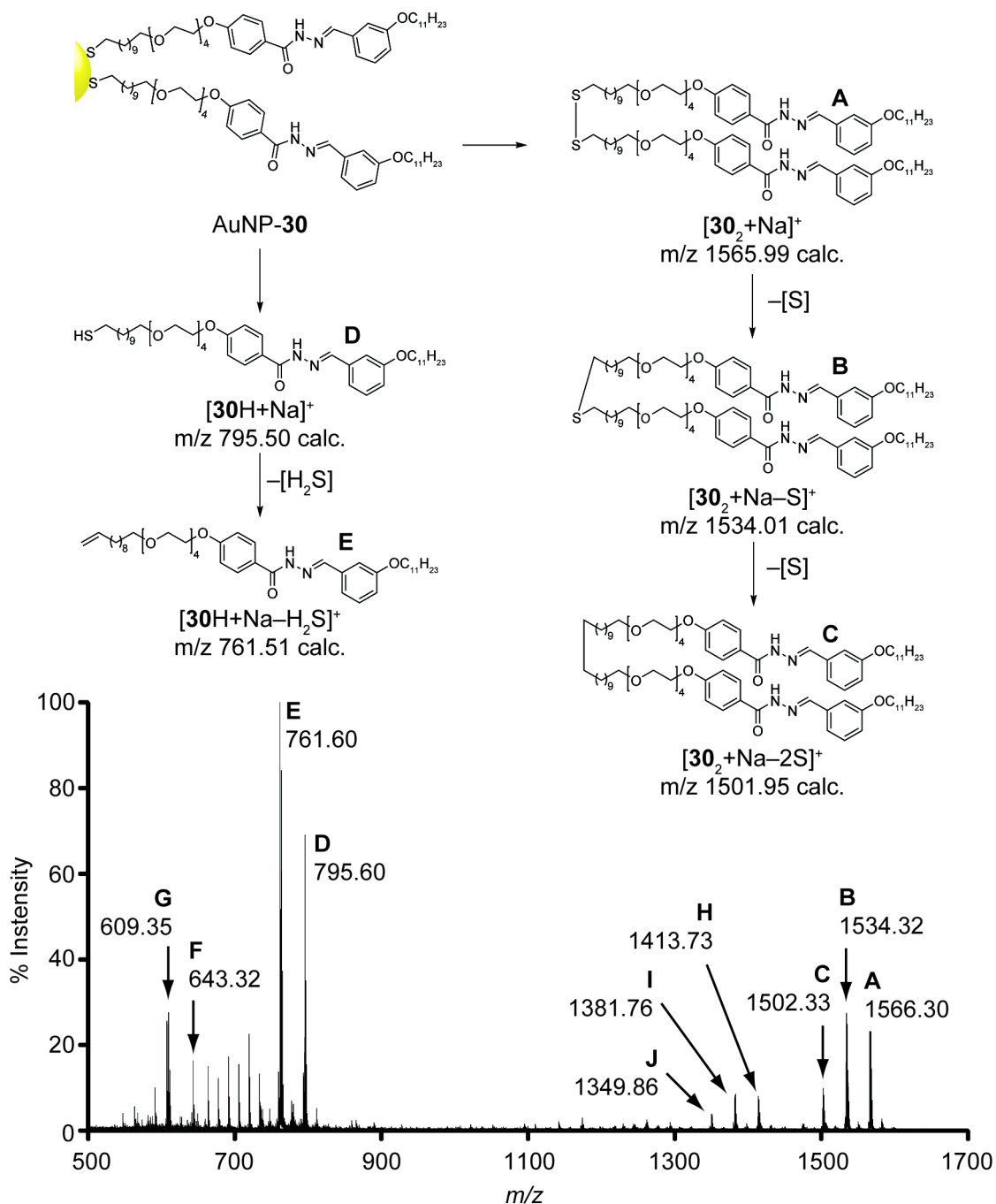
Figure 5.25 LDI mass spectrum and fragmentation pattern for AuNP-**30**. The ion corresponding to the disulfide of ligand **30** (peak A, [**30**$_2$+Na]$^+$: m/z 1566.30) undergoes a progressive loss of two sulfur atoms (peak B, [**30**$_2$–S+Na]$^+$: m/z 1534.32; peak C, [**30**$_2$–2S+Na]$^+$: m/z 1502.33). The ion corresponding to thiol **30**H (peak D, [**30**H+Na]$^+$: m/z 795.60) loses H$_2$S (peak E, [**30**H–H$_2$S+Na]$^+$: m/z 761.60), followed by progressive loss of CH$_2$ units. F): [**21**H+Na]$^+$: m/z 643.32. G): [**21**H–H$_2$S+Na]$^+$: m/z 609.35. H): [**21**•**30**+Na]$^+$: m/z 1413.73. I): [**21**•**30**–S+Na]$^+$: m/z 1381.76. J): [**21**•**30**–2S+Na]$^+$: m/z 1349.86.

5.8.1.2 Nanoparticulate structural characterisation: AuNP-30
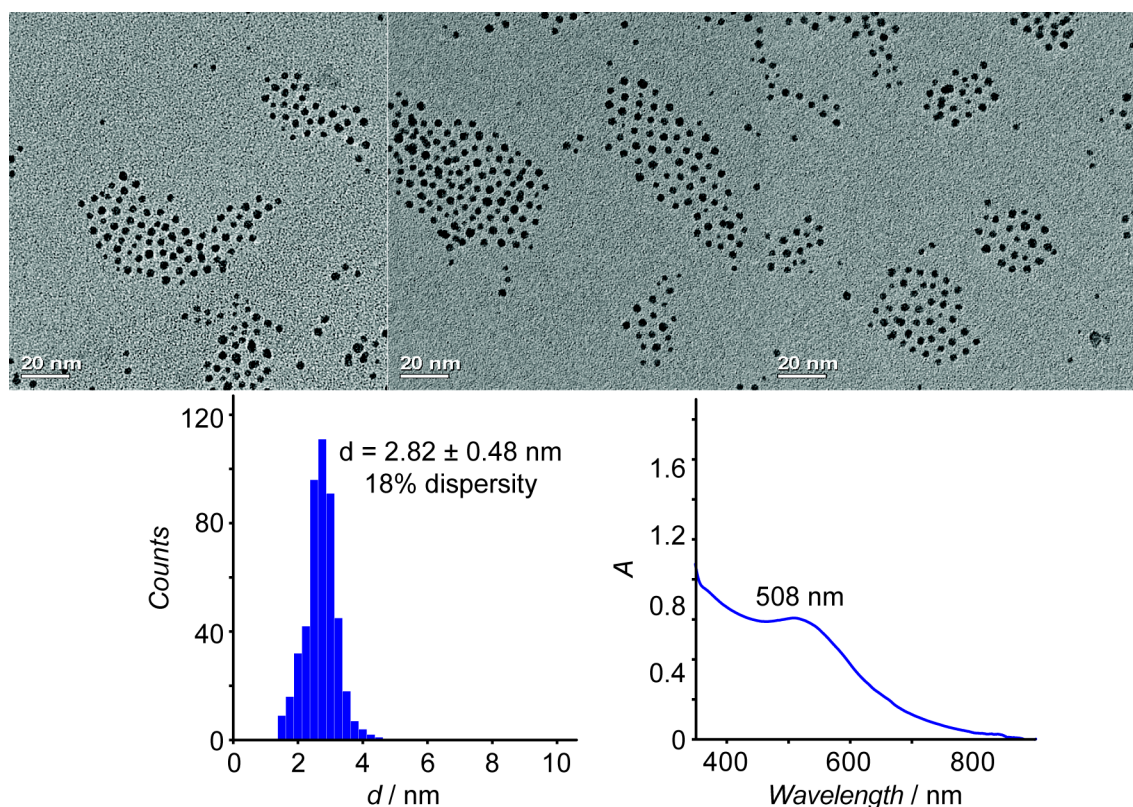
Figure 5.26   Representative TEM images of AuNP-**30** (scale bar 20 nm), size distribution (diameter 2.82 ± 0.48 nm, 18% dispersity) and UV-Vis spectrum (SPR λ_{max} = 508 nm).

5.8.1.3 Reversibility of the exchange (apolar organic to polar organic)

4-Fluorobenzaldehyde (33.8 μmol, 20 Eq, 50 μL) and CF_3CO_2H (8,45 μmol, 5 Eq, 50 μL) were added to a solution of AuNP-**30** (1.69 μmol in terms of ligand **30**, 500 μL) in D_2O/[D_7]DMF 1:99. The reaction mixture was heated at 50 °C overnight. The dark red solution was analysed by ^{19}F NMR to confirm the presence of AuNP-**21**. Then Et_2O was added to induce NP precipitation. The supernatant was discarded and the resulting black solid then was washed with MeOH/Et_2O 1:7 using the following procedure: NPs were dispersed in the solvent mixture (8 mL), sonicated for 15 min, and centrifuged (4000 rpm, 5 °C, 10 min). The operation was repeated three times and clean functionalised NPs (7.51 mg) were afforded displaying solubility properties intermediate between AuNP-**30** and AuNP-**21** (Scheme **5.1B3**). NMR analysis (Figure **5.27**) revealed peaks equal to those shown in NMR spectra of AuNP-**21** prepared by direct synthesis (Section **5.3.2.2**). LDI-MS analysis revealed fragments corresponding to both ligands **21** and **30** with similar intensities (Figure **4.6**). The material was again dried and dissolved in D_2O/[D_7]DMF 1:99 (500 μL) with fresh 4-fluorobenzaldehyde

(33.8 μmol, 20 Eq, 50 μL) and CF_3CO_2H (8,45 μmol, 5 Eq, 50 μL). The mixture was heated at 50 °C overnight. After precipitation and purification as before, the sample showed identical solubility properties (Scheme **5.1A2**) to those showed by a sample of AuNP-**21** prepared as discussed in Section **5.3.2.2** (Scheme **5.1A1**).
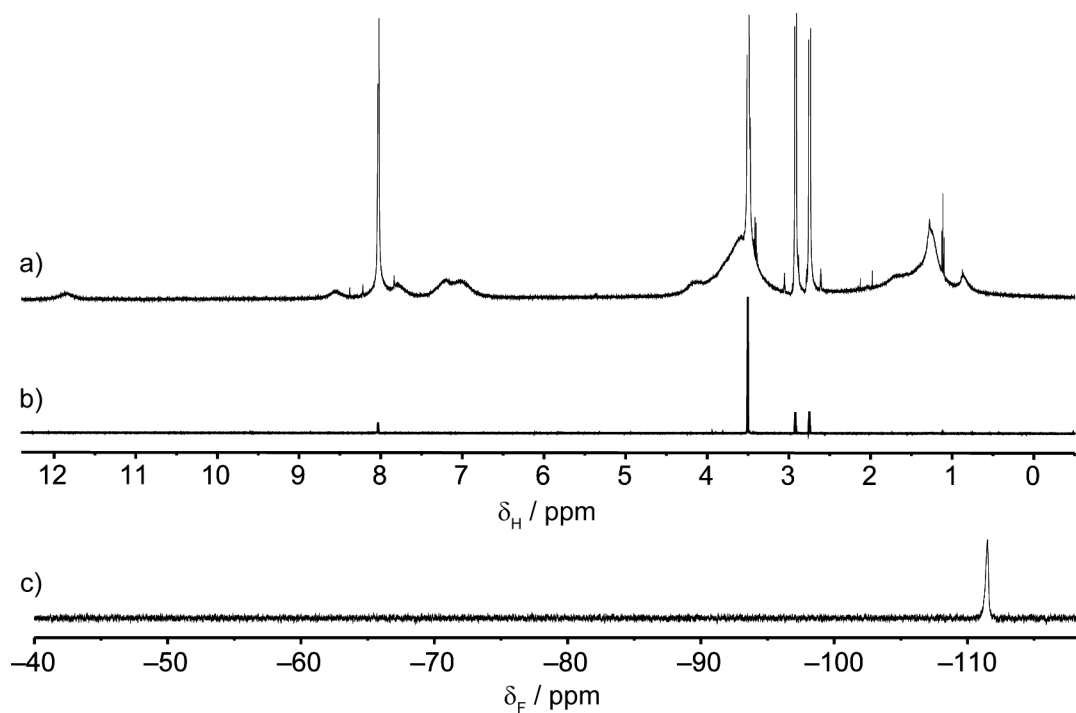
Figure 5.27   a): ^{1}H NMR ([D$_7$]DMF, 500.1 MHz, 295 K) of AuNP-**21**$_{0.9}$**30**$_{0.10}$ produced *via* exchange from AuNP-**30**. b): T_2-filtered spectrum (D21: 0.1 s). c): ^{19}F NMR ([D$_7$]DMF, 470.5 MHz, 295 K).

5.8.2 Solubility switching between AuNP-30 (apolar organic) and AuNP-31 (aqueous)
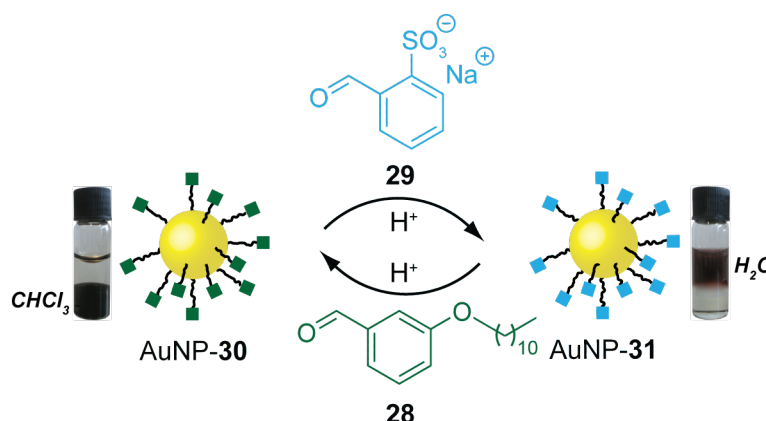
2-Formylbenzene sulfonic acid sodium salt **29** (53.5 μmol, 20 Eq, 50 μL) and CF_3CO_2H (13.4 μmol, 5 Eq, 50 μL) were added to a solution of AuNP-**30** (2.68 μmol in terms of ligand **30**, 500 μL) in D_2O/[D_8]THF 5:95. The reaction mixture was heated at 50 °C for 1 h, after which full NP precipitation had resulted. The supernatant solution was analysed by ^1H NMR to confirm the presence of displaced aldehyde **28** and then discarded. The black solid was washed with H_2O/THF 1:99 using the following procedure: NPs were dispersed in the solvent mixture (8 mL), sonicated for 15 min and centrifuged (4000 rpm, 5 °C, 10 min). The operation was repeated seven times and pure AuNP-**31** was obtained. Mean diameter: 2.62 ± 0.91 nm (35% dispersity). SPR λ_{max} = 519 nm (in H_2O).

^1H NMR (500.1 MHz, D_2O): δ 0.60–2.11 (m, CH_2), 2.58–4.19 (m, CH_2O), 6.38–8.61 (m, H_{Ar}), 9.00 (bs, 1H, CH=) ppm.

5.8.2.1 Nanoparticulate structural characterisation: AuNP-31
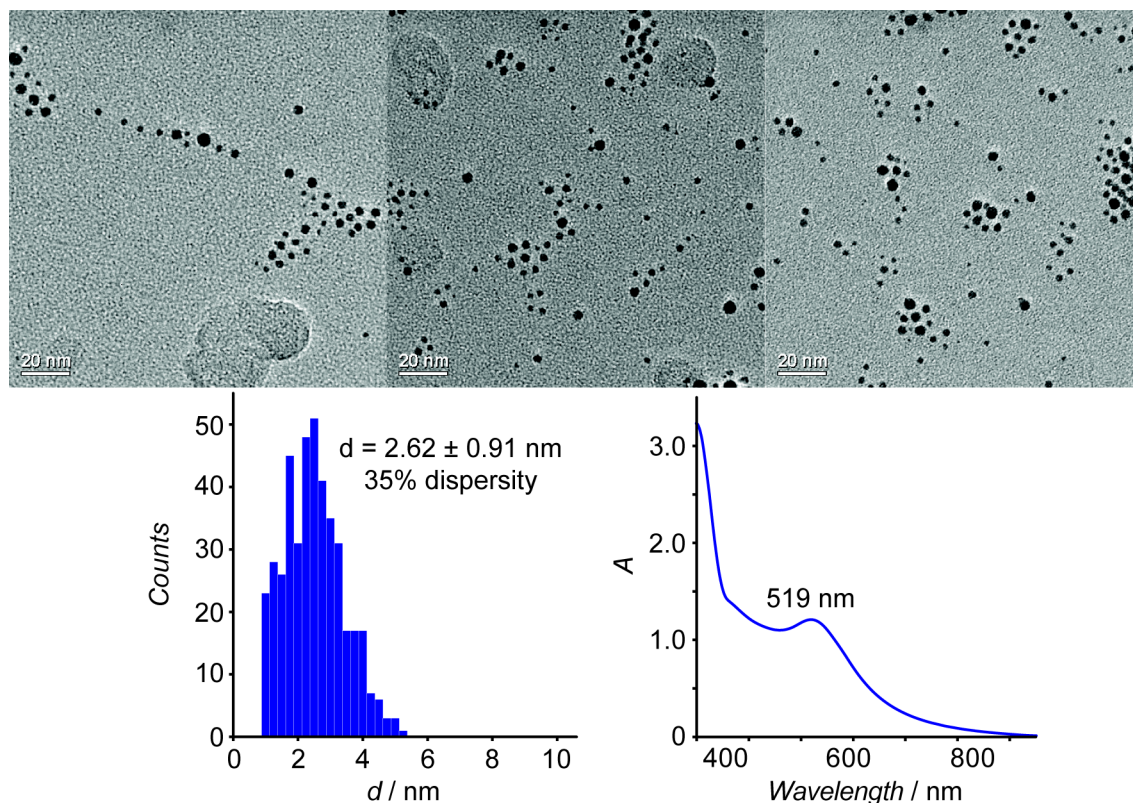
Figure 5.28　　Representative TEM images of AuNP-**31** (scale bar 20 nm). Size distribution (diameter 2.62 ± 0.91 nm, 35% dispersity) and UV-Vis spectrum (SPR λ_{max} = 519 nm).

5.8.2.2 Reversibility of the exchange (aqueous to apolar organic)

Aldehyde **28** (53.5 μmol, 20 Eq, 50 μL) and CF_3CO_2H (13.4 μmol, 5 Eq, 50 μL) were added to a solution of AuNP-**31** (2.68 μmol in terms of ligand **31**, 500 μL) in D_2O/[D_8]THF 1:9. The reaction mixture was heated at 50 °C. After 20 min a black solid precipitated from the reaction mix. The sample was further heated for 40 min to ensure full NP precipitation (Figure **5.29**).

The recovered black solid showed identical solubility properties and LDI-MS fragmentation pattern to AuNP-**30** prepared by other routes (Scheme **5.1B2**). In addition, LDI-MS analysis (Figure **5.29**) confirmed that the fragmentation pattern is identical to that shown for AuNP-**30** (Figure **5.25**).
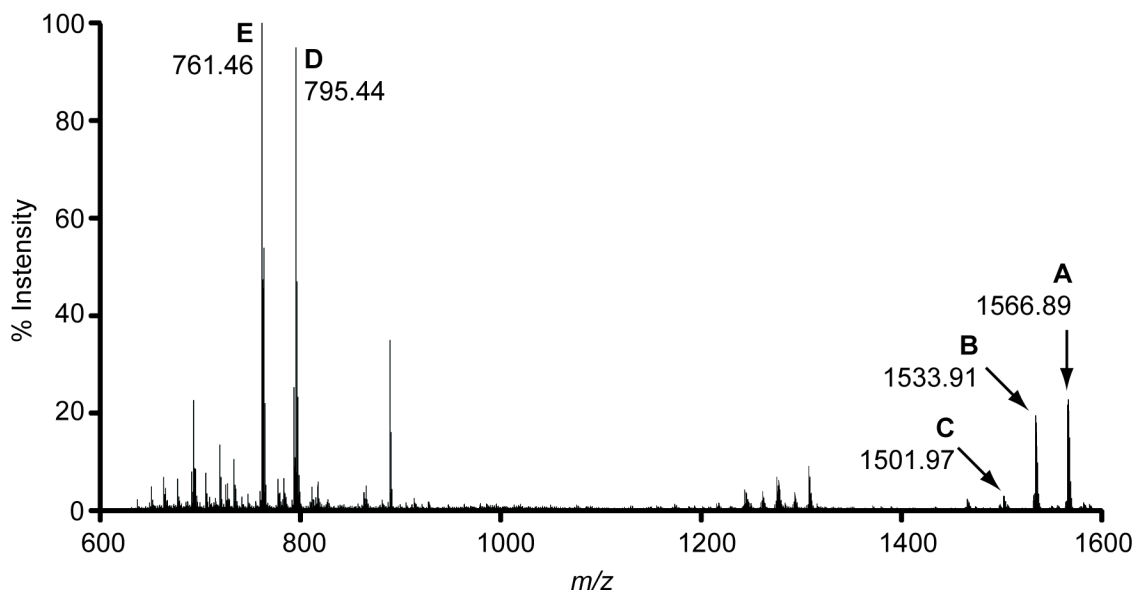
Figure 5.29   LDI mass spectrum of AuNP-**30** produced via exchange from AuNP-**31**. A): [**30**$_2$+Na]$^+$: m/z 1566.89. B): [**30**$_2$–S+Na]$^+$: m/z 1533.91. C): [**30**$_2$–2S+Na]$^+$: m/z 1501.97. D): [**30**H+Na]$^+$: m/z 795.44. E): [**30**H–H$_2$S+Na]$^+$: m/z 761.46.

5.8.3   Solubility switching between AuNP-21 (polar organic) and AuNP-31 (aqueous)
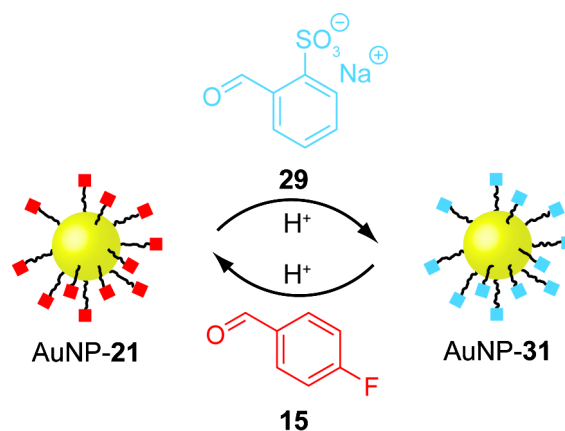
2-Formylbenzene sulfonic acid sodium salt (33.8 μmol, 20 Eq, 50 μL) and CF$_3$CO$_2$H (8.45 μmol, 5 Eq, 50 μL) were added to a solution of AuNP-**21** (1.69 μmol in terms of ligand **21**, 500 μL) in D$_2$O/DMF 1:9. The reaction mixture was heated at 50 °C overnight. The mixture was analysed by ^{1}H and ^{19}F NMR to confirm the presence of displaced 4-fluorobenzaldehyde. Then, Et$_2$O (7 mL) was added to induce NP precipitation. The supernatant solution was discarded and the black solid was washed with H$_2$O/THF 1:99 using the following procedure: NPs were dispersed in the solvent mixture (8 mL), sonicated for 15 min and centrifuged (4000 rpm, 5 °C, 10 min). The

operation was repeated three times and pure AuNP-**31** (14.8 mg) was obtained. Mean diameter: 3.35 ± 0.93 nm (28% dispersity). SPR λ_{max} = 541 nm (in H_2O).

The extent of hydrolysis was calculated as discussed in Section **5.8.1** and found to be 76%. Despite an incomplete exchange, the resulting purified NPs were soluble in water (Scheme **5.1C1**). LDI-MS analysis confirmed the presence of fragments corresponding to both ligands **21**H and **31**H (Figure **5.31**).
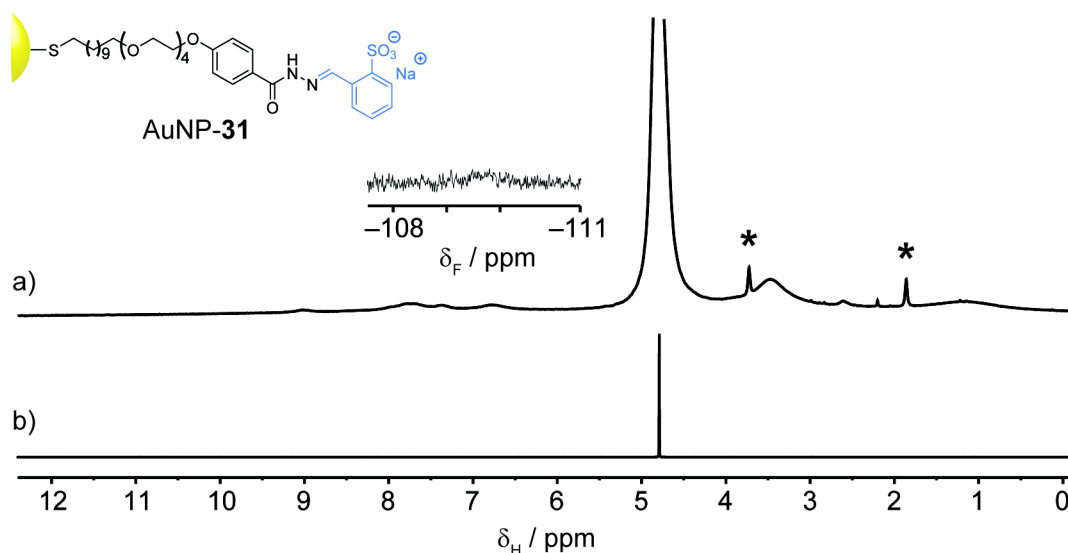
Figure 5.30   a): ^{1}H NMR (D_2O, 500.1 MHz, 295 K) of AuNP-**31** produced *via* exchange from AuNP-**21**. b): T_2-filtered spectrum (D21: 0.1 s). Inset: partial ^{19}F NMR (D_2O, 470.5 MHz, 295 K) showing the presence of AuNP-**21** not exchanged (< 24%). *: Residual THF.

5.8.3.1 LDI-MS analysis of AuNP-31

LDI analysis was performed as discussed in Sections **5.4** and **5.8.2**.[76,231]
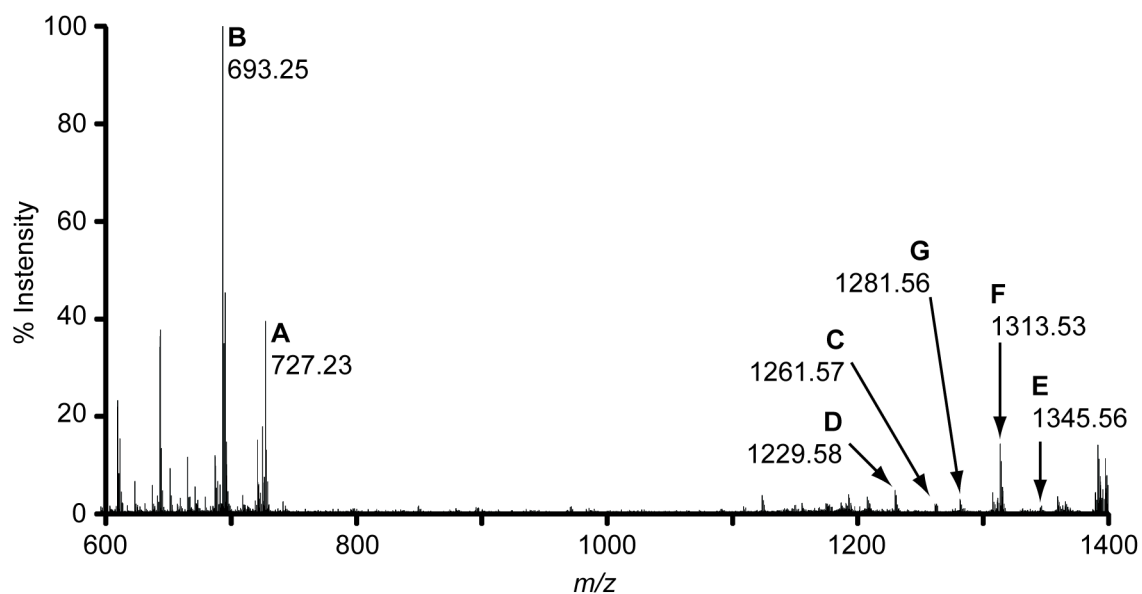
Figure 5.31   LDI mass spectrum of AuNP-**31** produced via exchange from AuNP-**21** (positive mode). A): [**31**H+Na]$^+$: m/z 727.23. B): [**31**H–H$_2$S+Na]$^+$: m/z 693.25. C): [**21**$_2$+Na]$^+$: m/z 1261.57. D): [**21**$_2$–S+Na]$^+$: m/z 1229.58. E): [**21**•**31**+Na]$^+$: m/z 1345.56. F): [**21**•**31**–S+Na]$^+$: m/z 1313.53. G): [**21**•**31**–S+Na]$^+$: m/z 1281.56.

5.8.3.2 Nanoparticulate structural functionalisation: AuNP-31 from AuNP-21
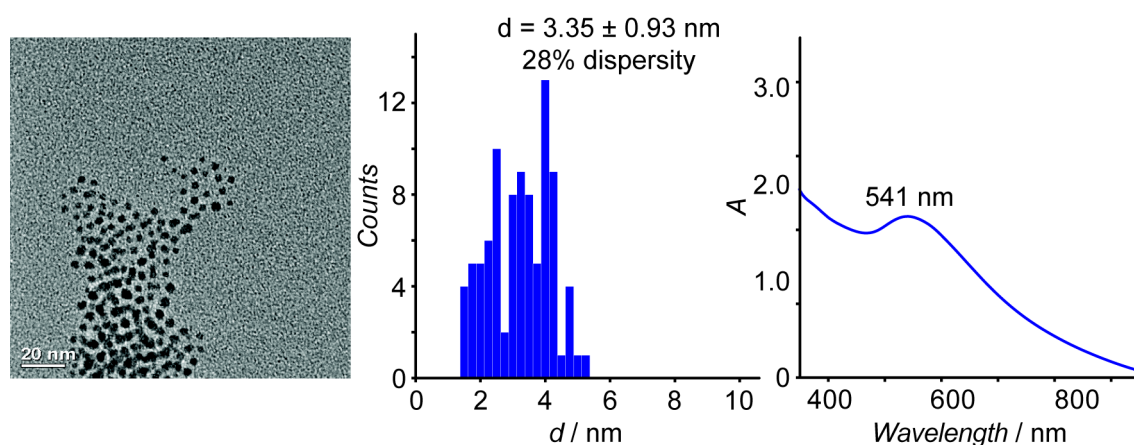
Figure 5.32   Representative TEM images of AuNP-**31** (scale bar 20 nm). Size distribution (diameter 3.35 ± 0.93 nm, 28% dispersity) and UV-Vis spectrum (SPR λ_{max} = 541 nm).

5.8.3.3 Reversibility of the exchange (aqueous to polar organic)

4-Fluorobenzaldehyde (33.8 μmol, 20 Eq, 50 μL) and CF_3CO_2H (8.45 μmol, 5 Eq, 50 μL) were added to a solution of AuNP-**31** (1.69 μmol in terms of ligand **31**, 500 μL) in D_2O/[D_7]DMF 1:9. The reaction mixture was heated at 50 °C overnight. The dark red solution was analysed by ^{19}F NMR to confirm the presence of AuNP-**21**. Then Et_2O was added to induce NP precipitation. The supernatant was discarded and the resulting black solid then was washed with DMF/Et_2O 1:7 using the following procedure: NPs were dispersed in the solvent mixture (8 mL), sonicated for 15 min, and centrifuged (4000 rpm, 5 °C, 10 min). The operation was repeated three times and clean functionalised NPs (7.56 mg) were afforded.

The recovered nanoparticles were no longer soluble in water (Scheme **5.1A3**). ^{19}F NMR confirmed the presence of the broad peak corresponding to AuNP-**21** (Figure **5.33**). LDI-MS analysis confirmed the presence of peaks corresponding to both ligands **21**H and **31**H (Figure **5.35**).
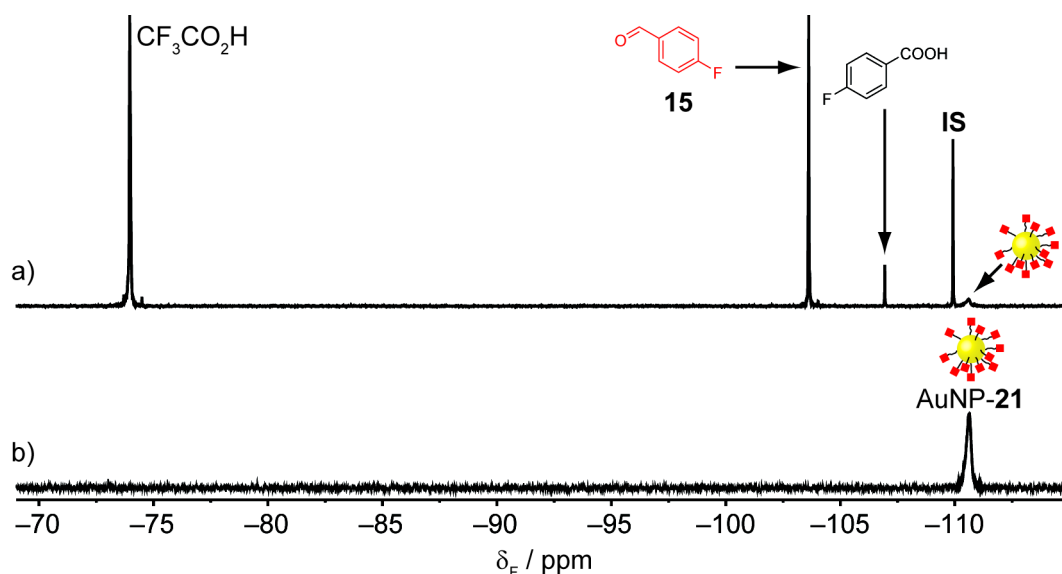
Figure 5.33 ^{19}F NMR (D_2O/[D_7]DMF 1:99, 470.5 MHz, 295 K). A): AuNP-**21** produced *via* exchange from AuNP-**31** after 24 h. B): AuNP-**21** after purification. **IS**: 3-fluoronitrobenzene (4.95 mM).
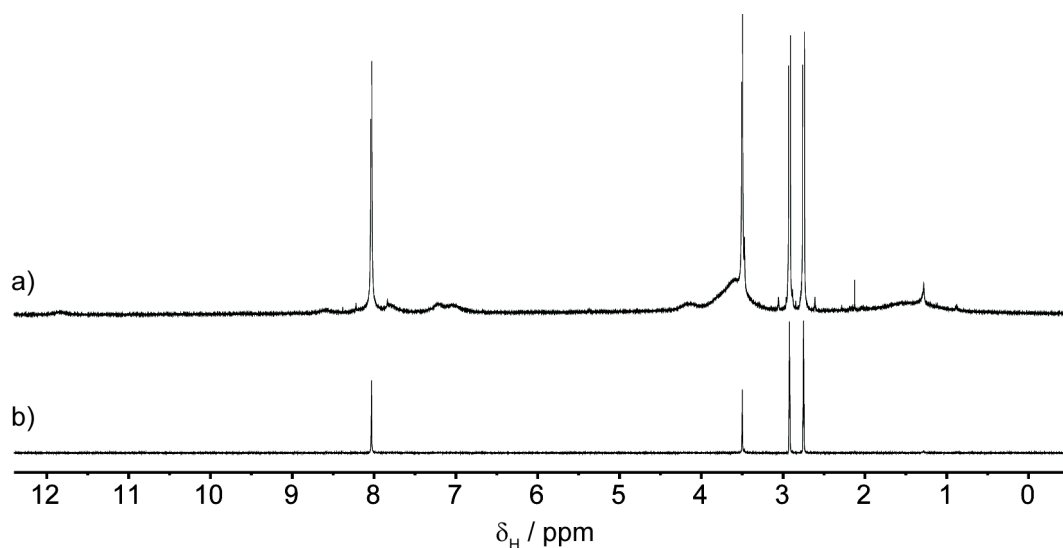
Figure 5.34   a): ^{1}H NMR ([D$_7$]DMF, 500.1 MHz, 295 K) of AuNP-**21** produced *via* exchange from AuNP-**31**. b): T_2-filtered spectrum (D21: 0.1 s).
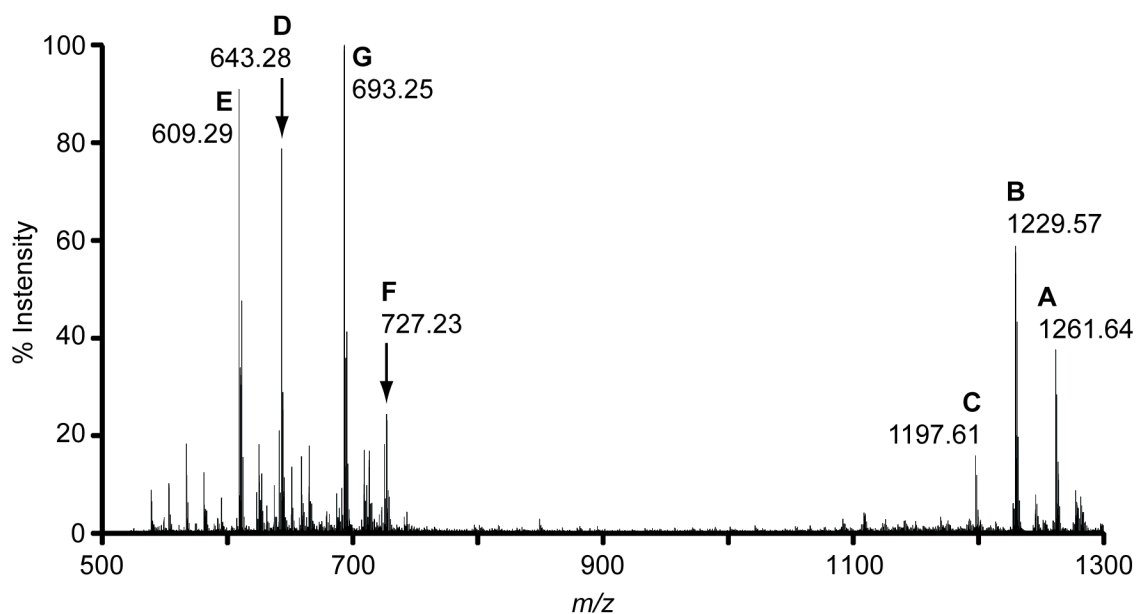
Figure 5.35   LDI mass spectrum of AuNP-**21** produced by exchange from AuNP-**31** (positive mode). A): [**21**$_2$+Na]$^+$: m/z 1261.64. B): [**21**$_2$–S+Na]$^+$: m/z 1229.57. C): [**21**$_2$–2S+Na]$^+$: m/z 1197.61. D): [**21**H+Na]$^+$: m/z 643.28. E): [**21**H–H$_2$S+Na]$^+$: m/z 609.29. F): [**31**H+Na]$^+$: m/z 727.23. G): [**31**H–H$_2$S+Na]$^+$: m/z 693.25.

5.9 Non-covalent aggregation of AuNP-30

5.9.1 AuNP-30 in chloroform
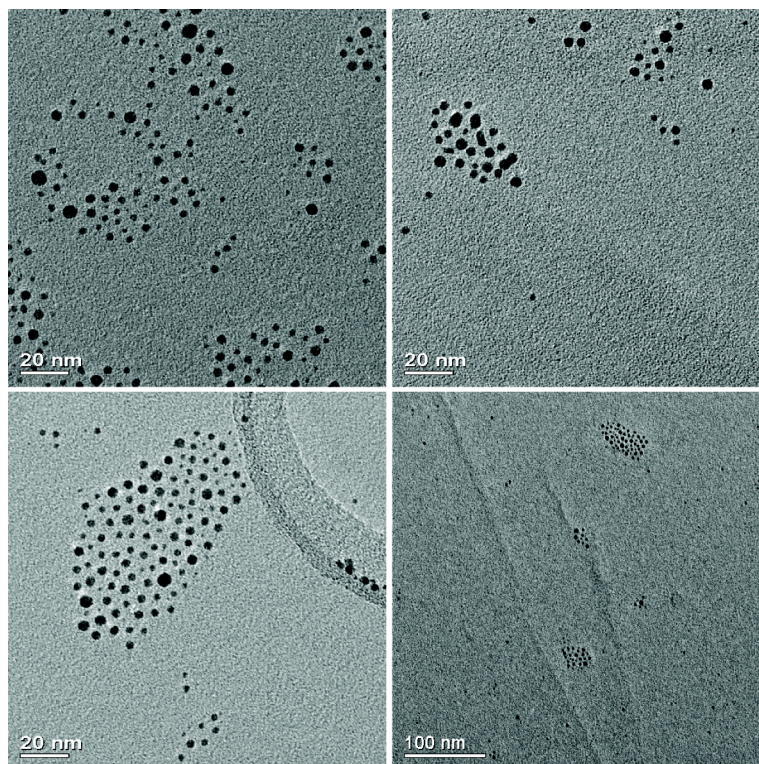
Figure 5.36 Representative TEM images of AuNP-**30** (scale bar 20 and 100 nm). NP core diameter: 2.84 ± 0.93 nm, 33% dispersity. Solvodynamic diameter: 7.44 ± 1.09 nm, 15% dispersity.

5.9.2   AuNP-30 in chloroform/tetrahydrofuran 1:1
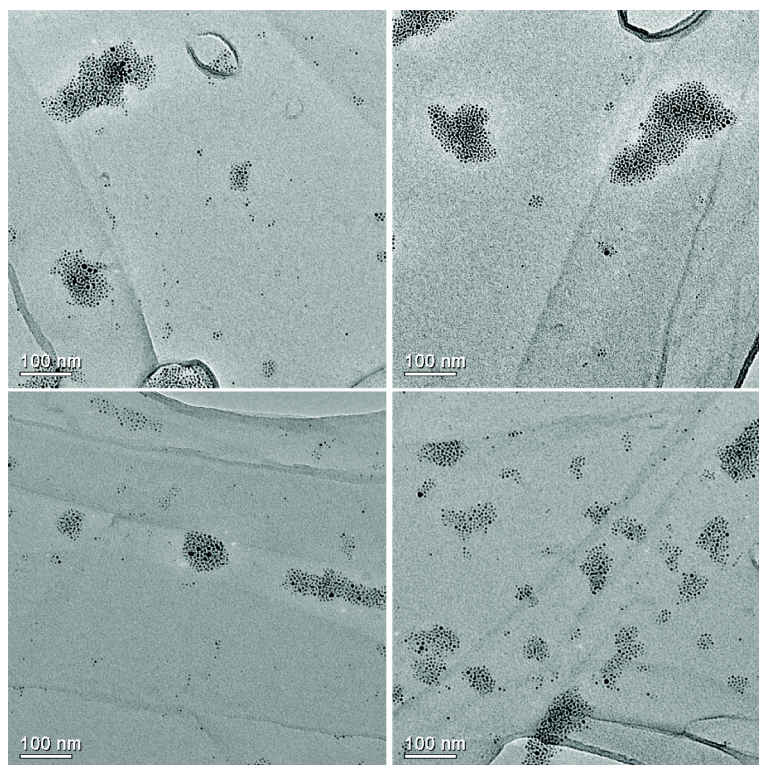
Figure 5.37   Representative TEM images of AuNP-**30** (scale bar 100 nm). Solvodynamic diameter: 70.24 ± 3.31 nm, 5% dispersity.

5.10 Assembly of AuNP-21 *via* hydrazone exchange

5.10.1 AuNP-21 before hydrazone exchange
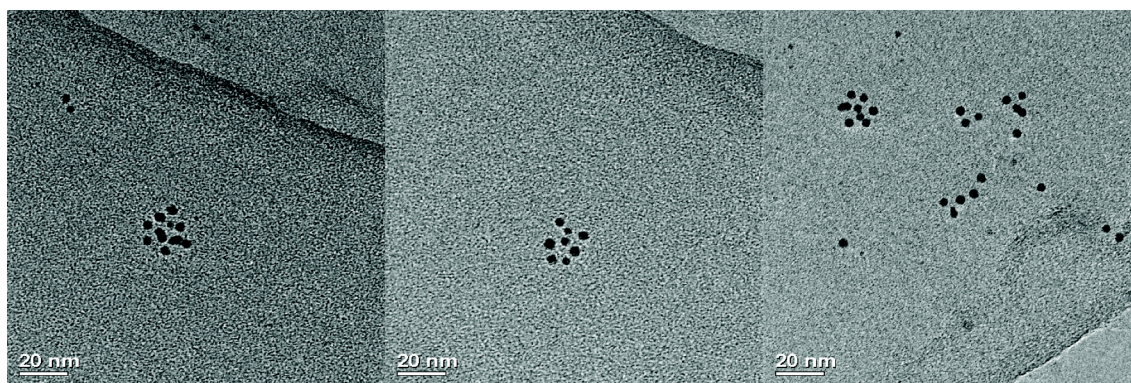
Figure 5.38   Representative TEM images of AuNP-**21** (scale bar 20 nm). NP core diameter: 2.88 ± 0.95 nm, 33% dispersity.

5.10.2 Assembly of AuNP-21 with terephthalaldehyde (0.5 equivalents) and trifluoroacetic acid (5 equivalents)
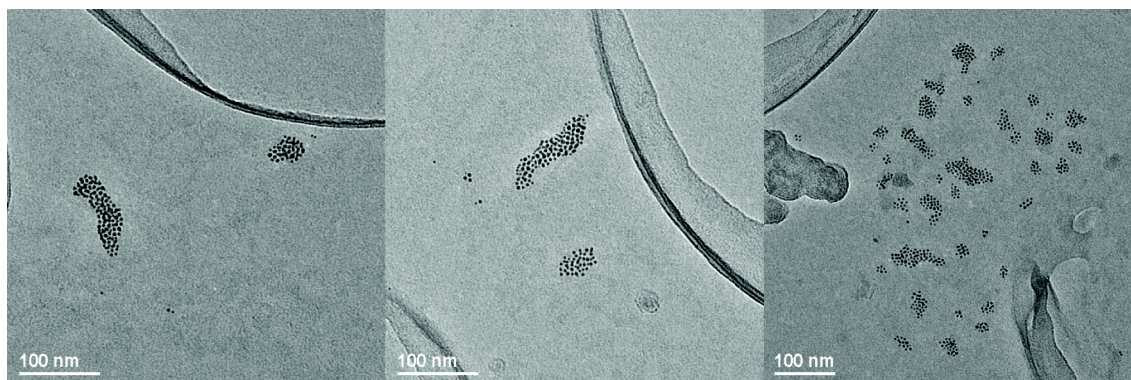
Figure 5.39   Representative TEM images of AuNP-**21** (scale bar 100 nm) with 0.5 Eq of terephthalaldehyde (with respect to **21**) after 21 days from addition of CF_3CO_2H (5 Eq with respect to **21**).

5.10.3 Assembly of AuNP-21 with terephthalaldehyde (1 equivalent) and trifluoroacetic acid (5 equivalents)
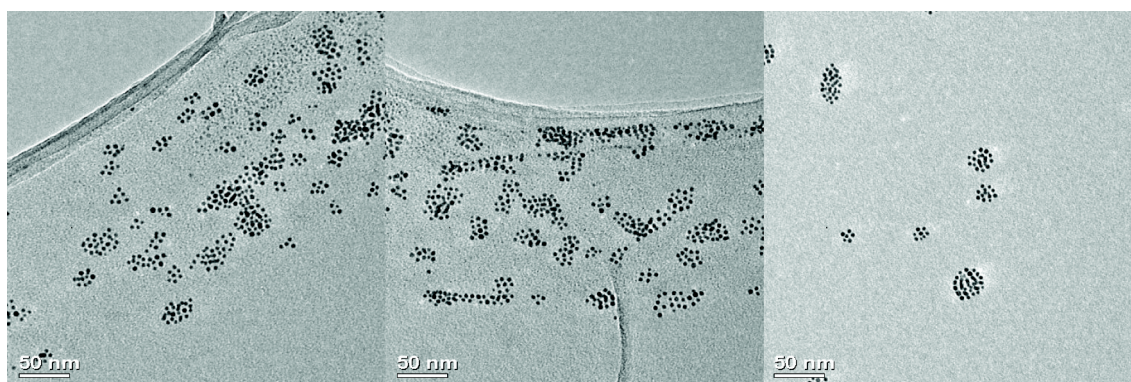
Figure 5.40   Representative TEM images of AuNP-**21** (scale bar 50 nm) with 1 Eq of terephthalaldehyde (with respect to **21**) after 21 days from addition of CF_3CO_2H (5 Eq with respect to **21**).

5.10.4 Assembly of AuNP-21 with terephthalaldehyde (5 equivalents) and trifluoroacetic acid (5 equivalents)
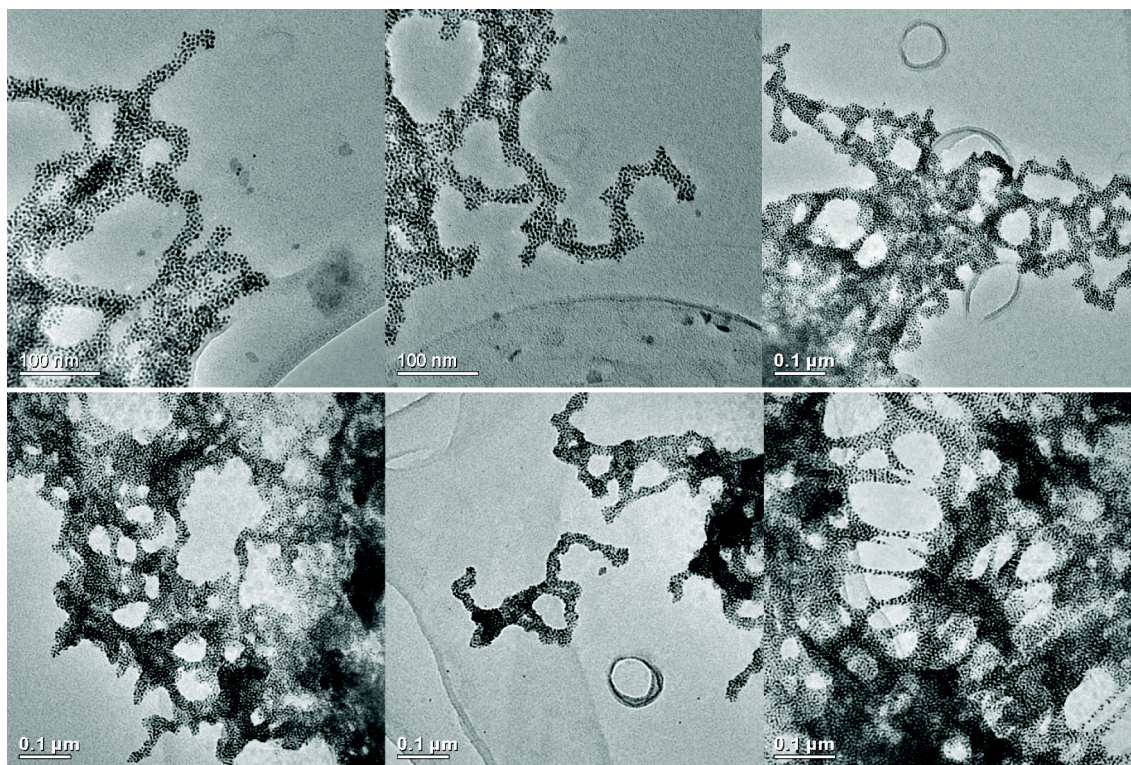
Figure 5.41   Representative TEM images of AuNP-**21** (scale bar 100 nm) with 5 Eq of terephthalaldehyde (with respect to **21**) after 21 days from addition of CF_3CO_2H (5 Eq with respect to **21**).
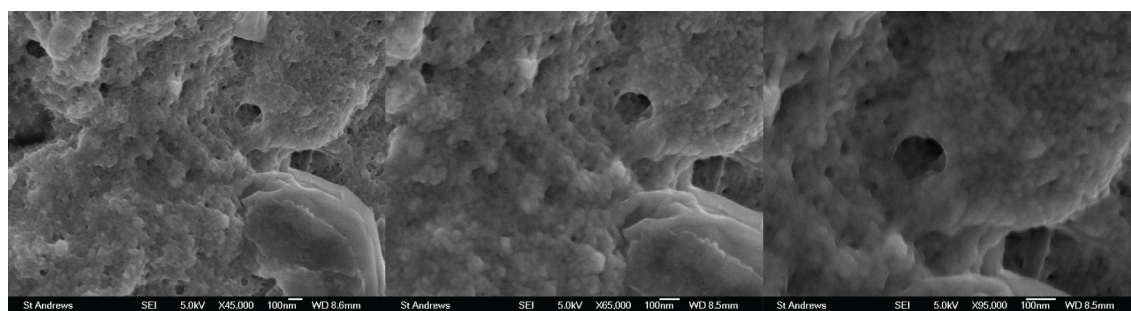
Figure 5.42   Representative scanning tunnelling microscopy images of AuNP-**21** (scale bar 100 nm) with 5 Eq of terephthalaldehyde (with respect to **21**) after 21 days from addition of CF_3CO_2H (5 Eq with respect to **21**).

5.10.5 Control experiment: AuNP-21 with terephthalaldehyde (0.5 equivalents)
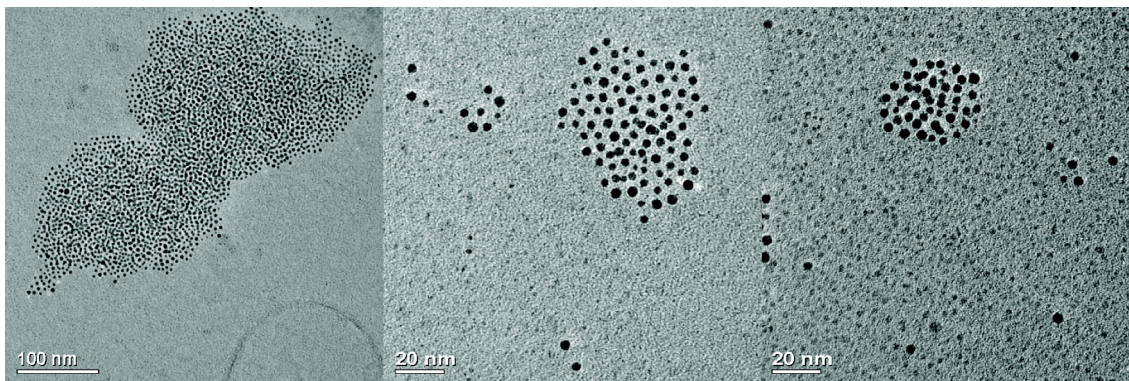
Figure 5.43   Representative TEM images of AuNP-**21** (scale bar 20 and 100 nm) with 0.5 Eq of terephthalaldehyde (with respect to **21**) after 21 days.

5.10.6 Control experiment: AuNP-21 with trifluoroacetic acid (5 equivalents)
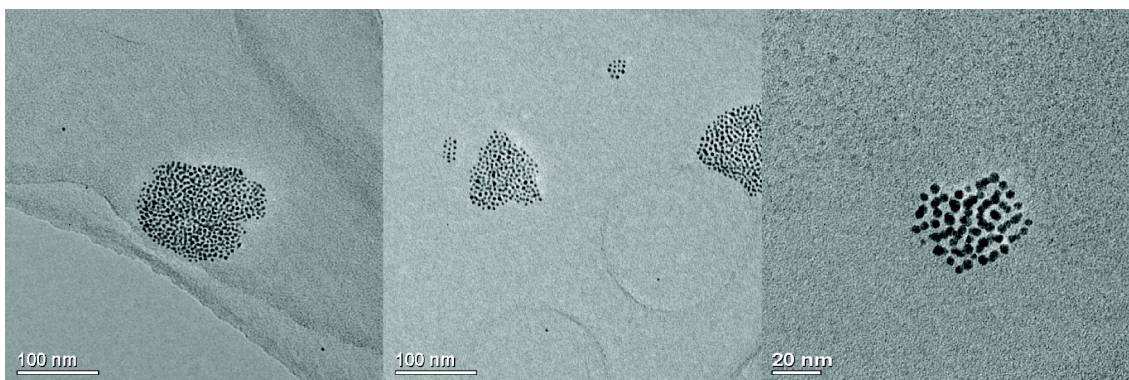
Figure 5.44   Representative TEM images of AuNP-**F** (scale bar 20 and 100 nm) after 21 days from addition of CF_3CO_2H (5 Eq with respect to **F**).

5.11 Tables

Table 5.2   Estimation of the nanoparticle concentration of 5 nm commercial gold colloid solution.[152] Summary of concentration values in Table **5.4**.

Entry	A	ε^a / $M^{-1}cm^{-1}$	Path / cm	$C^b_{(cuvette)}$ / M	Dilution factor	$C^b_{(sample)}$ / M
1	0.17461	1.03×10^7	0.5	3.39×10^{-8}	2.50	8.47×10^{-8}
2	0.10032	"	"	1.95×10^{-8}	3.75	7.30×10^{-8}

a: Molar extinction coefficient estimated with Huo's relationship.[149]
b: Concentration.

Table 5.3   Examples of the theoretical determination of the weight of functionalised gold nanoparticles for a known volume of TOAB-stabilised AuNP solution and the amount of ligand necessary to cover the total surface area.

	Entry	AuNP-**TOAB**c	AuNP-**TOAB**d
Diameter (d_{1NP})[a] / nm		5.00	4.81
Radius (r_{1NP}) / nm	d_{1NP} / 2	2.50	2.41
Volume of 1 AuNP (V_{1AuNP}) / nm^3	4/3 π r_{1NP}^3	65.45	58.27
Surface area of 1 AuNP (S_{1NP}) / nm^2	4 π r_{1NP}^2	78.54	72.68
Volume of 1 Au atom (V_{Au})[241] / nm^3	0.017		
Surface occupied by 1 ligand (S_{Lig})[151] / nm^2	0.241		
No. Au atoms per AuNP (N_{1AuNP})	V_{1NP} / V_{Au}	3850	3428
Mass of 1 AuNP (W_{1AuNP}) / g	N_{Au} / N_A × 197	1.26×10^{-18}	1.12×10^{-18}
No. ligands to cover 1 AuNP ($N_{Lig1AuNP}$)	S_{1NP} / S_{Lig}	367	340
HAuCl$_4$ for ligand exchange ($mmol_{HAuCl4}$) / mmol		1.2	1.2
Total weight of Au used for ligand exchange (W_{AuTot}) / g	$mmol_{HAuCl4}$ × 197 / 1000	0.2364	0.2364
Total No. of AuNPs in toluene ($N_{AuNPTot}$)	W_{AuTot} / W_{1AuNP}	1.88×10^{17}	2.11×10^{17}
Volume of toluene used ($V_{Toluene}$) / mL		112	112
Volume used for the exchange (V_{Exch}) / mL		12.4	16.4
No. AuNPs in the used volume ($N_{AuNPExch}$)	$N_{AuNPTot}$ × V_{Exch} / $V_{Toluene}$	2.08×10^{16}	3.09×10^{16}
No. Au atoms in the used volume (N_{AuExch})	$N_{AuNPExch}$ × N_{1AuNP}	8.00×10^{19}	1.06×10^{20}
Weight of Au in the used volume (W_{AuExch}) / mg	N_{AuExch} / N_A × 197 × 1000	26.17	34.62
No. Ligands for full coverage (N_{Full})	$N_{AuNPExch}$ × $N_{Lig1AuNP}$	7.63×10^{18}	1.05×10^{19}
MW of **4**H (MW) / g mol^{-1}		338.48	338.48
Weight of **4**H needed (W_{Full})[b] / mg	N_{Full} / N_A × MW × 1000	4.29	5.89
Theoretical sample weight / mg	W_{AuExch} + W_{Full}	**30.5**	**40.5**

[a]: The mean diameter is estimated using *ImageJ®*.
[b]: The upper value for the mass of AuNPs functionalised with hydrazone **4**H is estimated assuming that all the gold used to make the stock solution of TOAB-stabilised AuNPs (Section **5.3.1**) is completely transferred from the aqueous to the organic phase and is fully converted into colloidal stable NPs. It is also assumed that the NP size does not change after the ligand, all functionalised AuNPs are fully recovered after the work-up and all the TOAB is completely removed (Table **5.6**).

Table 5.4   Concentration of commercial gold colloid solutions.[152] Concentrations are reported as mean values of two UV-Vis measurements with different concentration. The molar extinction coefficient is determined from Huo's relationship (Equation **2.3**).[149]

Entry	Diameter / nm	ε / cm^{-1}M^{-1}	[AuNP] / nM
AuNP-**citrate**	5	1.03×10^7	78.9
AuNP-**citrate**	10	1.03×10^8	9.32
AuNP-**citrate**	20	1.03×10^9	0.91
AuNP-**citrate**	40	1.03×10^{10}	0.10

Table 5.5   Reaction conditions for ligand adsorption experiments on commercial citrate-capped AuNPs. None of the above conditions produced readily dispersed organic-soluble NPs.

Entry	Ligand	Diameter / nm	Solvent	TOAB	HCl	Reaction time
a	Hydrazide **2**	5	Toluene	NO	NO	24 h
b	Hydrazide **2**	5	Toluene	YES	NO	24 h
c	1-Decanethiol	5	Toluene	NO	YES	10 min
d	1-Decanethiol	5	Toluene	NO	YES	5 min
e	1-Decanethiol	5	Toluene	NO	NO	15 min
f	1-Decanethiol	5	CH_2Cl_2	NO	YES	15 min
g	1-Decanethiol	5	CH_2Cl_2	NO	NO	15 min
h	1-Decanethiol	5	$CHCl_3$	NO	YES	15 min
i	1-Decanethiol	5	$CHCl_3$	NO	NO	15 min
j	None	5	Toluene	NO	YES	15 min
k	1-Decanethiol	10	Toluene	NO	YES	15 min
l	1-Decanethiol	20	Toluene	NO	YES	15 min
m	1-Decanethiol	40	Toluene	NO	YES	15 min

Table 5.6 Preparation of TOAB-stabilised gold colloid solutions (AuNP-**TOAB***a–g*) and characterisation by TEM and UV-Vis spectroscopy (in toluene). SPR: surface plasmon resonance band.

Entry[a]	Au[b] / mmol	Diameter[c] / nm (dispersity)	λ_{max} (SPR) / nm
AuNP-**TOAB***a*	0.30	3.60 ± 1.41 (39%)	528
AuNP-**TOAB***b*	0.60	2.74 ± 0.85 (31%)	522
AuNP-**TOAB***c*	1.20	5.00 ± 1.41 (28%)	525
AuNP-**TOAB***d*	1.20	4.81 ± 1.34 (28%)	523
AuNP-**TOAB***e*	1.22	3.20 ± 1.11 (35%)	517
AuNP-**TOAB***f*	1.23	3.76 ± 1.14 (30%)	538
AuNP-**TOAB***g*	1.23	3.01 ± 0.92 (31%)	520

[a]: Au/TOAB/NaBH$_4$ ratio was kept constant (1:5:10).
[b]: [Au] was kept constant (30 mM).
[c]: Size distributions are expressed as mean ± s.d.

Table 5.7 Comparison between the theoretical mass for pure ligand functionalised AuNPs and the effective weight recovered after the work-up. See Table **5.3** for complete explanatory examples for the calculation of the theoretical mass.

Entry	NP stock solution	Ligand excess / Eq	Theoretical mass[a] / mg	Recovered mass / mg
a	AuNP-**TOAB***c*	100	30.5	**141**
b	"	100	30.5	**105**
c	"	100	30.5	**197**
d	"	50	30.5	**268**
e	AuNP-**TOAB***d*	50	40.5	**187**
f	"	50	40.5	**162**
g	"	50	40.5	**195**
h	"	50	40.5	**217**

References

[1]   H. Goesmann, C. Feldmann, *Angew. Chem. Int. Ed.* **2010**, *49*, 1362–1395.

[2]   G. Mie, *Ann. Phys.* **1908**, *25*, 377–455.

[3]   S. L. Logunov, T. S. Ahmadi, M. A. El-Sayed, J. T. Khoury, R. L. Whetten, *J. Phys. Chem. B* **1997**, *101*, 3713–3719.

[4]   R. Elghanian, J. J. Storhoff, R. C. Mucic, R. L. Letsinger, C. A. Mirkin, *Science* **1997**, *277*, 1078–1081.

[5]   K. L. Kelly, E. Coronado, L. L. Zhao, G. C. Schatz, *J. Phys. Chem. B* **2003**, *107*, 668–677.

[6]   A.-H. Lu, E. L. Salabas, F. Schüth, *Angew. Chem. Int. Ed.* **2007**, *46*, 1222–1244.

[7]   J. Dobson, *Nature Nanotech.* **2008**, *3*, 139–143.

[8]   A. Henglein, *J. Phys. Chem.* **1993**, *97*, 5457–5471.

[9]   H. Inouye, K. Tanaka, I. Tanahashi, K. Hirao, *Phys. Rev. B* **1998**, *57*, 11334–11340.

[10]   M. A. El-Sayed, *Acc. Chem. Res.* **2004**, *37*, 326–333.

[11]   H. Zhang, G. Schmid, U. Hartmann, *Nano Lett.* **2003**, *3*, 305–307.

[12]   J. Park, J. Joo, S. G. Kwon, Y. Jang, T. Hyeon, *Angew. Chem. Int. Ed.* **2007**, *46*, 4630–4660.

[13]   Y. Xia, Y. Xiong, B. Lim, S. E. Skrabalak, *Angew. Chem. Int. Ed.* **2009**, *48*, 60–103.

[14]   P. Zhao, N. Li, D. Astruc, *Coord. Chem. Rev.* **2013**, *257*, 638–665.

[15]   A. N. Shipway, E. Katz, I. Willner, *ChemPhysChem* **2000**, *1*, 18–52.

[16]   A. H. Alshehri, M. Jakubowska, A. Młożniak, M. Horaczek, D. Rudka, C. Free, J. D. Carey, *ACS Appl. Mater. Interfaces* **2012**, *4*, 7007–7010.

[17]   K. Saha, S. S. Agasti, C. Kim, X. Li, V. M. Rotello, *Chem. Rev.* **2012**, *112*, 2739–2779.

[18]   M. Haruta, M. Daté, *Appl. Catal., A* **2001**, *222*, 427–437.

[19] F. Porta, L. Prati, M. Rossi, G. Scari, *J. Catal.* **2002**, *211*, 464–469.

[20] A. Corma, P. Serna, *Science* **2006**, *313*, 332–334.

[21] N. Dimitratos, J. A. Lopez-Sanchez, G. J. Hutchings, *Chem. Sci.* **2012**, *3*, 20–44.

[22] R. A. Sperling, P. R. Gil, F. Zhang, M. Zanella, W. J. Parak, *Chem. Soc. Rev.* **2008**, *37*, 1896–1908.

[23] D. A. Giljohann, D. S. Seferos, W. L. Daniel, M. D. Massich, P. C. Patel, C. A. Mirkin, *Angew. Chem. Int. Ed.* **2010**, *49*, 3280–3294.

[24] A. Schroeder, D. A. Heller, M. M. Winslow, J. E. Dahlman, G. W. Pratt, R. Langer, T. Jacks, D. G. Anderson, *Nat. Rev. Cancer* **2012**, *12*, 39–50.

[25] S. J. Tan, M. J. Campolongo, D. Luo, W. Cheng, *Nature Nanotech.* **2011**, *6*, 268–276.

[26] W. R. Algar, D. E. Prasuhn, M. H. Stewart, T. L. Jennings, J. B. Blanco-Canosa, P. E. Dawson, I. L. Medintz, *Bioconjugate Chem.* **2011**, *22*, 825–858.

[27] J. I. Cutler, E. Auyeung, C. A. Mirkin, *J. Am. Chem. Soc.* **2012**, *134*, 1376–1391.

[28] Z. Nie, A. Petukhova, E. Kumacheva, *Nature Nanotech.* **2009**, *5*, 15–25.

[29] M.-C. Daniel, D. Astruc, *Chem. Rev.* **2004**, *104*, 293–346.

[30] C. Wanawongthai, A. Pongpeerapat, K. Higashi, Y. Tozuka, K. Moribe, K. Yamamoto, *Int. J. Pharm.* **2009**, *376*, 169–175.

[31] A. Gutsch, H. Mühlenweg, M. Krämer, *Small* **2005**, *1*, 30–46.

[32] V. K. LaMer, R. H. Dinegar, *J. Am. Chem. Soc.* **1950**, *72*, 4847–4854.

[33] J. Turkevich, P. C. Stevenson, J. Hillier, *Discuss. Faraday Soc.* **1951**, *11*, 55–75.

[34] G. Frens, *Nat. Phys. Sci.* **1973**, *241*, 20–22.

[35] J.-W. Park, J. S. Shumaker-Parry, *J. Am. Chem. Soc.* **2014**, *136*, 1907–1921.

[36] S. Kumar, K. S. Gandhi, R. Kumar, *Ind. Eng. Chem. Res.* **2007**, *46*, 3128–3136.

[37] I. Ojea-Jiménez, F. M. Romero, N. G. Bastús, V. Puntes, *J. Phys. Chem. C* **2010**, *114*, 1800–1804.

[38] K. R. Brown, M. J. Natan, *Langmuir* **1998**, *14*, 726–728.

[39] N. R. Jana, L. Gearheart, C. J. Murphy, *Langmuir* **2001**, *17*, 6782–6786.

[40] M. Brust, M. Walker, D. Bethell, D. J. Schiffrin, R. Whyman, *J. Chem. Soc., Chem. Commun.* **1994**, 801–802.

[41] R. Sardar, A. M. Funston, P. Mulvaney, R. W. Murray, *Langmuir* **2009**, *25*, 13840–13851.

[42] P. J. G. Goulet, R. B. Lennox, *J. Am. Chem. Soc.* **2010**, *132*, 9582–9584.

[43] Y. Li, O. Zaluzhna, B. Xu, Y. Gao, J. M. Modest, Y. J. Tong, *J. Am. Chem. Soc.* **2011**, *133*, 2092–2095.

[44] T. G. Schaaf, M. N. Shafigullin, J. T. Khoury, I. Vezmar, R. L. Whetten, W. G. Cullen, P. N. First, C. Gutiérrez-Wing, J. Ascensio, M. J. Jose-Yacamán, *J. Phys. Chem. B* **1997**, *101*, 7885–7891.

[45] N. Zheng, J. Fan, G. D. Stucky, *J. Am. Chem. Soc.* **2006**, *128*, 6550–6551.

[46] J. Song, D. Kim, D. Lee, *Langmuir* **2011**, *27*, 13854–13860.

[47] J. Kikuchi, K. Yasuhara, *Transmission Electron Microscopy (TEM). Supramolecular Chemistry: From Molecules to Nanomaterials*, **2012**.

[48] R. L. Whetten, J. T. Khoury, M. M. Alvarez, S. Murthy, I. Vezmar, Z. L. Wang, P. W. Stephens, C. L. Cleveland, W. D. Luedtke, U. Landman, *Adv. Mater.* **1996**, *8*, 428–433.

[49] C. L. Cleveland, U. Landman, M. N. Shafigullin, P. W. Stephens, R. L. Whetten, *Z. Phys. D* **1997**, *40*, 503–508.

[50] W. D. Pyrz, D. J. Buttrey, *Langmuir* **2008**, *24*, 11350–11360.

[51] K. A. Willets, R. P. Van Duyne, *Annu. Rev. Phys. Chem.* **2007**, *58*, 267–297.

[52] S. Eustis, M. A. El-Sayed, *Chem. Soc. Rev.* **2006**, *35*, 209–217.

[53] J. Lim, S. P. Yeap, H. X. Che, S. C. Low, *Nanoscale Res. Lett.* **2013**, *8*, 381.

[54] Z. Hens, J. C. Martins, *Chem. Mater.* **2013**, *25*, 1211–1221.

[55] R. H. Terrill, T. A. Postlethwaite, C. Chen, C.-D. Poon, A. Terzis, A. Chen, J. E. Hutchison, M. R. Clark, G. Wignall, J. D. Londono, R. Superfine, M. Falvo, C. S. Johnson, E. T. Samulski, R. W. Murray, *J. Am. Chem. Soc.* **1995**, *117*, 12537–12548.

[56] A. Badia, W. Gao, S. Singh, L. Demers, L. Cuccia, L. Reven, *Langmuir* **1996**, *12*, 1262–1269.

[57] A. C. Templeton, M. J. Hostetler, C. T. Kraft, R. W. Murray, *J. Am. Chem. Soc.* **1998**, *120*, 1906–1911.

[58] O. Kohlmann, W. E. Steinmetz, X.-A. Mao, W. P. Wuelfing, A. C. Templeton, R. W. Murray, C. S. Johnson, *J. Phys. Chem. B* **2001**, *105*, 8801–8809.

[59] M. J. Hostetler, J. E. Wingate, C.-J. Zhong, J. E. Harris, R. W. Vachet, M. R. Clark, J. D. Londono, S. J. Green, J. J. Stokes, G. D. Wignall, G. L. Glish, M. D. Porter, N. D. Evans, R. W. Murray, *Langmuir* **1998**, *14*, 17–30.

[60] G. Canzi, A. A. Mrse, C. P. Kubiak, *J. Phys. Chem. C* **2011**, *115*, 7972–7978.

[61] F. Rastrelli, S. Jha, F. Mancin, *J. Am. Chem. Soc.* **2009**, *131*, 14222–14224.

[62] D. Wu, A. Chen, C. S. Johnson, *J. Magn. Res. Ser. A* **1995**, *115*, 260–264.

[63] G. Pieters, A. Cazzolaro, R. Bonomi, L. J. Prins, *Chem. Commun.* **2012**, *48*, 1916–1918.

[64] G. Guarino, F. Rastrelli, P. Scrimin, F. Mancin, *J. Am. Chem. Soc.* **2012**, *134*, 7200–7203.

[65] G. Guarino, F. Rastrelli, F. Mancin, *Chem. Commun.* **2012**, *48*, 1523–1525.

[66] X. Liu, M. Yu, H. Kim, M. Mameli, F. Stellacci, *Nat. Commun.* **2012**, *3*, 1–9.

[67] J. L. Trevor, K. R. Lykke, M. J. Pellin, L. Hanley, *Langmuir* **1998**, *14*, 1664–1673.

[68] W. Gong, V. I. Elitzin, S. Janardhanam, C. L. Wilkins, I. Fritsch, *J. Am. Chem. Soc.* **2001**, *123*, 769–770.

[69] T. G. Schaaff, *Anal. Chem.* **2004**, *76*, 6187–6196.

[70] J. B. Tracy, G. Kalyuzhny, M. C. Crowe, R. Balasubramanian, J.-P. Choi, R. W. Murray, *J. Am. Chem. Soc.* **2007**, *129*, 6706–6707.

[71] J. B. Tracy, M. C. Crowe, J. F. Parker, O. Hampe, C. A. Fields-Zinna, A. Dass, R. W. Murray, *J. Am. Chem. Soc.* **2007**, *129*, 16209–16215.

[72] M. M. Alvarez, J. T. Khoury, T. G. Schaaff, M. Shafigullin, I. Vezmar, R. L. Whetten, *Chem. Phys. Lett.* **1997**, *266*, 91–98.

[73] K. M. Harkness, L. S. Fenn, D. E. Cliffel, J. A. McLean, *Anal. Chem.* **2010**, *82*, 3061–3066.

[74] K. M. Harkness, B. C. Hixson, L. S. Fenn, B. N. Turner, A. C. Rape, C. A. Simpson, B. J. Huffman, T. C. Okoli, J. A. McLean, D. E. Cliffel, *Anal. Chem.* **2010**, *82*, 9268–9274.

[75] K. M. Harkness, A. Balinski, J. A. McLean, D. E. Cliffel, *Angew. Chem. Int. Ed.* **2011**, *50*, 10554–10559.

[76] B. Yan, Z.-J. Zhu, O. R. Miranda, A. Chompoosor, V. M. Rotello, R. W. Vachet, *Anal. Bioanal. Chem.* **2010**, *396*, 1025–1035.

[77] C. A. Mirkin, R. L. Letsinger, R. C. Mucic, J. J. Storhoff, *Nature* **1996**, *382*, 607–609.

[78] A. P. Alivisatos, K. P. Johnsson, X. Peng, T. E. Wilson, C. J. Loweth, M. P. Bruchez, P. G. Schultz, *Nature* **1996**, *382*, 609–611.

[79] D. S. Seferos, D. A. Giljohann, H. D. Hill, A. E. Prigodich, C. A. Mirkin, *J. Am. Chem. Soc.* **2007**, *129*, 15477–15479.

[80] D. Zheng, D. S. Seferos, D. A. Giljohann, P. C. Patel, C. A. Mirkin, *Nano Lett.* **2009**, *9*, 3258–3261.

[81] D. A. Giljohann, D. S. Seferos, A. E. Prigodich, P. C. Patel, C. A. Mirkin, *J. Am. Chem. Soc.* **2009**, *131*, 2072–2073.

[82] C. D. Medley, J. E. Smith, Z. Tang, Y. Wu, S. Bamrungsap, W. Tan, *Anal. Chem.* **2008**, *80*, 1067–1072.

[83] S. Y. Park, A. K. R. Lytton-Jean, B. Lee, S. Weigand, G. C. Schatz, C. A. Mirkin, *Nature* **2008**, *451*, 553–556.

[84] R. J. Macfarlane, B. Lee, M. R. Jones, N. Harris, G. C. Schatz, C. A. Mirkin, *Science* **2011**, *334*, 204–208.

[85] R. J. Macfarlane, M. N. O'Brien, S. H. Petrosko, C. A. Mirkin, *Angew. Chem. Int. Ed.* **2013**, *52*, 5688–5698.

[86] D. Nykypanchuk, M. M. Maye, D. van der Lelie, O. Gang, *Nature* **2008**, *451*, 549–552.

[87] D. Sun, O. Gang, *J. Am. Chem. Soc.* **2011**, *133*, 5252–5254.

[88] A. K. Boal, F. Ilhan, J. E. DeRouchey, T. Thurn-Albrecht, T. P. Russell, V. M. Rotello, *Nature* **2000**, *404*, 746–748.

[89] T. Shirman, T. Arad, M. E. van der Boom, *Angew. Chem. Int. Ed.* **2010**, *49*, 926–929.

[90] C. Kim, S. S. Agasti, Z. Zhu, L. Isaacs, V. M. Rotello, *Nature Chem.* **2010**, *2*, 962–966.

[91] J. Zhang, R. J. Coulston, S. T. Jones, J. Geng, O. A. Scherman, C. Abell, *Science* **2012**, *335*, 690–694.

[92] R. de la Rica, R. M. Fratila, A. Szarpak, J. Huskens, A. H. Velders, *Angew. Chem. Int. Ed.* **2011**, *50*, 5704–5707.

[93] R. Klajn, M. A. Olson, P. J. Wesson, L. Fang, A. Coskun, A. Trabolsi, S. Soh, J. F. Stoddart, B. A. Grzybowski, *Nature Chem.* **2009**, *1*, 733–738.

[94] G. Pieters, C. Pezzato, L. J. Prins, *J. Am. Chem. Soc.* **2012**, *134*, 15289–15292.

[95] C. Pezzato, P. Scrimin, L. J. Prins, *Angew. Chem. Int. Ed.* **2014**, *53*, 2104–2109.

[96] R. Klajn, K. J. M. Bishop, B. A. Grzybowski, *Proc. Natl. Acad. Sci. U. S. A.* **2007**, *104*, 10305–10309.

[97] M. Brust, J. Fink, D. Bethell, D. J. Schiffrin, C. Kiely, *J. Chem. Soc., Chem. Commun.* **1995**, 1655–1656.

[98] D. Bethell, M. Brust, D. J. Schiffrin, C. Kiely, *J. Electroanal. Chem.* **1996**, *409*, 137–143.

[99] A. C. Templeton, M. J. Hostetler, E. K. Warmoth, S. Chen, C. M. Hartshorn, V. M. Krishnamurthy, M. D. E. Forbes, R. W. Murray, *J. Am. Chem. Soc.* **1998**, *120*, 4845–4849.

[100] A. C. Templeton, D. E. Cliffel, R. W. Murray, *J. Am. Chem. Soc.* **1999**, *121*, 7081–7089.

[101] S. Pathak, M. C. Davidson, G. A. Silva, *Nano Lett.* **2007**, *7*, 1839–1845.

[102] D. A. Fleming, C. J. Thode, M. E. Williams, *Chem. Mater.* **2006**, *18*, 2327–2334.

[103] E. Boisselier, L. Salmon, J. Ruiz, D. Astruc, *Chem. Commun.* **2008**, 5788–5790.

[104] J. L. Brennan, N. S. Hatzakis, T. R. Tshikhudo, N. Dirvianskyte, V. Razumas, S. Patkar, J. Vind, A. Svendsen, R. J. M. Nolte, A. E. Rowan, M. Brust, *Bioconjugate Chem.* **2006**, *17*, 1373–1375.

[105] Y.-P. Kim, W. L. Daniel, Z. Xia, H. Xie, C. A. Mirkin, J. Rao, *Chem. Commun.* **2010**, *46*, 76–78.

[106] G. Gasparini, M. Dal Molin, A. Lovato, L. J. Prins, *Dynamic Covalent Chemistry. Supramolecular Chemistry: From Molecules to Nanomaterials*, **2012**.

[107] S. J. Rowan, S. J. Cantrill, G. R. L. Cousins, J. K. M. Sanders, J. F. Stoddart, *Angew. Chem. Int. Ed.* **2002**, *41*, 898–952.

[108] P. T. Corbett, J. Leclaire, L. Vial, K. R. West, J.-L. Wietor, J. K. M. Sanders, S. Otto, *Chem. Rev.* **2006**, *106*, 3652–3711.

[109] J. Li, P. Nowak, S. Otto, *J. Am. Chem. Soc.* **2013**, *135*, 9222–9239.

[110] W. P. Jencks, *J. Am. Chem. Soc.* **1959**, *81*, 475–481.

[111] E. H. Cordes, W. P. Jencks, *J. Am. Chem. Soc.* **1962**, *84*, 832–837.

[112] E. H. Cordes, W. P. Jencks, *J. Am. Chem. Soc.* **1962**, *84*, 826–831.

[113] E. H. Cordes, W. P. Jencks, *J. Am. Chem. Soc.* **1962**, *84*, 4319–4328.

[114] B. M. Anderson, W. P. Jencks, *J. Am. Chem. Soc.* **1960**, *82*, 1773–1777.

[115] A. S. Stachissini, L. do Amaral, *J. Org. Chem.* **1991**, *56*, 1419–1424.

[116] J. Kalia, R. T. Raines, *Angew. Chem. Int. Ed.* **2008**, *47*, 7523–7526.

[117] A. Dirksen, S. Dirksen, T. M. Hackeng, P. E. Dawson, *J. Am. Chem. Soc.* **2006**, *128*, 15602–15603.

[118] A. Dirksen, P. E. Dawson, *Bioconjug. Chem.* **2008**, *19*, 2543–2548.

[119] V. T. Bhat, A. M. Caniard, T. Luksch, R. Brenk, D. J. Campopiano, M. F. Greaney, *Nature Chem.* **2010**, *2*, 490–497.

[120] S. R. Beeren, M. Pittelkow, J. K. M. Sanders, *Chem. Commun.* **2011**, *47*, 7359–7361.

[121] M. Wendeler, L. Grinberg, X. Wang, P. E. Dawson, M. Baca, *Bioconjugate Chem.* **2014**, *25*, 93–101.

[122] P. Crisalli, E. T. Kool, *J. Org. Chem.* **2013**, *78*, 1184–1189.

[123] P. Crisalli, E. T. Kool, *Org. Lett.* **2013**, *15*, 1646–1649.

[124] V. Getautis, M. Daskeviciene, V. Gaidelis, V. Jankauskas, *J. Photochem. Photobiol. A* **2005**, *175*, 39–44.

[125] V. Getautis, J. V. Grazulevicius, M. Daskeviciene, T. Malinauskas, D. Jankunaite, V. Gaidelis, V. Jankauskas, J. Sidaravicius, Z. Tokarski, *Polymer* **2005**, *46*, 7918–7922.

[126] J. Shao, J. P. Tam, *J. Am. Chem. Soc.* **1995**, *117*, 3893–3899.

[127] R.-M. Sebastián, G. Magro, A. Caminade, J. Majoral, *Tetrahedron* **2000**, *56*, 6269–6277.

[128] Q. Yuan, W. A. Yeudall, H. Yang, *Biomacromolecules* **2010**, *11*, 1940–1947.

[129] Y. Pu, S. Chang, H. Yuan, G. Wang, B. He, Z. Gu, *Biomaterials* **2013**, *34*, 3658–3666.

[130] Y. Chang, X. Meng, Y. Zhao, K. Li, B. Zhao, M. Zhu, Y. Li, X. Chen, J. Wang, *J. Colloid Interface Sci.* **2011**, *363*, 403–409.

[131] D. E. Prasuhn, J. B. Blanco-Canosa, G. J. Vora, J. B. Delehanty, K. Susumu, B. C. Mei, P. E. Dawson, I. L. Medintz, *ACS Nano* **2010**, *4*, 267–278.

[132] J. B. Blanco-Canosa, I. L. Medintz, D. Farrell, H. Mattoussi, P. E. Dawson, *J. Am. Chem. Soc.* **2010**, *132*, 10027–10033.

[133] S. S. Banerjee, D.-H. Chen, *Nanotechnology* **2008**, *19*, 505104.

[134] Q. Yuan, R. Venkatasubramanian, S. Hein, R. D. K. Misra, *Acta Biomater.* **2008**, *4*, 1024–1037.

[135] S. Aryal, J. J. Grailer, S. Pilla, D. A. Steeber, S. Gong, *J. Mater. Chem.* **2009**, *19*, 7879–7884.

[136] M. Prabaharan, J. J. Grailer, S. Pilla, D. A. Steeber, S. Gong, *Biomaterials* **2009**, *30*, 6065–6075.

[137] S. Aryal, C.-M. J. Hu, L. Zhang, *ACS Nano* **2010**, *4*, 251–258.

[138] P. E. Laibinis, G. M. Whitesides, D. L. Allara, Y.-T. Tao, A. N. Parikh, R. G. Nuzzo, *J. Am. Chem. Soc.* **1991**, *113*, 7152–7167.

[139] M. J. Hostetler, A. C. Templeton, R. W. Murray, *Langmuir* **1999**, *15*, 3782–3789.

[140] M. von Delius, E. M. Geertsema, D. A. Leigh, D.-T. D. Tang, *J. Am. Chem. Soc.* **2010**, *132*, 16134–16145.

[141] M. M. Bader, *Phosphorus, Sulfur. Silicon Relat. Elem.* **1996**, *116*, 77–92.

[142] X. Yu, C. Subramani, X. Yang, C. K. Kim, V. M. Rotello, *Macromol. Rapid Commun.* **2010**, *31*, 910–914.

[143] O. Ouari, F. Chalier, R. Bonaly, B. Pucci, P. Tordo, *J. Chem. Soc., Perkin Trans. 2* **1998**, 2299–2307.

[144] G. Durand, A. Polidori, O. Ouari, P. Tordo, V. Geromel, P. Rustin, B. Pucci, *J. Med. Chem.* **2003**, *46*, 5230–5237.

[145] M. Giersig, P. Mulvaney, *Langmuir* **1993**, *9*, 3408–3413.

[146] A. W. Shaffer, J. G. Worden, Q. Huo, *Langmuir* **2004**, *20*, 8343–8351.

[147] C. B. Murray, D. J. Norris, M. G. Bawendi, *J. Am. Chem. Soc.* **1993**, *115*, 8706–8715.

[148] W. Haiss, N. T. K. Thanh, J. Aveyard, D. G. Fernig, *Anal. Chem.* **2007**, *79*, 4215–4221.

[149] X. Liu, M. Atwater, J. Wang, Q. Huo, *Colloids Surf., B* **2007**, *58*, 3–7.

[150] G. A. Rance, D. H. Marsh, A. N. Khlobystov, *Chem. Phys. Lett.* **2008**, *460*, 230–236.

[151] H. Sellers, A. Ulman, Y. Shnidman, J. E. Eilers, *J. Am. Chem. Soc.* **1993**, *115*, 9389–9401.

[152] Gold colloid solutions (mean diameter 5, 10, 20, 40 nm) were purchased from BBInternational®.

[153] A. Manna, P.-L. Chen, H. Akiyama, T.-X. Wei, K. Tamada, W. Knoll, *Chem. Mater.* **2003**, *15*, 20–28.

[154] A. J. Kell, R. L. Donkers, M. S. Workentin, *Langmuir* **2005**, *21*, 735–742.

[155] D. S. Sidhaye, S. Kashyap, M. Sastry, S. Hotha, B. L. V Prasad, *Langmuir* **2005**, *21*, 7979–7984.

[156] Y. Negishi, U. Kamimura, M. Ide, M. Hirayama, *Nanoscale* **2012**, *4*, 4263–4268.

[157] O. Chovnik, R. Balgley, J. R. Goldman, R. Klajn, *J. Am. Chem. Soc.* **2012**, *134*, 19564–19567.

[158] Y. Luo, S. Korchak, H.-M. Vieth, R. Haag, *ChemPhysChem* **2011**, *12*, 132–135.

[159] J. Zhou, D. A. Beattie, R. Sedev, J. Ralston, *Langmuir* **2007**, *23*, 9170–9177.

[160] R. Klajn, L. Fang, A. Coskun, M. A. Olson, P. J. Wesson, J. F. Stoddart, B. A. Grzybowski, *J. Am. Chem. Soc.* **2009**, *131*, 4233–4235.

[161] The mean diameter of the gold nanoparticles was calculated using ImageJ 1.44o.

[162] D. V. Leff, L. Brandt, J. R. Heath, *Langmuir* **1996**, *12*, 4723–4730.

[163] L. O. Brown, J. E. Hutchison, *J. Am. Chem. Soc.* **1999**, *121*, 882–883.

[164] L. O. Brown, J. E. Hutchison, *J. Am. Chem. Soc.* **1997**, *119*, 12384–12385.

[165] A. Caragheorgheopol, V. Chechik, *Phys. Chem. Chem. Phys.* **2008**, *10*, 5029–5041.

[166] D. Berek, *J. Sep. Sci.* **2010**, *33*, 315–335.

[167] M. Gaborieau, P. Castignolles, *Anal. Bioanal. Chem.* **2011**, *399*, 1413–1423.

[168] P. Hong, S. Koza, E. S. P. Bouvier, *J. Liq. Chromatogr. Relat. Technol.* **2012**, *35*, 2923–2950.

[169] G.-T. Wei, F.-K. Liu, C. R. C. Wang, *Anal. Chem.* **1999**, *71*, 2085–2091.

[170] G.-T. Wei, F.-K. Liu, *J. Chromatogr. A* **1999**, *836*, 253–260.

[171] J. P. Novak, C. Nickerson, S. Franzen, D. L. Feldheim, *Anal. Chem.* **2001**, *73*, 5758–5761.

[172] J. P. Wilcoxon, J. E. Martin, P. Provencio, *Langmuir* **2000**, *16*, 9912–9920.

[173] A. M. Al-Somali, K. M. Krueger, J. C. Falkner, V. L. Colvin, *Anal. Chem.* **2004**, *76*, 5903–5910.

[174] H. Tsunoyama, Y. Negishi, T. Tsukuda, *J. Am. Chem. Soc.* **2006**, *128*, 6036–6037.

[175] S. Knoppe, J. Boudon, I. Dolamic, A. Dass, T. Bürgi, *Anal. Chem.* **2011**, *83*, 5056–5061.

[176] Bio-Beads[TM] S-X1 Support (200-400 Mesh) was purchased from Bio-Rad®.

[177] L. Schmidt, F. Emmerling, H. Kirmse, E. Kemnitz, *RSC Adv.* **2014**, *4*, 32–38.

[178] Y. S. Avadhut, J. Weber, E. Hammarberg, C. Feldmann, I. Schellenberg, R. Pöttgen, J. Schmedt auf der Günne, *Chem. Mater.* **2011**, *23*, 1526–1538.

[179] M. M. Bailey, C. M. Mahoney, K. E. Dempah, J. M. Davis, M. L. Becker, S. Khondee, E. J. Munson, C. Berkland, *Macromol. Rapid Commun.* **2010**, *31*, 87–92.

[180] Y. Song, R. W. Murray, *J. Am. Chem. Soc.* **2002**, *124*, 7096–7102.

[181] A. Dass, R. Guo, J. B. Tracy, R. Balasubramanian, A. D. Douglas, R. W. Murray, *Langmuir* **2008**, *24*, 310–315.

[182] C. Gentilini, F. Evangelista, P. Rudolf, P. Franchi, M. Lucarini, L. Pasquato, *J. Am. Chem. Soc.* **2008**, *130*, 15678–15682.

[183] M. Boccalon, P. Franchi, M. Lucarini, J. J. Delgado, F. Sousa, F. Stellacci, I. Zucca, A. Scotti, R. Spreafico, P. Pengo, L. Pasquato, *Chem. Commun.* **2013**, *49*, 8794–8796.

[184] A. G. Kanaras, F. S. Kamounah, K. Schaumburg, C. J. Kiely, M. Brust, *Chem. Commun.* **2002**, 2294–2295.

[185] A. Verma, V. M. Rotello, *Chem. Commun.* **2005**, 303–312.

[186] O. R. Miranda, H.-T. Chen, C.-C. You, D. E. Mortenson, X.-C. Yang, U. H. F. Bunz, V. M. Rotello, *J. Am. Chem. Soc.* **2010**, *132*, 5285–5289.

[187] D. M. L. Goodgame, C. A. O'Mahoney, S. D. Plank, D. J. Williams, *Polyhedron* **1993**, *12*, 2705–2710.

[188] T. E. Müller, J. C. Green, D. M. P. Mingos, C. M. McPartlin, C. Whittingham, D. J. Williams, T. M. Woodroffe, *J. Organomet. Chem.* **1998**, *551*, 313–330.

[189] J. Braun, K. Renggli, J. Razumovitch, C. Vebert, *Dynamic Light Scattering in Supramolecular Materials Chemistry. Supramolecular Chemistry: From Molecules to Nanomaterials*, **2012**.

[190] The extended, straight chain conformation of ligand **21** on AuNP-**21** was modelled using Maestro Version 9.9.013 by Tamara Kosikova. The S–F distance was subsequently determined using CrystalMaker® 9.10.4.

[191] L. Ramin, A. Jabbarzadeh, *Langmuir* **2011**, *27*, 9748–9759.

[192] D. I. Rozkiewicz, B. J. Ravoo, D. N. Reinhoudt, *Langmuir* **2005**, *21*, 6337–6343.

[193] T. Chang, D. I. Rozkiewicz, B. J. Ravoo, E. W. Meijer, D. N. Reinhoudt, *Nano Lett.* **2007**, *7*, 978–980.

[194] L. Tauk, A. P. Schröder, G. Decher, N. Giuseppone, *Nature Chem.* **2009**, *1*, 649–656.

[195] F. M. Mansfeld, H. Y. Au-Yeung, J. K. M. Sanders, S. Otto, *J. Syst. Chem.* **2010**, *1*, 12.

[196] S. A. Berg, B. J. Ravoo, *Soft Matter* **2014**, *10*, 69–74.

[197] W. P. Jencks, *Prog. Phys. Org. Chem.* **1964**, *2*, 63–128.

[198] S. Hoops, S. Sahle, R. Gauges, C. Lee, J. Pahle, N. Simus, M. Singhal, L. Xu, P. Mendes, U. Kummer, *Bioinformatics* **2006**, *22*, 3067–3074.

[199] C. R. Lindegren, C. Niemann, *J. Am. Chem. Soc.* **1949**, *71*, 1504.

[200] R. L. Hinman, *J. Org. Chem.* **1958**, *23*, 1587–1588.

[201] M. J. Hostetler, S. J. Green, J. J. Stokes, R. W. Murray, *J. Am. Chem. Soc.* **1996**, *118*, 4212–4213.

[202] A. C. Templeton, S. Chen, S. M. Gross, R. W. Murray, *Langmuir* **1999**, *15*, 66–76.

[203] V. Chechik, *J. Am. Chem. Soc.* **2004**, *126*, 7780–7781.

[204] Y. Song, T. Huang, R. W. Murray, *J. Am. Chem. Soc.* **2003**, *125*, 11694–11701.

[205] G. H. Woehrle, L. O. Brown, J. E. Hutchison, *J. Am. Chem. Soc.* **2005**, *127*, 2172–2183.

[206] M. De, S. Rana, H. Akpinar, O. R. Miranda, R. R. Arvizo, U. H. F. Bunz, V. M. Rotello, *Nature Chem.* **2009**, *1*, 461–465.

[207] J. Yang, J. Y. Lee, J. Y. Ying, *Chem. Soc. Rev.* **2011**, *40*, 1672–1696.

[208] N. Lala, S. P. Lalbegi, S. D. Adyanthaya, M. Sastry, *Langmuir* **2001**, *17*, 3766–3768.

[209] J. Liu, J. Alvarez, W. Ong, E. Román, A. E. Kaifer, *J. Am. Chem. Soc.* **2001**, *123*, 11148–11154.

[210] Y. Wang, J. F. Wong, X. Teng, X. Z. Lin, H. Yang, *Nano Lett.* **2003**, *3*, 1555–1559.

[211] M. Chen, W. Ding, Y. Kong, G. Diao, *Langmuir* **2008**, *24*, 3471–3478.

[212] W. W. Yu, E. Chang, C. M. Sayes, R. Drezek, V. L. Colvin, *Nanotechnology* **2006**, *17*, 4483–4487.

[213] A. M. Alkilany, A. I. Bani Yaseen, J. Park, J. R. Eller, C. J. Murphy, *RSC Adv.* **2014**, *4*, 52676–52679.

[214] J. C. Garcia-Martinez, R. M. Crooks, *J. Am. Chem. Soc.* **2004**, *126*, 16170–16178.

[215] O. M. Wilson, R. W. J. Scott, J. C. Garcia-Martinez, R. M. Crooks, *Chem. Mater.* **2004**, *16*, 4202–4204.

[216] M. R. Knecht, J. C. Garcia-Martinez, R. M. Crooks, *Langmuir* **2005**, *21*, 11981–11986.

[217] O. M. Wilson, R. W. J. Scott, J. C. Garcia-Martinez, R. M. Crooks, *J. Am. Chem. Soc.* **2005**, *127*, 1015–1024.

[218] A. Kumar, P. Mukherjee, A. Guha, S. D. Adyantaya, A. B. Mandale, R. Kumar, M. Sastry, *Langmuir* **2000**, *16*, 9775–9783.

[219] H. Yao, O. Momozawa, T. Hamatani, K. Kimura, *Chem. Mater.* **2001**, *13*, 4692–4697.

[220] K. S. Mayya, F. Caruso, *Langmuir* **2003**, *19*, 6987–6993.

[221] Z. Peng, T. Walther, K. Kleinermanns, *J. Phys. Chem. B* **2005**, *109*, 15735–15740.

[222] J. Simard, C. Briggs, A. K. Boal, V. M. Rotello, *Chem. Commun.* **2000**, 1943–1944.

[223] D. I. Gittins, F. Caruso, *Angew. Chem. Int. Ed.* **2001**, *40*, 3001–3004.

[224] L. Li, K. Leopold, M. Schuster, *J. Colloid Interface Sci.* **2013**, *397*, 199–205.

[225] J. M. McMahon, S. R. Emory, *Langmuir* **2007**, *23*, 1414–1418.

[226] L. Liu, T. L. Kelly, *Langmuir* **2013**, *29*, 7052–7060.

[227] X. Huang, B. Li, H. Zhang, I. Hussain, L. Liang, B. Tan, *Nanoscale* **2011**, *3*, 1600–1607.

[228] C. R. Mayer, E. Dumas, F. Sécheresse, *J. Colloid Interface Sci.* **2008**, *328*, 452–457.

[229] Y. Wu, C. Zhang, X. Qu, Z. Liu, Z. Yang, *Langmuir* **2010**, *26*, 9442–9448.

[230] A. M. Cioran, A. D. Musteti, F. Teixidor, Z. Krpetić, I. A. Prior, Q. He, C. J. Kiely, M. Brust, C. Viñas, *J. Am. Chem. Soc.* **2012**, *134*, 212–221.

[231] S. S. Thakur, P. Balaram, *J. Am. Soc. Mass Spectrom.* **2008**, *19*, 358–366.

[232] Z.-T. Li, X. Zhao, *Scanning Electron Microscopy. Supramolecular Chemistry: From Molecules to Nanomaterials*, **2012**.

[233] S. Biella, L. Prati, M. Rossi, *J. Catal.* **2002**, *206*, 242–247.

[234] A. Abad, C. Almela, A. Corma, H. García, *Tetrahedron* **2006**, *62*, 6666–6672.

[235] P. Haider, a Baiker, *J. Catal.* **2007**, *248*, 175–187.

[236] C. Marsden, E. Taarning, D. Hansen, L. Johansen, S. K. Klitgaard, K. Egeblad, C. H. Christensen, *Green Chem.* **2008**, *10*, 168–170.

[237] G. R. Fulmer, A. J. M. Miller, N. H. Sherden, H. E. Gottlieb, A. Nudelman, B. M. Stoltz, J. E. Bercaw, K. I. Goldberg, *Organometallics* **2010**, *29*, 2176–2179.

[238] V. A. Bloomfield, R. K. Dewan, *J. Phys. Chem.* **1971**, *75*, 3113–3119.

[239] W. Heller, *J. Phys. Chem.* **1965**, *69*, 1123–1129.

[240] A. Jouyban, S. Soltanpour, H.-K. Chan, *Int. J. Pharm.* **2004**, *269*, 353–360.

[241] D. V Leff, P. C. Ohara, J. R. Heath, W. M. Gelbart, *J. Phys. Chem.* **1995**, *99*, 7036–7041.

Appendix: Publication

Supramolecular Chemistry

Reversible Control of Nanoparticle Functionalization and Physicochemical Properties by Dynamic Covalent Exchange**

Flavio della Sala and Euan R. Kay*

Abstract: Existing methods for the covalent functionalization of nanoparticles rely on kinetically controlled reactions, and largely lack the sophistication of the preeminent oligonucleotide-based noncovalent strategies. Here we report the application of dynamic covalent chemistry for the reversible modification of nanoparticle (NP) surface functionality, combining the benefits of non-biomolecular covalent chemistry with the favorable features of equilibrium processes. A homogeneous monolayer of nanoparticle-bound hydrazones can undergo quantitative dynamic covalent exchange. The pseudomolecular nature of the NP system allows for the in situ characterization of surface-bound species, and real-time tracking of the exchange reactions. Furthermore, dynamic covalent exchange offers a simple approach for reversibly switching—and subtly tuning—NP properties such as solvophilicity.

Despite tremendous advances in the preparation of nanoparticles (NPs) from a range of materials,[1] manipulation and characterization of NP surface functionality remains a crucial challenge in the quest to exploit the often remarkable properties observed within this newfound region of chemical space. Direct incorporation of surface-bound functional molecules during NP synthesis is intrinsically restrictive, demanding compatibility with the synthesis conditions. Post-synthetic substitution of temporary surface species in a "ligand exchange" process can facilitate the introduction of a wider range of surface-bound functionalities, independent of the NP synthesis methods.[2] Yet, such processes are often irreversible, inefficient, and can lead to NP surface reconstruction or etching.

A generalizable synthetic approach whereby a set of NP "building blocks" may be predictably functionalized, manipulated, and assembled is therefore highly desirable. The potential of such a concept is well exemplified by oligonucleotide-functionalized nanomaterials.[3] Yet, biomolecular methods only operate within tightly defined conditions and offer limited scope for customization. On the other hand, non-biomolecular strategies will allow the full gamut of synthetic chemistry to be exploited in the optimization of nanomaterial structure, function, and properties. Innovative designs exploiting noncovalent interactions for NP functionalization,[4] aggregation,[5] and surface immobilization[6] have recently been explored, but these non-biomolecular systems cannot yet match the stability, specificity, and selectivity of oligonucleotide hybridization. Postsynthetic covalent modification of NP-bound monolayers is an attractive alternative, but traditionally this strategy has relied on kinetically controlled reactions,[7] which at best produce statistical mixtures of products and only offer one-shot opportunities for functionalization. Thermodynamically controlled covalent bond-forming reactions instead combine the error-correcting and stimuli-responsive features of equilibrium processes with the stability and structural diversity of covalent chemistry.[8] The first examples of dynamic covalent exchange taking place on 2D surface-confined molecular monolayers,[9a–c] or at the surface of self-assembled phospholipid bilayers,[9d,e] have recently been reported. We now show that such reactions may also be successfully performed on 3D NP-bound monolayers. We present prototypical "dynamic covalent NP building blocks": gold nanoparticles (AuNPs) bearing a homogeneous monolayer of *N*-aroylhydrazones (Figure 1), through which reversible control of NP functionalization and properties can be achieved.

[*] F. della Sala, Dr. E. R. Kay
EaStCHEM School of Chemistry, University of St Andrews
North Haugh, St Andrews KY16 9ST (UK)
E-mail: ek28@st-andrews.ac.uk

Supporting information for this article is available on the WWW under http://dx.doi.org/10.1002/anie.201409602.
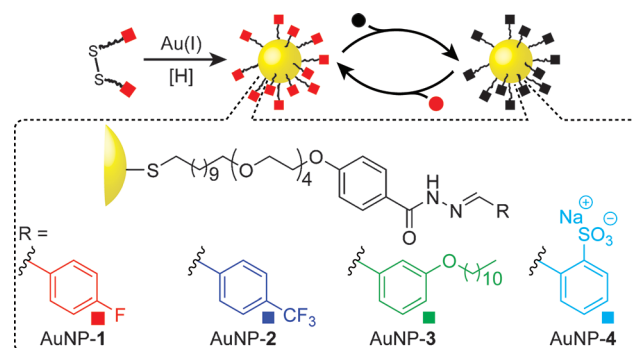
Figure 1. Preparation and reversible surface modification of a dynamic covalent NP building block exploiting *N*-aroylhydrazone surface monolayers.

Hydrazones display stability under a wide range of conditions, yet undergo covalent exchange reactions in the presence of acid or nucleophile catalysts,[10] making them particularly useful for creating dynamic covalent systems with good differentiation between kinetically labile and locked states.[11] This combination of behaviors likewise appeared ideal for a robust but exchangeable linkage for the construction of dynamic covalent AuNPs.[12] Ligand **1** bears an *N*-aroyl hydrazone unit, connected through an aliphatic linker to a thiolate functionality for binding to AuNP surfaces (Figure 2a).[13] The alkyl linker encourages the formation of
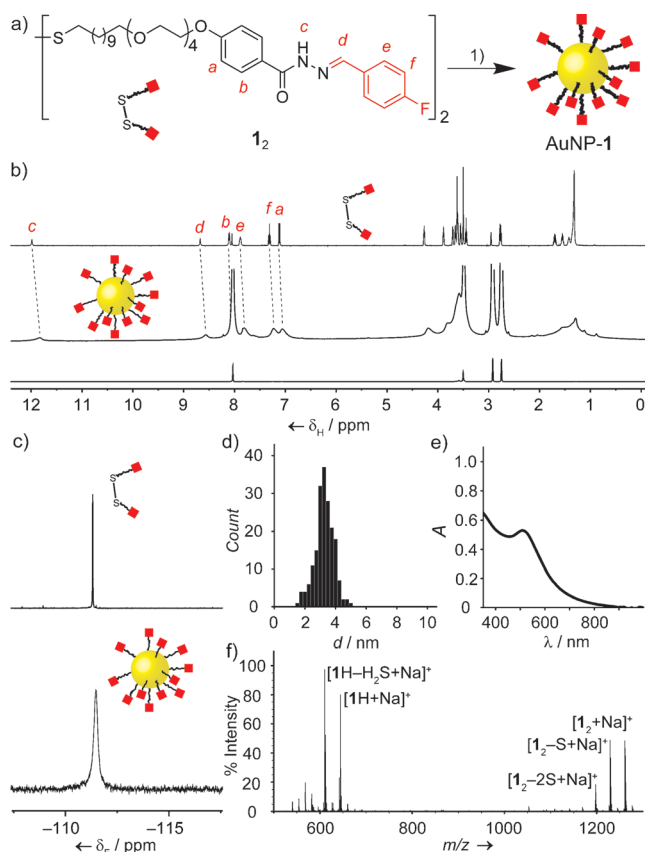

Figure 2. Synthesis and characterization of AuNP-**1**. a) Nanoparticle synthesis. 1) AuPPh₃Cl, borane *tert*-butylamine complex, DMF/THF 1:9, RT, 6 h. b) ¹H NMR spectra ([D₇]DMF, 500.1 MHz, 295 K): **1**₂ (top); AuNP-**1** (middle); AuNP-**1** T_2-filtered spectrum (bottom). Signals at 8.02, 3.50, 2.92, and 2.75 ppm correspond to residual non-deuterated solvent and water. c) ¹⁹F NMR spectra ([D₇]DMF, 470.5 MHz, 295 K): **1**₂ (top); AuNP-**1** (bottom). d) Size distribution of a representative batch of AuNP-**1** (mean diameter 3.39 ± 0.61 nm). e) UV/Vis spectrum of AuNP-**1** in DMF (SPR $\lambda_{max} = 509$ nm). f) LDI-MS of AuNP-**1**.

a well-ordered surface monolayer, maximizing van der Waals interactions between neighboring chains,[2a] whereas the outer tetraethylene glycol unit confers compatibility with polar solvents and conformational flexibility at the dynamic covalent reactive site.[14]

Gold nanoparticles bearing a homogeneous monolayer of **1** were prepared in a one-step, single-phase process,[15] which consistently yielded NPs of mean diameters in the range of

2.8–3.4 nm, with dispersities $< 20\%$ (Figures 2d and S6), and exhibiting a well-defined surface plasmon resonance (SPR, Figures 2e and S6). The absence of surfactants or temporary ligands facilitated the preparation of single-component monolayers, while all unbound contaminants could be removed by NP precipitation and washing. Verification of both comprehensive purification, and the structural integrity of NP-bound **1**,[16] were essential for being able to unambiguously characterize the surface-confined dynamic covalent processes. AuNP-**1** displays characteristically broad ¹H and ¹⁹F NMR spectra (Figure 2b and c) consisting only of the resonances expected for a single-component monolayer of **1**. The absence of nonsolvent unbound contaminants was confirmed by T_2-filtered ¹H NMR spectroscopy using the recently developed CPMG-*z* pulse sequence (Figures 2b, bottom, and S3).[17] Corroboration of the surface-bound molecular structure was provided by LDI-MS, whereby all major ions could be assigned as originating from desorbed **1** (Figures 2f and S4).[18] Finally, only products consistent with a homogeneous monolayer of **1** were detected after iodine-induced oxidative ligand stripping from AuNP-**1** (Figure S5).

Directly tracking reactions that occur on molecules confined to non-uniform faceted surfaces, within a heterogeneous population of NPs, presents several challenges. Inherently low concentrations, fast transverse relaxation, and chemical shift heterogeneity combine to yield broad, weak ¹H NMR spectra for NP-bound molecules (Figure 2b, middle), making quantitative deconvolution of resonances from structurally similar species extremely challenging.[19] Incorporating fluorine labels allowed us to exploit the significant chemical shift dispersion and excellent sensitivity of ¹⁹F NMR spectroscopy to interrogate the composition of hydrazone-bound monolayers before and after dynamic covalent exchange reactions (Figure 3).

A stable colloidal suspension of AuNP-**1** in 10% D₂O/[D₇]DMF was treated with an excess of *p*-(trifluoromethyl)-benzaldehyde (**5**) and CF₃CO₂H.[20] After 16 h at 50°C, ¹⁹F NMR spectroscopy showed that the signal for NP-bound *p*-fluorobenzylidene hydrazone **1** had decreased in intensity and two new resonances had appeared: one corresponding to free *p*-fluorobenzaldehyde (**6**), and another corresponding to NP-bound *p*-(trifluoromethyl)benzylidene hydrazone **2** (see Figure S10 for full sweep width crude and purified spectra). Unbound molecular species (released **6**, excess **5**, and CF₃CO₂H) were removed by NP precipitation and washing with nonsolvents, yielding a NP sample with a mixed monolayer comprising 90% hydrazone **2** and 10% hydrazone **1** (AuNP-**1**₀.₁**2**₀.₉, Figure 3b). By subjecting this sample again to the same exchange conditions, followed by purification as before, yielded a pure sample of AuNP-**2** (Figure 3b). A homogeneous monolayer of **2** was confirmed by ¹⁹F and ¹H NMR spectroscopy (Figures 3b, middle, S9, and S11), LDI-MS (Figures 3c, middle, and S12), and oxidative ligand stripping (Figure S13).[21]

The dynamic covalent exchange process is entirely reversible. Treatment of AuNP-**2** with **6**, under identical exchange conditions to before, produced a sample displaying a mixed monolayer of the two hydrazones in the ratio 1:1 (AuNP-**1**₀.₅**2**₀.₅, Figure 3b). Subjecting this sample to a further
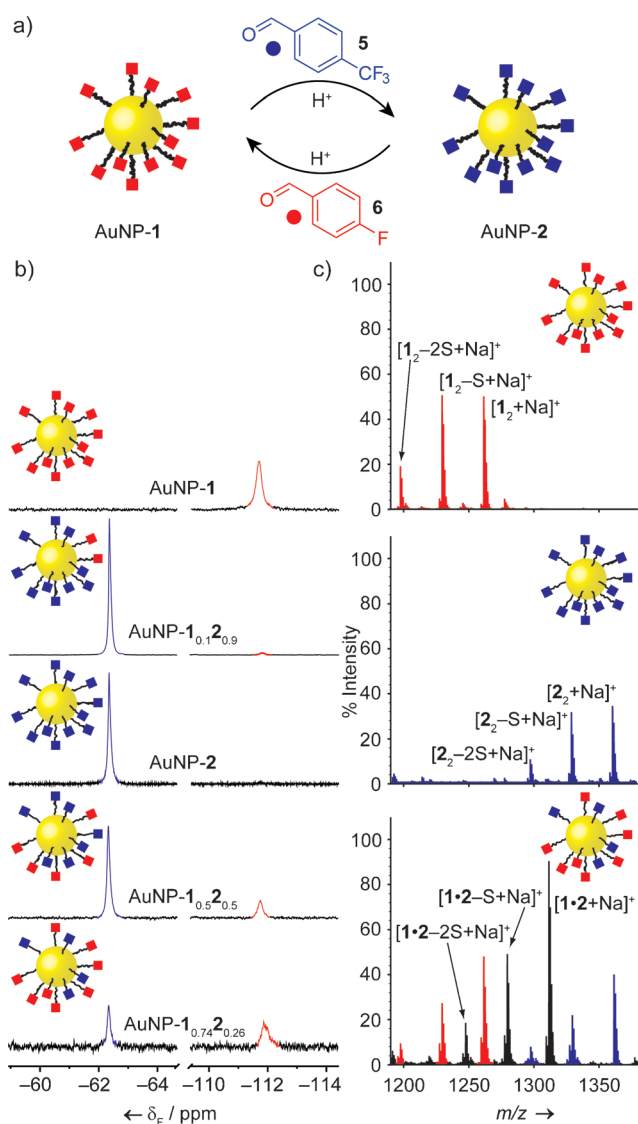
Figure 3. a) Hydrazone exchange between AuNP-**1** and AuNP-**2**. Conditions: aldehyde (20 equiv with respect to **1**), CF$_3$CO$_2$H (5 equiv with respect to **1**), D$_2$O/[D$_7$]DMF 1:9, 50°C. b) Partial ^{19}F NMR spectra ([D$_7$]DMF, 470.5 MHz, 295 K), from top to bottom: AuNP-**1**; AuNP-**1**$_{0.1}$**2**$_{0.9}$; AuNP-**2**; **1**$_{0.5}$**2**$_{0.5}$; AuNP-**1**$_{0.74}$**2**$_{0.26}$. c) Partial LDI-MS spectra of AuNP-**1** (top), AuNP-**2** (middle), and AuNP-**1**$_{0.74}$**2**$_{0.26}$ (bottom).

excess of **6** increased the ratio of hydrazones **1**:**2** in the monolayer to approximately 3:1 (AuNP-**1**$_{0.74}$**2**$_{0.26}$, Figure 3b). Peaks corresponding to mixed disulfide in the LDI-MS of AuNP-**1**$_{0.74}$**2**$_{0.26}$ (Figure 3c, bottom) indicate the intimate mixing of hydrazones on the NP surface,[18] whereas the lower extent of exchange in this reverse process is in line with the greater stability expected for the *p*-(trifluoromethyl)benzylidene hydrazone.[10c] Importantly, these mixed hydrazone samples allowed us to confirm that quantification of the monolayer composition by integrating the broad NP-bound ^{19}F NMR signals was consistent with the results of iodine-induced oxidative ligand stripping and subsequent analysis of the released molecular species (Figure S17).

The ability to quantify both NP-bound and unbound species using ^{19}F NMR spectroscopy allowed us to track hydrazone exchange in real time and explore the effects of surface confinement on reactivity. The concentrations of all four fluorinated species (AuNP-**1**, AuNP-**2**, **5**, **6**) were monitored during the exchange of AuNP-**1** with aldehyde **5**.[22] Comparing the resulting kinetic profile to that of a freely dissolved model compound under the same conditions (Figure S20) indicates a clear kinetic inhibition for the NP-bound reaction. Fitting to derive apparent rate constants (Table S1),[22] counterintuitively revealed the inhibitory effect to be stronger in one reaction direction (k_{NP}/k_{MOL} (F→CF$_3$) = 0.2) than the other (k_{NP}/k_{MOL}(CF$_3$→F) = 0.5), corresponding to an equilibrium endpoint that favors AuNP-**1** more strongly than predicted by the model reaction in bulk solution. Slower kinetics for the NP-bound process might be expected on the basis of simple steric arguments. However, it is unclear whether the very small increase in size on converting **1** to **2** can explain the differential effect on the exchange rates, or whether other intra-monolayer interactions or local concentration effects are also at play.

Mild and reversible methods for postsynthetic NP modification are highly desirable and would have significant benefits for nanomaterial property control, handling, and processability. For example, tuning solvent compatibility is often required to match an optimized NP synthesis route with a specific end application,[23] yet existing methods involve either encasing a nanoconstruct in a polymeric modifier, encapsulation in micelles, or completely replacing the surface ligands. The latter strategy may be considered as a dynamic exchange of the Au−S bond.[2] However, completely replacing the stabilizing monolayer is a relatively harsh and slow process. Whereas hydrazone exchange at 50°C (as described in Figure 3) reaches 90% exchange within 24 h, the ligand exchange of AuNP-**1** with disulfide **2**$_2$ takes several days to reach an endpoint exhibiting far lower conversion (63%) under analogous conditions (Figure S21), and does not proceed at all at ambient temperatures.[24] By exchanging only simple units on the periphery of the stabilizing monolayer, dynamic covalent exchange occurs rapidly under mild conditions; it furthermore avoids the necessity for multistep synthesis of several thiol-containing ligands, offers simple purification of the modified NPs from the molecular exchange species, and is entirely reversible.[24]

To demonstrate the potential of dynamic covalent exchange for reversible property control, we sought to introduce simple aldehyde exchange units, chosen to confer different solvophilic characteristics on our dynamic covalent AuNP building blocks (Figure 4). AuNP-**1** functionalized with *p*-fluorobenzylidene hydrazone showed good colloidal stability only in polar aprotic solvents such as DMF and DMSO (Figure 4, top). Treating AuNP-**1** with an excess of hydrophobic aldehyde **7** and CF$_3$CO$_2$H in 10% D$_2$O/[D$_7$]DMF at 50°C resulted in complete precipitation of the NPs within 1.5 h. The solid was easily recovered by centrifugation, and then purified from all molecular species by redispersion in methanol followed by precipitation with hexane. The resulting residue exhibited markedly different solubility properties to AuNP-**1** and could be readily redispersed in organic solvents of intermediate polarity, such as chloroform or tetrahydrofuran (AuNP-**3**, Figure 4, left).
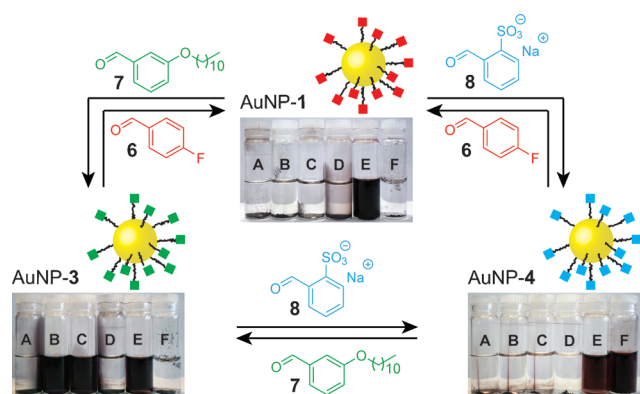
Figure 4. Reversible switching of AuNP solvophilicity properties by hydrazone exchange. For full conditions, see the SI, Section 11. Solvents in the inset pictures: A = hexane, B = chloroform, C = tetrahydrofuran, D = methanol, E = DMF, F = water.

Analysis of the reaction supernatant by ^{19}F NMR spectroscopy indicated > 95 % conversion of the starting NP-bound *p*-fluorobenzylidene hydrazones (Figure S23). On the other hand, ^{1}H NMR and LDI-MS analysis of the new NP sample (Figures S22 and S24) were consistent with the expected *m*-alkoxybenzylidene hydrazone. Clearly, dynamic covalent exchange of NP-bound hydrazones occurred to give AuNP-**3** and the consequent marked change in solvent compatibility.

In a similar manner, AuNP-**3** could be converted to AuNP-**4**, which showed excellent colloidal stability in water (Figure 4, right). *o*-Sulfonylbenzylidene hydrazone was confirmed as the major constituent of the NP-bound monolayer by a combination of ^{1}H NMR spectroscopy and LDI-MS (Figures S28–S30). Each of these exchange reactions proved to be entirely reversible, such that any of the three AuNP systems, exhibiting markedly different solvophilicity properties, could be accessed from either one of the other two by treatment with the appropriate aldehyde exchange unit (Figure 4 and Scheme S2). Interestingly, during the conversion of AuNP-**3** to AuNP-**1**, a sample was obtained exhibiting solubility properties that were intermediate between the two extremes (Scheme S2). That this state arises from a mixed monolayer of hydrazones **3** and **1** was confirmed by LDI-MS analysis, which presented ion fragments originating from both possible hydrazones in roughly equal intensities (Figure S27). Subjecting this material to a further round of exchange with aldehyde **6** then yielded a sample displaying indistinguishable physical and chemical properties to AuNP-**1** produced by all other routes. Thus, it is possible to access a continuum of AuNP solvophilicity characteristics across a remarkably wide range by fine-tuning the monolayer composition through the appropriate choice of exchange conditions.

Controlling the molecular details of NP surface functionality will be critical for realizing the full technological potential of nanomaterials. Dynamic covalent NP building blocks now offer a generalizable strategy for achieving this, using simple molecular designs and mild processes that are independent of the underlying NP material. The ability to reversibly tune surface functionality raises the prospect of smart NP-based devices with environment-responsive properties, or reconfigurable self-assembly capabilities. The pseu-

domolecular nature of 3D NP-bound monolayers allows the direct characterization of surface-bound chemical processes, offering fundamental insights into the influence of crowded environments on reactivity, which have not been so readily accessible from analogous 2D surface-bound systems.[8b] Determining the complex influence of nanoscale features, such as surface curvature and monolayer composition, on reactivity is the next step that can now be addressed in the development of dynamic covalent NP building blocks to become flexible and versatile nanomaterial synthons.[25]

[1] J. Park, J. Joo, S. G. Kwon, Y. Jang, T. Hyeon, *Angew. Chem. Int. Ed.* **2007**, *46*, 4630–4660; *Angew. Chem.* **2007**, *119*, 4714–4745.

[2] For leading references on ligand exchange, see: a) M. J. Hostetler, A. C. Templeton, R. W. Murray, *Langmuir* **1999**, *15*, 3782–3789; b) A. Caragheorgheopol, V. Chechik, *Phys. Chem. Chem. Phys.* **2008**, *10*, 5029–5041; c) A. Dong, X. Ye, J. Chen, Y. J. Kang, T. Gordon, J. M. Kikkawa, C. B. Murray, *J. Am. Chem. Soc.* **2011**, *133*, 998–1006.

[3] a) S. J. Tan, M. J. Campolongo, D. Luo, W. Cheng, *Nat. Nanotechnol.* **2011**, *6*, 268–276; b) R. J. Macfarlane, M. N. O'Brien, S. H. Petrosko, C. A. Mirkin, *Angew. Chem. Int. Ed.* **2013**, *52*, 5688–5698; *Angew. Chem.* **2013**, *125*, 5798–5809.

[4] a) C. Kim, S. S. Agasti, Z. Zhu, L. Isaacs, V. M. Rotello, *Nat. Chem.* **2010**, *2*, 962–966; b) G. Pieters, C. Pezzato, L. J. Prins, *J. Am. Chem. Soc.* **2012**, *134*, 15289–15292; c) C. Pezzato, P. Scrimin, L. J. Prins, *Angew. Chem. Int. Ed.* **2014**, *53*, 2104–2109; *Angew. Chem.* **2014**, *126*, 2136–2141.

[5] a) A. K. Boal, F. Ilhan, J. E. DeRouchey, T. Thurn-Albrecht, T. P. Russell, V. M. Rotello, *Nature* **2000**, *404*, 746–748; b) R. Klajn, K. J. M. Bishop, B. A. Grzybowski, *Proc. Natl. Acad. Sci. USA* **2007**, *104*, 10305–10309; c) R. Klajn, M. A. Olson, P. J. Wesson, L. Fang, A. Coskun, A. Trabolsi, S. Soh, J. F. Stoddart, B. A. Grzybowski, *Nat. Chem.* **2009**, *1*, 733–738; d) T. Shirman, T. Arad, M. E. van der Boom, *Angew. Chem. Int. Ed.* **2010**, *49*, 926–929; *Angew. Chem.* **2010**, *122*, 938–941; e) R. de laRica, R. M. Fratila, A. Szarpak, J. Huskens, A. H. Velders, *Angew. Chem. Int. Ed.* **2011**, *50*, 5704–5707; *Angew. Chem.* **2011**, *123*, 5822–5825; f) J. Zhang, R. J. Coulston, S. T. Jones, J. Geng, O. A. Scherman, C. Abell, *Science* **2012**, *335*, 690–694.

[6] a) X. Y. Ling, D. N. Reinhoudt, J. Huskens, *Chem. Mater.* **2008**, *20*, 3574–3578; b) D. Dorokhin, S.-H. Hsu, N. Tomczak, D. N. Reinhoudt, J. Huskens, A. H. Velders, G. J. Vancso, *ACS Nano* **2010**, *4*, 137–142; c) T. Shirman, R. Kaminker, D. Freeman, M. E. van der Boom, *ACS Nano* **2011**, *5*, 6553–6563.

[7] For a review, see: W. R. Algar, D. E. Prasuhn, M. H. Stewart, T. L. Jennings, J. B. Blanco-Canosa, P. E. Dawson, I. L. Medintz, *Bioconjugate Chem.* **2011**, *22*, 825–858.

[8] a) S. J. Rowan, S. J. Cantrill, G. R. L. Cousins, J. K. M. Sanders, J. F. Stoddart, *Angew. Chem. Int. Ed.* **2002**, *41*, 898–952; *Angew. Chem.* **2002**, *114*, 938–993; b) J. Li, P. Nowak, S. Otto, *J. Am. Chem. Soc.* **2013**, *135*, 9222–9239.

[9] a) D. I. Rozkiewicz, B. J. Ravoo, D. N. Reinhoudt, *Langmuir* **2005**, *21*, 6337–6343; b) T. Chang, D. I. Rozkiewicz, B. J. Ravoo, E. W. Meijer, D. N. Reinhoudt, *Nano Lett.* **2007**, *7*, 978–980; c) L. Tauk, A. P. Schröder, G. Decher, N. Giuseppone, *Nat. Chem.* **2009**, *1*, 649–656; d) F. M. Mansfeld, H. Au-Yeung, J. K. M. Sanders, S. Otto, *J. Syst. Chem.* **2010**, *1*, 12; e) S. A. Berg, B. J. Ravoo, *Soft Matter* **2014**, *10*, 69–74.

[10] a) E. H. Cordes, W. P. Jencks, *J. Am. Chem. Soc.* **1962**, *84*, 826–831; b) E. H. Cordes, W. P. Jencks, *J. Am. Chem. Soc.* **1962**, *84*, 4319–4328; c) W. P. Jencks, *Prog. Phys. Org. Chem.* **1964**, *2*, 63–128; d) A. Dirksen, S. Dirksen, T. M. Hackeng, P. E. Dawson, *J. Am. Chem. Soc.* **2006**, *128*, 15602–15603; e) J. Kalia, R. T. Raines, *Angew. Chem. Int. Ed.* **2008**, *47*, 7523–7526; *Angew. Chem.* **2008**, *120*, 7633–7636.

[11] a) G. R. L. Cousins, S.-A. Poulsen, J. K. M. Sanders, *Chem. Commun.* **1999**, 1575–1576; b) A. G. Orrillo, A. M. Escalante, R. L. E. Furlan, *Chem. Commun.* **2008**, 5298–5300; c) Z. Rodriguez-Docampo, S. Otto, *Chem. Commun.* **2008**, 5301–5303; d) M. von Delius, E. M. Geertsema, D. A. Leigh, *Nat. Chem.* **2010**, *2*, 96–101; e) J. F. Folmer-Andersen, J.-M. Lehn, *J. Am. Chem. Soc.* **2011**, *133*, 10966–10973; f) D. E. Whitaker, C. S. Mahon, D. A. Fulton, *Angew. Chem. Int. Ed.* **2013**, *52*, 956–959; *Angew. Chem.* **2013**, *125*, 990–993; g) J. Boekhoven, J. M. Poolman, C. Maity, F. Li, L. van der Mee, C. B. Minkenberg, E. Mendes, J. H. van Esch, R. Eelkema, *Nat. Chem.* **2013**, *5*, 433–437.

[12] Hydrazone and oxime linkages have previously been employed at low surface densities for the irreversible conjugation of biomolecules to NPs, but with no attempt to explore potential reversibility, see: a) N. Nagahori, M. Abe, S.-I. Nishimura, *Biochemistry* **2009**, *48*, 583–594; b) J. B. Blanco-Canosa, I. L. Medintz, D. Farrell, H. Mattoussi, P. E. Dawson, *J. Am. Chem. Soc.* **2010**, *132*, 10027–10033; c) X. Li, J. Guo, J. Asong, M. A. Wolfert, G.-J. Boons, *J. Am. Chem. Soc.* **2011**, *133*, 11147–11153.

[13] J. C. Love, L. A. Estroff, J. K. Kriebel, R. G. Nuzzo, G. M. Whitesides, *Chem. Rev.* **2005**, *105*, 1103–1169.

[14] A. G. Kanaras, F. S. Kamounah, K. Schaumburg, C. J. Kiely, M. Brust, *Chem. Commun.* **2002**, 2294–2295.

[15] N. Zheng, J. Fan, G. D. Stucky, *J. Am. Chem. Soc.* **2006**, *128*, 6550–6551.

[16] Model studies indicated that *N*-aroyl hydrazones such as **1** are stable under the AuNP synthesis conditions (see the Supporting Information, SI).

[17] F. Rastrelli, S. Jha, F. Mancin, *J. Am. Chem. Soc.* **2009**, *131*, 14222–14224.

[18] B. Yan, Z.-J. Zhu, O. R. Miranda, A. Chompoosor, V. M. Rotello, R. W. Vachet, *Anal. Bioanal. Chem.* **2010**, *396*, 1025–1035.

[19] Z. Hens, J. C. Martins, *Chem. Mater.* **2013**, *25*, 1211–1221.

[20] Colloidal stability of the AuNPs under the conditions used for hydrazone exchange was established independently, see SI.

[21] AuNP-**2** can also be prepared by direct synthesis from the appropriate disulfide, **2**$_2$, under conditions similar to those used for the preparation of AuNP-**1**. In the case of AuNP-**2**, however, a small amount of hydrazone reduction (<10%) was detected, together with a significantly larger mean NP diameter (>4.5 nm). This highlights one of the advantages of the dynamic covalent NP approach: allowing controlled manipulation of surface functionality within otherwise identical NP samples.

[22] Kinetic studies were performed in the presence of aldehyde **5** (1 equiv) and CF_3CO_2H (20 mM) at 25 °C. Subscripts "NP" and "MOL" are used to indicate parameters for the NP-bound and model bulk solution reactions, respectively. The kinetic parameters were determined by fitting using the COPASI software package: S. Hoops, S. Sahle, R. Gauges, C. Lee, J. Pahle, N. Simus, M. Singhal, L. Xu, P. Mendes, U. Kummer, *Bioinformatics* **2006**, *22*, 3067–3074. See SI for further discussion.

[23] J. Yang, J. Y. Lee, J. Y. Ying, *Chem. Soc. Rev.* **2011**, *40*, 1672–1696.

[24] See SI for further discussion and quantitative comparison of rates for these two processes.

[25] The nanoscale environment has recently been shown to affect physicochemical properties such as pK_a and redox potential: a) K. P. Browne, B. A. Grzybowski, *Langmuir* **2011**, *27*, 1246–1250; noncovalent interactions: b) M. Lucarini, P. Franchi, G. F. Pedulli, C. Gentilini, S. Polizzi, P. Pengo, P. Scrimin, L. Pasquato, *J. Am. Chem. Soc.* **2005**, *127*, 16384–16385; c) H. S. Mandal, H.-B. Kraatz, *J. Am. Chem. Soc.* **2007**, *129*, 6356–6357; d) H. D. Hill, S. J. Hurst, C. A. Mirkin, *Nano Lett.* **2009**, *9*, 317–321; and unimolecular and bimolecular photoreactions: e) A. J. Kell, R. L. Donkers, M. S. Workentin, *Langmuir* **2005**, *21*, 735–742; f) T. Zdobinsky, P. Sankar Maiti, R. Klajn, *J. Am. Chem. Soc.* **2014**, *136*, 2711–2714.